

Chapter 1

Introduction

Modern particle physics is described by a theory called the standard model (SM).

The SM describes a universe in which matter consists of particles of half-integer spin¹ called fermions. These fermions interact with each other through force mediating integer spin particles called bosons. This section will provide a basic outline of this theory as well as the known issues and need for a more basic theory.

1.1 Fundamental Particles

The SM matter in the universe is around 98% Hydrogen and Helium with the final 2% being heavier elements. To a very good approximation, the known matter in the universe consists of protons, neutrons, and electrons. Electrons are categorized in the standard model as leptons and are fundamental. Protons and neutrons are composites

¹Intrinsic angular momentum

CHAPTER 1. THEORETICAL MOTIVATION

of three quarks. The up quark (u) has $+2/3e^2$ charge, and the down quark (d) has $-1/3e$ charge, so the proton is an up-up-down combination and the neutron is down-down-up. These quark compounds are called hadrons and are categorized into two families: baryons (three quarks), and mesons (two quarks).

Although this is a good approximation of the known universe, through experimental and theoretical advances we know that there are more exotic phenomena that can be described by extending the known quarks and leptons to three generations. The three lepton generations are defined by the electron, muon, tau and their corresponding neutrinos. The $+2/3e$ charge quarks are the up, charm, and top; whereas the $-1/3e$ charge quarks are the down, strange, and bottom. These quarks and leptons are summarized in Table 1.1 along with their charge and mass.

Quarks and leptons define all known fermionic matter, with bosonic particles being responsible for particle interactions.

1.2 Fundamental Interactions

Interactions in the SM can be described by the four fundamental forces: electromagnetic, weak nuclear, strong nuclear, and gravity. These forces manifest by the exchange of a corresponding elementary boson. The intrinsic properties of these force carrying particles are responsible for the range and relative strength of the interaction.

The electromagnetic force is responsible for well known phenomena such as molec-

²e is the magnitude of the charge of the electron

CHAPTER 1. THEORETICAL MOTIVATION

particle	charge (e)	mass (MeV)
e	-1	0.5110
μ	-1	105.7
τ	-1	1777
ν_e, ν_μ, ν_τ	0	$< 2 \times 10^{-6}$
u	+2/3	2.3
d	-1/3	4.8
s	-1/3	95
c	+2/3	1.275×10^3
b	-1/3	4.18×10^3
t	+2/3	173.2×10^3

Table 1.1: List of SM fermions with their charge and mass. These particles all have spin 1/2.

ular bonds. This force is mediated by the photon, a massless, charge-less, spin 1 particle. The photon interacts with charged particles only. The fact that the photon is massless leads to the infinite range of the electromagnetic force.

The weak nuclear force manifests itself in nuclear decay, and is described by three force carrying bosons; the W^+, W^- , and Z . These bosons are massive, which leads to the weak force being short range. The W^\pm bosons have integer charge whereas the Z boson is charge-less, and all three have spin 1. The weak force is responsible for transitions between flavors³ of quarks (see Section 1.5). Quarks and leptons alike interact by the weak force.

The strong nuclear force is responsible for binding quarks together to form hadrons. The strong force describes the interactions of particles that carry color. Color is an intrinsic property of fundamental particles, and has three varieties; red, green and

³The six quark types

CHAPTER 1. THEORETICAL MOTIVATION

particle	charge (e)	spin	mass (GeV)
γ	0	1	0
W^\pm	± 1	1	80.4
Z	0	1	91.2
gl	0	1	0
gr	0	2	$< 6 \times 10^{-38}$

Table 1.2: List of SM force carrying bosons with their charge, mass and spin. The graviton has not yet been observed.

blue. This force is mediated by gluons, which are massless and interact with quarks.

The strong force is the strongest and shortest range of the known forces. The theory behind the strong force is described in more detail in Section 1.4

The known force carrying bosons and their properties are listed in table 1.2

The fourth known force, gravity, is both the most recognizable and least understood of the forces. All attempts at including gravity into the SM have failed, but hypothetically gravity should be mediated by the spin 2 graviton, which interacts with massive particles.. Gravity is by far the weakest of the fundamental forces.

1.3 Feynman Diagrams

Calculations in theoretical particle physics are facilitated by the use of feynman diagrams. Feynman diagrams are pictorial representations. These diagrams include the particles that interact (external lines), as well as the particles that mediate the interaction (internal lines), and where these external and internal lines intersect (vertices). An example diagram is shown in Figure 1.1. The electrons interact with a

CHAPTER 1. THEORETICAL MOTIVATION

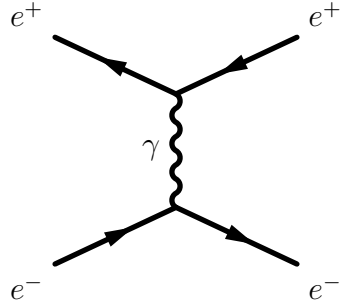


Figure 1.1: Feynman diagram depicting electron-positron scattering via the electromagnetic interaction.

photon (γ), and a force is observed. This diagram represents electromagnetic repulsion (coulomb force).

The rules governing the calculation of physical observables from these diagrams are defined by the theory of Quantum Electrodynamics (QED). Using these diagrams, the rules of QED let us calculate the matrix element (\mathcal{M}). \mathcal{M} can be related to physical quantities through the square modulus ($|\mathcal{M}|^2$), which is the probability density for a process to occur. From this, relevant quantities such as the cross section (see Section 2.1) of the process can be calculated.

Additionally, in the case that a particle decays we can evaluate the decay width (Γ). When a particle of mass M decays, there is a range of observed values of mass following a Breit-Wigner distribution centered at M . The decay width represents the width of this distribution at half the maximum. The average lifetime of the particle is $1/\Gamma$.

For a given process there can be multiple contributing diagrams, for instance for a calculation involving the Coulomb attraction shown in Figure 1.1, one must

CHAPTER 1. THEORETICAL MOTIVATION

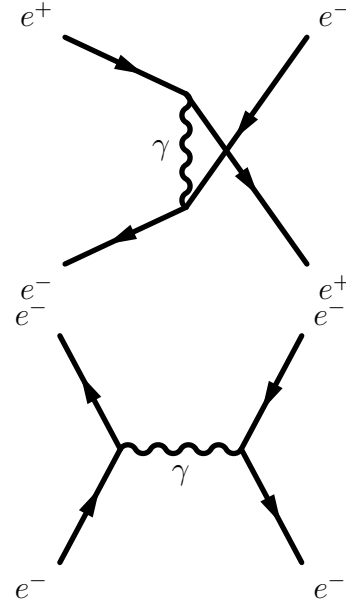


Figure 1.2: Feynman diagram depicting electron-positron scattering via the electromagnetic interaction in the u channel (top) and s channel (bottom).

also consider the diagrams shown in Figure 1.2, which have the same incoming and outgoing particles. Diagrams such as this interfere with each other constructively or destructively in the calculation of the matrix element, which can increase or decrease the cross section of the full process.

Vertices in a Feynman diagram are points where energy and momentum are conserved in the calculation. Each of the vertices contributes a factor of the coupling constant α to the matrix element computation. In the calculation of the full matrix element for the electron positron attraction shown in Figures 1.1 and 1.2, we must consider diagrams with higher vertex multiplicity such as those seen in Figure 1.3. To approximate \mathcal{M} in QED, we can perform an expansion in the vertex multiplicity n , summing over matrix elements within the same order i (\mathcal{M}_i^n). .

CHAPTER 1. THEORETICAL MOTIVATION

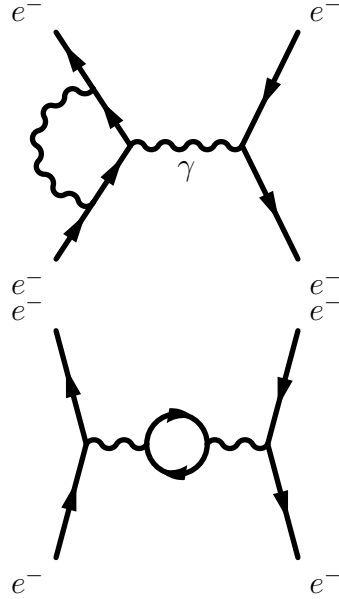


Figure 1.3: Feynman diagram depicting NLO electron-positron scattering.

$$\mathcal{M} = \sum_{n=1}^{\infty} \sum_i \mathcal{M}_i^n \quad (1.1)$$

Due to the fact that the coupling constant in QED is $1/137$, this expansion can terminate quickly because high n diagrams contribute much less to \mathcal{M} . A calculation involving all diagrams with the least number of vertices is called leading order. Calculations involving all diagrams with higher order contributions as well are called next-to leading order (NLO), next-to-next-to leading order (NNLO), etc.

Once the matrix element has been determined to an acceptable accuracy, we can extract the cross section in a straight forward manner. For the example electron-positron scattering process above the differential cross section has the following sim-

CHAPTER 1. THEORETICAL MOTIVATION

plified equation due to the special case of identical mass particles:

$$\left(\frac{d\sigma}{d\Omega} \right)_{CM} = \frac{|\mathcal{M}|^2}{64\pi^2 E_{cm}^2} \quad (1.2)$$

1.4 Quantum Chromodynamics

Quantum chromodynamics (QCD) is the theory describing the strong force, and is of particular importance for this thesis. The strong force is mediated by gluons which interact with particles that carry color. In QED, the photon is not charged, and thus can not interact with itself, however in QCD the gluon carries color and thus can interact with itself. Additionally, whereas the addition of a vertex greatly reduces the cross section in QED, the strong coupling constant α_s is of order 1, so higher order diagrams can contribute substantially to the measurement. This means that QCD processes are much more difficult to calculate than QED processes.

However, α_s is not constant, and in fact increases as the distance scale of an interaction increases (see Figure 1.4). This property of the the strong interaction is called asymptotic freedom. For high $|q^2|$, α_s has the following form:

$$\alpha_s(|q^2|) = \frac{\alpha_s(\mu^2)}{1 + (\alpha_s(\mu^2)/12\pi)(11n - 2f)\ln(|q^2|/\mu^2)} \quad (1.3)$$

CHAPTER 1. THEORETICAL MOTIVATION

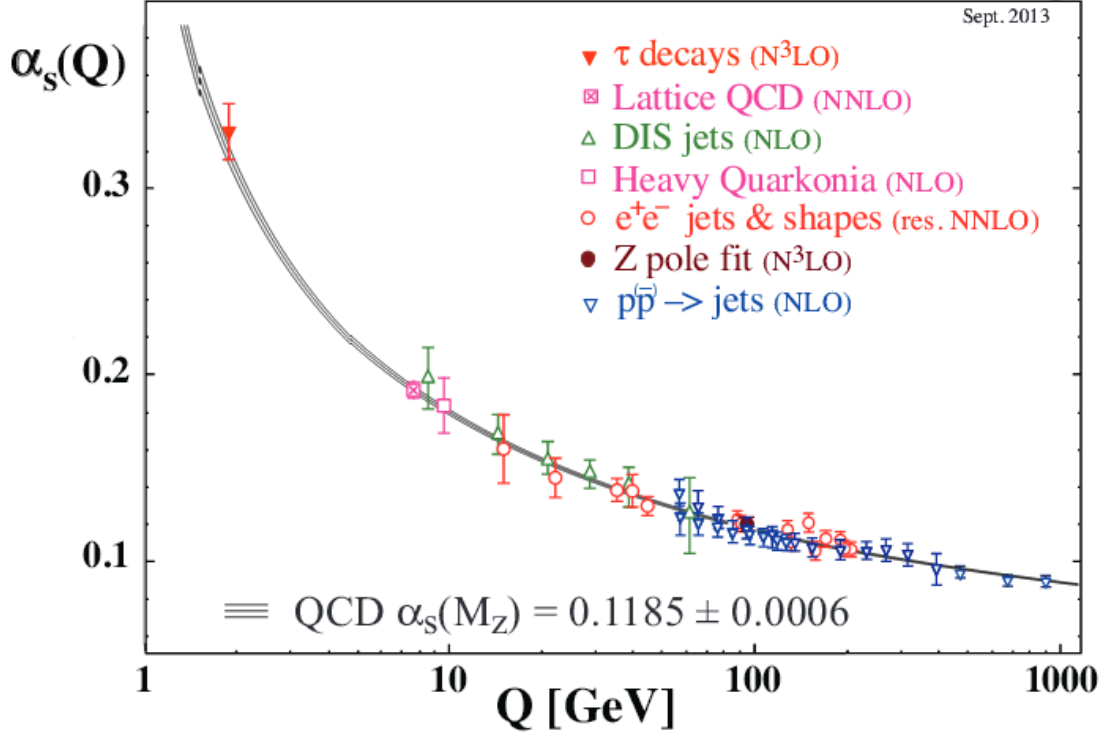


Figure 1.4: The QCD coupling constant α_s as a function of the energy scale Q .

where n is the number of colors (3), and f is the number of flavors (6), and μ^2 is some arbitrary energy where $\alpha_s(\mu^2) < 1$. Therefore because $11n > 2f$, α_s will decrease as energy increases.

Therefore as the distance between two quarks increases, so do the forces holding them together. This large force at a characteristic distance ($\sim 10^{-15}$ m) is the reason why it is difficult to observe a free quark (quark confinement). Although quarks can not be observed alone, there are ways of precisely determining the physical properties of free quarks through reconstruction of their decay products.

When a quark pair is produced with a high momentum, their separation increases

CHAPTER 1. THEORETICAL MOTIVATION

quickly. As the separation of these quarks increases, the energy of the QCD field between them increases as well. If this separation is high enough, the energy between the quarks will reach a threshold where quark pair production is energetically favorable. At this threshold, the constituent quarks are then joined by these pair produced quarks. Additional quark pairs can be created many times, and the initial quark is detected as many hadrons that are collimated into a stream of particles called a jet. This process is called hadronization,

The α_s parameter is low at short distances (or equivalently high energy); just like in QED, the impact of higher order diagrams is low. This allows the calculation of QCD diagrams using a finite perturbative expansion, and allows us to only consider only free quarks in high energy QCD calculations. The characteristic interaction energy where free quarks can be considered is around 400MeV, which is much lower than energy scales considered in this thesis, so we will only be referring to free quark interactions.

1.5 The Weak Force

The weak force is felt by quarks and leptons alike. It is weaker than both the electromagnetic and the strong force, which leads to longer decay times for weakly decaying particles. The weak force is responsible for changing of quark flavor in an interaction. A vertex involving a change in quark flavor contributes a factor of V_{ij}

CHAPTER 1. THEORETICAL MOTIVATION

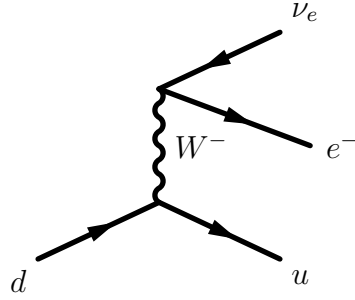


Figure 1.5: Feynman diagram depicting beta decay via the weak interaction.

to the matrix element, where V_{ij} is an element of the Cabibbo Kobayashi Maskawa (CKM) matrix (shown in Figure 1.6). For example, the calculation of the diagram in Figure 1.5 (beta decay) includes a factor of $V_{ud} = 0.97427$. The CKM matrix is roughly diagonal, which means that a process which changes quark generation is rare.

Weak force interactions are dependent on the chirality of the interacting particle. Chirality for massless particles is dependent on the relative orientation of the momentum and spin axes. Particles with momentum and spin aligned are referred to as right-handed, and particles with the momentum axis opposite to spin are left-handed⁴. For massive particles this concept is generalized such that right- and left-handed components of a wavefunction can be extracted by using the right-handed operator $(1+\gamma^5)/2$ and the left-handed operator $(1-\gamma^5)/2$. The W boson only interacts with left-handed fermions whereas the Z boson interacts with right- and left-handed fermions with differing strengths.

⁴This convention is reversed for anti-particles

$$V_{\text{CKM}} = \begin{pmatrix} 0.97427 \pm 0.00014 & 0.22536 \pm 0.00061 & 0.00355 \pm 0.00015 \\ 0.22522 \pm 0.00061 & 0.97343 \pm 0.00015 & 0.0414 \pm 0.0012 \\ 0.00886^{+0.00033}_{-0.00032} & 0.0405^{+0.0011}_{-0.0012} & 0.99914 \pm 0.00005 \end{pmatrix}$$

Figure 1.6: The CKM quark mixing matrix.

1.6 Electroweak Symmetry Breaking

Through the electroweak symmetry breaking mechanism, the mass of the W and Z bosons, and all fermions can be generated in the SM. We consider a scalar potential of the form:

$$V(\Phi) = m^2 \Phi^\dagger \Phi + \lambda (\Phi^\dagger \Phi)^2 \quad (1.4)$$

$$\Phi = \frac{1}{\sqrt{2}} \begin{pmatrix} \sqrt{2}\phi^+ \\ \phi^0 + ia^0 \end{pmatrix} \quad (1.5)$$

where Φ is the Higgs field. A plot of this potential can be seen in Figure 1.7. The minimum of the potential is not at $V(0)$, and this point is unstable. The Higgs field has a non-zero vacuum expectation value (VEV).

Using the Higgs Lagrangian

$$\mathcal{L} = (D_\mu \Phi)^\dagger (D_\mu \Phi) - V(\Phi) \quad (1.6)$$

$$(D_\mu \Phi) = (\partial_\mu + ig\sigma^\alpha W_\mu^\alpha/2 + ig'YB_\mu/2)\Phi \quad (1.7)$$

we can extract the masses of the W and Z bosons as

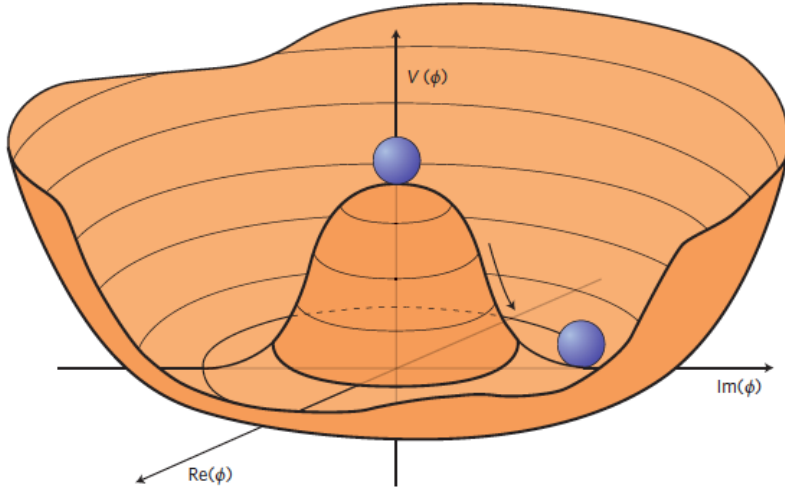


Figure 1.7: The Higgs potential..

$$M_W^2 = \frac{g^2 v^2}{4} \quad (1.8)$$

$$M_Z^2 = \frac{(g'^2 + g^2)v^2}{4} \quad (1.9)$$

One new particle is predicted, a massive chargeless spin 0 particle called the Higgs boson. A particle consistent with the Higgs boson has been discovered in 2012 at the LHC.

1.7 Beyond the Standard Model

The SM is possibly the most successful theory in physics, but also one that is ultimately incomplete. We know that there are physical phenomena that the SM

CHAPTER 1. THEORETICAL MOTIVATION

does not predict. The presence of dark matter and dark energy in the universe [1] is not currently explained by the SM. Given that dark matter and energy account for approximately 95% of the universe, this is not a small issue. The SM does not explain the observation of neutrino oscillations [2], which implies that neutrinos have mass. The SM also does not naturally explain the relative values of fundamental constants such as why the weak force is 10^{33} times as strong as gravity. This issue is known as the hierarchy problem, and it is assumed that a complete theory would have a natural explanation for the seemingly random values of these constants.

It is essential for a complete understanding of the universe that we probe beyond the standard model (BSM) theories that provide solutions to these issues. Theories involving compact extra dimensions [3] for example provide a natural explanation to the hierarchy problem. In these theories forces propagate in higher dimensions that are compactified. In this theory, the propagation of SM massive fields in higher dimensions leads to discrete modes, which are detectable as new massive particles. The propagation of the SM W or Z leads to excited modes that are referred to as the W' and Z' . A novel way to look for BSM physics then is to attempt the creation and detection of massive states such as these bosons. In this thesis we discuss one such search for a W' boson.

The W' boson is a particle predicted by many BSM theories such as Little Higgs [4], Composite Higgs models [5], and Noncommuting Extended Technicolor [6].

Chapter 2

Experimental Setup

To look for BSM physics, we want to create new massive particles. For this, we collide lighter particles at a high energy. The energy released in the collision can manifest in more massive particles due to the concept of mass-energy equivalence ($E=mc^2$). The collision may create one of these new particles, and from it's decay products an experimenter can reconstruct the properties of BSM physics that created the massive state.

For the measurements presented in this thesis, we collide high energy proton beams, which are designed to produce a high collision energy in comparison to fixed-target or electron-positron collisions.

2.1 Luminosity and Cross Section

To understand how many occurrences of any physical process to expect in a set of collisions, we need to define at a minimum the concepts of luminosity, L , and cross section, σ .

The cross section of a process is a measurement of how likely a collision will result in the process of interest. The phrase cross section refers to the physical cross section of a classical target and is thus measured in units of area. In a high energy collision, the cross section no longer refers to the physical dimensions of the target, and can be calculated directly from Feynman diagrams. The areas associated with these cross sections is very small and is measured in barns (b), which is $10^{-28}m^2$. BSM physics signatures have cross sections that are generally on the order of picobarns (pb) or femptobarns (fb). The process cross section is highly dependent of the energy of the collision and is why it is very important to have large, high energy accelerators for the discovery of new physics. The cross section of some SM processes are shown in Figure 2.1.

Luminosity is a measure of the intensity of the colliding beams and is the number of collisions expected per unit time per unit area. To look for BSM physics, we need to collect an ensemble of useful collisions (events), and thus higher luminosity leads to a larger ensemble and higher statistical precision. Additionally, collecting data over time leads to a larger ensemble, so the time-integrated luminosity is a more useful variable to describe the total amount of data collected, which is reported in fb^{-1} .

CHAPTER 2. EXPERIMENTAL SETUP

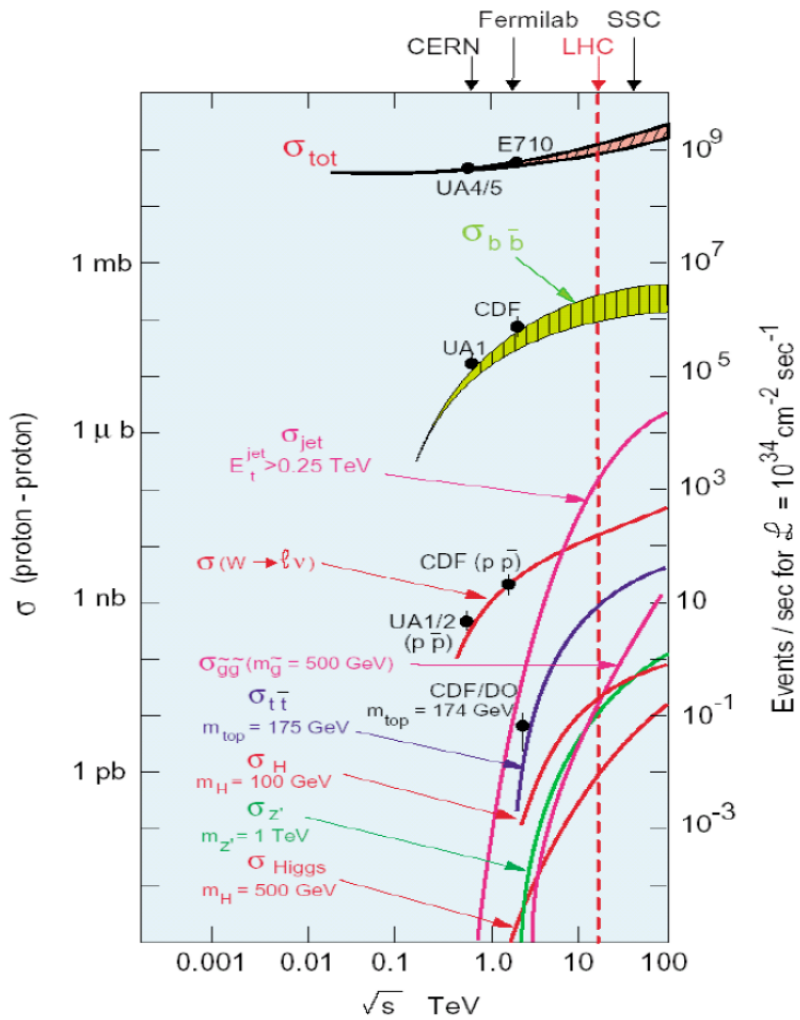


Figure 2.1: Standard model cross sections as a function of collision energy.

CHAPTER 2. EXPERIMENTAL SETUP

Given in relevant collider properties, the luminosity can be defined as:

$$L = \frac{\gamma f k_B N_p^2}{4\pi\epsilon\beta^*} F \quad (2.1)$$

where γ is the Lorentz factor, f is the frequency of revolution, k_B is the number of bunches in the beam, N_p is the number of protons per bunch, ϵ is the transverse emittance, β^* is the betatron function, and F is a reduction factor based on the crossing angle.

With these two concepts we can extract the predicted number of events for a given process, N_i :

$$N_i = \int L dt \times \sigma_i \quad (2.2)$$

2.2 The LHC

The Large Hadron Collider (LHC) is a particle accelerator designed to reach collisions energies far surpassing any previous design. The LHC is a synchrotron that accelerates protons to 99.999997% the speed of light. These proton beams are then collided at a center-of-mass energy (\sqrt{s}) of 8 TeV.

The life of a proton at the LHC starts out as hydrogen gas within the injector of LINAC 2 linear accelerator. The atoms are ionized using an electric field, stripping the electron. The resulting proton is accelerated using an oscillating electric field.

CHAPTER 2. EXPERIMENTAL SETUP

The protons are accelerated in a straight line to an energy of 50MeV, or 31%the speed of light.

At this energy, linear acceleration is not practical, and the protons enter the Proton Synchrotron Booster (PSB). The PSB is composed of four 157 m circumference superimposed synchrotrons that accelerate the protons using electric fields that are synchronized to the revolution frequency of the beams. The protons are kept on the circular accelerator with a magnetic field directed into the plane formed by the accelerator ring, which increases in strength as the protons gain energy. After the acceleration from the booster, the protons are at en energy of 1.4GeV, or 92%the speed of light.

After the PSB, the protons enter the Proton Synchrotron (PS), a 628 m circumference synchrotron, which accelerates the protons to 25GeV, or 99.93%the speed of light. After the PS, the protons enter the Super Proton Synchrotron (SPS), a 7 km circumference synchrotron, which accelerates the protons to 450GeV, or 99.9998%the speed of light.

Finally, the beams enter the LHC. This is the final synchrotron ring, with a circumference of 27 km. After the SPS, the protons are inserted into the LHC in one of two evacuated tunnels depending on which direction around the ring the beam is to travel.

The LHC uses 1232 dipole magnets to keep the protons in the ring as they accelerate. which provide an 8.3 T field over their length. In order to deliver such a field, the

CHAPTER 2. EXPERIMENTAL SETUP

magnets use superconducting niobium-titanium cables. These cables are cooled by superfluid helium to -271.3 C in order to achieve this superconductivity. During each revolution the energy of each proton in the LHC ring increases by 5 MeV. After being fully accelerated in the LHC, the protons are at an energy of 4TeV, or 99.999997%the speed of light.

The proton beams are then directed together for collisions in four positions around the ring. Each beam in the LHC ring contains 2808 bunches of protons, and each bunch contains 110 billion protons. These bunches need to be collimated in order to maximize collision frequency, which is accomplished by the use of 392 focusing quadrupole magnets. Each of these collision points houses its own detector, ALICE (A Large Ion Collider Experiment), ATLAS (A Toroidal LHC Apparatus), CMS (Compact Muon Solenoid), and LHCb (Large Hadron Collider beauty). The ALICE detector is primarily used for experiments involving heavy ion collisions that expand the current understanding of concepts such as the quark-gluon plasma and quark confinement LHCb is specialized for physics involving b quarks, such as measuring CP violation parameters from b-hadron interactions.

CMS and ATLAS are large general purpose detectors. These detectors are used for many different types of physics searches, and are the two detectors responsible for the Higgs boson discovery. For the purposes of this thesis we will be concentrating on the CMS detector

These accelerator segments and detectors can be shown in Figure 2.2.

CHAPTER 2. EXPERIMENTAL SETUP

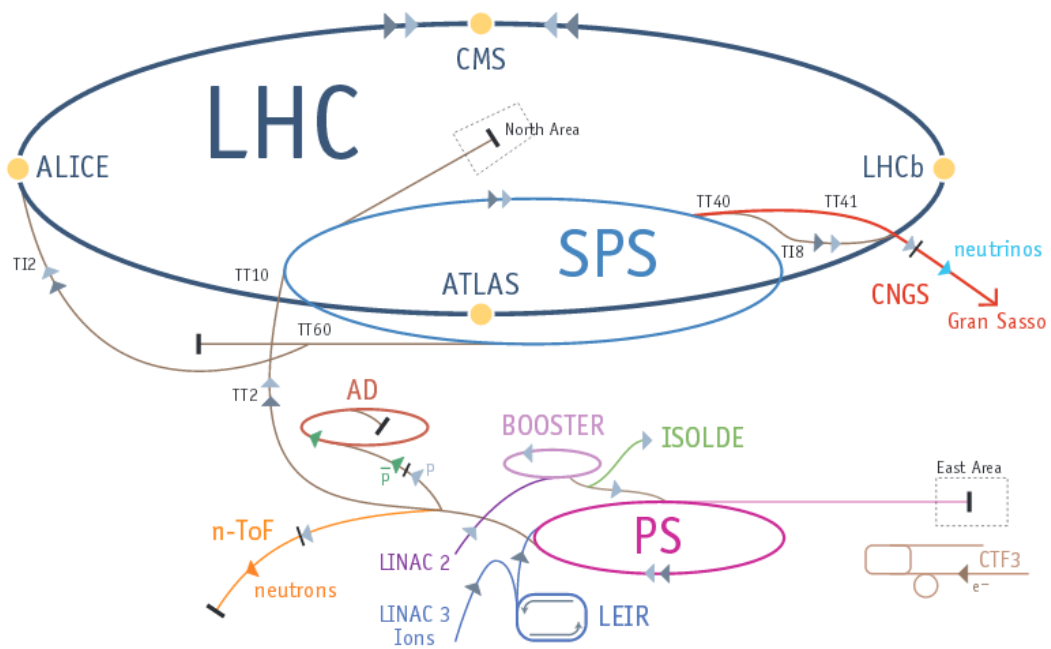


Figure 2.2: A diagram of the LHC.

2.3 CMS detector

Here we will detail the basics of the CMS detector subsystems, for a more complete description, see Reference [7]. The purpose of the CMS detector is to measure properties of particles that are created in a collision such as the energy and trajectory. The detector needs to supply enough information so that particles can be reconstructed and classified. Generally, we can reconstruct most physics signatures by analyzing electrons, muons, photon, charged hadrons, and neutral hadrons. The CMS detector has dedicated algorithms and systems that are specifically designed to identify each of these categories.

In order to reconstruct these particles, we impose a uniform axial magnetic field throughout the inner detector with the use of a superconducting magnet.

The trajectory of charged particles is important to extract information such as charge and momentum. The process of reconstructing the trajectory of these particles is called tracking. Near the interaction point tracks are very dense, and tracking becomes very difficult. In this region we use a fine array of silicon pixels that register a charge particles position based on charge deposited in the device. Additional measurements are made by a second series of silicon detectors called the Silicon Strip Tracker. Using a series of these position measurements, we can fit a charged particle track.

Energy can be measured by the use of calorimeter systems. A calorimeter is a detector designed such that a particle will deposit all of its energy within the detector

CHAPTER 2. EXPERIMENTAL SETUP

in the form of photons, which can be detected to extract a measure of the total energy. These systems are subdivided into the Electromagnetic Calorimeter (ECAL) and Hadronic Calorimeter (HCAL). The ECAL uses scintillation crystals to detect particles that interact primarily with the electromagnetic force such as electrons and photons. Hadrons pass through the ECAL with minimal loss and deposit energy in the HCAL, which uses layers of absorber and scintillator to first create a shower of secondary particles, and then measure the total energy of these secondary particles.

The detection of muons requires a specially designed system that lies outside of the ECAL, HCAL, and magnet. Muons pass through the ECAL and HCAL without losing a substantial fraction of their energy. To reconstruct the trajectory of muons, we use several different tracking systems both inside and outside the magnet.

See Figure 2.3 for a diagram of the full detector, and Figure 2.4 for a cross-sectional view of the detector subsystems.

2.3.1 Pixel Tracker

The closest detector system to the interaction point is the silicon pixel tracking system. This system extends from a radius of 4 cm to 11 cm in the barrel, and is designed to track charged particles in a very dense environment. This is achieved with three arrays of two dimensional silicon pixels placed at a radii of 4.4 cm, 7.3 cm, and 10.2 cm, as well as two endcap disks for a total of 65 million pixels. When a charged particle traverses one of the $100 \mu\text{m} \times 150 \mu\text{m}$ pixels, it imparts enough

CHAPTER 2. EXPERIMENTAL SETUP

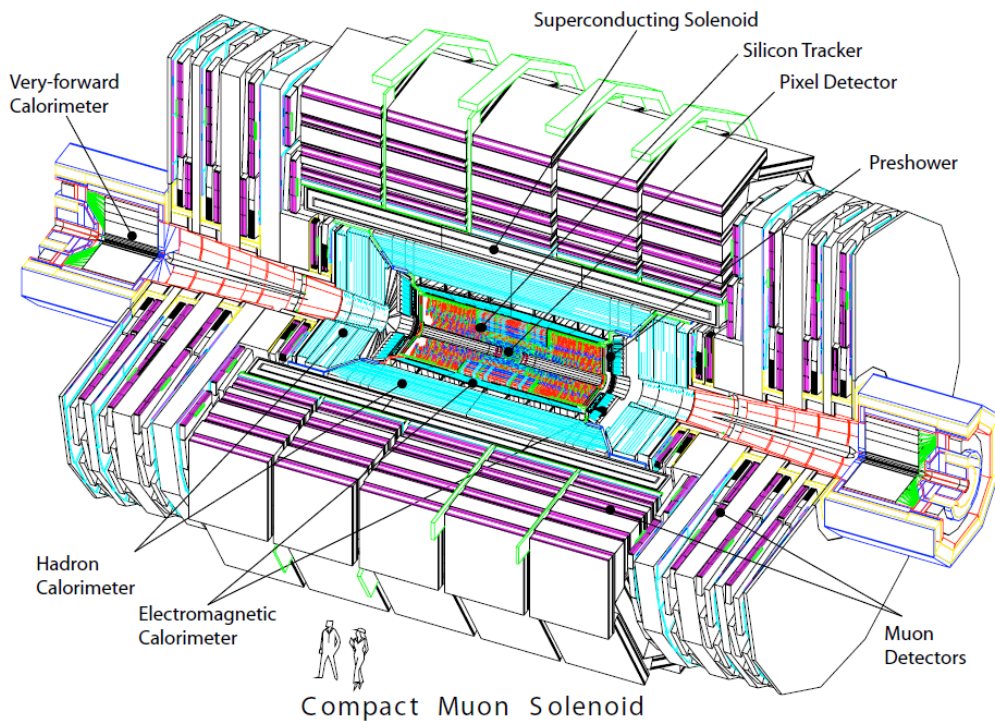


Figure 2.3: A diagram of the full CMS detector.

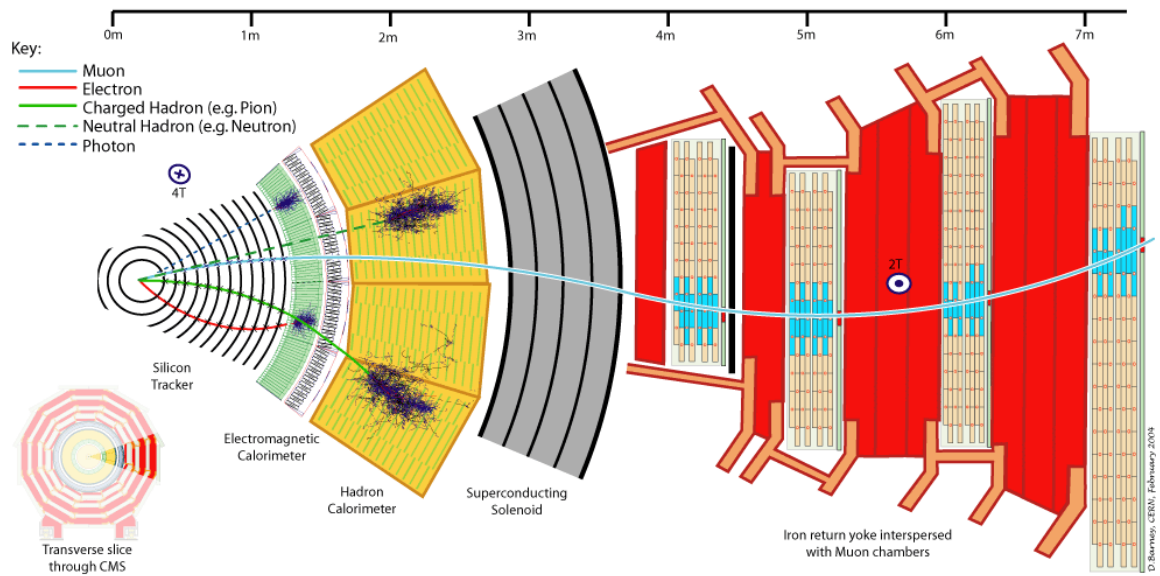


Figure 2.4: A cross-sectional view of the CMS detector.

CHAPTER 2. EXPERIMENTAL SETUP

energy to the silicon to eject an electron. The electrons and their corresponding hole are detected on the pixel surface as a signal. This signal allows us to extract a position measurement for the charged particle.

The entire system exists in a magnetic field, so the trajectory of the electrons and holes are deflected in the r, ϕ plane before detection. The angle of this Lorentz drift is 23° , which causes the electron-hole pairs to be detected over a wide region covering multiple pixels. This effect improves the spacial resolution to $10 \mu\text{m}$ in $r-\phi$ space due to the fact that the charge center can be reconstructed by more measurements, whereas the z resolution is $20 \mu\text{m}$ due to the fact that there is no magnetic deflection in this direction. The pixel detectors in the endcap disks are angled at 20° in a turbine-like design to take advantage of this effect.

Figure 2.5 shows a diagram of the full pixel detector.

2.3.2 Silicon Strip Tracker

Outside of the silicon pixel tracker out to a radius of 130 cm in the barrel lies the silicon strip tracking system. This system consists ten arrays of silicon strips that work in much the same way as the pixel detectors.

The system is segmented into the inner barrel, outer barrel, inner disk, and endcap segments. The inner barrel segment ($20 \text{ cm} < r < 55 \text{ cm}$) uses four arrays of $10 \text{ cm} \times 80 \mu\text{m}$ silicon microstrips . The outer barrel ($55 \text{ cm} < r < 130 \text{ cm}$) uses six arrays of large pitch $25 \text{ cm} \times 180 \mu\text{m}$ silicon microstrips.

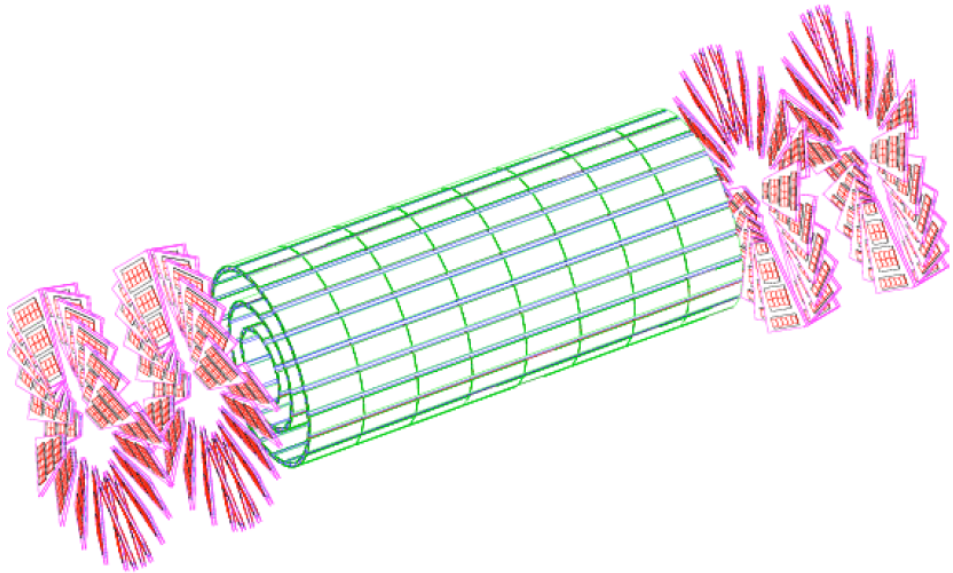


Figure 2.5: A diagram of the pixel detector.

The endcap silicon strip detector consists of nine disks from $120 \text{ cm} < z < 280 \text{ cm}$. The inner disk segment contains three smaller disks that connect the inner barrel and endcap segments.

Figure 2.6 shows a diagram of the silicon tracker.

2.3.3 Electromagnetic Calorimeter

The ECAL is designed to provide energy information for electrons and photons. These particles will typically deposit all of their energy within the detector, which is detectable as photons.

To do this, the ECAL uses 61200 lead tungstate (PbWO_4) scintillation crystals in the barrel and 7324 in each endcap. Lead tungstate is chosen as a scintillation

CHAPTER 2. EXPERIMENTAL SETUP

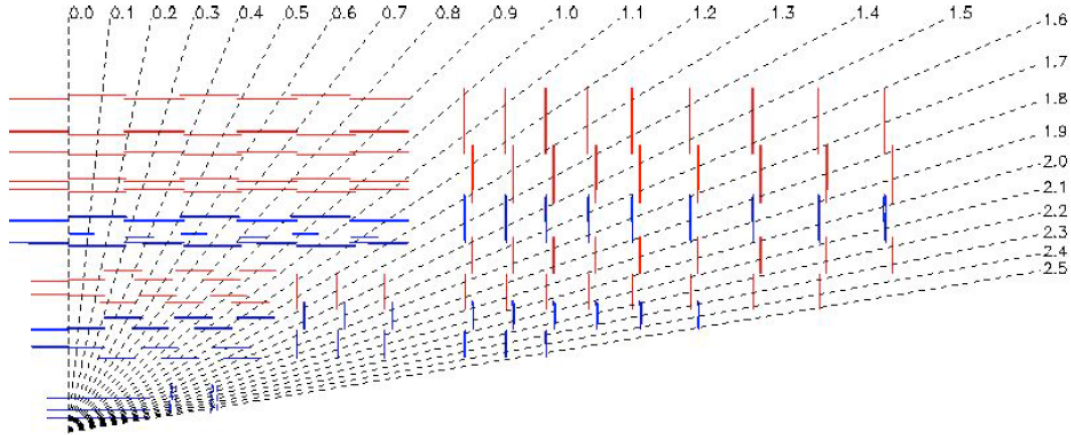


Figure 2.6: A diagram of the silicon tracking system.

material because it has a short radiation length (0.89 cm), fast response (25 ns for 80% of light), and can withstand harsh radiation environments (10 Mrad). The light emitted is around 30 photons per MeV for the energy of the particle of interest, which is somewhat low. Therefore, the ECAL uses avalanche photodiodes in the barrel and voltage phototriodes in the endcap segments to amplify the signal upon readout.

The endcap regions of the ECAL include a preshower detector that is used to distinguish high energy photons from decaying pions. A pion decaying to two closely spaced photons can mimic one high energy photon to the 2.2 cm wide ECAL crystals. The preshower is able to distinguish these events with a finer granularity (2 mm) silicon strip detector.

Figure 2.7 shows a diagram of the ECAL.

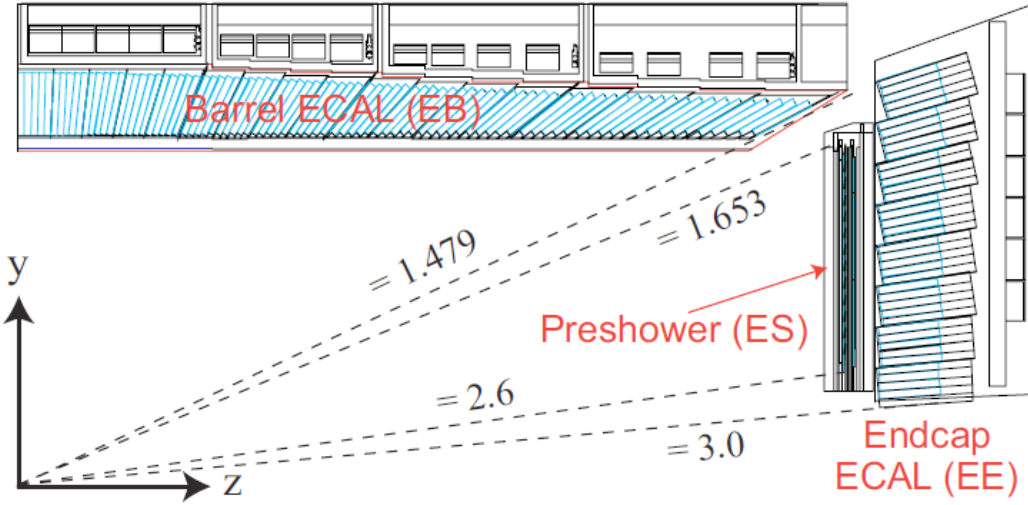


Figure 2.7: A diagram of the ECAL system.

2.3.4 Hadronic Calorimeter

The HCAL is designed to give the energy of charged and neutral hadrons, which generally lose very little energy in the ECAL. The HCAL is segmented into the inner barrel (inside the magnet), outer barrel (outside the magnet), endcap, and forward (close to the beamline).

The HCAL uses alternating layers of absorber and scintillator to calculate the energy of these hadrons. The absorber creates a cascade of secondary particles that emit photons in the scintillator which can then be detected and summed to reconstruct the energy of the initial hadron. The photons emitted in the scintillator are carried to the photodetectors by optical waveguides. The HCAL uses hybrid photodiodes to detect the scintillation light and provide a signal that can be used to extract the total energy of the hadron.

CHAPTER 2. EXPERIMENTAL SETUP

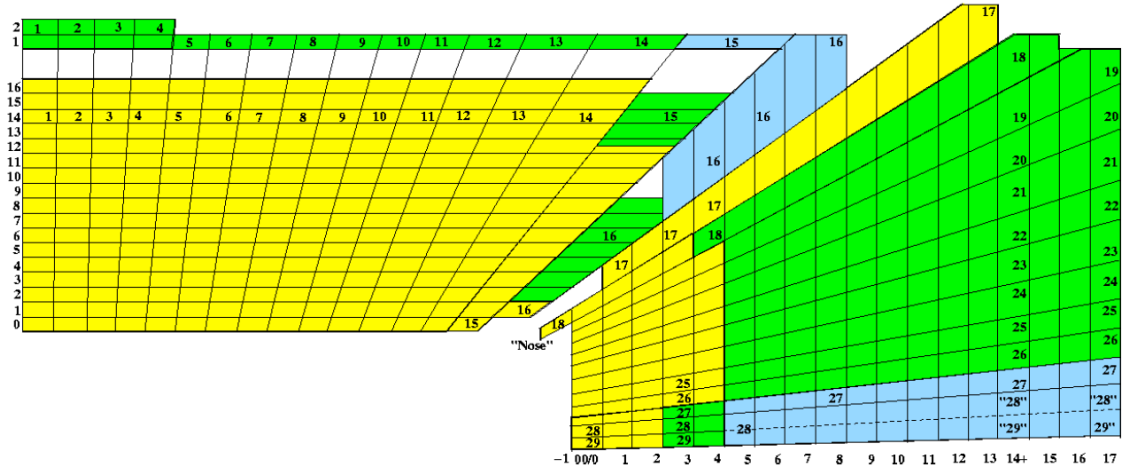


Figure 2.8: A diagram of the HCAL system.

Figure 2.8 shows a diagram of the HCAL.

2.3.5 Magnet

A charged particle moving perpendicular to a magnetic field follows a helical trajectory. The curvature of this helix is dependent on the momentum of the particle, and the handedness is dependent on the charge. Therefore, by immersing the tracking volume in an axial magnetic field we can get an accurate measurement of these properties. The stronger the magnetic field, the more precise these measurements can be for a high energy particle due to the more distinct curvature. To produce this field, CMS employs the largest superconducting magnet ever built.

The design goal for the magnet is to be able to reproduce high momentum muons. The benchmark used for this is to have a momentum resolution of $\Delta p/p \leq 10\%$ at

CHAPTER 2. EXPERIMENTAL SETUP

a muon momentum of 1 TeV. To achieve this, we employ a solenoid with a length of 12.9 m and bore of 5.9 m. The coils of this solenoid are superconducting niobium-titanium, which produce a uniform 3.8 T magnetic field in the interior. The coils are wound in four layers, for a total of 2168 turns that carry 19.5 kA of current.

The magnet additionally provides structural support to withstand the weight of the CMS detector as well as the magnetic force exerted from it's own magnetic field.

2.3.6 Muon System

The reconstruction of muons and electrons starts at the inner silicon tracking system. Whereas electrons deposit their energy in the ECAL, a muon will traverse the ECAL and HCAL without significant interaction because a muon is around 200 times as massive. Muons are of interest to the Higgs discovery as well as BSM physics, and an accurate determination of the muon energy is also required for determination of the total event energy and missing energy. Therefore, the CMS detector has a large system purely designed to reconstruct muons, which lies outside all other detector systems at CMS.

The muon system is comprised of a gaseous detectors interleaved with iron. The iron is saturated with the return field of the magnet, which creates a magnetic field at one half of the internal field strength and oriented in the opposite direction. The three layers of this “return yoke” system bends muons to get an accurate measure of the momentum outside of the magnet.

CHAPTER 2. EXPERIMENTAL SETUP

The trajectory of the muons is reconstructed with three types of gaseous detectors. The detectors work on the same basic principle, where an incoming muon ionizes the gas creating an electron-hole pair. The electron is detected by the anode, and the hole is detected by a cathode. A coincidence of these two measurements gives a measure of the position and time that a muon traversed the detector. With a series of these measurements, a trajectory can be fit, and physical quantities of interest can be reconstructed.

In the barrel region ($|\eta| < 1.2$), drift tubes are used because the neutron flux and magnetic field are low. A drift tube is a detector consisting of a gas filled tube with an anode wire. The ionized electron from the gas volume travels to the anode wire, and a measurement of position is made. The detection of this electron registers the position along the wire (z coordinate). The $r\phi$ coordinate within the drift tube cross sectional can be calculated by using the drift time of the ionized electrons to the anode.

In the endcap region, where the magnetic field and neutron flux are high, cathode strip chambers are used. Cathode strip chambers are trapezoidal in shape with six gas gaps for ionization. These gas gaps each have one plane of cathode strips pointing radially outward and one plane of anode wires oriented perpendicular to the cathode.

In both the barrel and endcap regions, resistive plate chambers are used. These detectors are composed of two parallel resistive plates separated by a gas gap. The design goal of the resistive plate chambers is to complement the cathode strip cham-

CHAPTER 2. EXPERIMENTAL SETUP

bers and drift tubes to give two independent measurements of position. Additionally, resistive plate chambers offer very quick and accurate time resolution. This offers a quick approximation of the muon momentum which is useful for the trigger system and matching a muon track to a bunch crossing.

The muon system and inner tracker both contribute to the trajectory measurement of a muon. In terms of momentum resolution, the inner tracker offers much better sensitivity up to around 200 GeV. After 200 GeV, the muon system starts to significantly improve the momentum measurement.

Figure 2.9 shows a diagram of the muon system.

2.3.7 Trigger

The LHC delivers around 1 billion proton-proton collisions per second. However, because of the current computing limitations, the CMS detector system can only write around 100 collisions per second as data. Therefore, a trigger system is developed to distinguish the most potentially interesting physics signatures.

The L1 trigger takes information from the calorimeter and muon systems and their correlations. When one of these detectors produces a signal, the information takes $3.2 \mu\text{s}$ to reach the L1 processing area and return to the detector. The L1 processing time for the information for a maximum of $1 \mu\text{s}$ where the decision is made to keep the event to search for potential physics signatures. The L1 has various algorithms designed to keep “trigger primitives”, which can be objects such as high p_T muons,

CHAPTER 2. EXPERIMENTAL SETUP

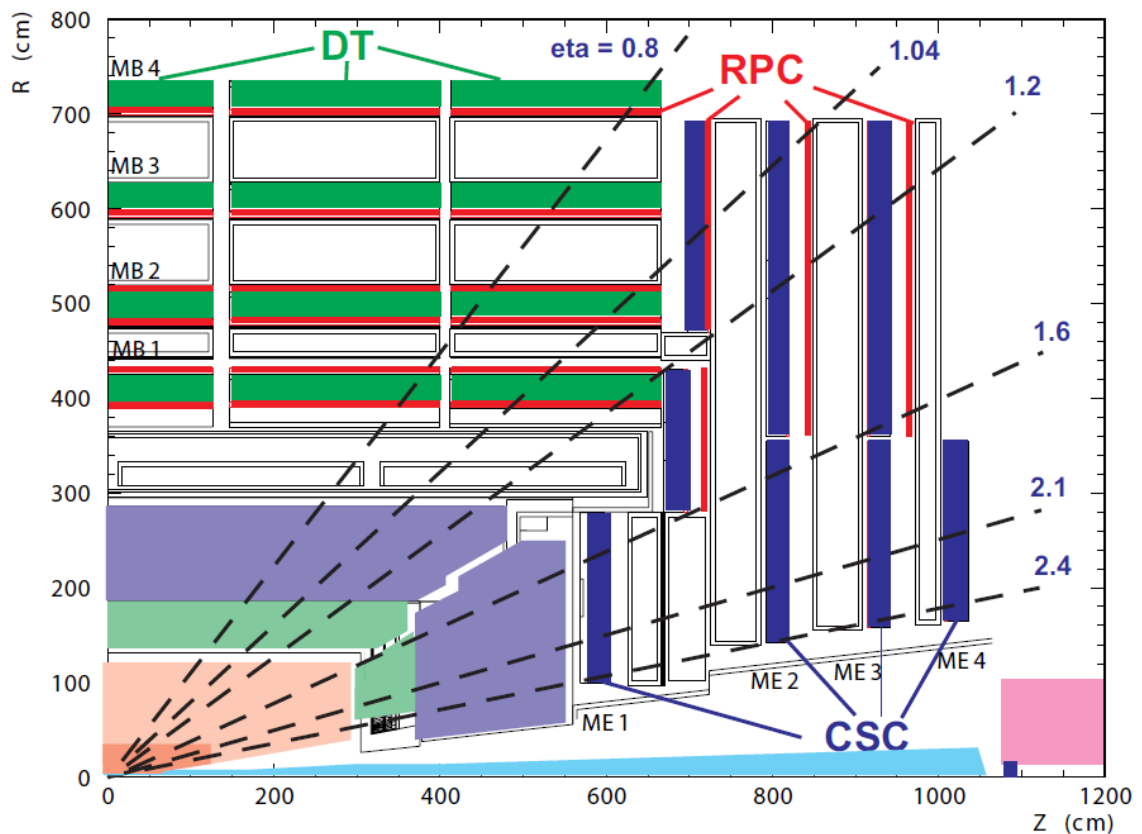


Figure 2.9: A diagram of the muon system.

CHAPTER 2. EXPERIMENTAL SETUP

electrons, jets or full event information like total energy or E_T^{miss} . The L1 trigger only saves on average of 1 out of every 1000 events.

After the L1 trigger, the trigger primitive events are processed by the high level trigger (HLT). The HLT again saves only 1 out of 1000 of these events. The processing time for the HLT algorithm is longer than the L1 system, and to extract the potentially exciting physics objects the algorithm performs partial event reconstruction. An event that enters the HLT algorithm is first analyzed based on the output of the calorimeters and muon system, then pixel tracking is performed, then finally full tracking. An event that passes the L1 and HLT is then put into storage for analysis.

Chapter 3

Introduction to the W' Search

Many beyond the Standard Model (BSM) theories predict new massive gauge bosons. This note presents a search for a heavy partner of the Standard Model (SM) W gauge boson, generally referred to as the W' (see Chapter 1.7). We focus on the $W' \rightarrow t\bar{b}$ decay mode motivated by the ability to lower QCD multijet background in this channel when compared to light flavor hadronic decay modes.

The primary signal under investigation is a W' particle in which the interaction with quarks is defined by the following Lagrangian,

$$\mathcal{L} = \frac{V_{q_i q_j}}{2\sqrt{2}} g_w \bar{q}_i \gamma_\mu (a_{qi,qj}^R (1 + \gamma^5) + a_{qi,qj}^L (1 - \gamma^5)) W' q_j + \text{H.c.}, \quad (3.1)$$

This is the most general, lowest-dimensional, model-independent effective Lagrangian for the W' boson. Here $a_{qi,qj}^L$, $a_{qi,qj}^R$ are the left- and right-handed couplings of W' to

CHAPTER 3. INTRODUCTION TO THE W' SEARCH

quarks. For a SM-like W' , $a_{qi,qj}^L = 1$, $a_{qi,qj}^R = 0$.

Searches for a high mass W' resonance have been performed at the Tevatron [8,9] and at CMS [10–12] and ATLAS [13] at the LHC. Currently, the most stringent limits on W' cross-sections exclude a right-handed W' particle with mass below 2.05 TeV at the 95% C.L. In this analysis we do not consider W' lighter than ~ 1.3 TeV since there are stringent limits on W' production at these masses.

We present a search for $W' \rightarrow t\bar{b}$ followed by the fully hadronic decay chain $t \rightarrow W + b$ followed by $W \rightarrow$ hadrons. This differs from [10] since the final state is comprised of only jets. In our kinematic regime of interest ($M_{W'} \gtrsim 1.3$ TeV) the top quark is quite energetic, and due to its Lorentz boost, the angular separation between its immediate decay products will be small. The jets resulting from the hadronization of the b quark and the light quarks from W boson from the top decay usually overlap, resulting in one ‘fat’ jet. This search uses special techniques to identify the substructure of this top jet, and further selection based on substructure information as well as b -tagging strongly suppresses the QCD background.

The search uses 19.7 fb^{-1} of 8 TeV data collected from the CMS experiment in 2012.

Chapter 4

Analysis Strategy

The focus of this analysis are heavy resonances decaying into $t\bar{b}$. Thus the $W' \rightarrow t\bar{b}$ decay results in a mostly dijet topology, with the b and top jets being predominantly back-to-back.

After requiring a high transverse momentum, the primary sources of background are QCD multijet and SM $t\bar{t}$ production due to the high abundance of QCD present by requiring a dijet topology and the high $t\bar{t}$ production contribution fraction that remains after top jet discrimination.

Of these two main sources, QCD multijet production is dominant and is estimated by a data driven technique similar to [14]. We invert certain substructure cuts used to identify top jets to define sideband regions; we keep the cut on the mass of the top jet to avoid the kinematic bias in forming the invariant mass distribution of the top-b candidate. One sideband region is used to measure the average b-tagging rate, which

CHAPTER 4. ANALYSIS STRATEGY

is then applied to pre-b-tag data to obtain the QCD estimate. The other sidebands are then used to check the performance of the QCD estimation in data.

The SM $t\bar{t}$ contribution is estimated from Monte Carlo simulation. We also subtract the pre-tagged $t\bar{t}$ from the pre-tagged data sample when measuring the average b-tagging rate. The measurement of the average b-tagging rate is then independent of $t\bar{t}$, and the $t\bar{t}$ contribution is added at the end as a separate background component. The contribution of the single top production to the background was found to be negligible.

The data and background components are then used as templates by the Bayesian statistical procedure to set the exclusion limits on W' . This procedure uses a binned likelihood to calculate limits for the signal cross-section in the $W' \rightarrow t\bar{b}$ branching fraction. We use the limit setting framework “Theta” [15], which calculates exclusion limits using a shape based approach.

Chapter 5

Data Sample and Event Selection

The data sample used for this analysis corresponds to $19.7 \pm 0.5 \text{ fb}^{-1}$ of integrated luminosity collected in 2012 at $\sqrt{s} = 8 \text{ TeV}$. See Table 5.1 for a summary of the datasets used in the analysis. Generation of Standard Model $t\bar{t}$ and single top events is performed by Powheg. The Monte Carlo simulation samples used for background estimation can be found in table 5.1.

5.1 Signal Samples

The Lagrangian presented in equation 3.1 has been implemented in CompHEP [18] and used for event generation. The mass of the top quark was set to 172.5 GeV. Pythia was used for hadronization. The CTEQ6M parton distribution functions were selected and the QCD scale was set to the W' invariant mass. The width of the W'

CHAPTER 5. DATA SAMPLE AND EVENT SELECTION

Jet Datasets	
Dataset	Luminosity (pb ⁻¹)
/Jet/Run2012A-22Jan2013-v1/AOD	888
/JetHT/Run2012B-22Jan2013-v1/AOD	4403
/JetHT/Run2012C-22Jan2013-v1/AOD	7052
/JetHT/Run2012D-22Jan2013-v1/AOD	7414
Total Analyzed Luminosity	19757
Monte Carlo Datasets	
Dataset	Cross-section(pb)
TT_Mtt-700to1000_CT10_TuneZ2star_8TeV-powheg-tauola	245.8 (NNLO)
TT_Mtt-1000toInf_CT10_TuneZ2star_8TeV-powheg-tauola	245.8 (NNLO)
T_t-channel_TuneZ2star_8TeV-powheg-tauola	56.4 (NNLO)
Tbar_t-channel_TuneZ2star_8TeV-powheg-tauola	30.7 (NNLO)
Tbar_tW-channel-DR_TuneZ2star_8TeV-powheg-tauola	11.1 (NNLO)
T_tW-channel-DR_TuneZ2star_8TeV-powheg-tauola	11.1 (NNLO)
T_s-channel_TuneZ2star_8TeV-powheg-tauola	3.79 (NNLO)
Tbar_s-channel_TuneZ2star_8TeV-powheg-tauola	1.76 (NNLO)
QCD_Pt-300to470_TuneZ2star_8TeV_pythia6	1759.6
QCD_Pt-470to600_TuneZ2star_8TeV_pythia6	113.9
QCD_Pt-600to800_TuneZ2star_8TeV_pythia6	27.0
QCD_Pt-800to1000_TuneZ2star_8TeV_pythia6	3.57
QCD_Pt-1000to1400_TuneZ2star_8TeV_pythia6	0.738
QCD_Pt-1400to1800_TuneZ2star_8TeV_pythia6	0.0335

Table 5.1: Primary datasets and Monte Carlo samples used. Including the corresponding integrated luminosity or cross-section of each dataset [16, 17].

CHAPTER 5. DATA SAMPLE AND EVENT SELECTION

resonance and cross-sections were obtained from CompHEP numerical calculations.

The generation was performed using the $2 \rightarrow 4$ process $W' \rightarrow t ; t \rightarrow Wb ; W \rightarrow q_i q_j$, where q_i and q_j represent quarks. W decays including b quarks are not considered due to the negligible branching fraction. The process preserves all spin correlations between production and decay.

The W' generation can be performed using three different couplings.

- W'_R - The purely right-handed W' where $a_{qi,qj}^L=0$, $a_{qi,qj}^R=1$
- W'_L - The purely left-handed W' where $a_{qi,qj}^L=1$, $a_{qi,qj}^R=0$
- W'_{LR} - The mixed-coupling W' where $a_{qi,qj}^L=1$, $a_{qi,qj}^R=1$

Because of the SM-like couplings of W'_L and W'_{LR} , we must consider the interference between SM single top and signal. The W'_R Monte Carlo samples were generated without SM single top. The right-handed W' samples used in this analysis are given in table 5.2. The cross-sections listed here are leading order. The cross-sections used in the main analysis are scaled to next-to leading order with a multiplicative k factor of 1.2 which is extracted from [19]. The left-handed and mixed-coupling W' samples used in this analysis are given in table 5.3 and 5.4 respectively. In order to have sufficient statistical precision in the signal region, these samples have a loose generator level p_T cut of 200 GeV set on the b jet from the W' decay. The effect of this pre-selection is investigated in section 5.3.

CHAPTER 5. DATA SAMPLE AND EVENT SELECTION

Right-Handed Signal Samples

Dataset	$\Gamma_{W'}(\text{GeV})$	(LO) Cross-Section (pb)
SingletopWprimeTToHad_M-1300_right_TuneZ2star_8TeV-comphep	43.7	0.4852
SingletopWprimeTToHad_M-1500_right_TuneZ2star_8TeV-comphep	50.0	0.2198
SingletopWprimeTToHad_M-1700_right_TuneZ2star_8TeV-comphep	57.3	0.1038
SingletopWprimeTToHad_M-1900_right_TuneZ2star_8TeV-comphep	64.1	0.0507
SingletopWprimeTToHad_M-2100_right_TuneZ2star_8TeV-comphep	70.9	0.0254
SingletopWprimeTToHad_M-2300_right_TuneZ2star_8TeV-comphep	77.6	0.0131
SingletopWprimeTToHad_M-2700_right_TuneZ2star_8TeV-comphep	91.2	0.0039

Table 5.2: Signal samples used in the analysis. Quoted cross-section and $\Gamma_{W'}$ were obtained from the CompHEP generator. A k factor of 1.2 is implemented on the quoted cross-sections.

CHAPTER 5. DATA SAMPLE AND EVENT SELECTION

Left-Handed Signal Samples

Dataset	$\Gamma_{W'}(\text{GeV})$	(LO) Cross-Section (pb)	Selection Efficiency
SingletopWprimeTToHad_M-1300_left_TuneZ2star_8TeV-comphep	43.7	0.4248	0.157
SingletopWprimeTToHad_M-1500_left_TuneZ2star_8TeV-comphep	50.0	0.2622	0.104
SingletopWprimeTToHad_M-1700_left_TuneZ2star_8TeV-comphep	57.3	0.1669	0.0679
SingletopWprimeTToHad_M-1900_left_TuneZ2star_8TeV-comphep	64.1	0.1237	0.0507
SingletopWprimeTToHad_M-2100_left_TuneZ2star_8TeV-comphep	70.9	0.1047	0.0429
SingletopWprimeTToHad_M-2300_left_TuneZ2star_8TeV-comphep	77.6	0.0971	0.0397
SingletopWprimeTToHad_M-2700_left_TuneZ2star_8TeV-comphep	91.2	0.0933	0.0379

Table 5.3: Left-Handed signal samples used in the analysis. Quoted cross-section and $\Gamma_{W'}$ were obtained from the CompHEP generator. A k factor of 1.2 is implemented on the quoted cross-sections. The cross sections listed here take into account the generator level b jet p_T cut, and represent the visible cross section. The efficiency of this cut is provided under the column labeled Selection Efficiency.

CHAPTER 5. DATA SAMPLE AND EVENT SELECTION

Mixed Signal Samples

Dataset	$\Gamma_{W'}(\text{GeV})$	(LO) Cross-Section (pb)	Selection Efficiency
SingletopWprimeTToHad_M-1300_mixed_TuneZ2star_8TeV-comphep	87.4	0.9327	0.290
SingletopWprimeTToHad_M-1500_mixed_TuneZ2star_8TeV-comphep	101.0	0.4743	0.172
SingletopWprimeTToHad_M-1700_mixed_TuneZ2star_8TeV-comphep	114.6	0.2700	0.105
SingletopWprimeTToHad_M-1900_mixed_TuneZ2star_8TeV-comphep	128.2	0.1776	0.0711
SingletopWprimeTToHad_M-2100_mixed_TuneZ2star_8TeV-comphep	141.7	0.1334	0.0540
SingletopWprimeTToHad_M-2300_mixed_TuneZ2star_8TeV-comphep	155.3	0.1128	0.0458
SingletopWprimeTToHad_M-2700_mixed_TuneZ2star_8TeV-comphep	182.4	0.0986	0.0400

Table 5.4: Mixed-Coupling signal samples used in the analysis. Quoted cross-section and $\Gamma_{W'}$ were obtained from the CompHEP generator. A k factor of 1.2 is implemented on the quoted cross-sections. The cross sections listed here take into account the generator level b jet p_T cut, and represent the visible cross section. The efficiency of this cut is provided under the column labeled Selection Efficiency.

5.2 Trigger Selection

Due to our interest in highly boosted jets, our data was taken using the HLT_HT750 trigger, which requires the event to have H_t of at least 750 GeV. The trigger efficiency is measured in data and Monte Carlo by investigating the looser HLT_HT550 trigger. The selection used for this measurement includes a loose kinematic selection. We require two jets with $p_T > 300$ GeV and the cut described in Section 5.9. The denominator is defined as passing this selection and the HLT_HT550 trigger, whereas the numerator is required to pass the selection and both the HLT_HT550 and HLT_HT750 trigger. The efficiency is shown in Figure 5.1 and is parameterized as a function of summed leading and sub-leading jet p_T . The extracted trigger efficiency is used to weight the Monte Carlo samples used in the analysis to account for the loss in efficiency in the turn-on. We do not observe perfect agreement in data and Monte Carlo, so we use the trigger efficiency derived from data to weight our Monte Carlo samples.

5.3 Signal Characteristics

The W' boson of interest is very massive, and produces highly boosted top quarks. The decay products of these top quarks become more collimated as the boost increases. When the top decays hadronically, we observe one merged jet over the two distinct jets that would be detected at a lower boost. This jet has a large character-

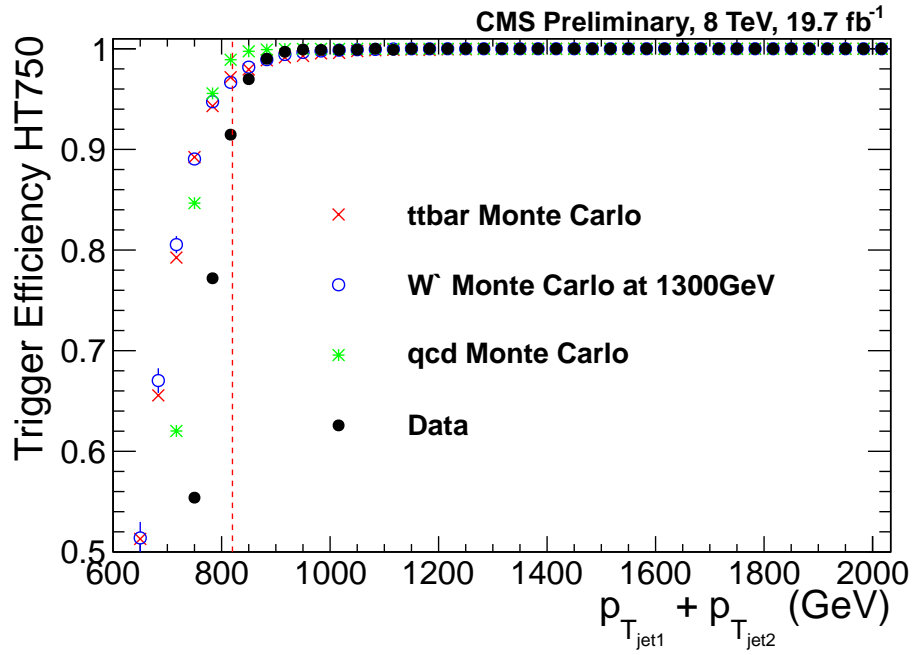


Figure 5.1: Trigger efficiency of HLT-HT750 measured as a function of the summed p_T of the leading and sub-leading jets. The red dashed line indicates the minimum for the analysis, at which point the trigger is nearly fully efficient.

istic radius and a distinct substructure. This high energy jet merging is investigated in Figure 5.2. Here, the ‘top candidate’ is just the leading jet in the event. It is also required to be hemispherically separated from a Monte Carlo truth b jet. This jet is generally a merged W boson at low p_T and a merged top at high p_T . The ‘W candidate’ (used for the bottom plots) is assembled from the pair of generator level non-b quarks that are close to the W mass (within 2.0 GeV). The central feature of this analysis is using this jet merging to discriminate signal from background.

We place a generator level p_T cut on the b quark from the W’ decay in the left-handed and mixed-coupling W’ samples (see Section 5.1). To investigate the effect

CHAPTER 5. DATA SAMPLE AND EVENT SELECTION

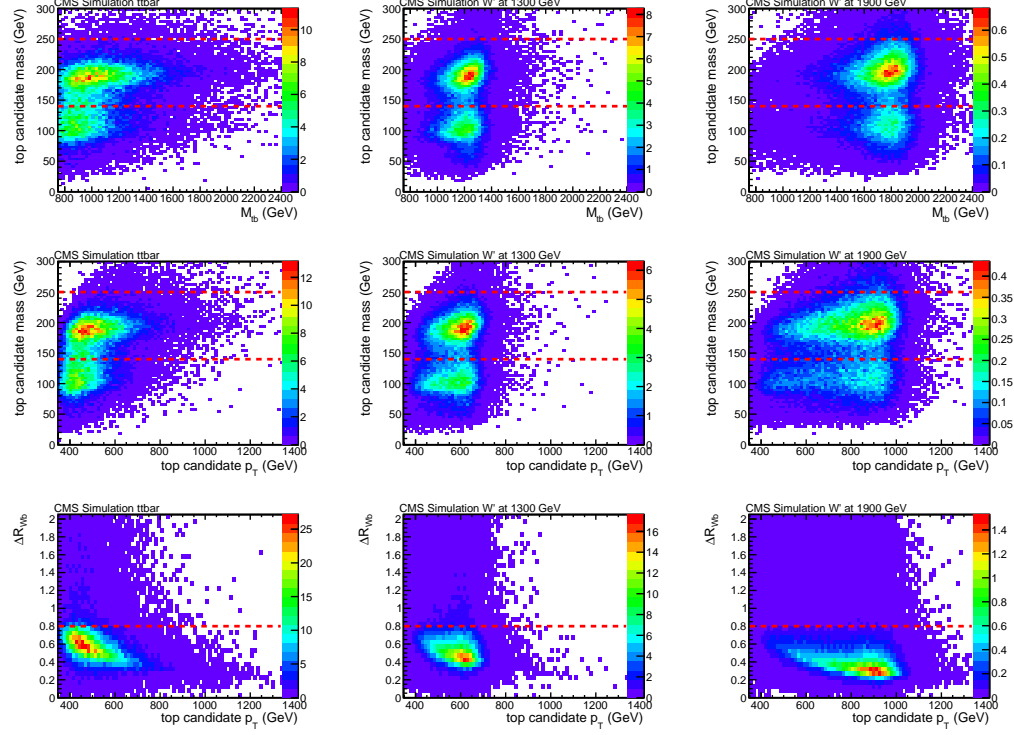


Figure 5.2: Investigation of top merging within Monte Carlo samples of interest. $t\bar{t}$ (left) W'_R Monte Carlo at 1300GeV (middle) W'_R Monte Carlo at 1900GeV (right). The red lines on the top and middle plots indicate the top candidate mass cut in the full selection (see Section 5.8). The red line on the bottom plots indicate the characteristic jet radius used to investigate fully merged top jets (see Section 5.4).

of this pre-selection, we look at the effect of an even tighter cut. Figure 5.3 shows the ratio of generator level b p_T cuts. The denominator requires a generation level p_T cut of 200 GeV and the numerator requires a generation level p_T cut of 230 GeV. This ratio is parameterized in the p_T of the CA8 jet that the generation particle is matched to ($\Delta R < 0.5$ is used for matching). The turn on of this tighter cut is well below the analysis level cut of 370 GeV. Thus, the effect of the generation level b p_T cut on selections requiring the analysis level p_T cut is negligible.

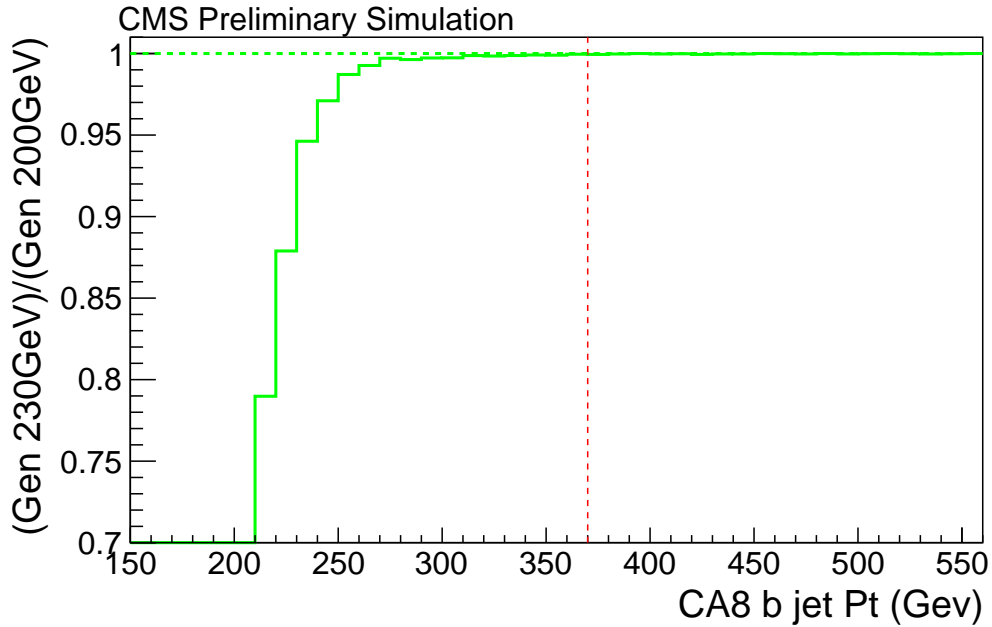


Figure 5.3: Ratio of CA8 p_T using the generation level b p_T cut of 230 GeV and 200 GeV. The red line is the analysis level p_T cut of 370 GeV. The sample used for this study is W'_{LR} at 1300 GeV

5.4 Jet Reconstruction

All data is reconstructed using CMSSW 5.3.x, and uses jet energy corrections from FT_53_V21_AN5 [20]. The Particle Flow reconstruction algorithm is used to reconstruct all data and Monte Carlo samples used for the analysis. This algorithm uses information from all sub-detectors to categorize particles as muons, electrons, photons as well as charged and neutral hadrons. Charged hadrons identified as pileup are removed from the inputs to the jet clustering algorithms by Charged Hadron Subtraction (CHS). Pileup vertices are identified as vertices that have a lower p_T than the primary vertex. Isolated charged leptons are removed, and neutral pileup compo-

CHAPTER 5. DATA SAMPLE AND EVENT SELECTION

nents are removed with a residual area-based method. For more detail, see [14]. The PF candidates are then used to create ‘Particle Flow jets’ as follows. Jet clustering is performed with a sequential recombination algorithm which compiles jets by merging the minimum of $d_{ij} = \min(k_{Ti}^{2m}, k_{Tj}^{2m})\Delta_{ij}/R$ where $\Delta_{ij} = \sqrt{(y_i - y_j)^2 + (\phi_i - \phi_j)^2}$. We use the Cambridge-Aachen (CA) [21,22] algorithm implemented by FastJet 3 [23,24], which assigns a value of $m = 0$, and thus is not weighted by p_T . An R value of 0.8 is used for the analysis. The CA algorithm has been shown to be more efficient than the the k_T and the anti- k_T algorithms for finding hard subjets [25].

We use anti- k_T jet energy corrections for all jets in the analysis. The jet energy corrections derived are adequate for the CA $R = 0.8$ jet algorithm for the jet momenta considered here as can be seen from 7 TeV studies in simulation comparing AK5 and CA8 jets [14]. We use the 2012 prescription for jet energy corrections [26]. We apply AK7 Particle Flow with charged hadron subtraction (AK7PFchs) jet energy corrections for all data and Monte Carlo samples.

5.5 Event Pre-selection

The following pre-selection is applied:

- The event must have a good primary vertex as computed by a deterministic annealing filter (DAF) ($|z_{\text{Primary Vertex}}| < 24$ cm, $N_{\text{DOF}} > 6$).
- Two jets with $|y| < 2.4$

CHAPTER 5. DATA SAMPLE AND EVENT SELECTION

- Only two jets with $p_T > 150$ GeV
- Leading Jet $p_T > 450$ GeV & Sub-leading Jet $p_T > 370$ GeV
- Loose Particle Flow jet identification [27] is applied
- Leading and sub-leading jet are separated by $|\Delta y| < 1.6$
 - This cut is described in Section 5.9
- Beam background events are removed using the following requirements:
 - In events with at least 10 tracks, a minimum of 25% of these tracks must be high purity tracks.

The requirement that there are only two jets with $p_T > 150$ GeV is useful for vetoing "three-prong" trijet events, which could impact the kinematics of the top-W candidate invariant mass distribution and bias the background estimate.

5.6 $t\bar{t}$ p_T Re-weighting

In order to correct for known differences in the top p_T spectrum between data and $t\bar{t}$ Monte Carlo, we re-weight Monte Carlo using the Generator level p_T of the top and anti-top with the recommended prescription. With p_{T_t} and $p_{T_{\bar{t}}}$ being the generator p_T of the top and anti-top respectively, the scale factor applied to each event in the

$t\bar{t}$ Monte Carlo expectation is:

$$SF = \sqrt{e^{0.156 - 0.00137 p_{T_t}} \times e^{0.156 - 0.00137 p_{T_{\bar{t}}}}} \quad (5.1)$$

Although this procedure was not designed for the kinematic range in our analysis, we prefer to use the prescription as it is more consistent with our measurement of the $t\bar{t}$ normalization (see Section 6.5).

5.7 Pileup Correction

We re-weight our Monte Carlo samples to account for differences due to pileup using the recommended procedure. To create a scale factor for number of primary vertices, we use Monte Carlo truth to extract the number of pileup interactions. Then we compare this to the mean number of interactions per crossing from data. This is extracted using the pileup distribution from the rereco datasets listed in table 5.1. For this calculation we use the suggested minbias cross-section of 69.4 mb. The scale factor is then the data distribution divided by the distribution in Monte Carlo and is applied to the signal and $t\bar{t}$ Monte Carlo samples to improve data to Monte Carlo agreement. Figure 5.5 shows the distribution of reconstructed primary vertices in Data, $t\bar{t}$, and signal Monte Carlo before and after the re-weighting has been applied. The pileup correction has very little effect on the eventual M_{tb} full selection, as seen in Figure 5.6, for W'_R signal Monte Carlo at the 1900 GeV mass point. Similarly,

CHAPTER 5. DATA SAMPLE AND EVENT SELECTION

there is little effect $t\bar{t}$ Monte Carlo as can be seen in Figure 5.7. A study has been conducted to investigate the effect of the suggested systematic uncertainty of 5% on the as can be seen in Chapter 8. Figure 5.4 shows the number of primary vertices in data and signal Monte Carlo with respect to discrimination variables used to separate signal from background.

5.8 Combined CMS Top Tagging Algorithm

The CMS top tagging algorithm takes CA jets with $R = 0.8$ as input. The algorithm first attempts to decompose the CA jet into two primary subjets, and then performs a secondary decomposition to attempt to split the subjets into secondary subjets [28]. In this process, particles with low p_T or a large angular distance from the jet center are omitted. The top tagging algorithm is based on the following cuts

- **Jet Mass** $140 \text{ GeV} < m_{\text{jet}} < 250 \text{ GeV}$ - The mass of the CA jet is required to be consistent with the top quark mass.
- **Number of Subjets** $N_{\text{subjets}} > 2$ - The number of subjets found by the algorithm must be at least 3.
- **Minimum Pairwise Mass** $m_{\text{min}} > 50 \text{ GeV}$ - The three highest p_T subjets are taken pairwise, and each pair's invariant mass is calculated. m_{min} is the mass of the pair with the lowest invariant mass. The minimum pairwise mass must be close to the W mass.

CHAPTER 5. DATA SAMPLE AND EVENT SELECTION

Figure 5.8 shows the comparison of Signal and QCD Monte Carlo for the above top tagging selection. Here, the N-subjettiness and subjet b-tagging cuts are not applied.

The N-subjettiness algorithm can be used for boosted top jet identification [29].

N-subjettiness defines τ_N variables as follows

$$\tau_N = \frac{1}{d_0} \sum_i p_{T,i} \min\{\Delta R_{1,i}, \Delta R_{2,i}, \dots, \Delta R_{N,i}\} \quad (5.2)$$

where $\Delta R_{J,i}$ is between the subjet candidate and a constituent particle. d_0 is a normalization factor

$$d_0 = \sum_i p_{T,i} R_0 \quad (5.3)$$

where R_0 is the characteristic jet radius used by the jet clustering algorithm. For this analysis we use the one pass kt method of subjet axes minimization. τ_N is a measure of how consistent the jet energy is with originating from N subjets. Additional discrimination power when using N-subjettiness variables is achieved by cutting on the ratio of two of these variables. Figure 5.9 shows τ_3/τ_2 comparison using signal and QCD Monte Carlo samples. We use the standard operating point of $\tau_3/\tau_2 < 0.55$ [28] in the full selection.

The use of b-tagging algorithms on subjets is described in [30]. We apply the Combined Secondary Vertex b-tagging algorithm to all of the subjets found by the CA declustering sequence described above. The optimal discrimination variable when

CHAPTER 5. DATA SAMPLE AND EVENT SELECTION

using subjet b-tagging is the maximum discriminant out of the three or four subjets found. Figure 5.10 shows the maximum subjet CSV b discriminant comparison using signal and QCD Monte Carlo samples. We use the standard CSV working point $SJ_{\text{CSVMAX}} > 0.679$.

Substructure variables in the signal region have known differences in data and Monte Carlo [28]. We use the top tagging scale factor with the addition of subjet b-tagging and N-subjettiness discrimination that is extracted from efficiency comparisons of data and Monte Carlo in a highly pure semileptonic $t\bar{t}$ sample. The scale factor for this effect is 1.04 and is applied to the signal Monte Carlo samples used in the main analysis. There is a 13% uncertainty on this scale factor which is purely statistical, as the study is dominated by statistical uncertainty. The scale factor is obtained from the plots shown in Figure 5.11.

5.9 Delta Rapidity Cut

At high $M_{t\bar{b}}$, jets that originate from QCD multijet production are widely separated in rapidity (high Δy). However the jets originating from a high mass $t\bar{b}$ resonance do not exhibit such pronounced separation. The effect is not pronounced over the entire $M_{t\bar{b}}$ spectrum, but for high values of $M_{t\bar{b}}$ the analysis can achieve greater separation of signal and background. We therefore place a cut on $|\Delta y| < 1.6$ for the full selection. The value for this cut was chosen by investigating the

CHAPTER 5. DATA SAMPLE AND EVENT SELECTION

Signal/ $\sqrt{\text{Background}}$ distribution in events that have $M_{t\bar{b}} > 2000$ GeV. Because it is not as effective over the entire $M_{t\bar{b}}$ range, the value is set slightly off the peak to minimize loss of signal efficiency. Figure 5.12 shows the comparison of $|\Delta y|$ for high $M_{t\bar{b}}$ in signal and QCD MC. Here, the N-subjettiness and subjet b-tagging cuts are not applied.

5.10 b-jet Identification

To enhance the sensitivity of the analysis, the Combined Secondary Vertex (CSV) b-tagging algorithm is applied to the subleading jet. We use the standard operating point CSVM ($\text{CSV} > 0.679$). Due to the fact that our signal content contains only $t\bar{b}$ and the only Monte Carlo used in background estimation is $t\bar{t}$, the Monte Carlo to data scale factor used in the analysis for b-tagging is the b-tagging Scale Factor for b quarks (SF_b). We use the suggested scale factor parameterized in p_T with the following functional form for b candidate jet $p_T < 800$ GeV

$$SF_b = 0.938887 + 0.00017124 \times p_T - 2.76366 \times 10^{-7} \times p_T^2 \quad (5.4)$$

Any b candidate jet with $p_T > 800$ GeV is weighted with SF_b evaluated at 800 GeV. The parameterized SF_b is the suggested EPS13 prescription [30] from the b-tagging POG generated from measurements in both muon-jet and ttbar data representing

CHAPTER 5. DATA SAMPLE AND EVENT SELECTION

20 fb^{-1} of integrated luminosity. The uncertainty associated with this scale factor parameterization is described in Chapter 8. b-tagging operating points and scale factors have been validated for use with anti-kt jets with a R value of 0.5 (AK5 jets). In our kinematic regime it is assumed that the change in cone size will have a small effect. We apply an additional 2% systematic uncertainty to the signal Monte Carlo samples used in the analysis. This is a conservative estimate of the uncertainty, validated by the following study:

For the 2700 GeV signal sample, we included both AK5 and CA8 jets in the event selection. All jets considered were required to be in our pt range ($p_T > 350 \text{ GeV}$). We attempt to match a CA8 jet to the corresponding AK5 jet using a constraint on η and ϕ ($\Delta R < 0.3$). The results were 579041 CA8 jets pass pt cut, of these, 567155 pass the η , ϕ matching to AK5 jets. Of the matched jets, 96.9% record the same value for the CSV cut (pass or fail). In addition, the ratio of b-tagging efficiencies for both AK5 and CA8 were found to be within a 2% deviation (see Figure 5.13). To rule out a bias based on the known differences in pt for CA8 and AK5 jets, the efficiencies and uncertainties were extracted from plots using only the pt of the CA8 jet. The fit on the b-tagging efficiency ratio for CA8 and AK5 jets can be interpreted as an upper bound on the uncertainty due to this effect. We also checked this process for 1300 GeV and 1900 GeV signal samples and found results consistent with this 2% error. We have verified this systematic uncertainty with the BTV group, and it is approved for use in our analysis.

CHAPTER 5. DATA SAMPLE AND EVENT SELECTION

After the full top tagging selection is complete, there is a substantial fraction of $t\bar{t}$ in the full selection. Additionally, there is a large uncertainty in the $t\bar{t}$ Monte Carlo contribution, so discriminating signal from $t\bar{t}$ becomes important. In W' signal Monte Carlo, the sub-leading b candidate jet is usually a true b jet, but in $t\bar{t}$ this jet is commonly a merged W or top jet. To this effect, the b candidate jet is required to have a mass $M_b < 70$ GeV in the full selection. The value for this cut is set near the peak of the Signal/ $\sqrt{\text{Background}}$ distribution (see Figure 5.14).

5.11 Reconstruction of W' Invariant Mass

The full selection for the reconstruction of the W' invariant mass then includes the following offline cuts.

- One jet with $p_T > 450$ GeV identified with the CMS top tagging algorithm as well as subjet b-tagging and N-subjettiness discrimination.
- One jet with $p_T > 370$ GeV with a CSVM b tag and mass < 70 GeV
- $|\Delta\phi| > \pi/2$ between the two jets
- $|\Delta y|$ between the two jets < 1.6

The cutflow for this selection in data, $t\bar{t}$ Monte Carlo, and right-handed W' signal Monte Carlo can be found in Table 5.5. Figure 5.15 shows this full selection in signal Monte Carlo for various W' masses.

CHAPTER 5. DATA SAMPLE AND EVENT SELECTION

Sample	Number of Selected Events							C_{SV}
	$2 jets$	p_T	$ \Delta y $	M_{top}	$N_{subjets}$	M_{miss}	$S/J_{CSV\text{MAX}}$	
Data	13854873±3722	4305244±2075	3376771±1638	992349±996	557489±747	318520±564	50642±225	4463±67 277±17
QCD	—	—	—	—	—	—	—	— 248±4
ttbar	12185±27.3	4718±17.9	4220±16.9	3217±14.4	2742±13.3	2508±12.6	1689±10.0	1024±7.8 178±3.6
$M(W_R) = 1900$	806±1.4	739±1.3	553±1.2	429±1.0	340±0.9	304±0.9	170±0.6	88±0.4 68±0.4
$M(W_R) = 2100$	401±0.7	372±0.7	268±0.6	209±0.5	163±0.4	143±0.4	76±0.3	38±0.2 29±0.2
$M(W_L) = 1900$	796±2.4	703±2.3	531±2.0	414±1.8	312±1.6	274±1.5	138±1.0	58±0.6 44±0.6
$M(W_L) = 2100$	430±1.6	364±1.5	268±1.3	205±1.1	152±1.0	130±0.9	63±0.6	27±0.4 20±0.3 4±0.2

Table 5.5: The number of selected events after successive selections as scaled to an integrated luminosity of 19.7 fb^{-1} . Table reads left to right where the current column implies the previous selection. The quoted uncertainty is statistical only. QCD background expectation is only recorded for the full selection, as the average b-tagging rate takes into account the QCD background b fraction increase from b-tagging and subjet b-tagging. The first column additionally represents the hemispherical $\delta\phi$ selection between the leading jets. The column labeled p_T represents the p_T selection placed on both leading jets. The signal events are normalized to theory cross-section.

CHAPTER 5. DATA SAMPLE AND EVENT SELECTION

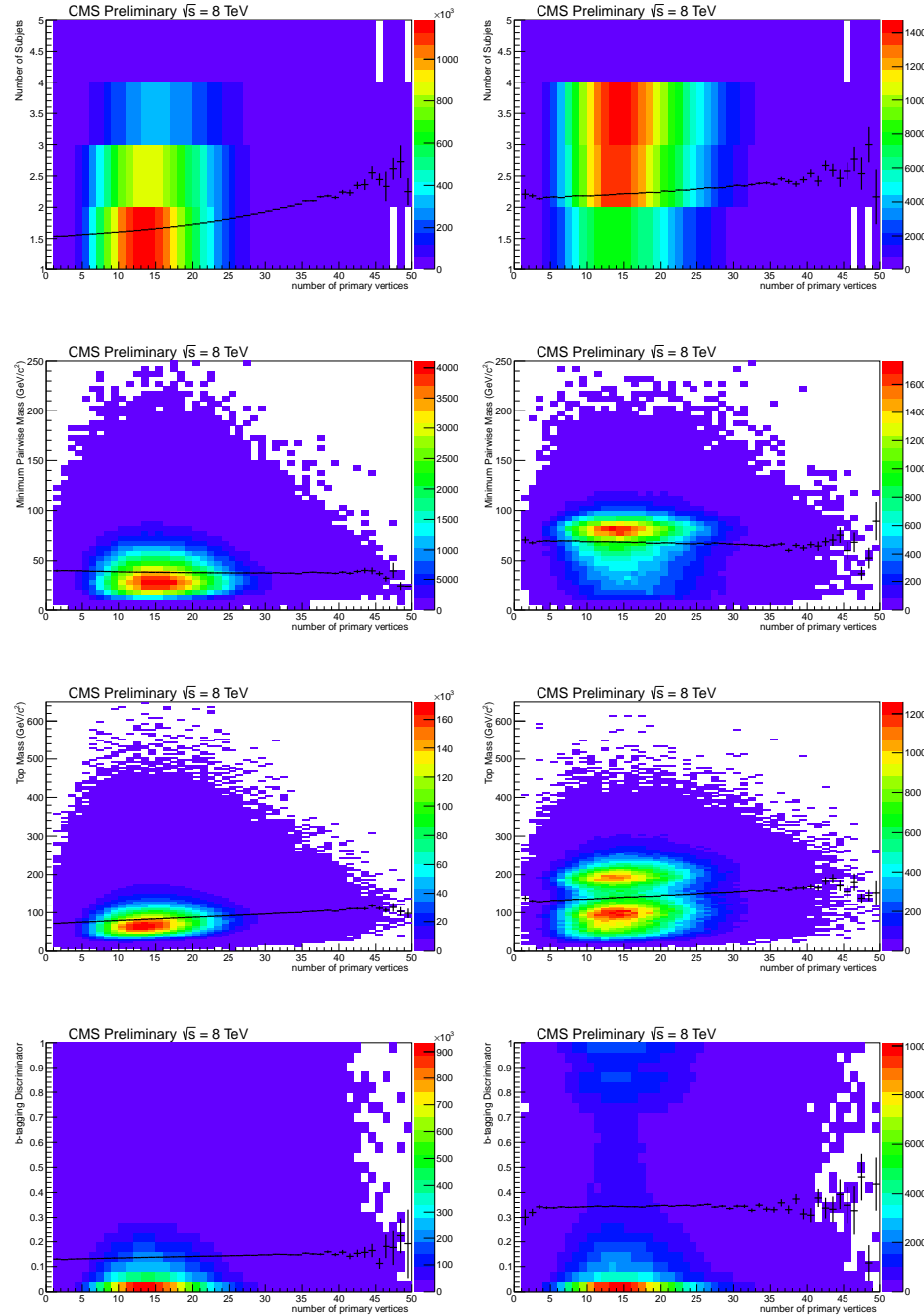


Figure 5.4: Number of primary vertices in data and signal Monte Carlo vs (a) Number of Subjets (b) Minimum Pairwise Mass (c) Top Mass (d) CSV b discriminant

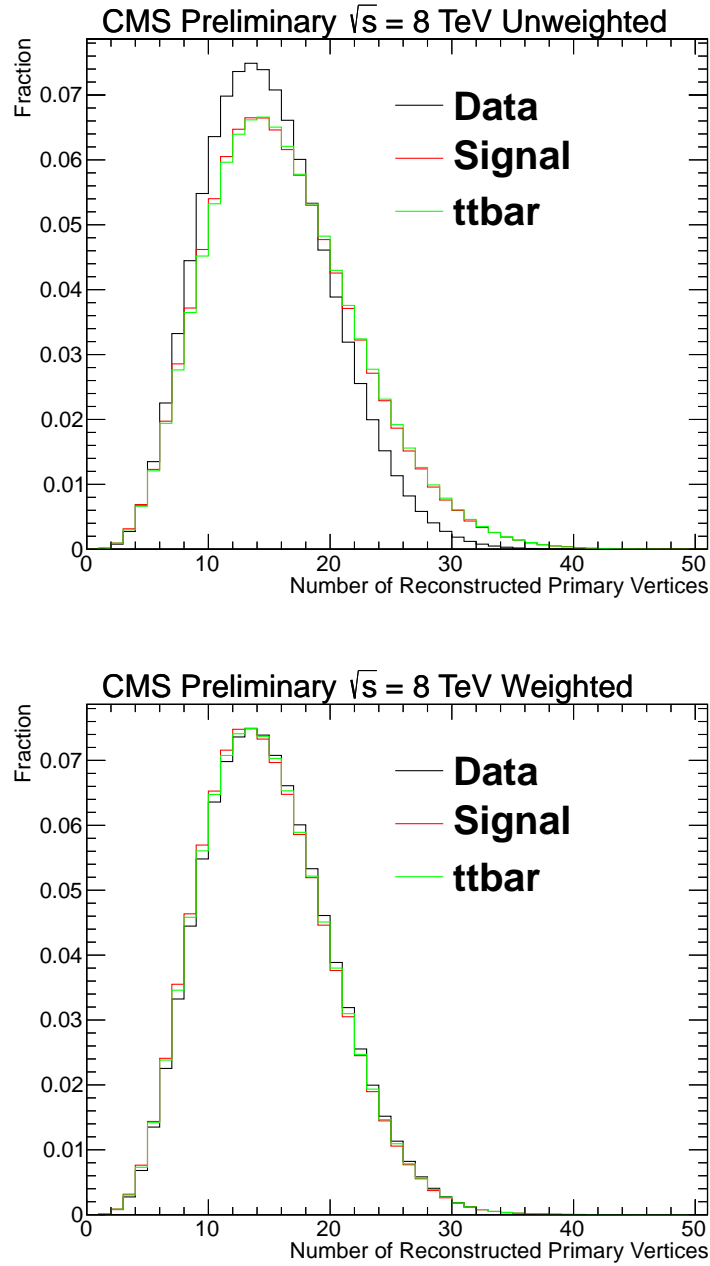


Figure 5.5: Number of reconstructed primary vertices before pileup re-weighting (top) and after pileup re-weighting (bottom). Here, no analysis cuts have been applied and the signal mass point is 1900 GeV

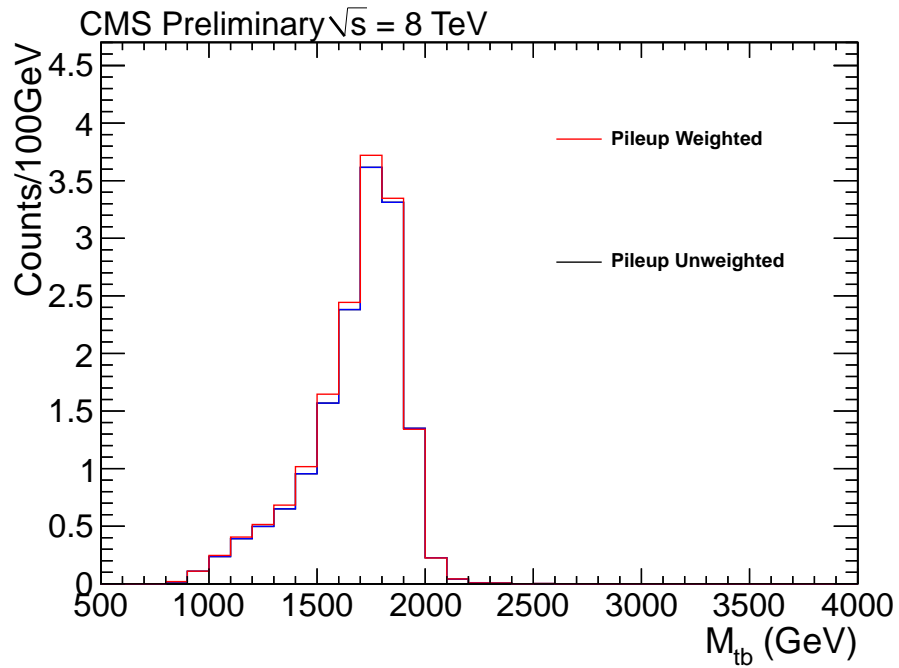
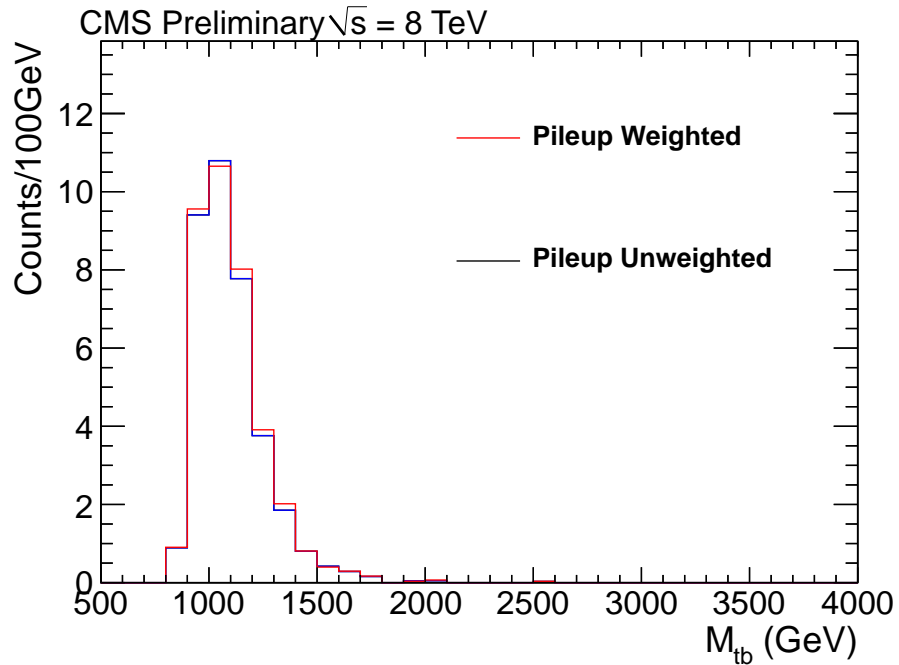


Figure 5.6: Effect of pileup-re-weighting on the Signal Monte Carlo.


 Figure 5.7: Effect of pileup-re-weighting on the $t\bar{t}$ Monte Carlo.

CHAPTER 5. DATA SAMPLE AND EVENT SELECTION

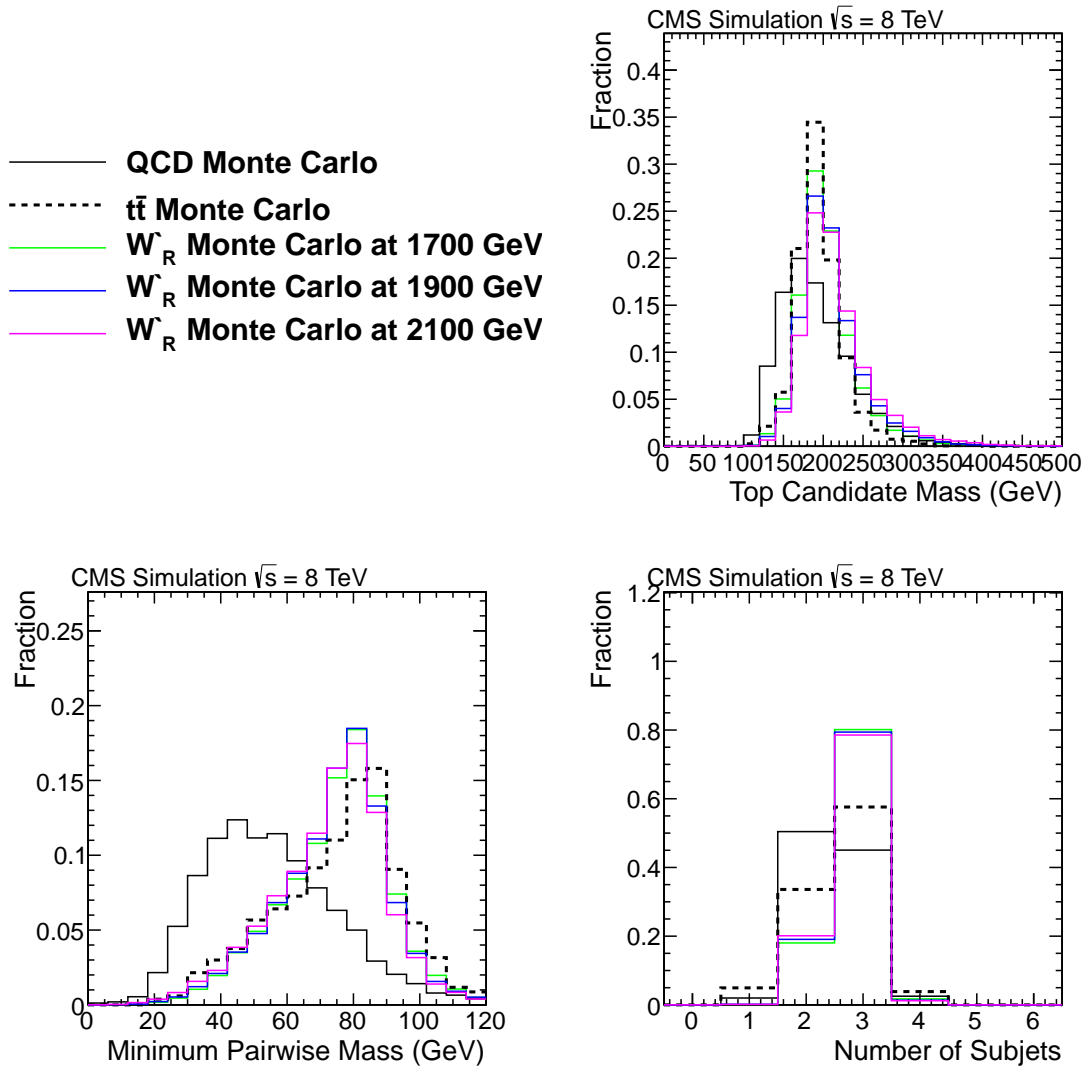


Figure 5.8: Comparison of the top Jet Mass, Number of Subjets, and Minimum Pairwise Mass in Signal and QCD Monte Carlo. The cms top tagging selection is applied with the exception of the variable being plotted.

CHAPTER 5. DATA SAMPLE AND EVENT SELECTION

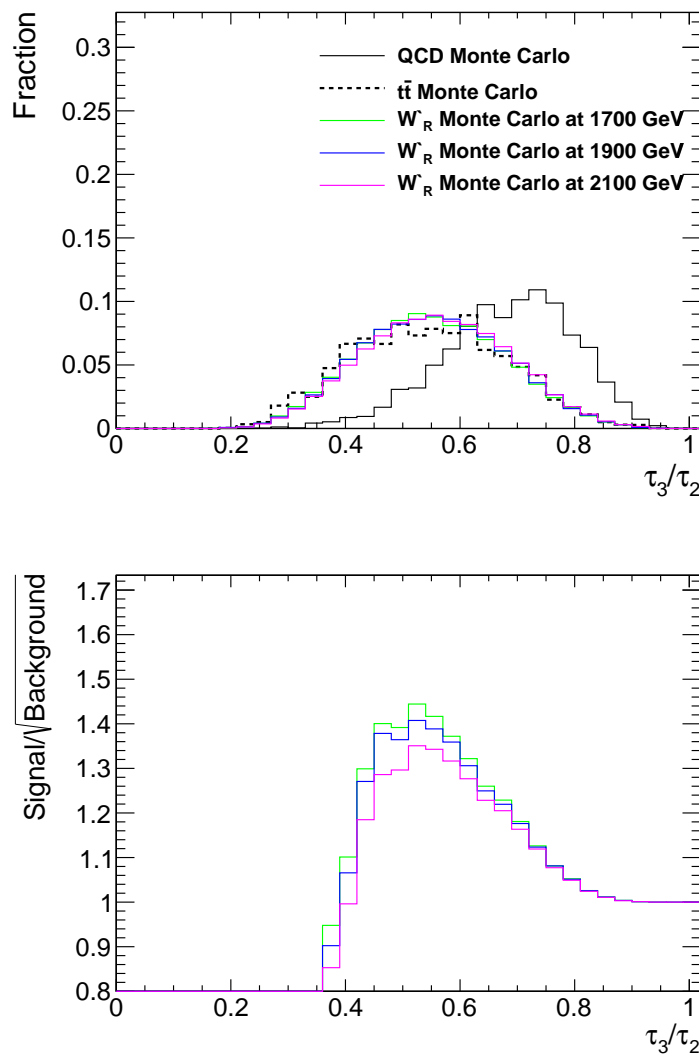


Figure 5.9: τ_3/τ_2 distributions in Signal and QCD Monte Carlo samples (top). Plot of Signal/ $\sqrt{\text{Background}}$ (bottom), derived from the top plot.

CHAPTER 5. DATA SAMPLE AND EVENT SELECTION

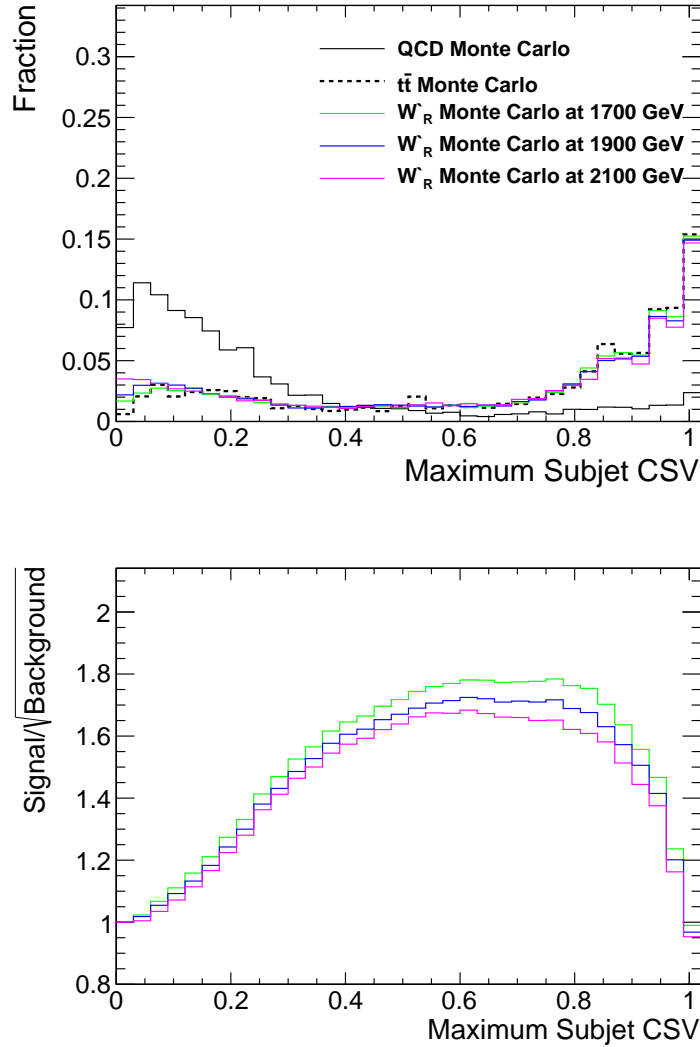


Figure 5.10: Maximum subjet CSV distributions in Signal and QCD Monte Carlo samples (top). Plot of Signal/ $\sqrt{\text{Background}}$ (bottom), derived from the top plot.

CHAPTER 5. DATA SAMPLE AND EVENT SELECTION

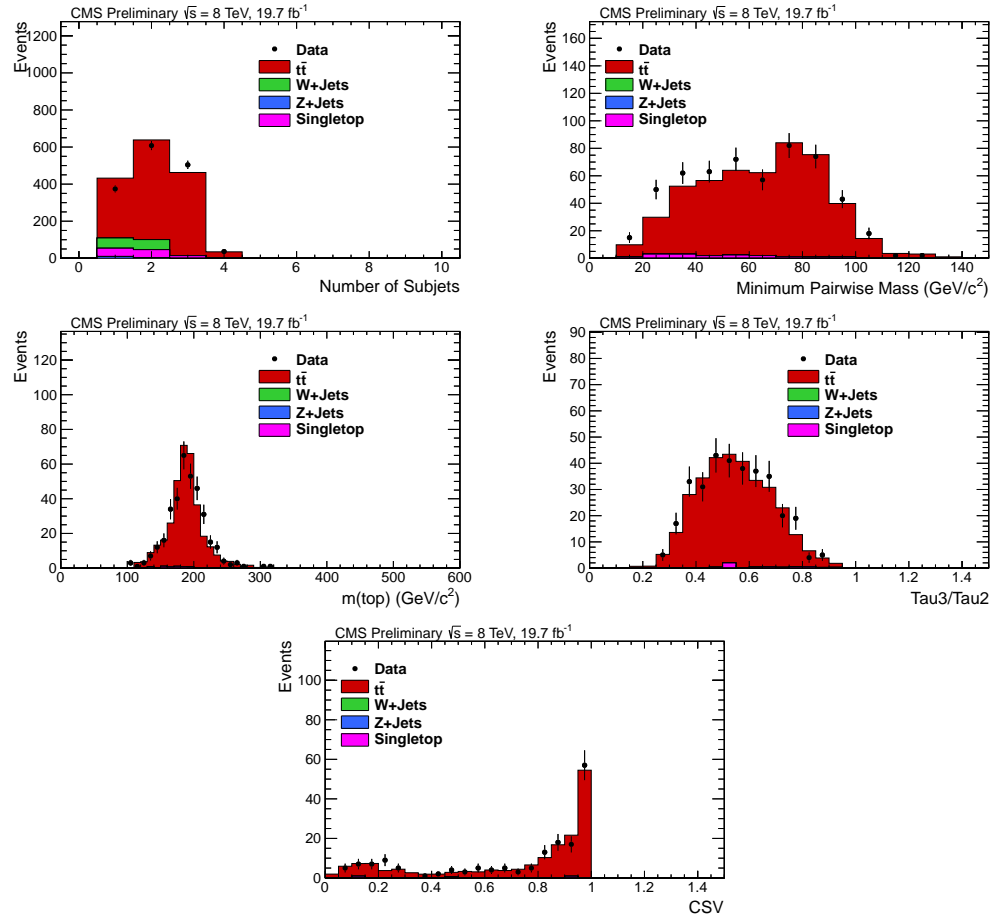


Figure 5.11: a.)Number of subjets, b.)minimum pairwise subjet mass, c.)jet mass, d.) τ_3/τ_2 , and e.)maximum subjet CSV for fully-merged top candidates found in the semileptonic $t\bar{t}$ sample, used to evaluate the top-tagging efficiency SF. These Figures are extracted using the Powheg $t\bar{t}$ Monte Carlo Sample.

CHAPTER 5. DATA SAMPLE AND EVENT SELECTION

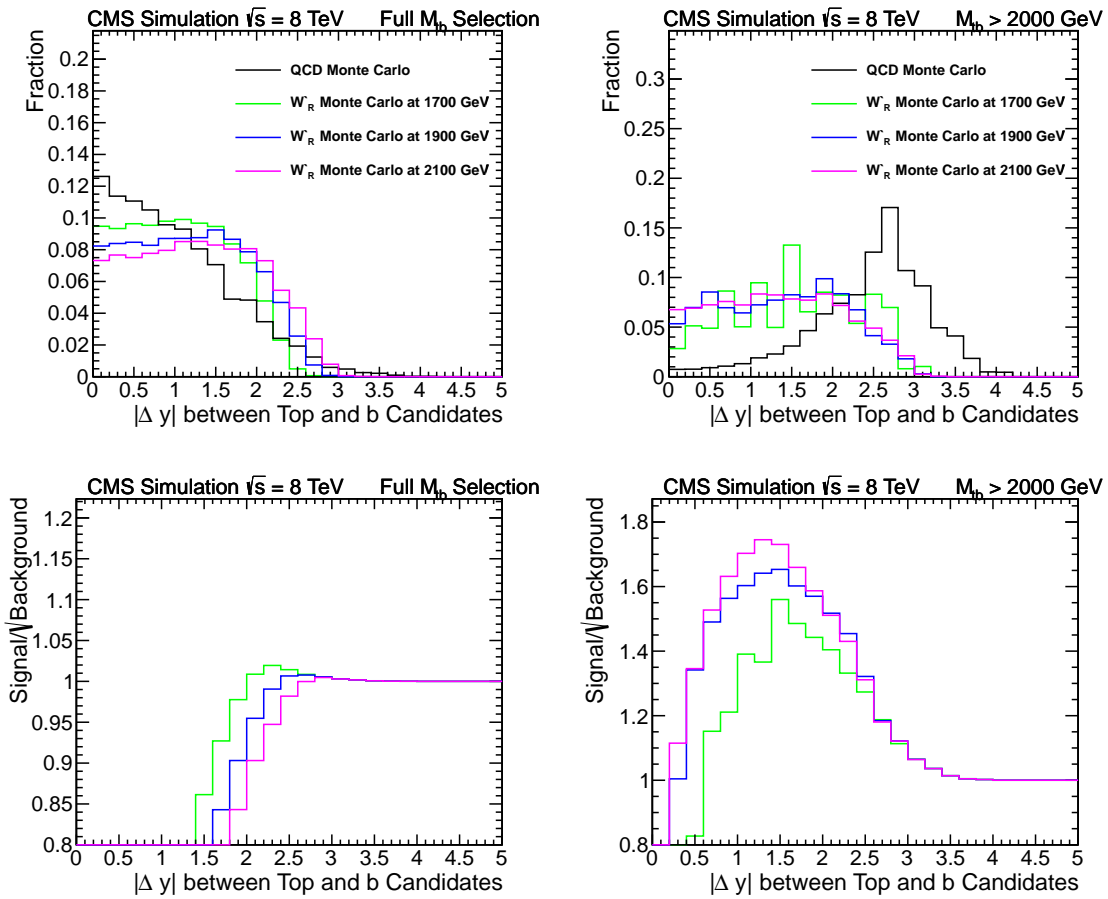


Figure 5.12: Comparison of $|\Delta y|$ in signal and QCD Monte Carlo for the full selection and only events with $M_{t\bar{b}} > 2000$ GeV

CHAPTER 5. DATA SAMPLE AND EVENT SELECTION

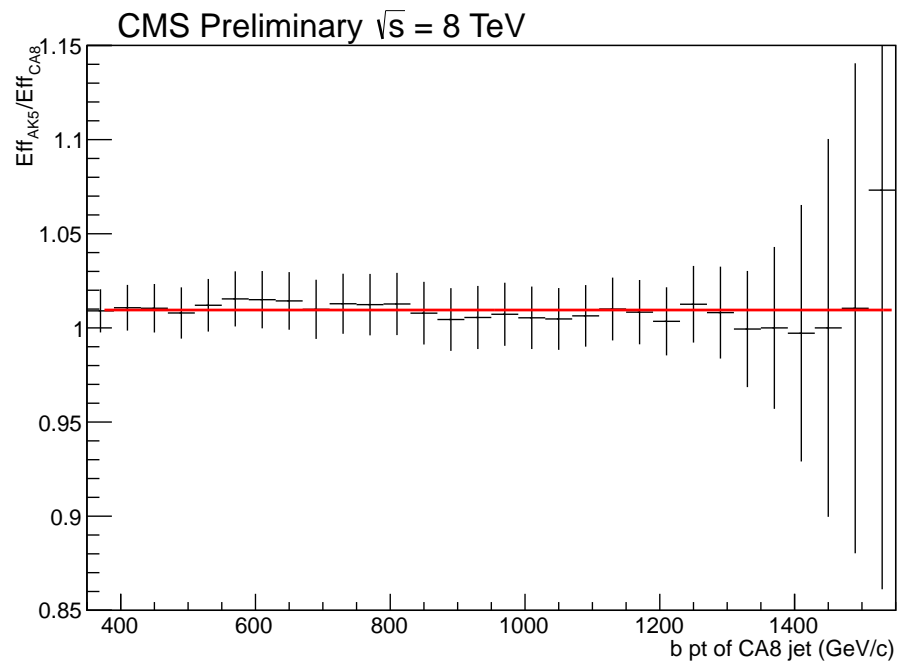


Figure 5.13: Ratio of the AK5 b-tagging rate to the CA8 b-tagging rate. Fitting this to a constant gives us a value of 1.0098 ± 0.0031 . This can be considered an upper limit on the uncertainty for the change in SF_b for CA8 jets

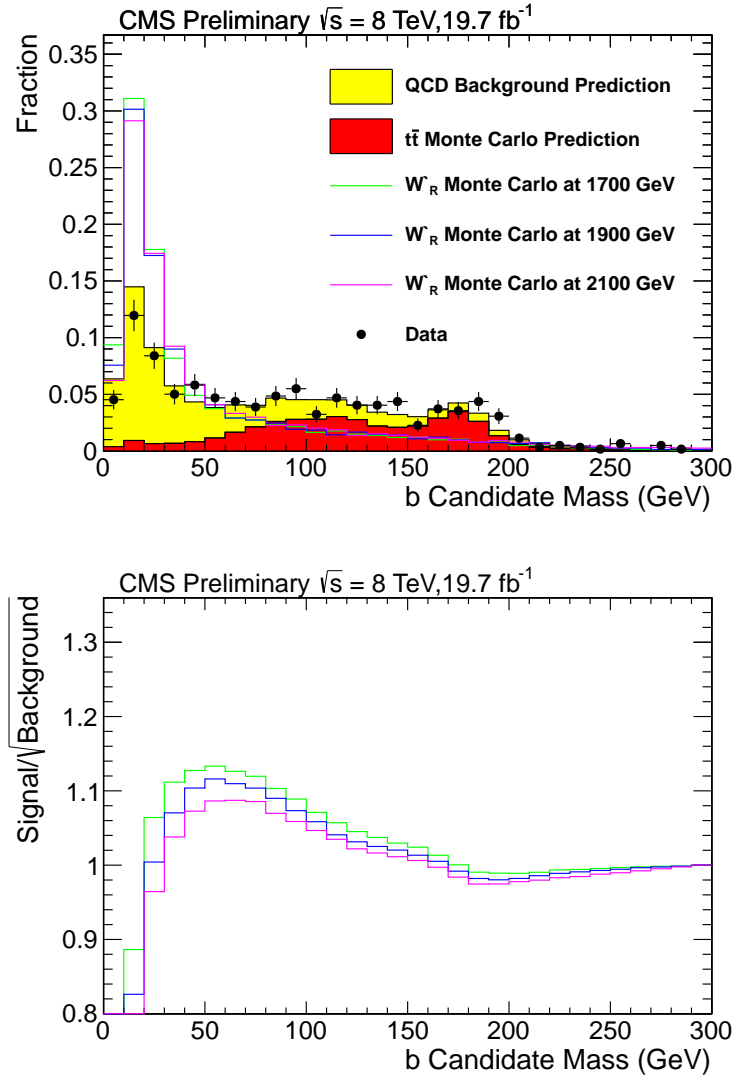


Figure 5.14: b candidate mass distributions in data, background, and signal. Plot of $\text{Signal}/\sqrt{\text{Background}}$ (bottom), derived from the top plot. This plot includes the full top tagging selection using the background estimation procedure outlined in Chapter 6.

CHAPTER 5. DATA SAMPLE AND EVENT SELECTION

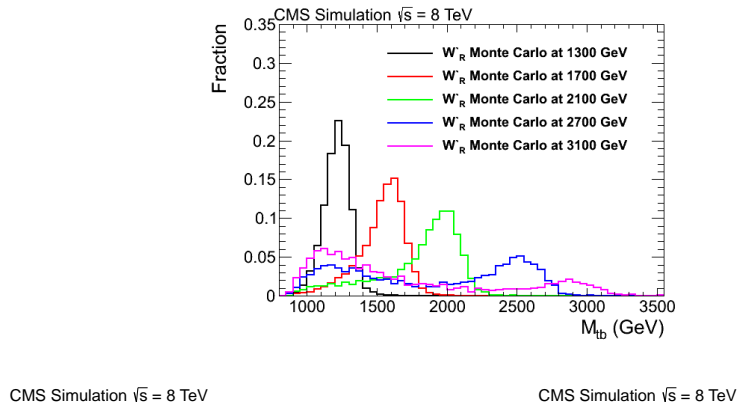


Figure 5.15: Full selection applied to W'_R (top) W'_L (bottom-left) and W'_{LR} (bottom-right). The bimodal structure seen in the M_{tb} spectrum for high W' mass is a feature common to high-mass large-width resonances and represents the superposition of a W' resonance and a rapidly falling parton distribution function.

Chapter 6

Background Estimation

An essential part of the analysis is the data driven estimation of the QCD background. The background estimate relies on extracting the average b-tagging rate of a QCD jet in our signal region. We extract this rate by making use of the following sideband.

6.1 Substructure Sideband

We define the substructure sideband as events passing all signal region cuts but explicitly failing the top jet substructure cut on the number of subjets. Additionally, to ensure similar parton flavor distributions in the signal region and sideband (Figure

CHAPTER 6. BACKGROUND ESTIMATION

6.1), we also include subjet CSV discrimination. The top jet sideband is defined as:

$$140 < m_{\text{jet}} < 250 \text{ GeV} \quad (6.1)$$

$$N_{\text{subjets}} \leq 2 \quad (6.2)$$

$$SJ_{\text{CSVMAX}} \geq 0.679 \quad (6.3)$$

The Minimum Pairwise Mass variable described in Section 5.8 is not defined in this choice of sideband.

6.2 QCD Background Estimation

The estimation of QCD background is performed by extracting the probability to tag a b jet in the sideband. The primary assumption used in background estimation is that the average b-tagging probability for QCD multijets in the signal region is nearly identical to the sideband. Figure 6.1 shows the parton flavor distribution for signal region and sideband in QCD MC, the nearly identical composition can be considered motivation for the previous assumption.

To extract a QCD background estimate, we weight the events that pass the full selection in the signal region before the b-tagging requirement is applied by the average b-tagging probability (measured in the top jet sideband). This gives us an accurate expectation of the QCD background in the signal region. The b-tagging rate is de-

CHAPTER 6. BACKGROUND ESTIMATION

fined as the inverse ratio of the number of b candidate jets, defined as $p_T > 370$ GeV jets in the hemisphere opposite the top jet to the number of b candidate jets that are b-tagged.

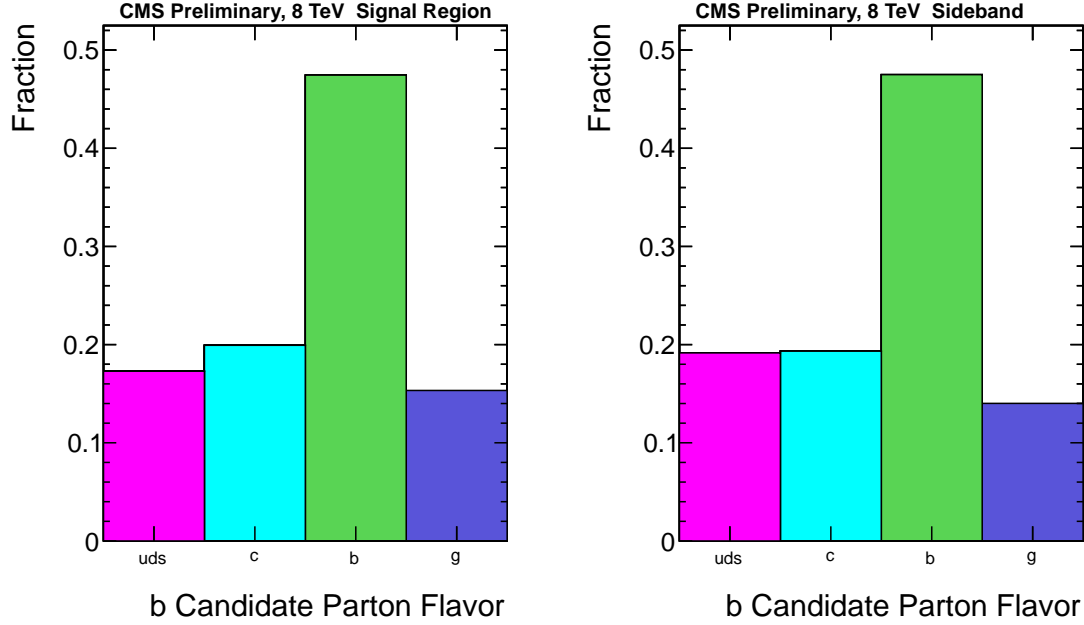


Figure 6.1: Comparison of jet parton flavor composition from the signal region and sideband.

The parameterization of the average b-tagging rate is two dimensional and considers both the $|\eta|$ and p_T of the b candidate jets. We break down data into three distinct regions in $|\eta|$.

- Low ($0.0 < |\eta| \leq 0.5$)
- Transition ($0.5 < |\eta| \leq 1.15$)
- High ($1.15 < |\eta| \leq 2.4$)

CHAPTER 6. BACKGROUND ESTIMATION

The regions in $|\eta|$ are then individually parameterized in p_T to produce the average b-tagging rate. We perform this parameterization of the b-tagging rate in an attempt to constrain the kinematic correlations inherent in b-tagging.

To smooth out the binning of the average b-tagging rate, a study of functional fits was conducted for the average b-tagging rate (see Figure 8.14). We chose the bifurcated polynomial fit based on observed representation of the data. The fitting function is as follows

$$f(x) = \begin{cases} p_0 + p_1x + p_2(x - a)^2, & \text{if } x < a \\ p_0 + p_1x + p_3(x - a)^2, & \text{if } x \geq a \end{cases} \quad (6.4)$$

Here, the parameters p_0 through p_3 are inputs to the fitting algorithm, and x is the p_T of the b candidate jet. The parameter a is the bifurcation point, and is chosen manually for each region in η . It is chosen to be 500 GeV, 500 GeV, and 550 GeV for the low, transition, and high η regions respectively. This piecewise function allows for two characteristic ranges to fit a polynomial, which makes a good fit for the different functional forms of the average b-tagging rate regions that we use.

The errors on the average b-tagging rate are then extracted using the full covariance matrix as obtained from output of the fitting algorithm. Additionally, we assign a systematic uncertainty to cover the choice of the fit function (see Chapter 8) based on several alternative functional forms. Figure 6.2 shows the tags (numerator) and

probes (denominator) of the tagging rate. Figure 6.3 shows the three fitted average b-tagging rates parameterized in p_T .

6.3 $t\bar{t}$ Subtraction

The $t\bar{t}$ contribution to background is computed from Monte Carlo that passes the full selection. To avoid double-counting, we must remove $t\bar{t}$ from our QCD estimate. In creating the b-tagging rate, the $t\bar{t}$ contribution to the numerator and denominator is subtracted away using $t\bar{t}$ Monte Carlo. Additionally, we account for the $t\bar{t}$ contamination of the QCD background estimate by applying the average b-tagging rate to $t\bar{t}$ Monte Carlo in the same way as data. This is a measure of $t\bar{t}$ that is expected to fall through the QCD background estimate and is subtracted away.

6.4 Sideband Closure

In order to investigate the applicability and versatility of the QCD background estimation in data, we apply the average b-tagging rate to sideband regions of our top tagging selection. First, we define the following sideband:

- **Jet Mass** $140 \text{ GeV} < m_{\text{jet}} < 250 \text{ GeV}$
- **Number of Subjets** $N_{\text{subjets}} > 2$
- **Minimum Pairwise Mass** $m_{\text{min}} \leq 50 \text{ GeV}$

CHAPTER 6. BACKGROUND ESTIMATION

	η_1	η_2	η_3
pretag QCD	15922 (99.77%)	14396 (99.79%)	5494 (99.81%)
tagged QCD	924 (99.17%)	847 (99.16%)	285 (99.54%)
pretag $t\bar{t}$	37 (0.23%)	31 (0.21%)	11 (0.19%)
tagged $t\bar{t}$	8 (0.83%)	7 (0.84%)	1 (0.46%)
pretag signal at 1300GeV	108 (0.67%)	77 (0.53%)	17 (0.30%)
tagged signal at 1300GeV	37 (3.94%)	24 (2.87%)	4 (1.44%)
pretag signal at 1500GeV	62 (0.39%)	39 (0.27%)	8 (0.14%)
tagged signal at 1500GeV	17 (1.86%)	11 (1.28%)	2 (0.67%)
pretag signal at 1700GeV	31 (0.19%)	19 (0.13%)	3 (0.06%)
tagged signal at 1700GeV	8 (0.82%)	4 (0.53%)	1 (0.25%)
pretag signal at 1900GeV	15 (0.09%)	9 (0.06%)	1 (0.02%)
tagged signal at 1900GeV	3 (0.31%)	2 (0.20%)	0 (0.07%)
pretag signal at 2100GeV	7 (0.04%)	4 (0.03%)	0 (0.01%)
tagged signal at 2100GeV	1 (0.13%)	1 (0.09%)	0 (0.03%)

Table 6.1: Number of tagged and pretagged events for each background sample and percent contribution to overall average b-tagging rates. Additionally, signal samples are investigated. The percents indicated are out of the total QCD + $t\bar{t}$ expectation and the signal samples are scaled to theory cross-section.

- **N-subjettiness** $\tau_3/\tau_2 \geq 0.55$
- **Subjet b-Tagging** $SJ_{CSVMAX} \geq 0.679$

This region lies outside of the signal region and sideband used for average b-tagging rate determination. The selection also has a very low yield of $t\bar{t}$, making it ideal for investigating the QCD background contribution. The average b-tagging rate used for this closure test is extracted from the same sideband as the signal region, and applied to pre-b-tagged events. The closure test can be seen in Figure 6.4.

Additionally, we can define the following sideband

- **Jet Mass** $140 \text{ GeV} < m_{\text{jet}} < 250 \text{ GeV}$

CHAPTER 6. BACKGROUND ESTIMATION

- **Number of Subjets** $N_{\text{subjets}} > 2$
- **Minimum Pairwise Mass** $m_{\min} > 50 \text{ GeV}$
- **N-subjettiness** $\tau_3/\tau_2 < 0.55$
- **Subjet b-Tagging** $SJ_{\text{CSVMAX}} \leq 0.679$

The closure test can be seen in Figure 6.5.

6.5 Deriving the normalization of the SM $t\bar{t}$ production

In order to study the contribution from $t\bar{t}$ to the full background estimate, we turn to a sideband defined by inverting the b candidate mass requirement in the signal region. This selection has an amplified $t\bar{t}$ fraction and is statistically independent from all other sidebands in the analysis. This makes the selection ideal for extracting the $t\bar{t}$ fraction in data. In order to extract this fraction, we compare the data-driven QCD background and $t\bar{t}$ Monte Carlo expectation to the selection in data.

We perform a template fit to the invariant mass of the b candidate, using scaled $t\bar{t}$ Monte Carlo as one template, and the QCD background prediction as the other. The fit allows the QCD background template to move only within its errors, whereas the normalization on $t\bar{t}$ is unconstrained. The optimal parameterization for this fit is in

CHAPTER 6. BACKGROUND ESTIMATION

a variable that has distinctly different shapes in $t\bar{t}$ and QCD. We therefore use the b candidate mass, which minimizes the correlation between the QCD and $t\bar{t}$ templates within the fit. The fit can be seen in Figure 6.6. For this maximum likelihood fit we use the Theta package.

Additionally, the fit implements the $t\bar{t}$ subtraction in the QCD estimate by fitting un-subtracted QCD to the $t\bar{t}$ full selection. The output of the fitter is then corrected by $(1+S/F)$, where S/F is the ratio of the number of events in $t\bar{t}$ subtracted selection to the $t\bar{t}$ full selection.

This study suggests after all scale factors applied in the analysis, the $t\bar{t}$ contribution needs to be amplified by 1.23 ± 0.24 . This normalization is used for all $t\bar{t}$ distributions in the analysis, and the uncertainty is then the full normalization uncertainty for $t\bar{t}$.

CHAPTER 6. BACKGROUND ESTIMATION

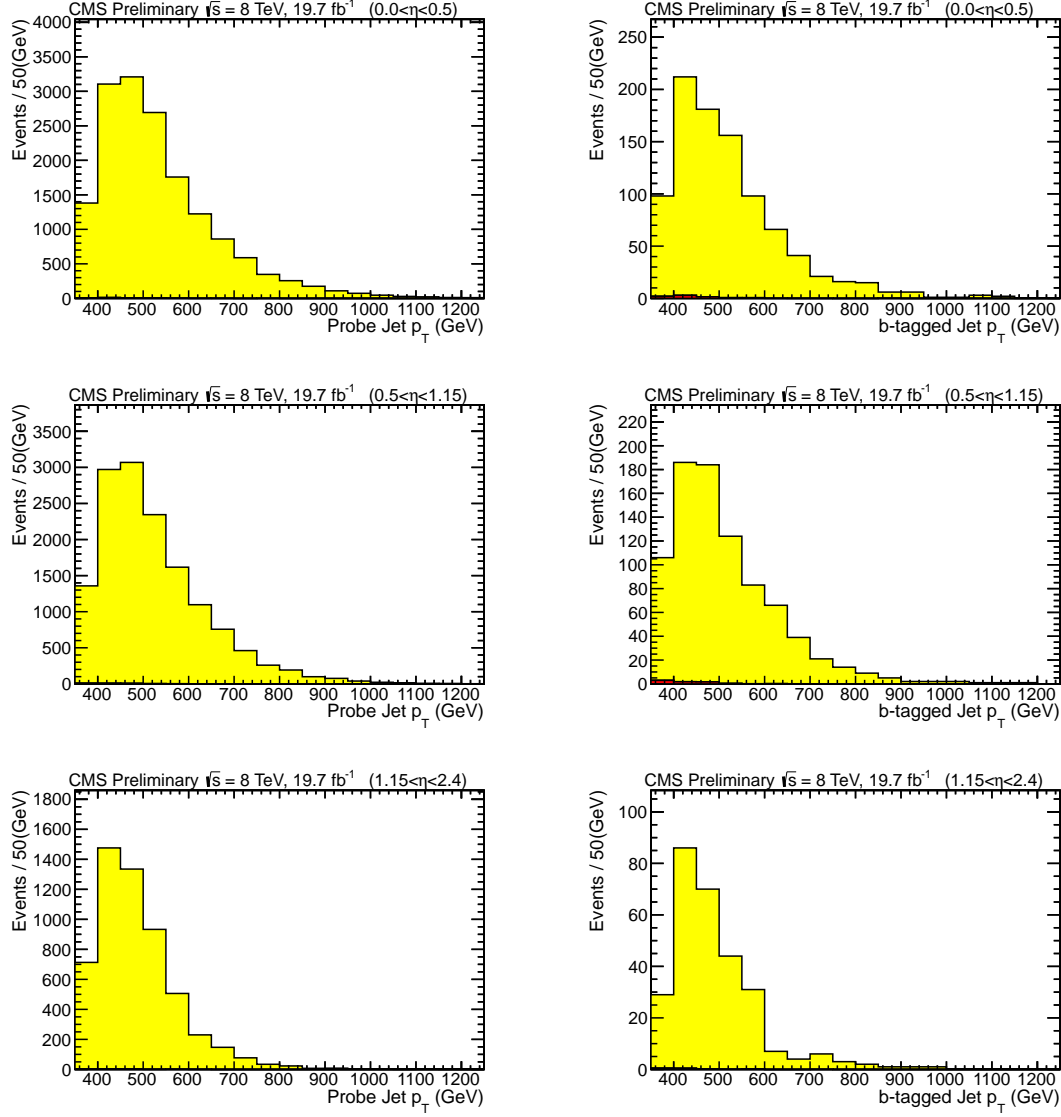


Figure 6.2: The tags and probes used for the average b-tagging rate in each of the three regions in $|\eta|$. Here, tags are the numerator and probes are the denominator of the average b-tagging rate

CHAPTER 6. BACKGROUND ESTIMATION

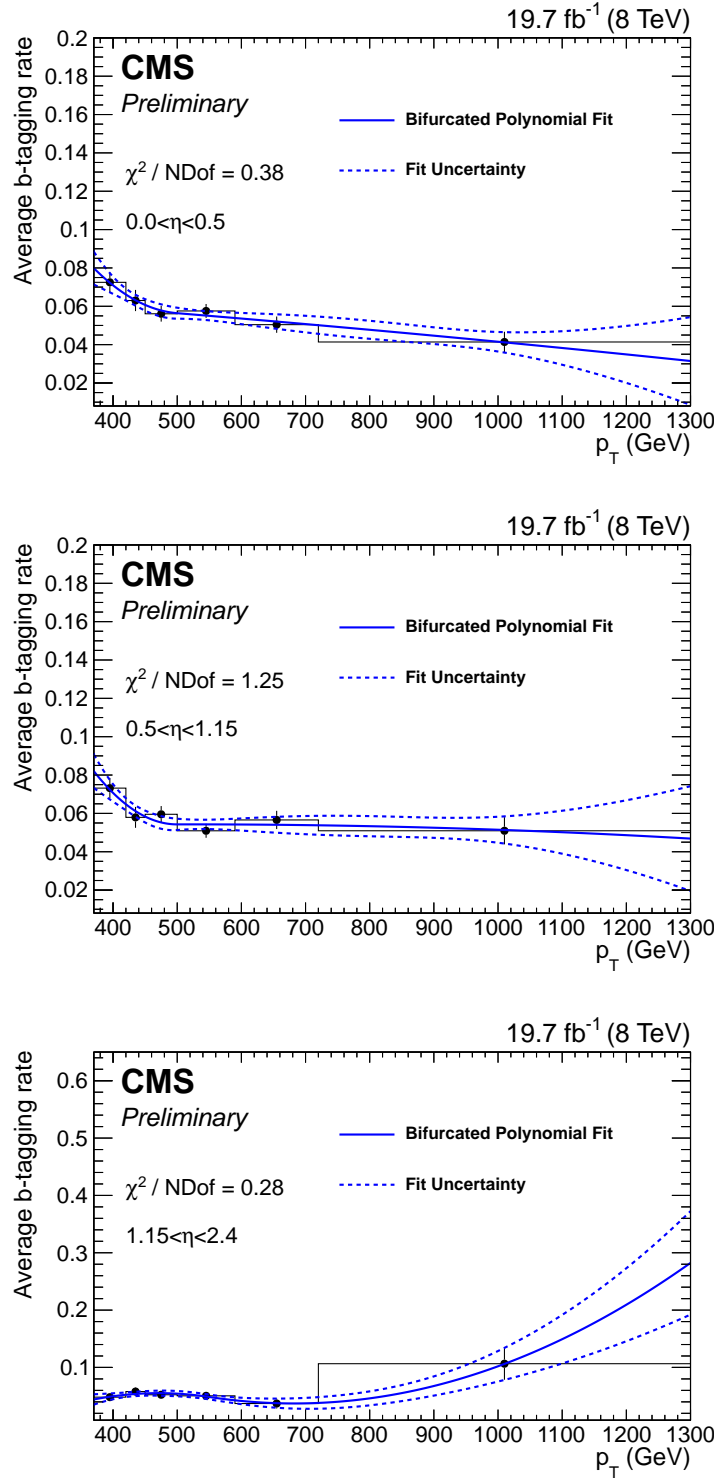


Figure 6.3: p_T parameterized average b-tagging rate from (a) Low η region (b) Transition η region (c) High η region. The average b-tagging rate is shown in black, the polynomial fit is shown in blue, and the propagated errors from the fit are shown as a blue dashed line.

CHAPTER 6. BACKGROUND ESTIMATION

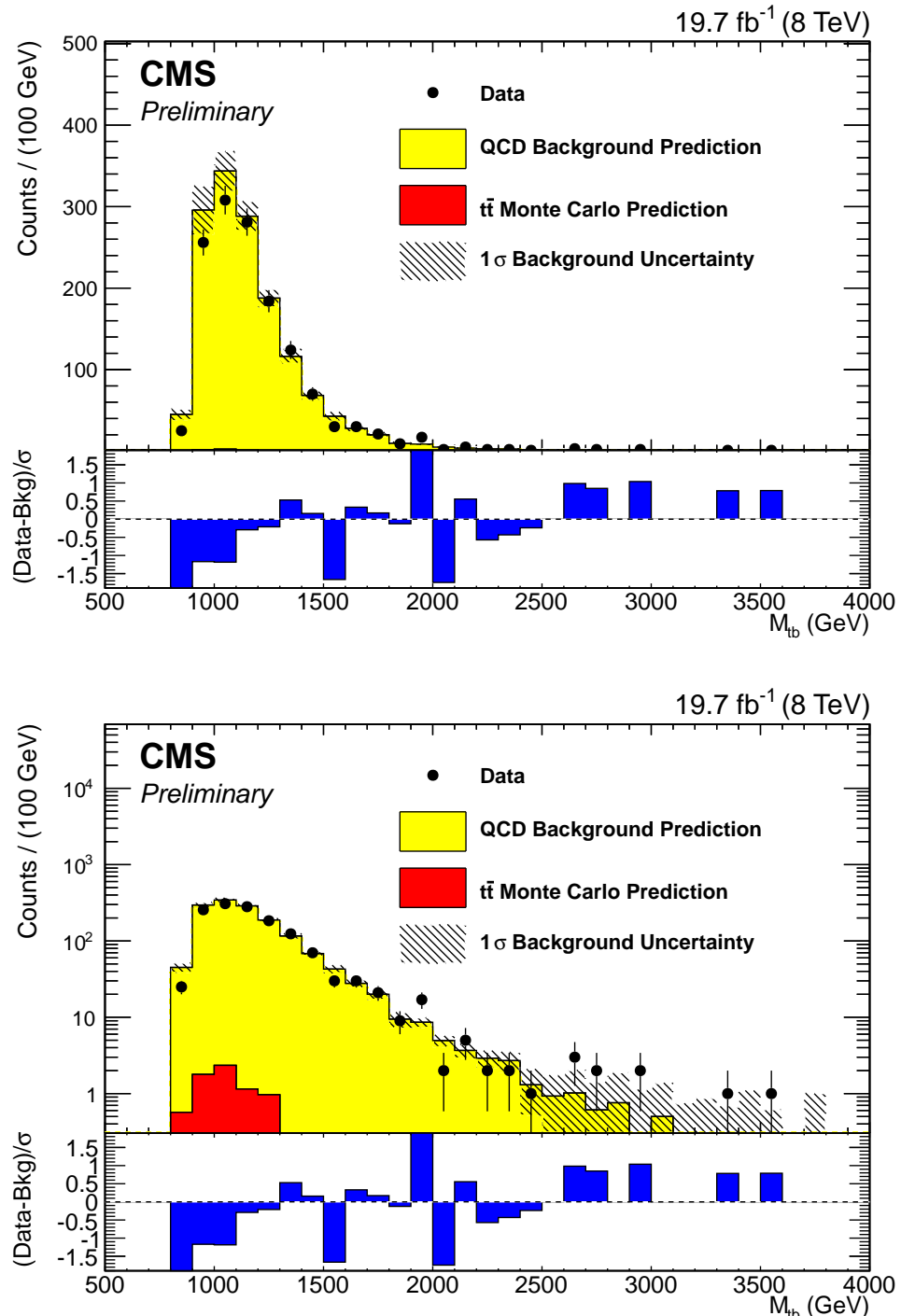


Figure 6.4: A plot of M_{tb} in the control region defined by inverting the minimum pairwise mass and N-subjettiness cuts used in the full selection. The top and bottom plots are the same but with linear and log y-axis scale.

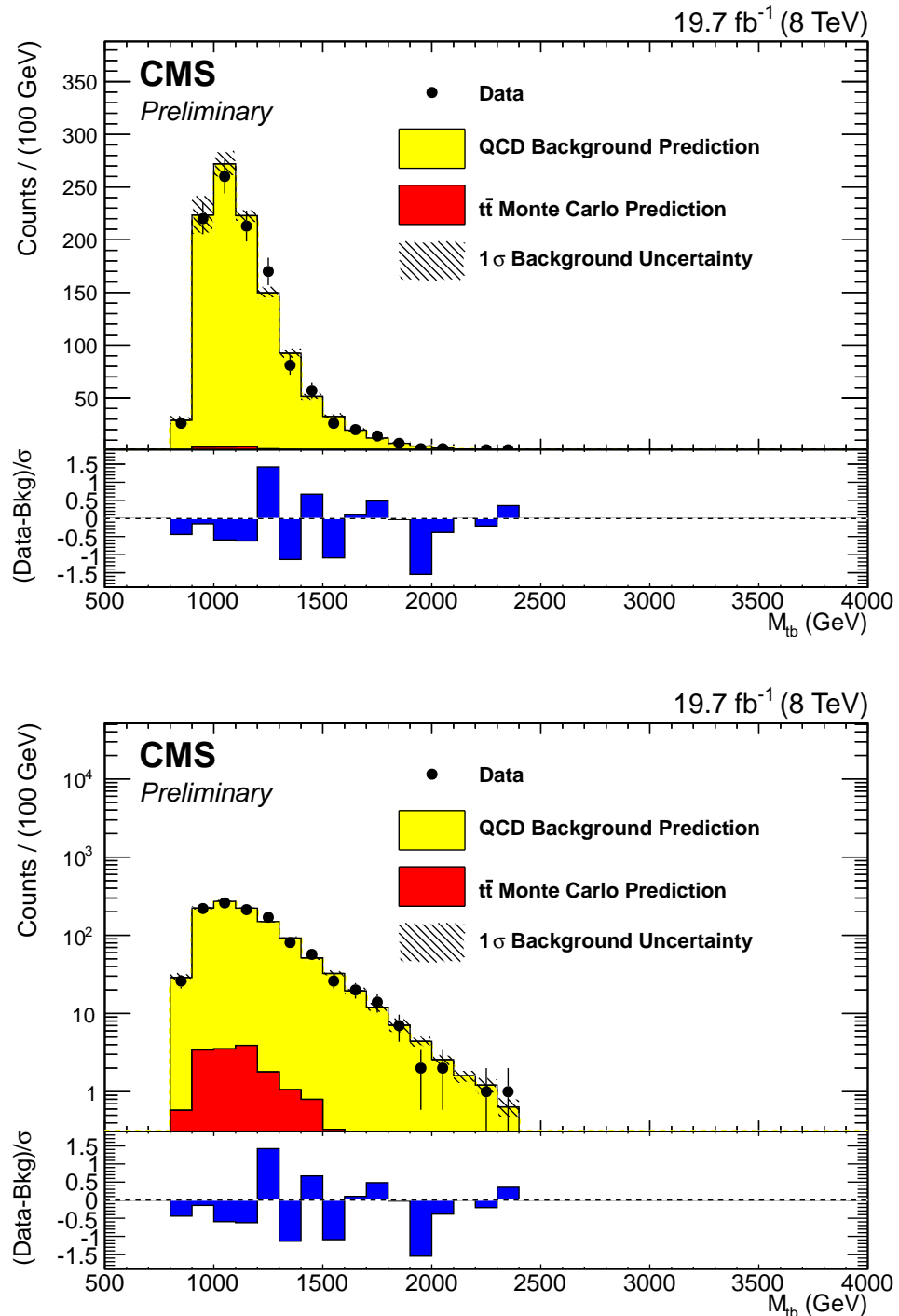


Figure 6.5: A plot of M_{tb} in the control region defined by inverting the subjet b tagging cut used in the full selection. The top and bottom plots are the same but with linear and log y-axis scale.

CHAPTER 6. BACKGROUND ESTIMATION

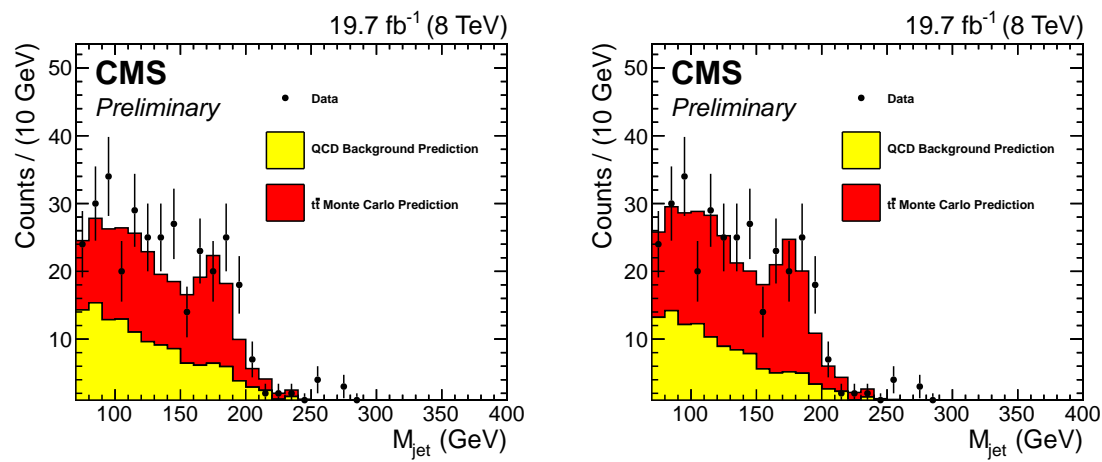


Figure 6.6: b candidate mass as extracted from the b candidate mass inverted side-band. Pre fraction fit (left) and post fraction fit (right).

Chapter 7

Data Results

After closure of the background estimation procedure within control regions, we first apply the background estimate to a loose selection that contains all of the full selection cuts with the exception of subjet b-tagging and N-subjettiness. The agreement using this selection can be seen in figure 7.1.

After observing agreement is the loose selection, we investigate the full selection. The final results are shown in Figure 7.2. We proceed to compute limits on the W' cross-section. Background estimation of selected relevant variables can be seen in Figures 7.3 and 7.4.

CHAPTER 7. DATA RESULTS

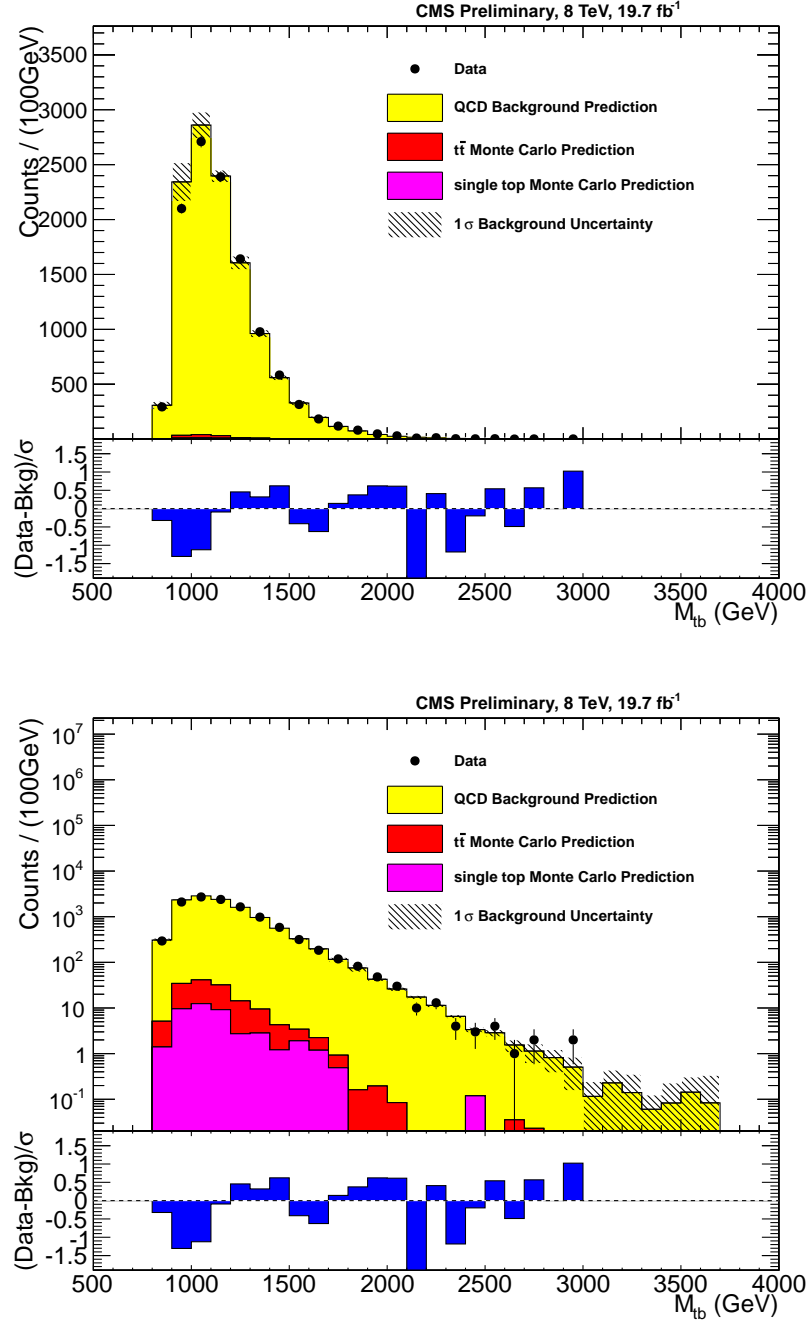


Figure 7.1: A plot of the full selection before N-subjettiness and subjet b-tagging discrimination. Here we investigate the data-background agreement in a loose selection before looking at the full top tagging selection. Top and bottom plots are the same but with linear and log y-axis scale.

CHAPTER 7. DATA RESULTS

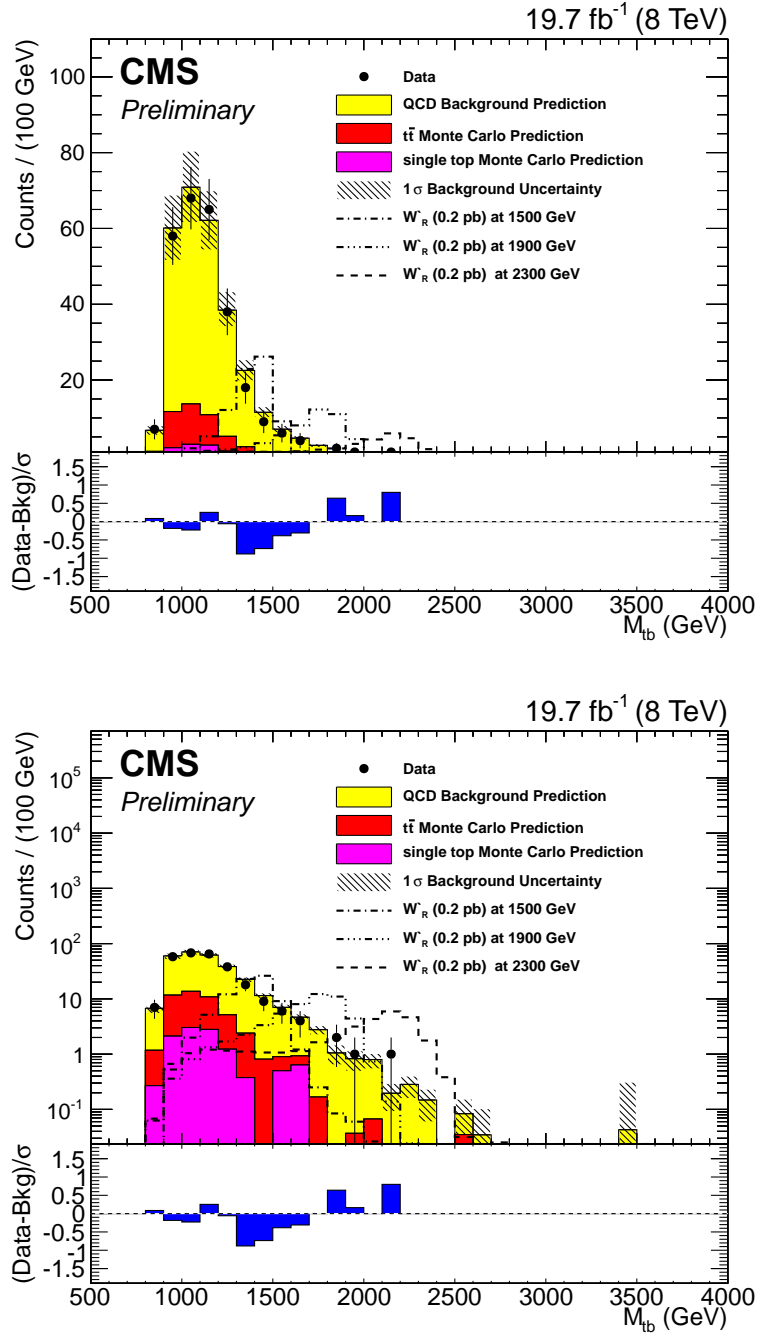


Figure 7.2: A plot of the full selection comparing data, signal and background. The single top contribution is not considered when setting limits. The normalization for the signal samples is set to a cross-section of 0.2 pb. Top and bottom plots are the same but on linear and log y-axis scale.

CHAPTER 7. DATA RESULTS

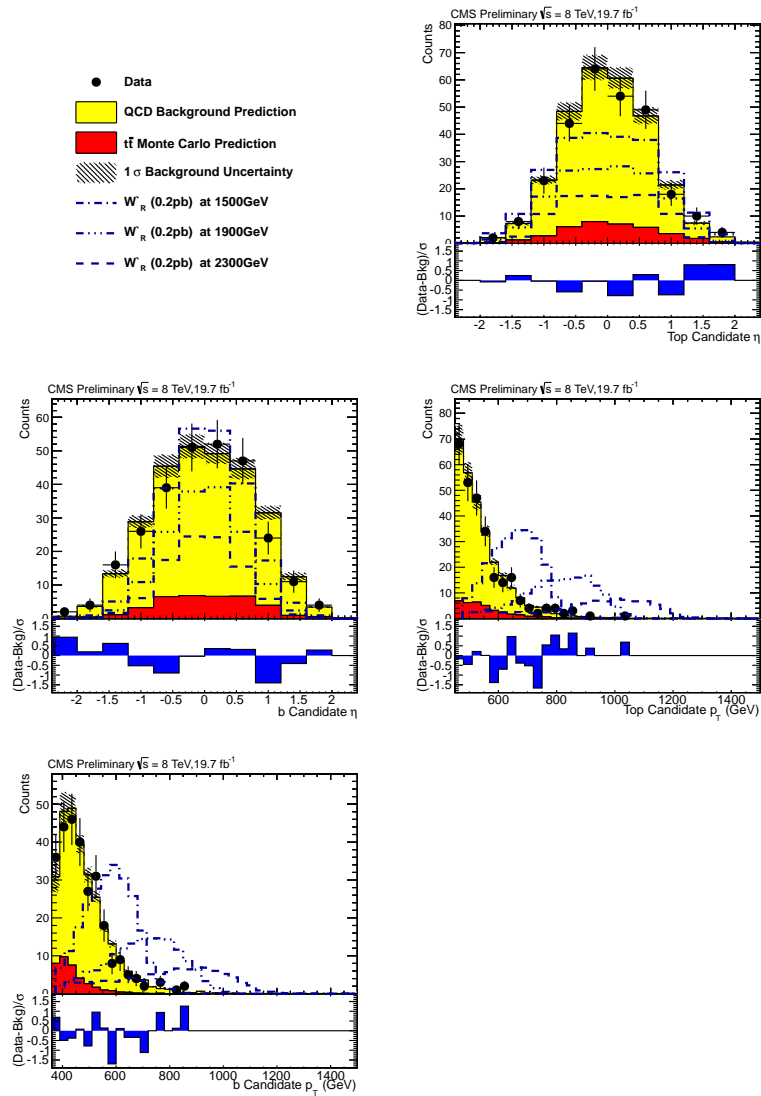


Figure 7.3: Background estimation of kinematic variables. The error bars shown are from the three primary sources; uncertainty on the fit, choice of fit, $t\bar{t}$ normalization, and $t\bar{t} Q^2$ uncertainty

CHAPTER 7. DATA RESULTS

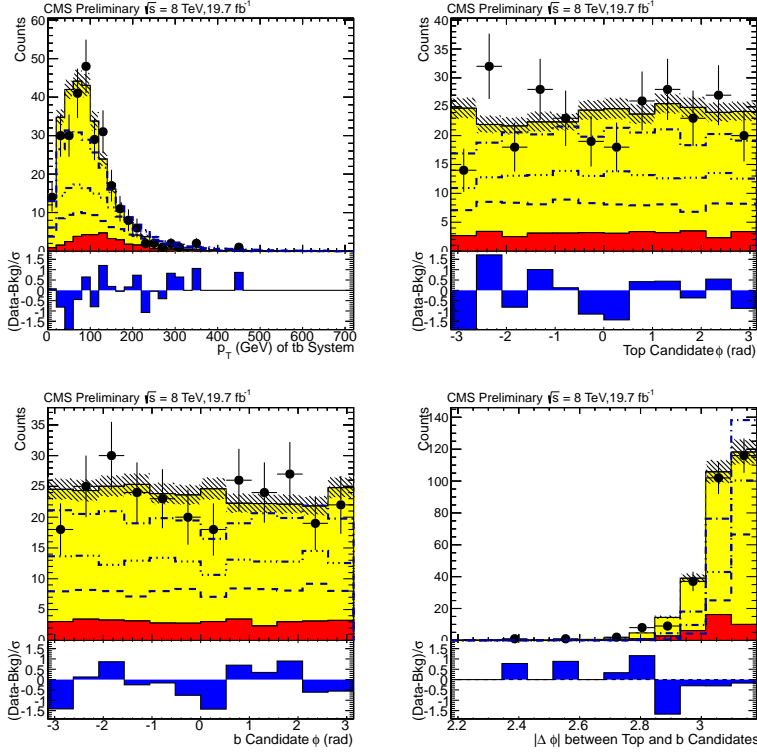


Figure 7.4: Background estimation of kinematic variables. The error bars shown are from the three primary sources; uncertainty on the fit, choice of fit, $t\bar{t}$ normalization, and $t\bar{t} Q^2$ uncertainty

Chapter 8

Systematic Uncertainties

Various systematics are taken into account, both on our expected signal and background estimate. Some systematic uncertainties will affect only the normalization of certain event rates, and are reported as overall normalization uncertainties. Other systematics affect the shapes of the reconstructed signal or backgrounds, as well as their normalization. The Systematic uncertainties that are used in the analysis are summarized in table 9.2.

8.1 Jet Energy Scale

We evaluate the effect of uncertainty on the jet energy scale on samples derived from Monte Carlo simulation. To do so, we vary the jet four-momentum up and down by the jet energy scale uncertainty, which we take to be 3%. We include p_T and η

CHAPTER 8. SYSTEMATIC UNCERTAINTIES

dependent corrections to the jet energies, as well as uncertainties from the difference in measured and simulated W masses [31].

Varying the jet momentum can cause a jet to fall below or rise above the p_T cut in the analysis, thus shifting the invariant mass spectrum of the signal and reconstructed $t\bar{t}$ samples. Figure 8.4 shows the systematic shapes from the jet energy scale on the $t\bar{t}$ distribution. Jet Energy scale variation on signal Monte Carlo is shown in Figure 8.3 for 1300 GeV, 1900 GeV, and 2300 GeV mass points.

8.2 Trigger

We include an uncertainty based on the measured trigger efficiency for all Monte Carlo Samples. The trigger efficiency is discussed in Section 5.2. To obtain shape systematics from this effect, we vary the trigger by half the trigger *inefficiency*. The effects of this on the $t\bar{t}$ distribution is shown in Figure 8.6. Trigger weighting on signal Monte Carlo is shown in Figure 8.5 for 1300 GeV, 1900 GeV, and 2300 GeV mass points. The uncertainty is low in the mass range of interest for limit setting.

8.3 Jet Energy Resolution

We apply a systematic due to the known differences in jet energy resolution in data and simulation. We use η dependent smearing (see [31]) as recommended by the JER group. We apply this systematic uncertainty to the $t\bar{t}$ distribution (as seen

CHAPTER 8. SYSTEMATIC UNCERTAINTIES

in Figure 8.8). Jet Energy Resolution variation on signal Monte Carlo is shown in Figure 8.7 for 1300 GeV, 1900 GeV, and 2300 GeV mass points.

8.4 Jet Angular Resolution

A smearing of 10% is assumed on η and ϕ and shape uncertainties are generated by considering smearing 10% lower and higher. We apply this systematic uncertainty to the $t\bar{t}$ distribution (as seen in Figure 8.10). Jet Angular Resolution variation on signal Monte Carlo is shown in Figure 8.9 for 1300 GeV, 1900 GeV, and 2300 GeV mass points. The effect is very small and thus not considered in setting limits.

8.5 PDF Uncertainty

The uncertainty in the parton distribution function used for Monte Carlo sample generation is investigated. We take the average of the $\pm 1\sigma$ eigenvalue variation of the pdf master equations [32] for the NNPDF, MSTW2008nnlo, and CT10 pdf sets to weight the signal and $t\bar{t}$ Monte Carlo samples and investigate the impact on the full selection. The PDF set that provides the maximum uncertainty is then used for the $\pm 1\sigma$ PDF uncertainty. For $t\bar{t}$ and signal this set is NNPDF. PDF variation on signal Monte Carlo is shown in Figure 8.11 for 1300 GeV, 1900 GeV, and 2300 GeV mass points. PDF variation on $t\bar{t}$ Monte Carlo is shown in Figure 8.12. The effect is very small and thus not considered in setting limits.

p_T range	Absolute Error on SF_b
320 GeV < p _T < 400 GeV	0.0313175
400 GeV < p _T < 500 GeV	0.0415417
500 GeV < p _T < 600 GeV	0.0740446
600 GeV < p _T < 800 GeV	0.0596716

Table 8.1: Absolute Error applied to the b-tagging Scale Factor

8.6 Pileup

A study of pileup uncertainty is conducted by varying the minimum bias cross-section by 5% as a measure of systematic uncertainty. The results can be seen in figure 8.13. The effect is very small and thus not considered in setting limits.

8.7 b-Tagging Scale Factor Uncertainty

The uncertainty in the b-tagging scale factor described in Section 5.10 is applied based on the b candidate p_T. The binning and associated errors listed below are the suggested EPS13 prescription generated from measurements in both muon-jet and ttbar data representing 20 fb⁻¹ of integrated luminosity. The absolute uncertainty on SF_b for a b candidate jet within the listed p_T range is applied as shown in table 8.1 for p_T < 800 GeV. B candidate jets with p_T > 800 GeV are assigned an uncertainty equal to twice the listed value for 600 GeV < p_T < 800 GeV

8.8 Q^2 Scale Uncertainty

We use additional $t\bar{t}$ samples generated with twice and half the nominal Q^2 scale used in the $t\bar{t}$ samples listed in table 5.1. These samples vary the renormalization and factorization scales to account for missing higher order corrections in our simulation. Figure 8.1 shows the shape based uncertainty due to this effect.

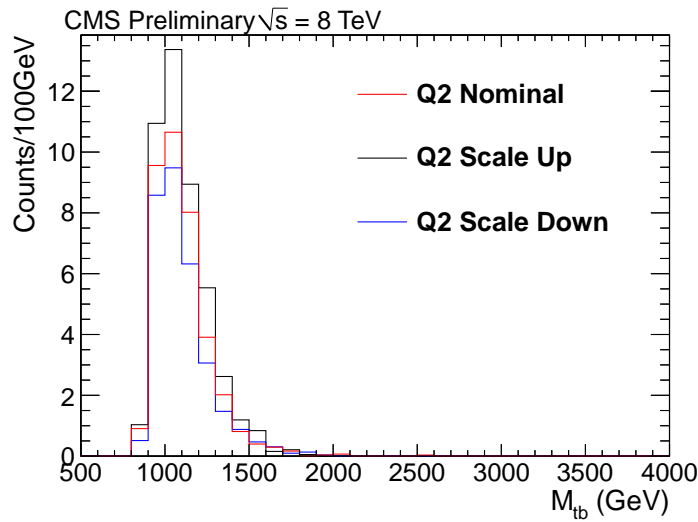


Figure 8.1: Q^2 systematic variation for $t\bar{t}$ Monte Carlo

8.9 $t\bar{t}$ p_T Re-weighting

The uncertainty related to the p_T re-weighting scheme presented in Section 5.6 is taken as the difference between the weighted and unweighted $t\bar{t}$ spectrum. This uncertainty can be seen in figure 8.2. This is the dominant uncertainty for $t\bar{t}$.

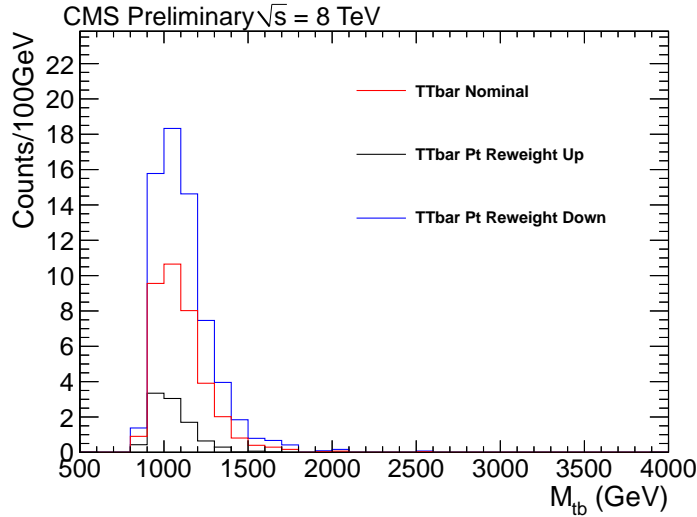


Figure 8.2: p_T re-weighting systematic variation for $t\bar{t}$ Monte Carlo

8.10 Normalization Uncertainties

As mentioned in Section 6.5, the uncertainty due to the overall normalization scale factor used for $t\bar{t}$ is extracted from data and is 19%.

We must apply a 13% uncertainty on the top tagging scale factor described in Section 5.8 to signal Monte Carlo events due to uncertainty in the difference in subject efficiency from data to Monte Carlo.

As mentioned in Section 5.10, we add a 2% uncertainty to the signal estimates from the AK5 vs. CA8 scale factor on b-tagging efficiency.

We also include a 2.6% uncertainty in the luminosity for the signal Monte Carlo [33].

8.11 Uncertainties related to the QCD Background Estimate

We use the result of the fit to the average b-tagging rate (see Chapter 6) to weight pre b-tagged events in order to create the QCD background estimate. Uncertainties in the fitting algorithm and statistical uncertainties in the sideband are taken into account (see figure 6.3). Statistical uncertainties in the pre b tagged signal region are also taken into account.

8.11.1 Choice of the functional form for the average b-tagging rate

The functional form used is a bifurcated polynomial. However there is a systematic uncertainty associated with this choice. The uncertainties due to this effect are taken into account by studying alternative functional forms seen in figure 8.14. The background estimation from these alternative fits are seen in figure 8.15. The uncertainty due to the choice of fit is taken as the Mean Squared Error of these alternative backgrounds bin by bin and can be seen in figure 8.16.

8.11.2 Two-dimensional vs. three-dimensional parameterization of the average b-tagging rate

Additionally, we place an uncertainty on the inability of the background estimate to capture all kinematic correlations through the parameterization of the average b-tagging rate in p_T and η . This uncertainty is calculated by investigating a parameterization in p_T η and M_{tb} . We define P_i as the average b-tagging rate described in Chapter 6 in one η bin and P_{ij} as the average b-tagging rate if parameterized with M_{tb} as well. P_{ij} can be seen in figure 8.17. Each bin in P_i can be thought of as a column average over all M_{tb} bins per p_T bin. If P_{ij} a function of M_{tb} (index j) is not constant, then averaging over P_{ij} over j while projecting onto M_{tb} axis to obtain the QCD background estimate can result in a bias. For more in-depth discussion on this effect, please see Section 19.1.4.

We assess the approximate size of the uncertainty due to our choice of parameterization by explicitly comparing the three-dimensional and two-dimensional background estimates in the sideband. Using these two parameterizations, the uncertainty in the M_{tb} distribution due to parameterization is approximately $\sum_{j=0}^n m_{ij}(P_{ij} - P_i)$ where m_{ij} refers to the number of pretag events for a bin in p_T and M_{tb} . Fig. 8.18 shows the uncertainty due to this effect. These uncertainties are taken in quadrature to produce an overall uncertainty in the data derived background estimate that is applied in a shape based manner in the limit-setting macro.

Rate Effects of Systematic Uncertainties										
Sample	CA bitag SF	QCD total	b-tagging	JES	Lumi	p _T Reweight	JER	Q ²	Subjet SF	Trigger
qed	—	+9.05,-8.94	—	+4.49,-4.49	-0.42,+0.49	+16.49,-15.27	—	—	—	—
ttbar	—	—	—	+6.08,-6.08	-0.27,+0.29	+2.06,-3.85	+2.60,-2.53	+21.77,-14.96	-74.04,+77.89	+0.30,-0.30
1300	+2.00,-1.96	—	—	+6.08,-6.08	-0.27,+0.29	+2.06,-3.85	+2.60,-2.53	—	+12.50,-11.11	+0.06,-0.06
1500	+2.00,-1.96	—	—	+6.48,-6.48	-0.03,+0.17	-0.29,-0.19	+2.60,-2.53	—	+12.50,-11.11	+0.02,-0.02
1700	+2.00,-1.96	—	—	+6.94,-6.94	-0.02,+0.12	-1.27,+1.17	+2.60,-2.53	—	+12.50,-11.11	+0.01,-0.01
1900	+2.00,-1.96	—	—	+8.12,-8.12	-0.08,+0.09	-1.76,+1.78	+2.60,-2.53	—	+12.50,-11.11	+0.01,-0.01
2100	+2.00,-1.96	—	—	+9.39,-9.39	+0.06,-0.05	-1.81,+1.61	+2.60,-2.53	—	+12.50,-11.11	+0.01,-0.01
2300	+2.00,-1.96	—	—	+10.01,-10.01	+0.02,+0.09	-1.76,+1.24	+2.60,-2.53	—	+12.50,-11.11	+0.02,-0.02
2700	+2.00,-1.96	—	—	+9.49,-9.49	-0.25,+0.08	-0.33,+0.47	+2.60,-2.53	—	+12.50,-11.11	+0.04,-0.04

Table 8.2: Rate effects of the systematic uncertainties as extracted from Theta. The numbers listed under sample specify W_R signal Monte Carlo mass.

CHAPTER 8. SYSTEMATIC UNCERTAINTIES

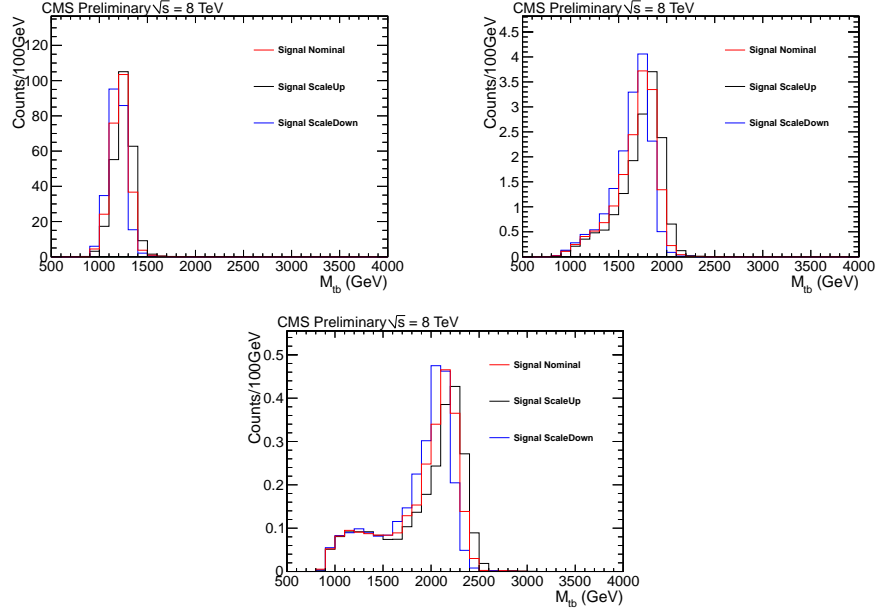


Figure 8.3: Jet Energy Scale systematic variation for Right-handed W' Monte Carlo at the following mass points (a) $M_{W'} = 1300 \text{ GeV}$ (b) $M_{W'} = 1900 \text{ GeV}$ (c) $M_{W'} = 2300 \text{ GeV}$

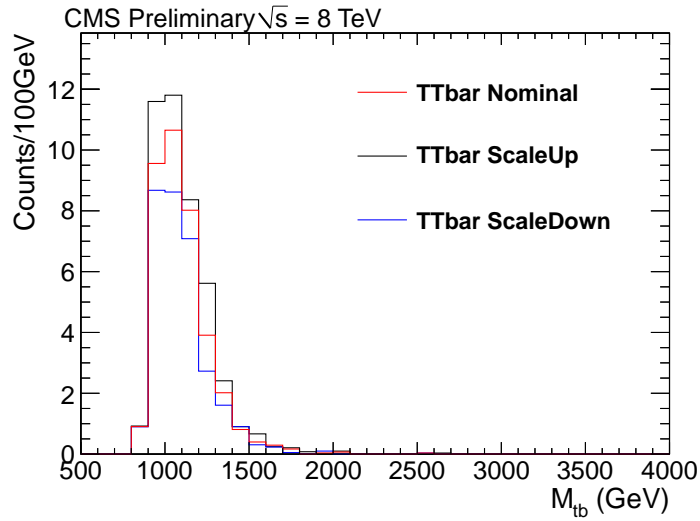


Figure 8.4: Jet Energy Scale systematic variation for $t\bar{t}$ Monte Carlo

CHAPTER 8. SYSTEMATIC UNCERTAINTIES

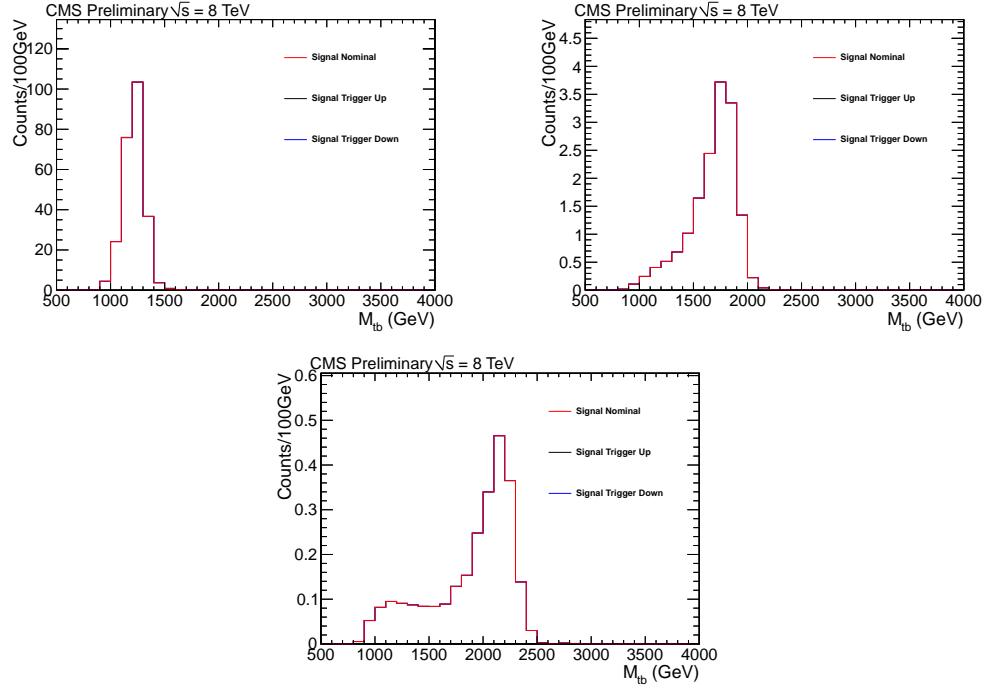


Figure 8.5: Trigger Weighting systematic variation for Right-handed W' Monte Carlo at the following mass points (a) $M_{W'} = 1300 \text{ GeV}$ (b) $M_{W'} = 1900 \text{ GeV}$ (c) $M_{W'} = 2300 \text{ GeV}$

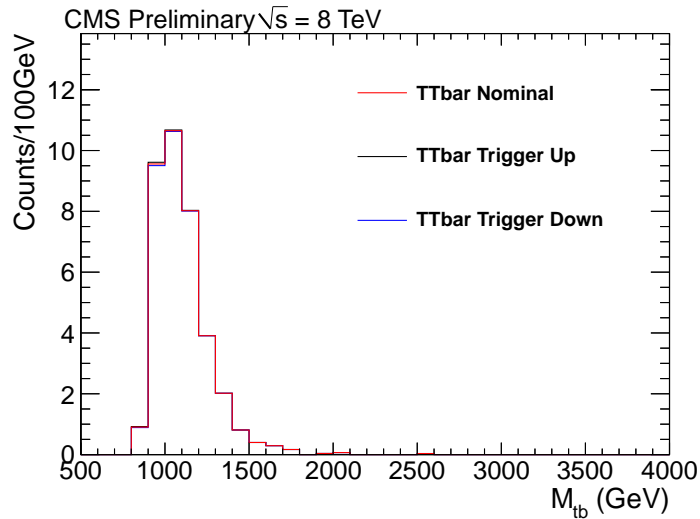


Figure 8.6: Trigger Weighting systematic variation for $t\bar{t}$ Monte Carlo

CHAPTER 8. SYSTEMATIC UNCERTAINTIES

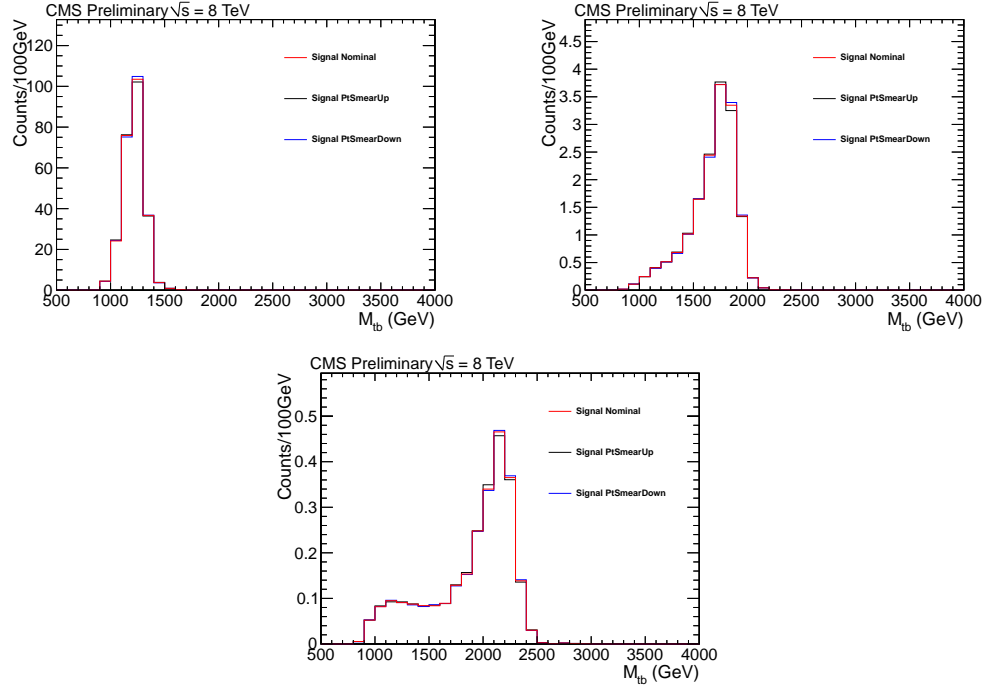


Figure 8.7: Jet Energy Resolution systematic variation for Right-handed W' Monte Carlo at the following mass points (a) $M_{W'} = 1300 \text{ GeV}$ (b) $M_{W'} = 1900 \text{ GeV}$ (c) $M_{W'} = 2300 \text{ GeV}$

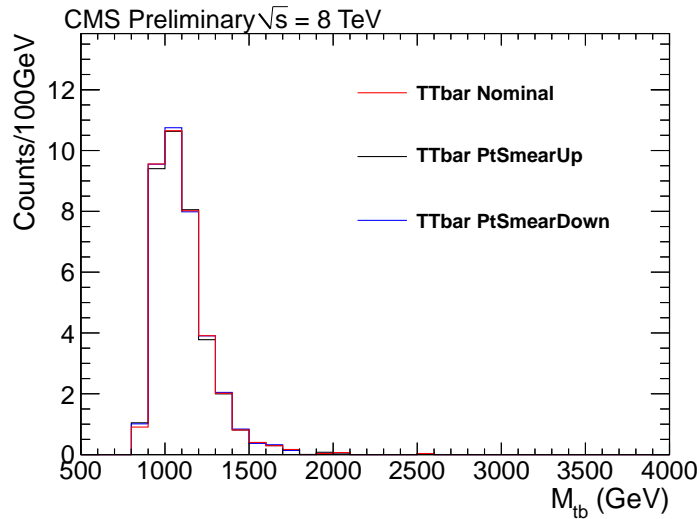


Figure 8.8: Jet Energy Resolution systematic variation for $t\bar{t}$ Monte Carlo

CHAPTER 8. SYSTEMATIC UNCERTAINTIES

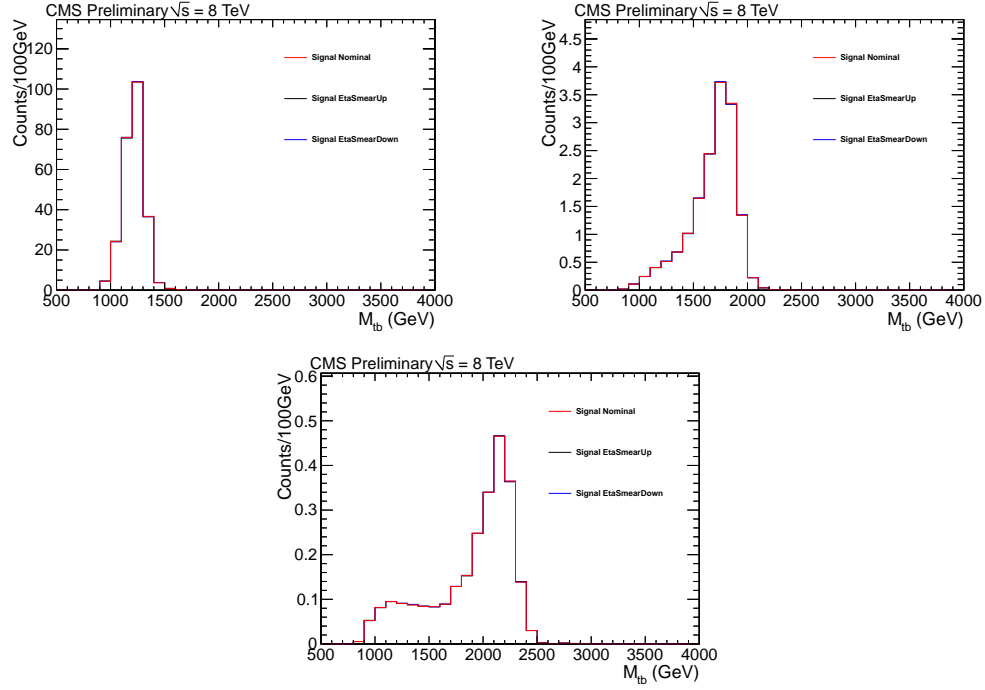


Figure 8.9: Jet Angular Resolution systematic variation for Right-handed W' Monte Carlo at the following mass points (a) $M'_W = 1300 \text{ GeV}$ (b) $M'_W = 1900 \text{ GeV}$ (c) $M'_W = 2300 \text{ GeV}$

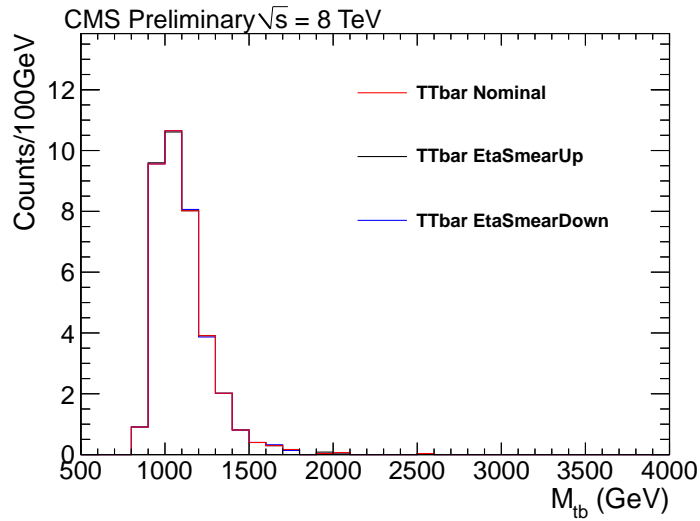


Figure 8.10: Jet Angular Resolution systematic variation for $t\bar{t}$ Monte Carlo

CHAPTER 8. SYSTEMATIC UNCERTAINTIES

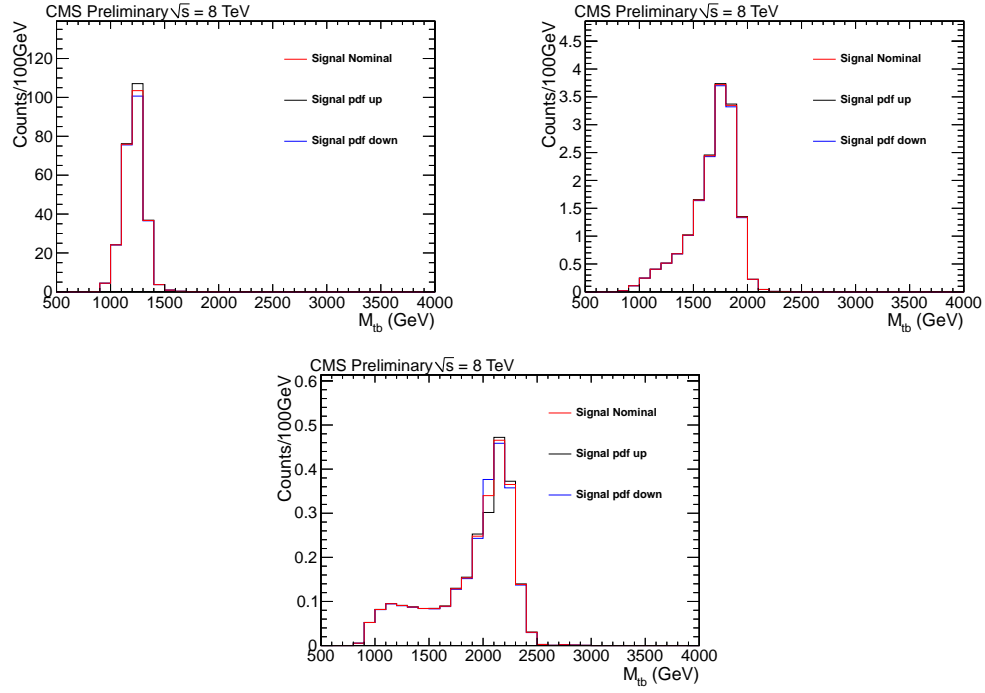


Figure 8.11: PDF systematic variation for Right-handed W' Monte Carlo at the following mass points (a) $M'_W = 1300 \text{ GeV}$ (b) $M'_W = 1900 \text{ GeV}$ (c) $M'_W = 2300 \text{ GeV}$

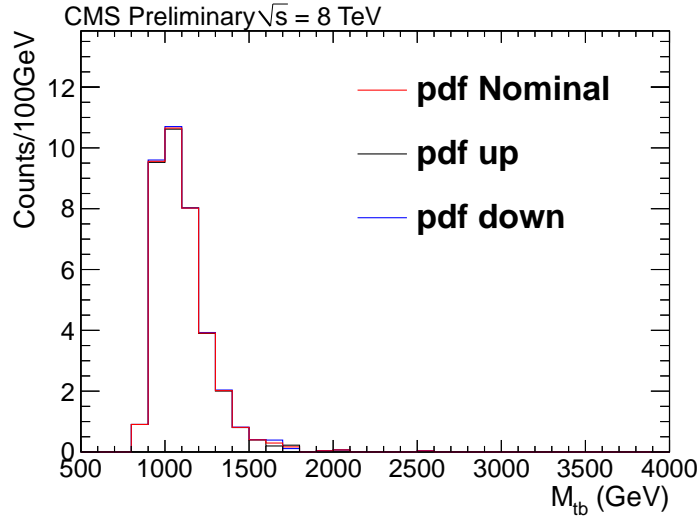


Figure 8.12: PDF systematic variation for $t\bar{t}$ Monte Carlo

CHAPTER 8. SYSTEMATIC UNCERTAINTIES

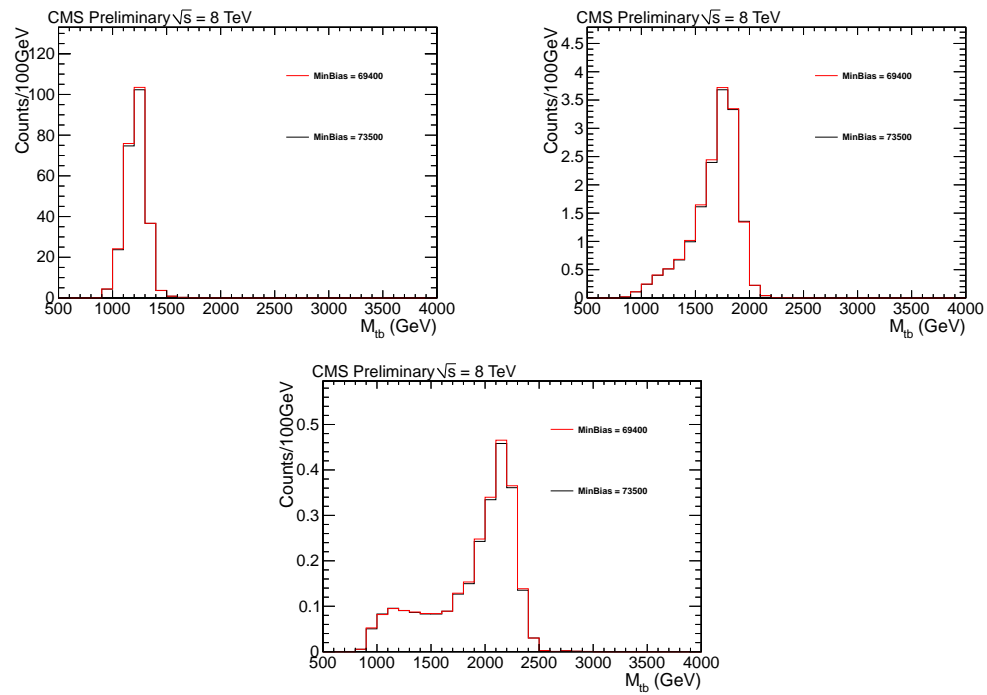


Figure 8.13: Pileup systematic variation for Right-handed W' Monte Carlo at the following mass points (a) $M_{W'} = 1300 \text{ GeV}$ (b) $M_{W'} = 1900 \text{ GeV}$ (c) $M_{W'} = 2300 \text{ GeV}$

CHAPTER 8. SYSTEMATIC UNCERTAINTIES

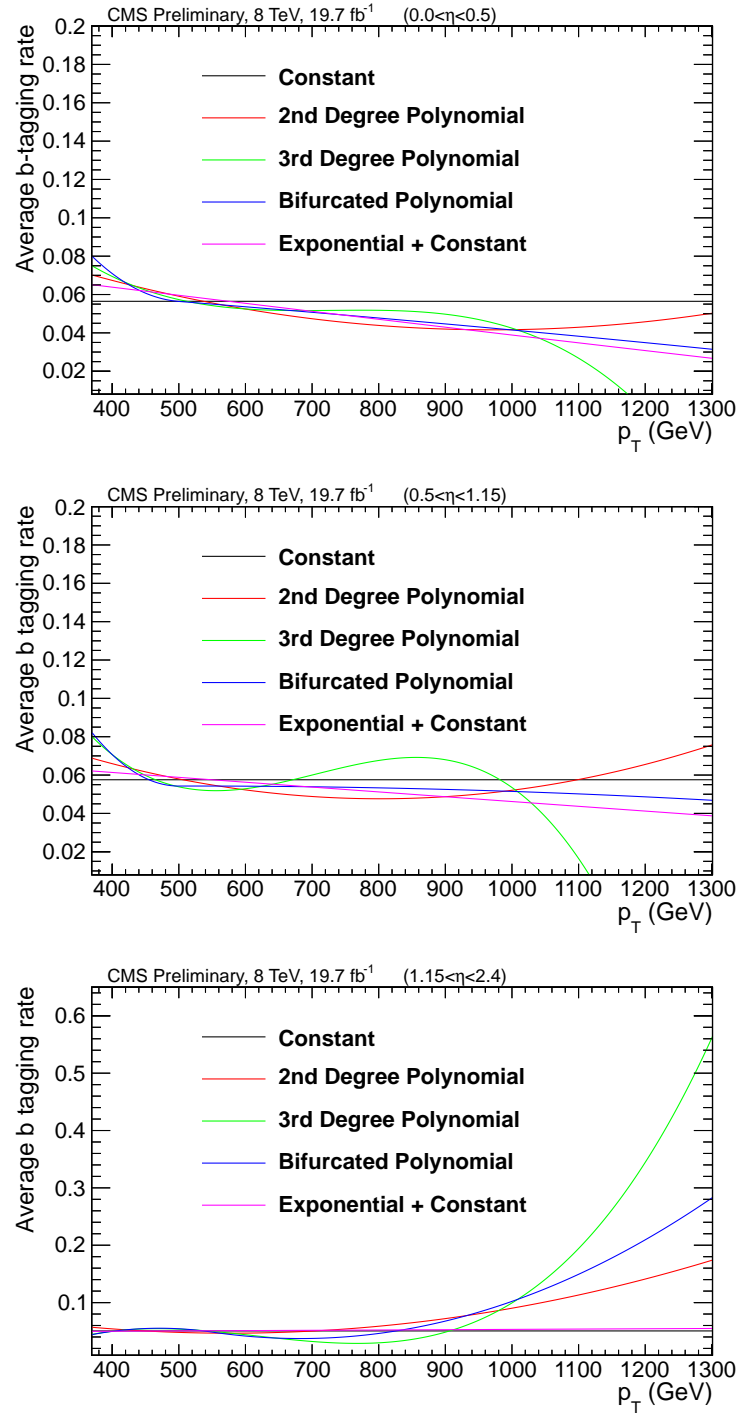


Figure 8.14: Alternative fit functions for the average b-tagging rate in η regions (a) Low (b) Transition (c) High

CHAPTER 8. SYSTEMATIC UNCERTAINTIES

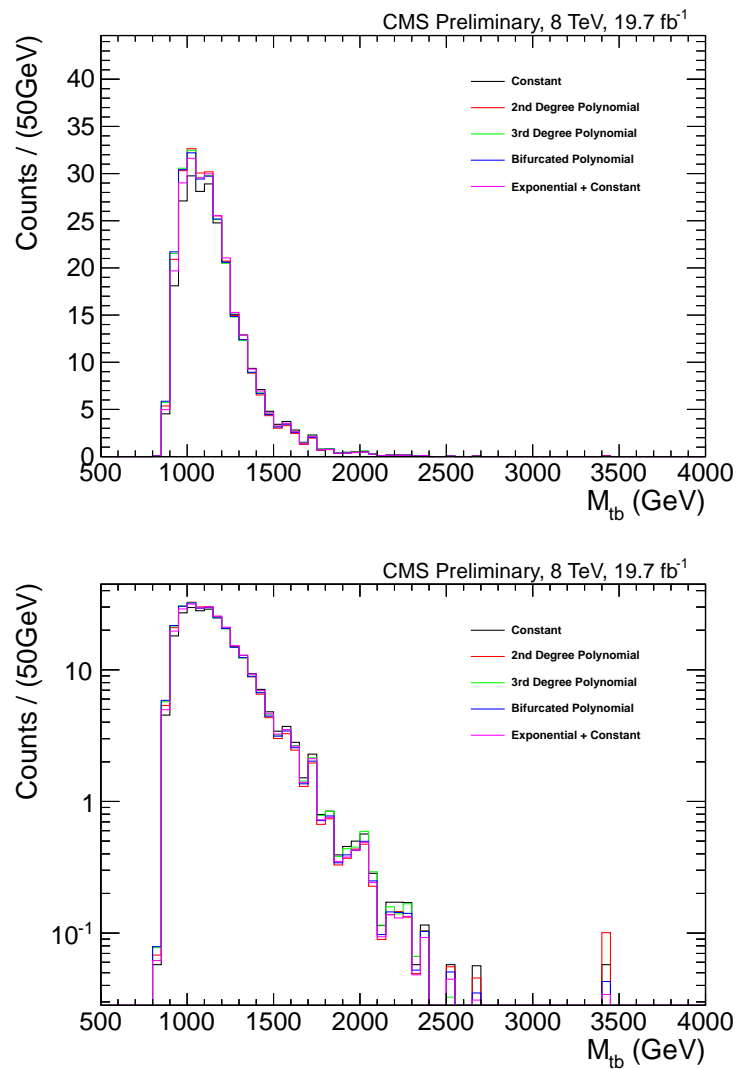


Figure 8.15: QCD background estimation from alternative fit functions seen in 8.14. Top and bottom plots are the same but on linear and log y-axis scale.

CHAPTER 8. SYSTEMATIC UNCERTAINTIES

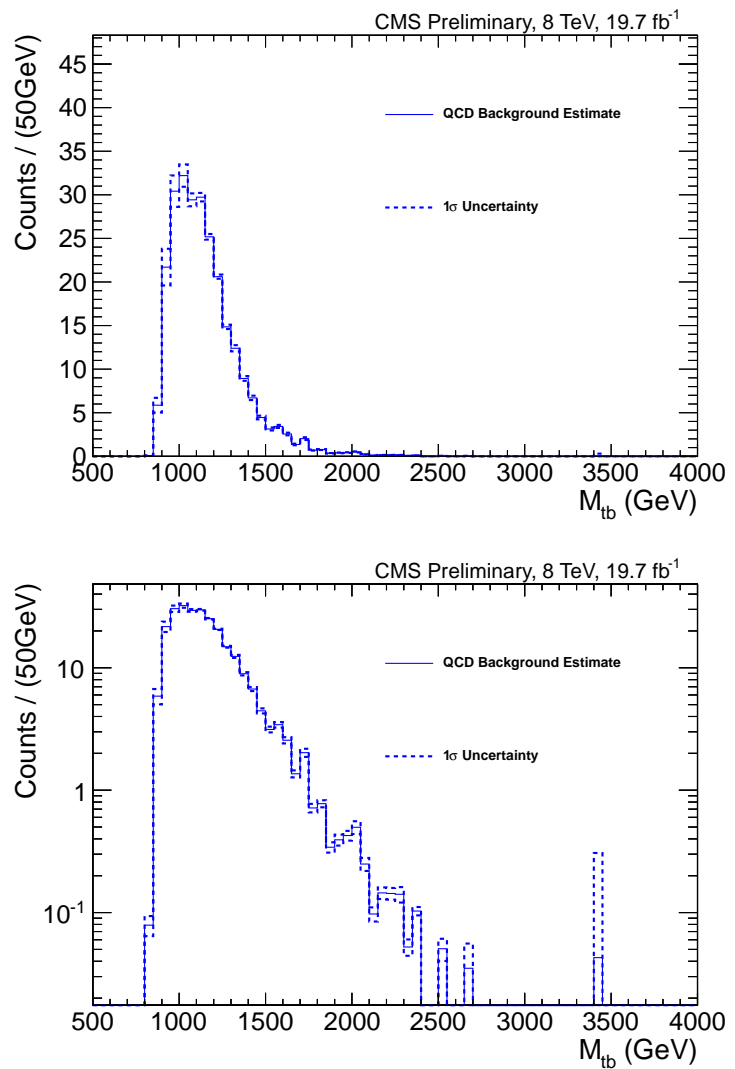


Figure 8.16: Uncertainty on the choice of fit as extracted from the alternative background estimations seen in 8.15. Top and bottom plots are the same but on linear and log y-axis scale.

CHAPTER 8. SYSTEMATIC UNCERTAINTIES

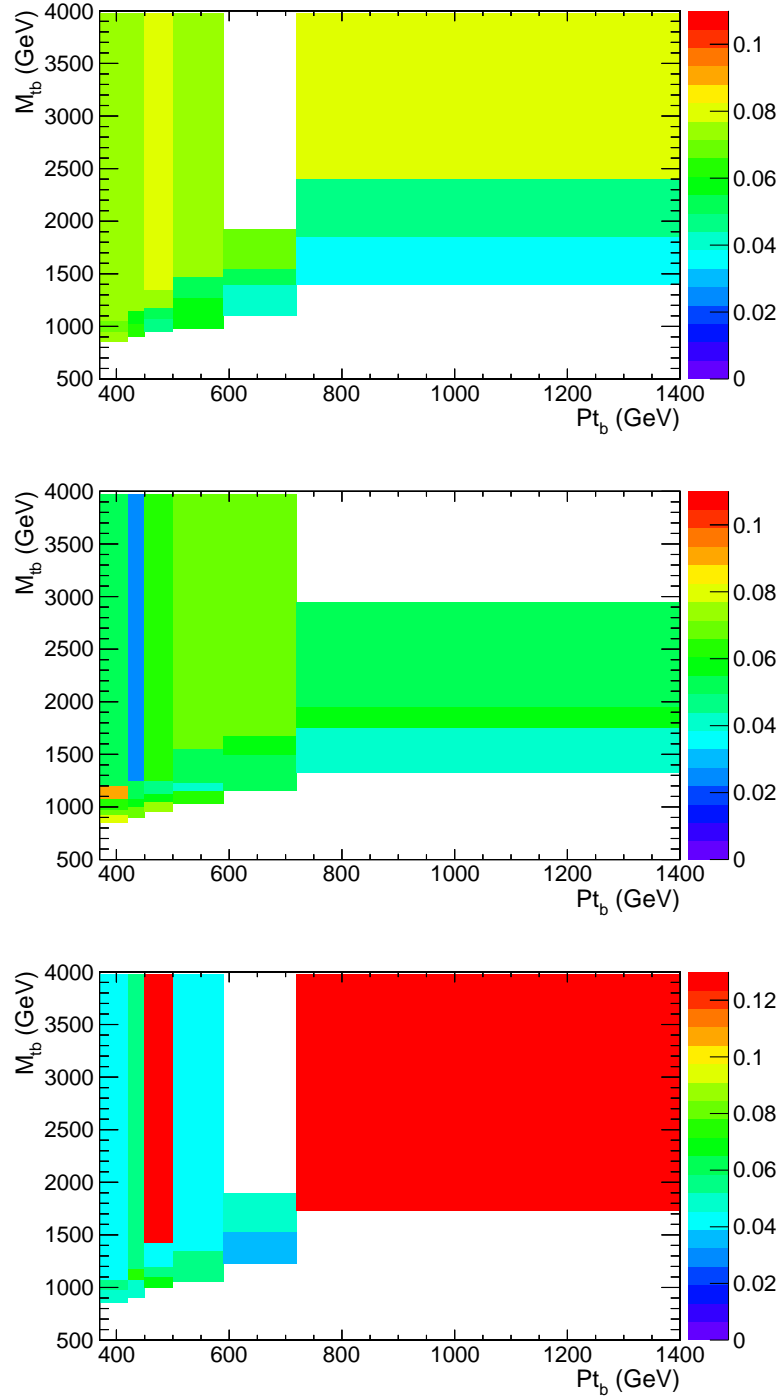


Figure 8.17: Two dimensional parameterization of average b-tagging rate in p_{T_b} and M_{tb} . The x axis binning is identical to the binning in Chapter 6. The y-axis is binned adaptively to approximate equivalent statistics over each y-axis bin per x axis bin. (a) Low η Region (b) Transition η Region (c) High η Region

CHAPTER 8. SYSTEMATIC UNCERTAINTIES

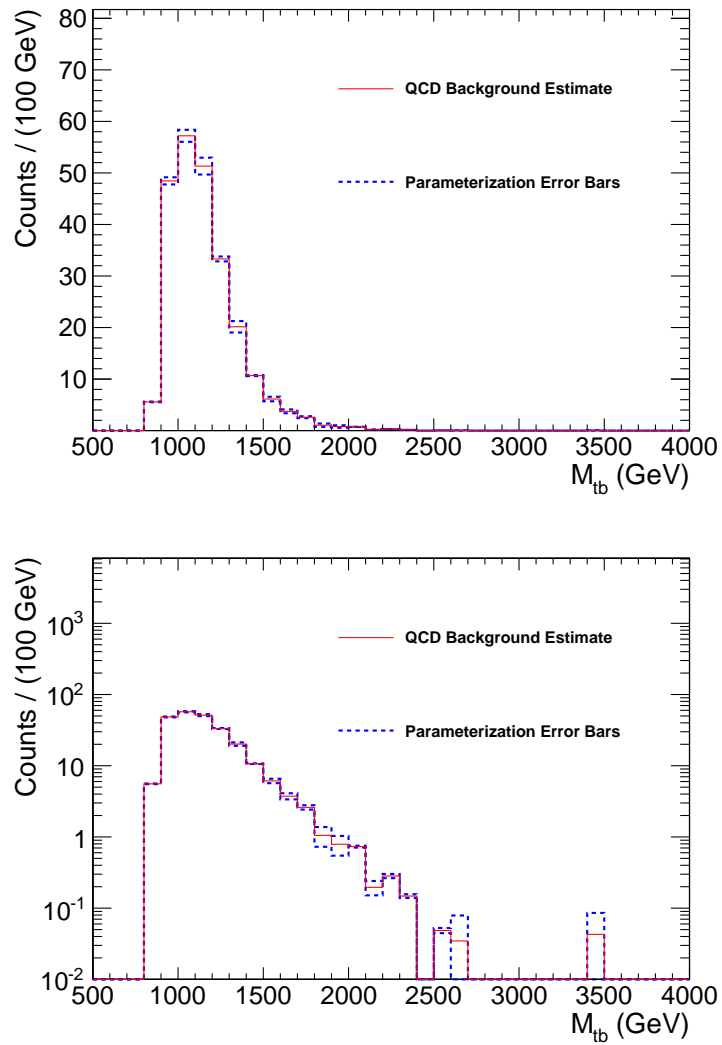


Figure 8.18: Uncertainty on the parameterization choice. Top and bottom plots are the same but on linear and log y-axis scale.

Chapter 9

Results

9.1 Limits

We set limits on the production cross-section of the W'_R boson. We compare the number of observed events to the number of events expected given the new physics model. We use the following formula:

$$N_{\text{expected}} = \sigma_{W'_R} \times B_{W'_R \rightarrow tb; W \rightarrow \text{hadrons}} \times \varepsilon \times L \quad (9.1)$$

where $\sigma_{W'_R}$ is the W'_R cross-section, $B_{W'_R \rightarrow tb; W \rightarrow \text{hadrons}}$ is the branching ratio $W'_R \rightarrow t\bar{b}$ with the W decay constrained to the hadronic branching fraction, ε is the signal efficiency corrected by data-driven scale factors and L is the integrated luminosity of our dataset.

CHAPTER 9. RESULTS

We perform a shape analysis using the M_{tb} distribution. We use a binned likelihood fit to compare the distribution from the W' boson signal hypothesis with the Standard Model distribution produced by our background estimation procedure.

To set shape based limits, the Theta package [15] is used. We use a Bayesian method to extract 95% CL upper limits on the production of a right-handed W' particle.

A Poisson model is used in each bin of our analysis. For each bin, the mean of the Poisson distribution is:

$$\mu_i = \sum_k \beta_k \times T_{k,i} \quad (9.2)$$

here, k includes the signal and background models, and T represents the fraction of events expected for each process k in bin i .

The likelihood function is then:

$$L(\beta_k) = \prod_i^{N_{bins}} \frac{\mu_i \times e^{-\mu_i}}{N_i^{data}!} \quad (9.3)$$

Where μ_i is the mean of the Poisson distribution in bin i , given in terms of T , the number of events expected from the process k .

The Theta package performs pseudoexperiments to calculate 68% and 95% upper bounds on the limit bands. The pseudoexperiments take into account systematic effects as nuisance parameters. These nuisance parameters are varied within their

CHAPTER 9. RESULTS

Cross-Section Upper Limits				
$M_{t\bar{b}}$	observed	expected	expected 1σ	expected 2σ
1300	0.146	0.117	0.080,0.166	0.057,0.229
1500	0.059	0.078	0.056,0.112	0.040,0.163
1700	0.050	0.066	0.047,0.097	0.034,0.130
1900	0.055	0.062	0.043,0.091	0.032,0.126
2100	0.064	0.064	0.046,0.093	0.036,0.140
2300	0.073	0.069	0.052,0.098	0.042,0.147
2700	0.093	0.106	0.082,0.146	0.071,0.211

Table 9.1: W'_R cross-section upper limits for given $M_{t\bar{b}}$ values. Cross-section is in units of pb.

uncertainties and the posterior is refitted for each pseudoexperiment.

The uncertainty in the jet energy scale, Q^2 scale, p_T re-weighting, trigger, SF_b , QCD background uncertainties, and jet energy resolution are taken as shape based uncertainties, and the other sources of uncertainty are taken as overall normalizations.

The limits from Theta are shown in Figure 9.1.

9.2 Generalized Coupling Limits

To set limits on generic couplings, we use the procedure outlined in [10]. The full selection for the left-handed and mixed-coupling samples (described in section 5) can be seen in Figure 5.15. For limit setting, we weight our templates (single top, W'_R ,

CHAPTER 9. RESULTS

Nuisance Parameters											
Sample	JER	JES	QCD total	b-tagging	Q^2	Trigger	CA btag SF	p_T Re-weight	Lumi	$t\bar{t}$ Norm	Subjet SF
wp1300	0.031 ± 1.186	-0.722 ± 0.855	-0.486 ± 0.637	-0.030 ± 1.014	-0.278 ± 1.337	0.002 ± 1.000	0.000 ± 1.006	0.183 ± 0.649	0.000 ± 1.000	0.105 ± 1.007	0.000 ± 1.001
wp1500	0.067 ± 1.111	-0.905 ± 0.370	-0.483 ± 0.532	0.197 ± 0.884	0.420 ± 0.840	0.006 ± 1.969	0.119 ± 1.683	-0.133 ± 0.481	0.155 ± 1.428	0.116 ± 0.901	-0.116 ± 0.934
wp1700	0.694 ± 1.168	-0.727 ± 0.556	-0.381 ± 0.523	0.058 ± 0.950	0.482 ± 1.697	0.070 ± 1.045	0.013 ± 1.700	-0.031 ± 1.462	0.017 ± 1.462	0.173 ± 0.911	0.093 ± 0.971
wp1900	0.137 ± 1.795	-0.501 ± 0.302	-0.340 ± 0.540	-0.013 ± 1.039	0.128 ± 0.285	-0.004 ± 1.999	0.020 ± 1.981	-0.043 ± 0.473	0.026 ± 1.968	0.109 ± 0.895	0.118 ± 1.136
wp2100	0.086 ± 1.333	-0.617 ± 0.745	-0.468 ± 0.524	-0.011 ± 0.989	0.511 ± 0.947	0.000 ± 1.997	-0.002 ± 1.981	0.030 ± 0.514	-0.003 ± 1.967	0.125 ± 0.905	-0.013 ± 1.129
wp2300	0.074 ± 1.079	-0.685 ± 0.780	-0.500 ± 0.714	-0.016 ± 1.015	0.477 ± 0.714	0.000 ± 1.002	0.000 ± 1.980	-0.001 ± 0.561	0.000 ± 1.964	0.131 ± 0.939	0.000 ± 1.090
wp2700	0.259 ± 1.349	-0.643 ± 1.077	-0.396 ± 0.550	-0.054 ± 1.144	0.316 ± 0.824	-0.004 ± 1.997	0.000 ± 1.994	-0.029 ± 0.476	0.000 ± 1.991	0.103 ± 0.894	0.001 ± 1.793

Table 9.2: Nuisance parameters after the fit. This the nominal value found for the nuisance parameter after the fit in units of input sigma. The numbers listed under sample specify W'_R signal Monte Carlo mass.

CHAPTER 9. RESULTS

W' , W'_{LR}) using the following cross-sections respectively:

$$\begin{aligned}\sigma_{SM} &= \sigma_{\text{singletop}} \\ \sigma_R &= \left((a_{ud}^L a_{tb}^L)^2 + (a_{ud}^R a_{tb}^R)^2 - \frac{1}{2} \left((a_{ud}^L a_{tb}^R)^2 + (a_{ud}^R a_{tb}^L)^2 \right) - a_{ud}^L a_{tb}^L \right) \sigma_{W'_R} \\ \sigma_L &= \left(a_{ud}^L a_{tb}^L - \frac{1}{2} \left((a_{ud}^L a_{tb}^R)^2 + (a_{ud}^R a_{tb}^L)^2 \right) \right) \sigma_{W'_L} \\ \sigma_{LR} &= \frac{1}{2} \left((a_{ud}^L a_{tb}^R)^2 + (a_{ud}^R a_{tb}^L)^2 \right) \sigma_{W'_{LR}}\end{aligned}\tag{9.4}$$

Where $\sigma_{W'_{ij}}$ refers to the cross-section for right, left or mixed-coupling samples and $\sigma_{\text{singletop}}$ is the standard model s-channel single top cross-section. We assume $a_{ud} = a_{tb}$. The templates are then summed and limits can be set using the resultant yield as the signal process for the given values of a^L and a^R . Because the left-handed and mixed-coupling samples cannot be separated from SM single top, we set limits on the couplings a^L and a^R . The Theta package is used for this computation and limits are calculated using combinations of the couplings from 0 to 1 in increments of 0.1. Using these limits, we find where $M_{W'}$ cross-section limits align with theory prediction and plot these values in the a^L and a^R plane. These points are where we can exclude the a^L and a^R coupling combinations for the standard model plus W' hypothesis at the given W' mass. The results are shown in Figure 9.2. For this procedure, no systematic uncertainty is considered for the single top contribution due to the fact that statistical uncertainty dominates in these templates (see Figure 9.3).

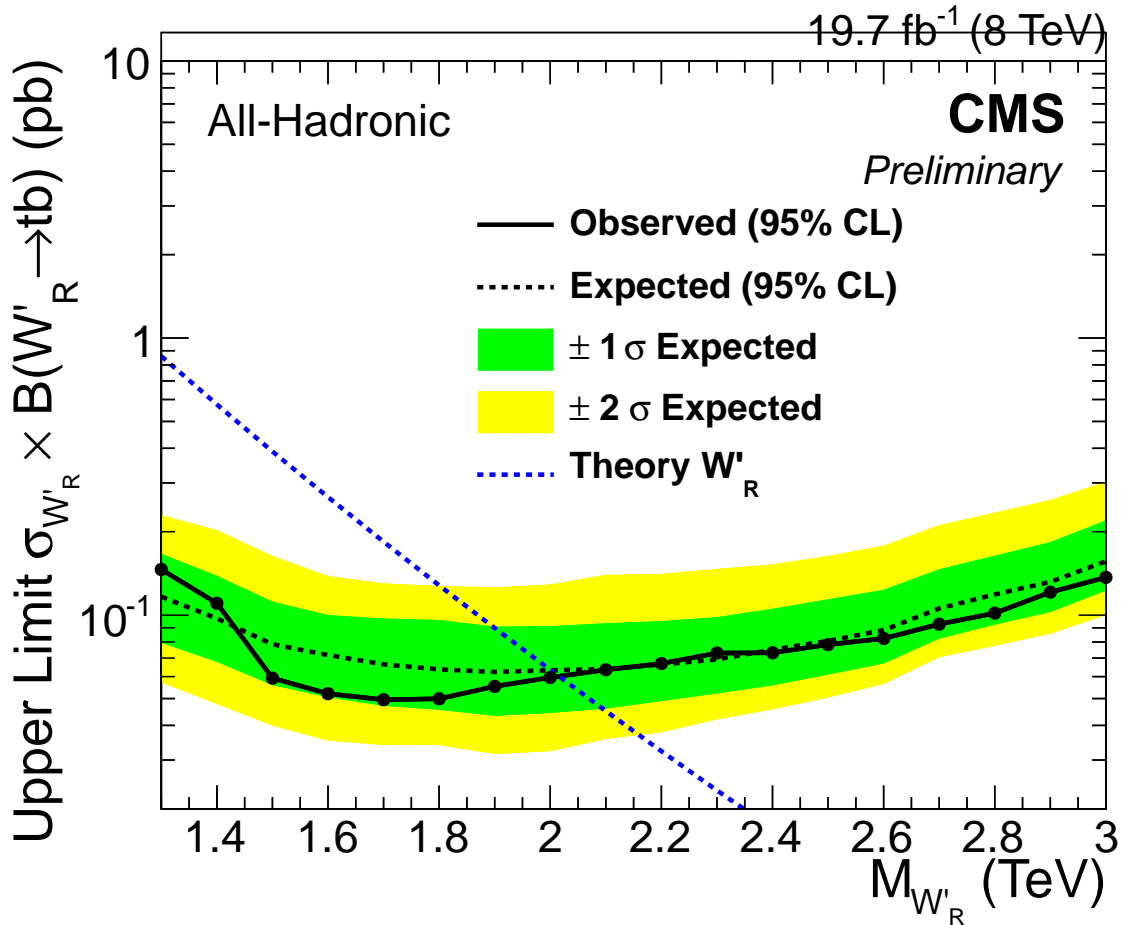


Figure 9.1: The W'_R boson 95% C.L. production cross-section limits. The expected (black) and observed (red) limits as well as W'_R boson theoretical cross-section (blue) are plotted for comparison. The uncertainty in the expected limit band is shown in light ($\pm 1\sigma$) and dark grey ($\pm 2\sigma$). These limits were extracted using the Theta limit setting framework.

CHAPTER 9. RESULTS

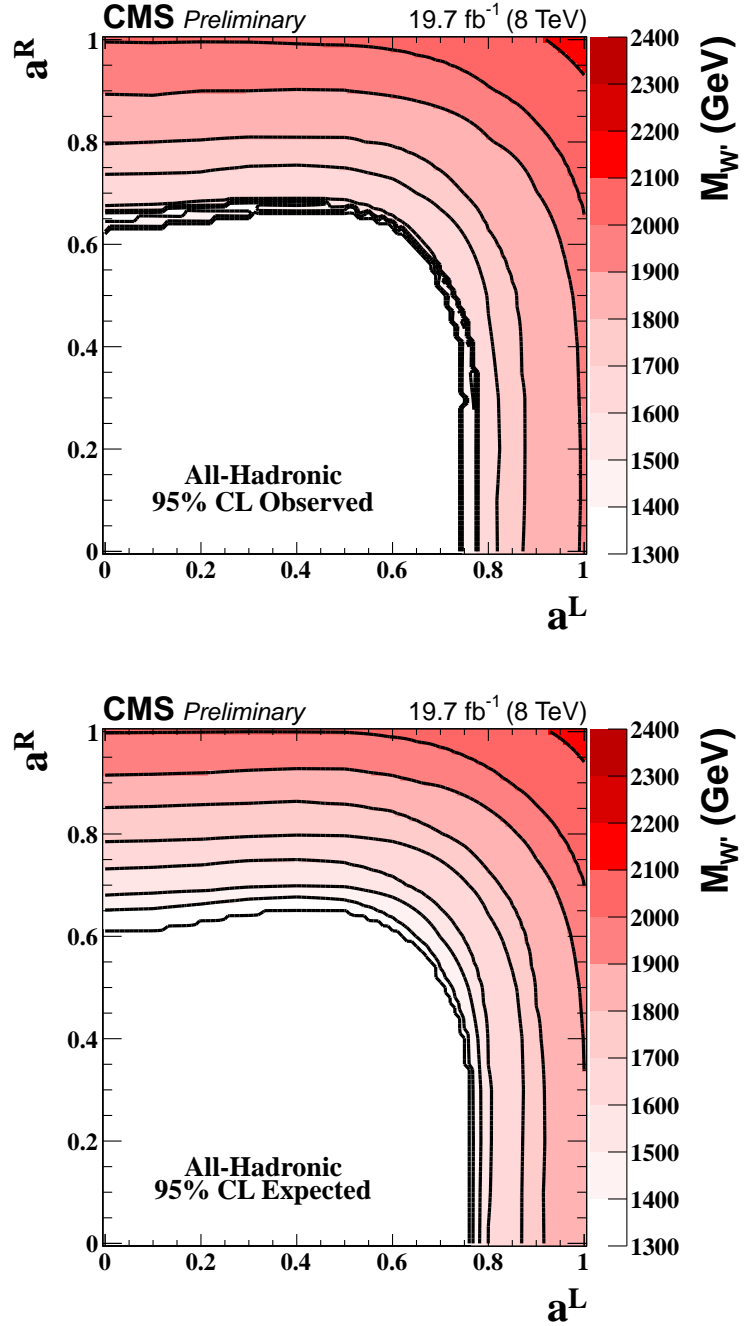


Figure 9.2: Plots of $M_{W'}$ as a function of a^L and a^R . The z axis colors indicate $M_{W'}$ where the theoretical cross section intersects the observed or expected limit band. The top (bottom) plot shows observed (expected) limits.

CHAPTER 9. RESULTS

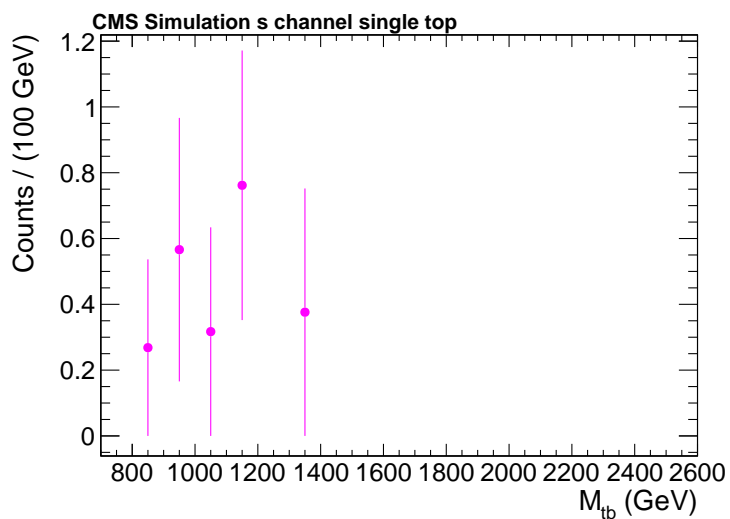


Figure 9.3: Standard model s-channel single top production used for the generalized coupling analysis.

Chapter 10

Combination

To enhance the sensitivity of the measurement of the W' cross-section upper limit as well as the limit set on coupling strengths, the fully-hadronic and semileptonic ($W' \rightarrow tb \rightarrow \ell\nu bb$) W' decay channels have been combined. The analysis of the semileptonic channel is documented in [34]. The fully-hadronic channel includes W' signal generated from a mass of 1300 GeV to 3100 GeV, whereas the semileptonic channel has mass points generated from 800 GeV to 3000 GeV. Therefore, the region of combined sensitivity ranges from W' mass of 1300 GeV to 3000 GeV. Below this region, the semileptonic channel limits are quoted.

There are points within the region of combined sensitivity where the signal sample exists for the semileptonic channel but not for the all-hadronic channel. These intermediate mass points are reproduced using RooFit template morphing to interpolate the shape of the M_{tb} spectrum. The generation level b p_T selection placed on the

CHAPTER 10. COMBINATION

left-handed and mixed coupling W' samples is taken into account by interpolating the selection efficiency for the interpolated mass points.

In combining the analysis sensitivity, the uncertainty sources Jet Energy Scale, Jet Energy Resolution, b-tagging scale factor, and luminosity 8 are correlated, and the remaining are left uncorrelated. Different generators are used for the $t\bar{t}$ production Monte Carlo simulation, so the Q^2 scale and p_T re-weighting uncertainties are not correlated.

The W'_R combined cross-section upper limits are shown in figure 10.1. Here, a W'_R boson with mass less than 2.15 TeV is excluded at the 95% C.L. Combined limits on the W' coupling strengths is shown in figure 10.2.

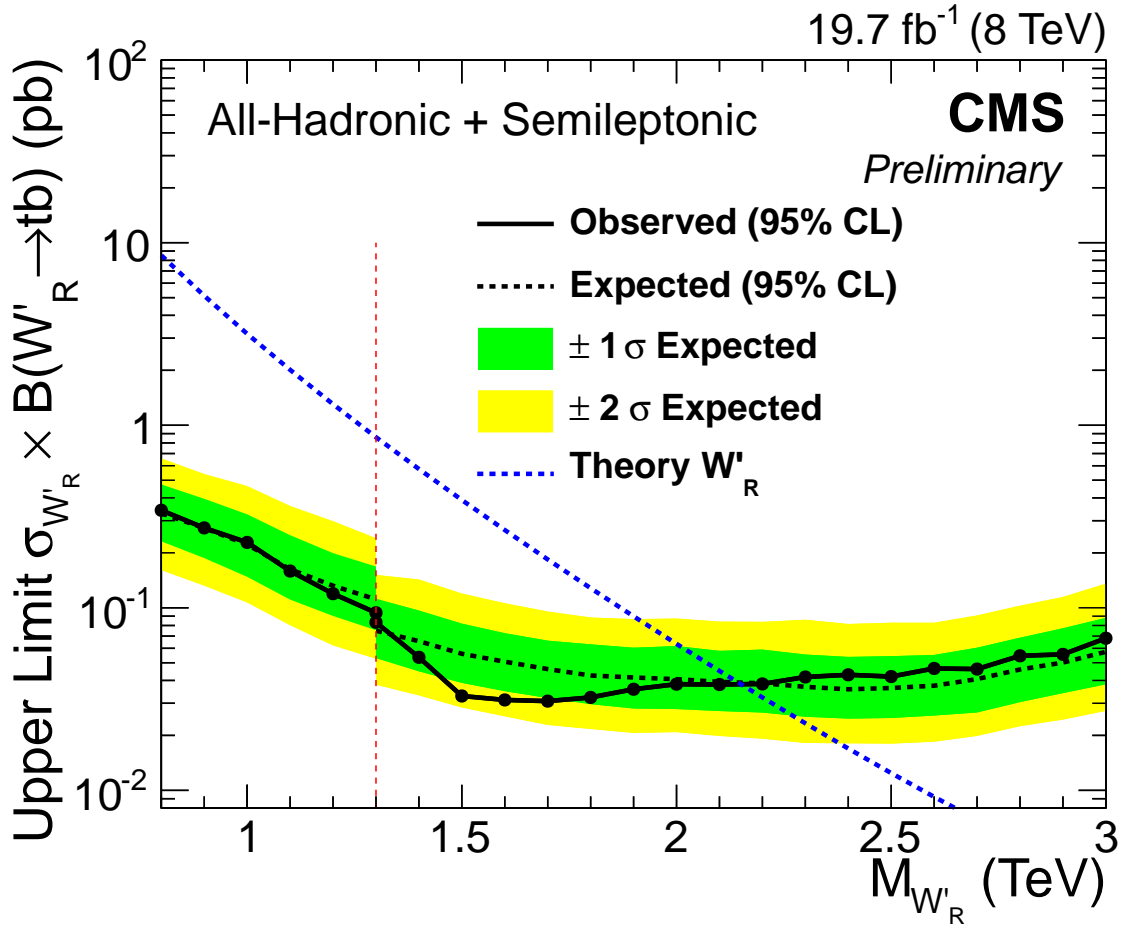


Figure 10.1: The W'_R boson 95% C.L. production cross-section limits for the combined semileptonic and all-hadronic channels. The expected (solid-black) and observed (dashed-black) limits as well as W'_R boson theoretical cross-section (dashed-blue) are plotted for comparison. The uncertainty in the expected limit band is shown in green ($\pm 1\sigma$) and yellow ($\pm 2\sigma$). The left of the red dashed line shows limits purely from the semileptonic channel. The right of the red dashed line shows limits using combined sensitivity from the semileptonic and all-hadronic channels. These limits were extracted using the Theta limit setting framework.

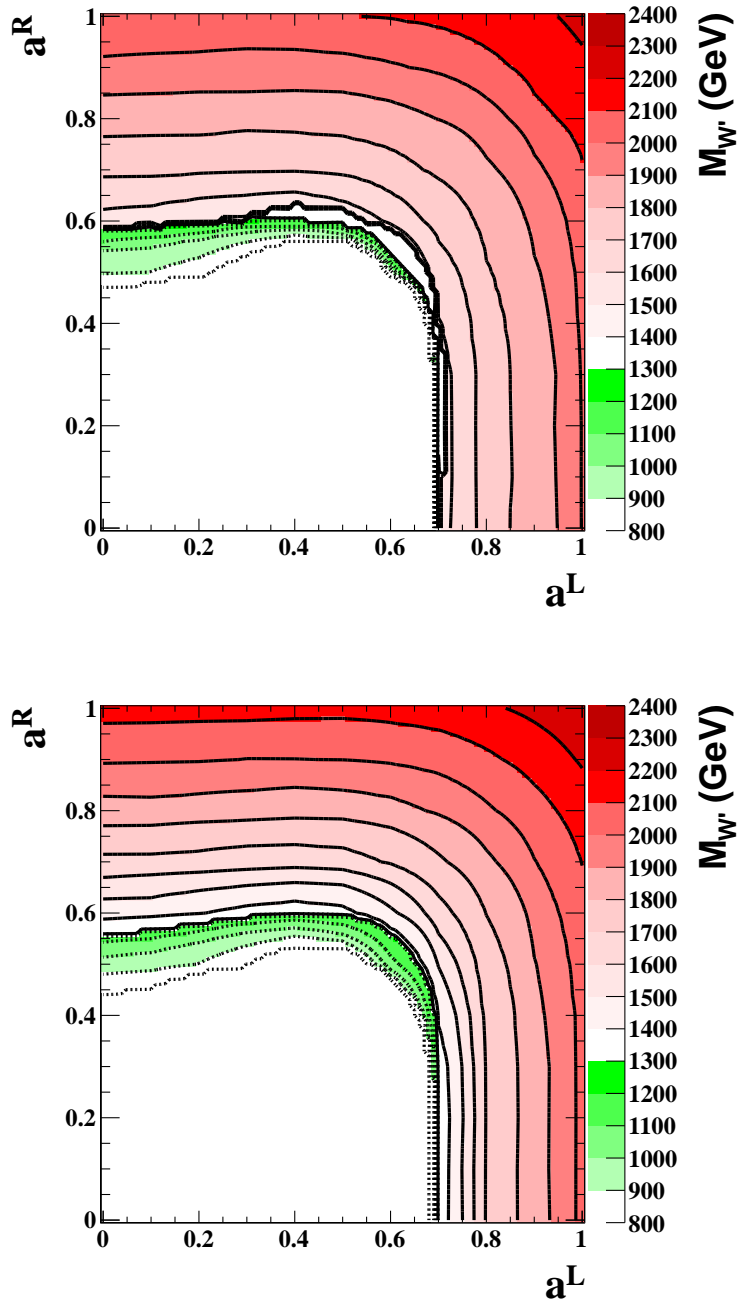


Figure 10.2: Plots of $M_{W'}$ as a function of a^L and a^R . The z axis colors indicate $M_{W'}$ where the theoretical cross section intersects the observed or expected limit band. The red coloration indicates combined sensitivity, green indicates that the limits are purely from the semileptonic channel. The top (bottom) plot shows observed (expected) limits.

Chapter 11

Introduction to the b* Search

The focus of this analysis is a Beyond the Standard Model (BSM) predicted [35] excited b quark referred to as b*. The decay mode considered in this analysis is $b^* \rightarrow tW$, as it is dominant in the b* mass region of interest.

b* production at the LHC takes place through the strong interaction. The lagrangian describing this interaction is as follows:

$$\mathcal{L}_{production} = \frac{g_s}{2\Lambda} G_{\mu\nu} \bar{b} \sigma^{\mu\nu} (\kappa_L^b P_L + \kappa_R^b P_R) b^* + H.c. \quad (11.1)$$

b* $\rightarrow tW$ decay takes place through the weak interaction and is described through the following lagrangian.

CHAPTER 11. INTRODUCTION TO THE B^* SEARCH

$$\mathcal{L}_{decay} = \frac{g_2}{\sqrt{2}} W_\mu^+ \bar{t} \gamma^\mu (g_L P_L + g_R P_R) b^* + H.c. \quad (11.2)$$

We consider three hypotheses for the right- and left-handed couplings.

$$\text{left-handed: } \kappa_L^b = g_L = 1 \text{ and } \kappa_R^b = g_R = 0 \quad (11.3)$$

$$\text{right-handed: } \kappa_L^b = g_L = 0 \text{ and } \kappa_R^b = g_R = 1 \quad (11.4)$$

$$\text{vectorlike : } \kappa_L^b = g_L = 1 \text{ and } \kappa_R^b = g_R = 1 \quad (11.5)$$

Searches for the b^* quark in the tW decay mode have been performed at the ATLAS detector at the LHC [36]. Using 19.7fb^{-1} of integrated luminosity at 8TeV , we exclude a left-handed b^* quark couplings between 0.99TeV and 1.40TeV

Similar to the W' search described in the previous chapters, the b^* quark region of interest is high mass. Therefore, similar boosted techniques are used to identify the top quark decay products and reduce the QCD background. Additionally, similar methods are used to estimate the background due to the success of these methods in the W' search.

Chapter 12

Analysis Strategy

Similar to the W' search, the primary sources of background are QCD multijet and SM $t\bar{t}$ production.

The QCD background component is estimated by a tagging rate based data driven technique similar to the W' search (see section 6.2). We invert the W candidate mass requirement in order to define a control region with negligible signal contribution. This region is used to investigate the mistagging rate for the top tagging algorithm used in the analysis. This top-mistagging rate is then used to weight events in lieu of a top-tag in our full selection. This allows for an estimation of the QCD background component with a low signal pollution component. This procedure is first applied to a control region in order to investigate any potential bias, and is then applied to the signal region selection (see Section 14.1).

The shape of the Standard Model $t\bar{t}$ production contribution is estimated from

CHAPTER 12. ANALYSIS STRATEGY

Monte Carlo simulation. The normalization of this contribution is measured in a third control region that is enriched in $t\bar{t}$ production (see Section 14.4).

The data and background components are then used as templates by the Bayesian statistical procedure identical to the W' search

Chapter 13

Data Sample and Event Selection

The data sample used for this analysis corresponds to $19.7 \pm 0.5 \text{ fb}^{-1}$ of integrated luminosity collected in 2012 at $\sqrt{s} = 8 \text{ TeV}$. See Table 5.1 for a summary of the datasets used in the analysis.

13.1 Signal Samples

The b^* generation is performed using two different coupling hypotheses.

- b_R^* - The purely right-handed b^* where $\kappa_L^b = g_L = 0$, $\kappa_R^b = g_R = 1$
- b_L^* - The purely left-handed b^* where $\kappa_L^b = g_L = 1$, $\kappa_R^b = g_R = 0$

The right- and left-handed b^* samples used in this analysis are given in table 13.1 and 13.2 respectively. The vectorlike b_{LR}^* signal template is created by summing the right- and left-handed templates after normalization to theory cross-section.

Right-Handed Signal Samples

Dataset	Cross-Section (pb)
Bstar_fullHad_right_M-800_TuneZ2star_8TeV-madgraph	1.36
Bstar_fullHad_right_M-900_TuneZ2star_8TeV-madgraph	0.662
Bstar_fullHad_right_M-1000_TuneZ2star_8TeV-madgraph	0.336
Bstar_fullHad_right_M-1100_TuneZ2star_8TeV-madgraph	0.178
Bstar_fullHad_right_M-1200_TuneZ2star_8TeV-madgraph	0.0966
Bstar_fullHad_right_M-1300_TuneZ2star_8TeV-madgraph	0.0540
Bstar_fullHad_right_M-1400_TuneZ2star_8TeV-madgraph	0.0310
Bstar_fullHad_right_M-1500_TuneZ2star_8TeV-madgraph	0.0181
Bstar_fullHad_right_M-1600_TuneZ2star_8TeV-madgraph	0.0108
Bstar_fullHad_right_M-1700_TuneZ2star_8TeV-madgraph	0.00652
Bstar_fullHad_right_M-1800_TuneZ2star_8TeV-madgraph	0.00399
Bstar_fullHad_right_M-1900_TuneZ2star_8TeV-madgraph	0.00249
Bstar_fullHad_right_M-2000_TuneZ2star_8TeV-madgraph	0.00156

Table 13.1: Right handed signal samples along with the cross sections used in the analysis.

Left-Handed Signal Samples

Dataset	Cross-Section (pb)
Bstar_fullHad_left_M-800_TuneZ2star_8TeV-madgraph	1.36
Bstar_fullHad_left_M-900_TuneZ2star_8TeV-madgraph	0.662
Bstar_fullHad_left_M-1000_TuneZ2star_8TeV-madgraph	0.336
Bstar_fullHad_left_M-1100_TuneZ2star_8TeV-madgraph	0.178
Bstar_fullHad_left_M-1200_TuneZ2star_8TeV-madgraph	0.0966
Bstar_fullHad_left_M-1300_TuneZ2star_8TeV-madgraph	0.0540
Bstar_fullHad_left_M-1400_TuneZ2star_8TeV-madgraph	0.0310
Bstar_fullHad_left_M-1500_TuneZ2star_8TeV-madgraph	0.0181
Bstar_fullHad_left_M-1600_TuneZ2star_8TeV-madgraph	0.0108
Bstar_fullHad_left_M-1700_TuneZ2star_8TeV-madgraph	0.00652
Bstar_fullHad_left_M-1800_TuneZ2star_8TeV-madgraph	0.00399
Bstar_fullHad_left_M-1900_TuneZ2star_8TeV-madgraph	0.00249
Bstar_fullHad_left_M-2000_TuneZ2star_8TeV-madgraph	0.00156

Table 13.2: Left handed signal samples along with the cross sections used in the analysis.

13.2 Trigger Selection

Similar to the W' search, we use the `HLT-HT750` trigger. The trigger efficiency is measured in data and Monte Carlo by investigating the looser `HLT-HT550` trigger. The selection used for this measurement includes a loose kinematic selection in which we require two jets with $p_T > 300$ GeV. The denominator is defined as passing this selection and the `HLT-HT550` trigger, whereas the numerator is required to pass the selection and both the `HLT-HT550` and `HLT-HT750` trigger. The efficiency is shown in Figure 13.1 and is parameterized as a function of summed leading and sub-leading jet p_T . The extracted trigger efficiency is used to weight the Monte Carlo samples used in the analysis to account for the loss in efficiency in the turn-on. We do not observe perfect agreement in data and Monte Carlo, so we use the trigger efficiency derived from data to weight our Monte Carlo samples, and therefore use a conservative uncertainty on the efficiency measurement (see section 16). The red dashed line in figure 13.1 indicates the minimum for the analysis, at which point the trigger is nearly fully efficient.

13.3 Event Pre-selection

The following pre-selection is applied:

- The event must have a good primary vertex as computed by a deterministic annealing filter (DAF) ($|z_{\text{Primary Vertex}}| < 24$ cm, $N_{\text{DOF}} > 6$).

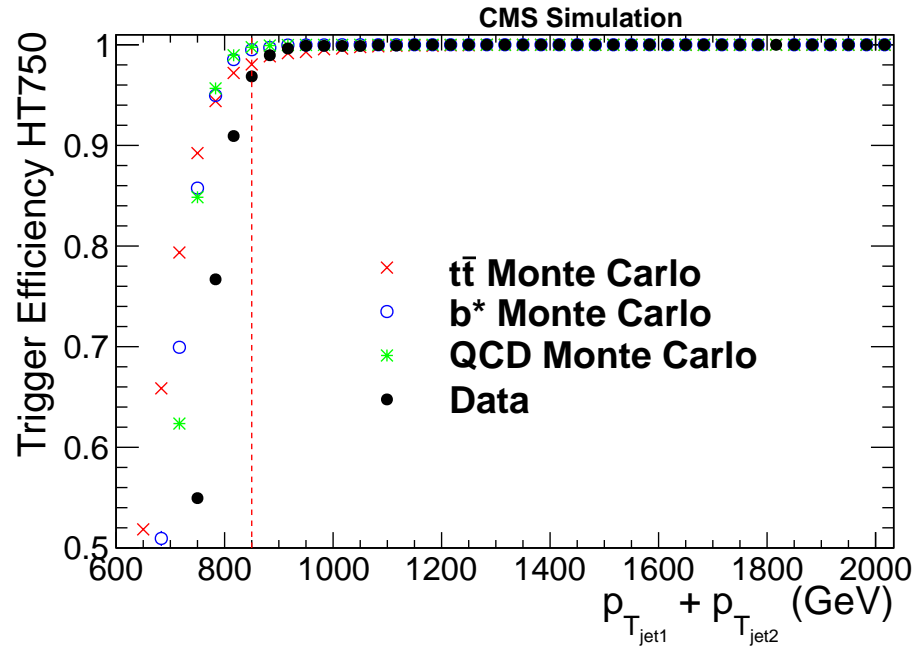


Figure 13.1: Trigger efficiency of HLT-HT750 measured as a function of the summed p_T of the leading and sub-leading jets.

- Two jets with $|y| < 2.4$
- Exactly two jets with $p_T > 150$ GeV
- Leading Jet & Sub-leading Jet $p_T > 425$ GeV
- Loose Particle Flow jet identification [27] is applied
- Beam background events are removed using the following requirements:
 - In events with at least 10 tracks, a minimum of 25% of these tracks must be high purity tracks.

Here we do not include the $|\Delta y|$ discrimination used in the W' search due to the fact that the expected b^* mass exclusion point is lower, and this cut is highly energy dependent.

13.4 Pileup Correction

We re-weight our Monte Carlo samples to account for differences due to pileup using the recommended procedure (see Section 5.7). Figure 13.2 shows the distribution of reconstructed primary vertices in data, $t\bar{t}$, and signal Monte Carlo before and after the re-weighting has been applied. The pileup correction has very little effect on the eventual M_{tW} full selection, as seen in Figure 13.3, for b_R^* signal Monte Carlo at the 1300 GeV mass point. Similarly, there is little effect $t\bar{t}$ Monte Carlo as can be seen in Figure 13.4. A study has been conducted to investigate the effect of the suggested systematic uncertainty of 5% on the minbias cross-section as can be seen in Section 16.

13.5 Combined CMS Top Tagging Algorithm

The CMS top tagging algorithm is described in detail in Section 5.8. Figure 13.5 shows τ_3/τ_2 comparison using signal and QCD Monte Carlo samples. We use the

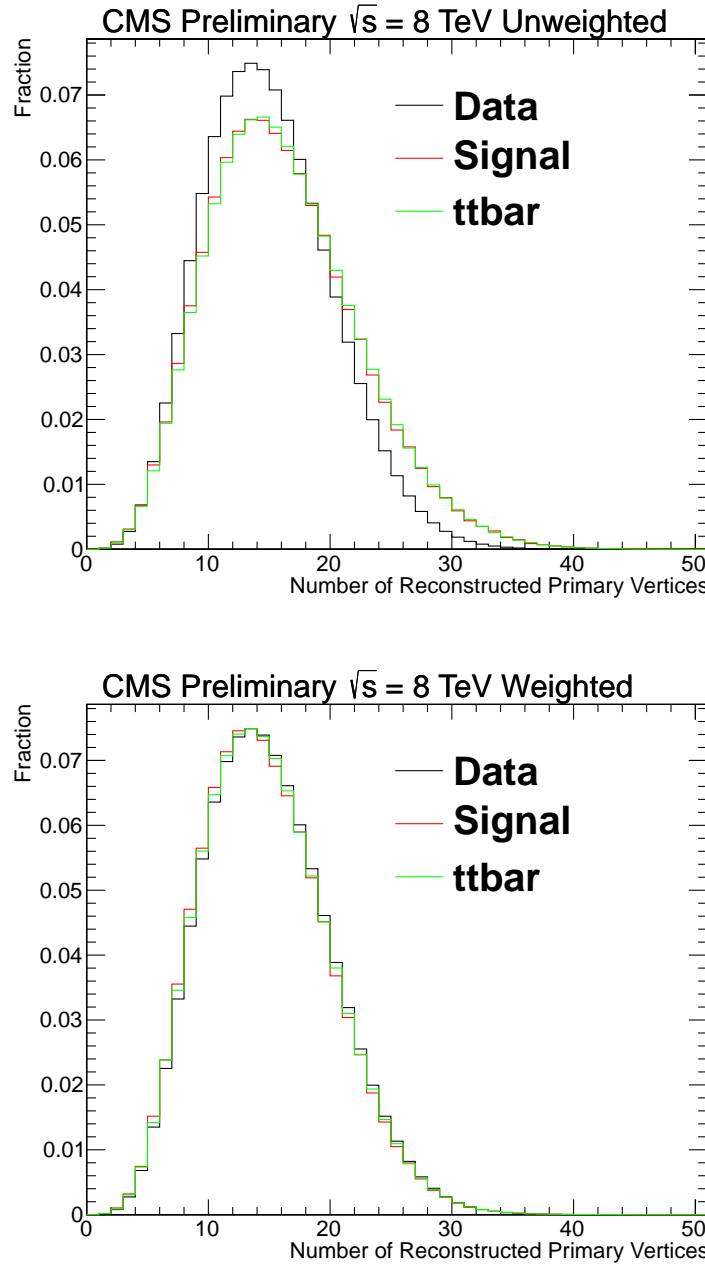


Figure 13.2: Number of reconstructed primary vertices before pileup re-weighting (top) and after pileup re-weighting (bottom). Here, no analysis cuts have been applied and the signal is $b_R^* 1000 \text{ GeV}$

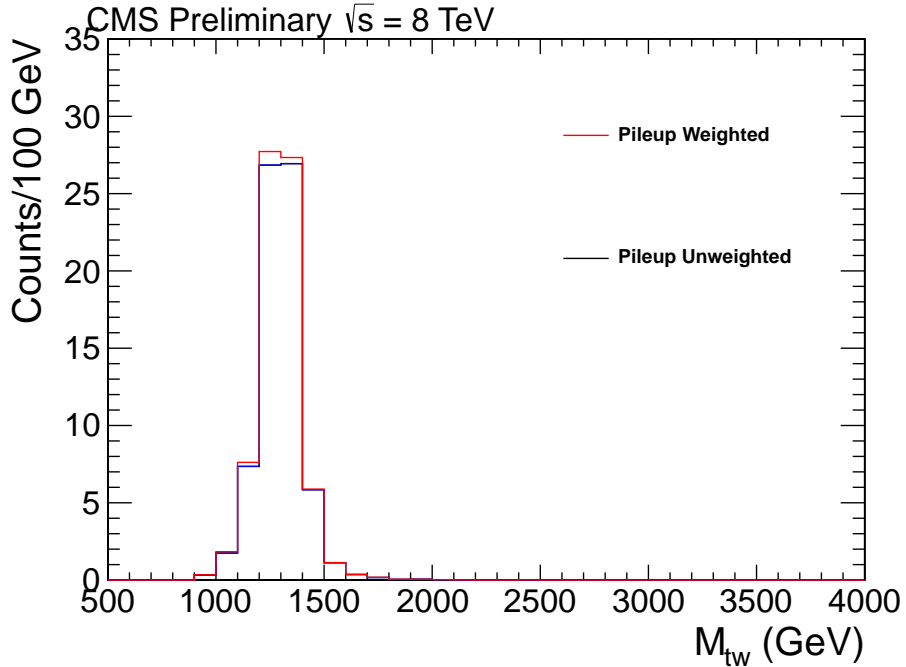


Figure 13.3: Effect of pileup re-weighting on the right-handed b^* Signal Monte Carlo.

standard operating point of $\tau_3/\tau_2 < 0.55$ in the full selection. Figure 13.6 shows the maximum subjet CSV b discriminant comparison using signal and QCD Monte Carlo samples. We use the standard CSV working point $SJ_{CSVMAX} > 0.679$.

13.6 W Jet Identification

The W boson daughter if the b^* quark will also be boosted. Just as the CMS top tagging algorithm discriminates signal from background using the merged top jet, the boosted W boson tagging discriminates signal from background by using a merged W jet. For this we constrain the jet mass to the W boson range, and use the N-subjettiness algorithm. To identify the two subjets of the W boson, the N-subjettiness

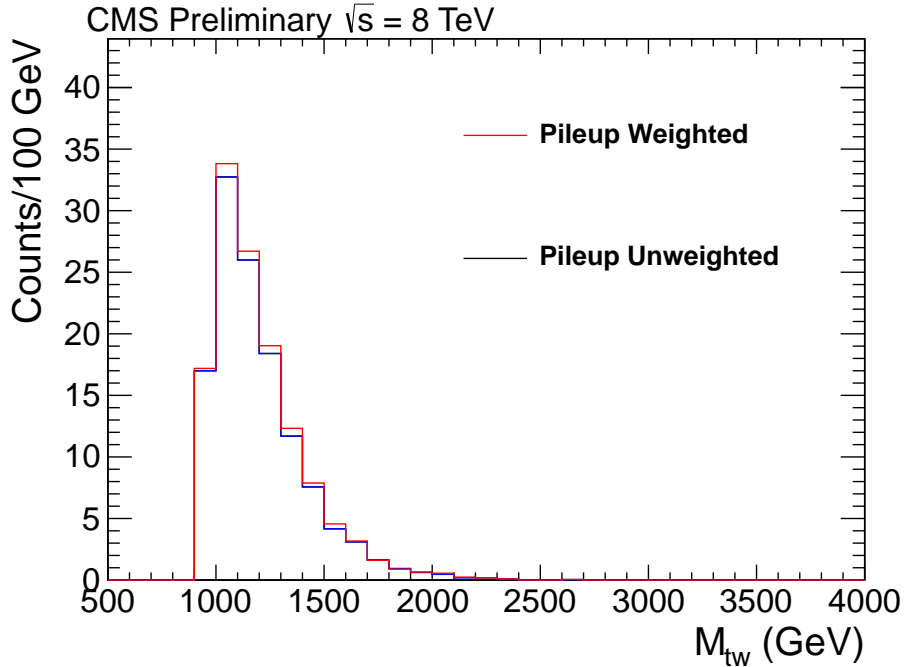


Figure 13.4: Effect of pileup re-weighting on the $t\bar{t}$ Monte Carlo.

variable used is τ_2/τ_1 due to the fact that the jet energy is more consistent with two subjects than one.

- **Jet Mass** $70 \text{ GeV} < m_{\text{jet}} < 100 \text{ GeV}$ - The mass of the CA jet is required to be consistent with the W boson mass.
- **N-subjettiness** $\tau_2/\tau_1 < 0.5$ - The ratio of the N-subjettiness variables τ_2 and τ_1 should be low, as the W jet is more consistent with two subjects than one.

13.7 Reconstruction of b^* invariant mass

The full selection for the reconstruction of the b^* invariant mass then includes the following offline cuts.

- One jet with $p_T > 425$ GeV with the CMS top tagging algorithm as well as subjet b-tagging and N-subjettiness discrimination.
- One jet with $p_T > 425$ GeV with a boosted W tag
- $|\Delta\phi| > \pi/2$ between the two jets

After this selection, the b^* invariant mass is reconstructed using the top-W candidate mass (M_{tW}). The cutflow for this selection in data, $t\bar{t}$ Monte Carlo, and b^* signal Monte Carlo can be found in Table 13.3. Figure 13.7 shows this full selection in signal Monte Carlo for various b^* masses.

CHAPTER 13. DATA SAMPLE AND EVENT SELECTION

Sample	$\geq 2 jets$	$exactly 2 jets$	p_T	M_{top}	$N_{subjets}$	$Minmass$	τ_3/τ_2	SJ_{CSVMAX}	M_W	τ_2/τ_1
Data	18868018	13854873	3545312	1047669	593104	337754	39409	7334	800	318
QCD	—	—	—	—	—	—	—	—	—	211
tbar	13214	10453	3533	2683	2338	2146	1295	934	174	129
$M(b^{*R}) = 800$	3930	3334	388	233	196	175	99	67	40	33
$M(b^{*R}) = 900$	4300	3782	854	445	385	345	212	149	106	91
$M(b^{*R}) = 1000$	3136	2769	1407	789	681	614	381	276	217	183
$M(b^{*R}) = 1100$	1976	1730	1191	732	631	572	350	251	192	161
$M(b^{*R}) = 1200$	1183	1031	808	538	460	421	254	180	137	114
$M(b^{*R}) = 1300$	705	607	507	357	304	280	166	116	88	73
$M(b^{*R}) = 1400$	429	365	318	232	196	181	105	72	55	45
$M(b^{*R}) = 1500$	255	216	193	145	121	112	64	43	33	27
$M(b^{*R}) = 1600$	155	131	118	91	76	70	39	26	19	16
$M(b^{*R}) = 1700$	97	80	74	57	47	43	24	16	12	9
$M(b^{*R}) = 1800$	59	49	45	35	29	27	15	9	7	5
$M(b^{*R}) = 1900$	37	30	28	22	18	17	9	6	4	3
$M(b^{*R}) = 2000$	23	19	18	14	12	10	5	3	2	2
$M(b^{*L}) = 800$	3855	3259	374	227	179	159	84	55	31	26
$M(b^{*L}) = 900$	4223	3712	838	472	376	330	186	129	88	75
$M(b^{*L}) = 1000$	3103	2744	1356	810	637	555	309	221	173	147
$M(b^{*L}) = 1100$	1959	1722	1172	757	601	532	292	204	157	131
$M(b^{*L}) = 1200$	1180	1028	797	548	436	389	210	144	109	91
$M(b^{*L}) = 1300$	703	606	503	365	290	262	138	93	70	58
$M(b^{*L}) = 1400$	423	361	313	235	187	170	87	58	44	36
$M(b^{*L}) = 1500$	254	215	191	146	116	105	53	34	25	21
$M(b^{*L}) = 1600$	155	130	117	92	73	66	33	20	15	12
$M(b^{*L}) = 1700$	95	79	73	58	45	41	20	12	9	7
$M(b^{*L}) = 1800$	59	49	45	36	28	25	12	7	5	4
$M(b^{*L}) = 1900$	37	30	28	23	18	16	8	4	3	2
$M(b^{*L}) = 2000$	23	19	18	14	11	10	5	3	2	< 1

Table 13.3: Cutflow Table. Table reads left to right where the current column implies the previous cuts. QCD expectation is only recorded for the full selection, due to the fact that the background estimate is only valid after top tagging. The first column implies the $p_T > 150$ GeV preselection for any jet. The second column additionally represents the delta phi selection between the leading jets. The column labeled p_T represents the p_T cut placed on both leading jets.

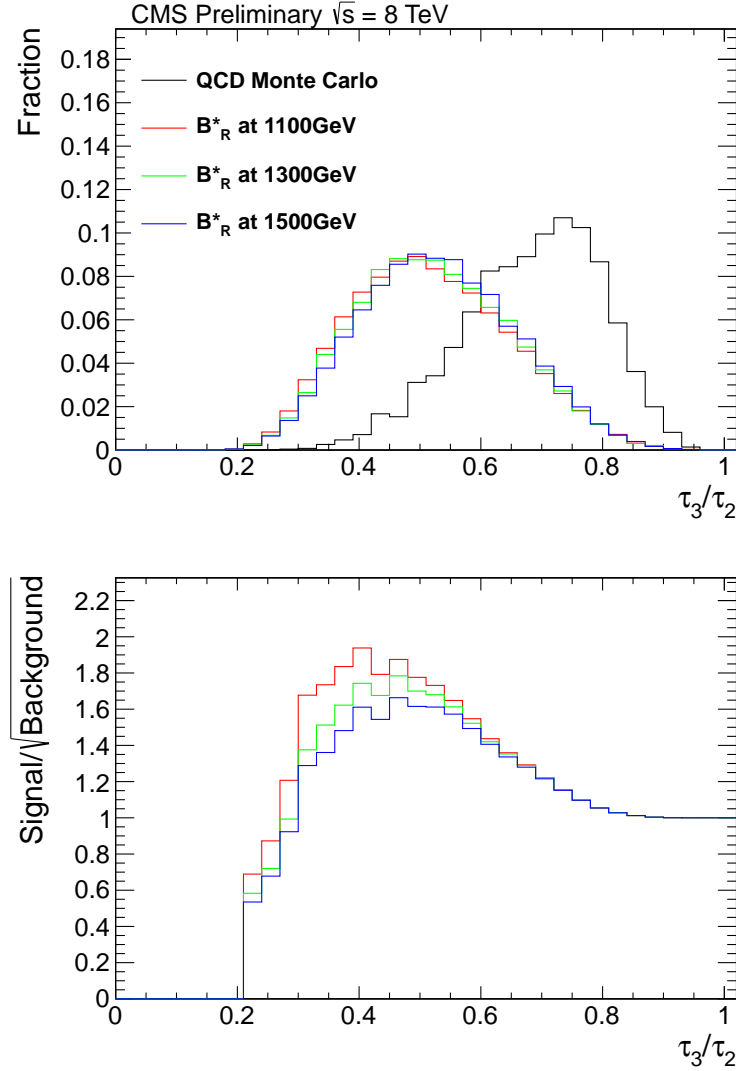


Figure 13.5: τ_3/τ_2 distributions in Signal and QCD Monte Carlo samples (top). The selection here includes the full signal region with the exception of subjet b-tagging in order to preserve QCD Monte Carlo statistics. Plot of Signal/ $\sqrt{\text{Background}}$ (bottom), derived from the top plot.

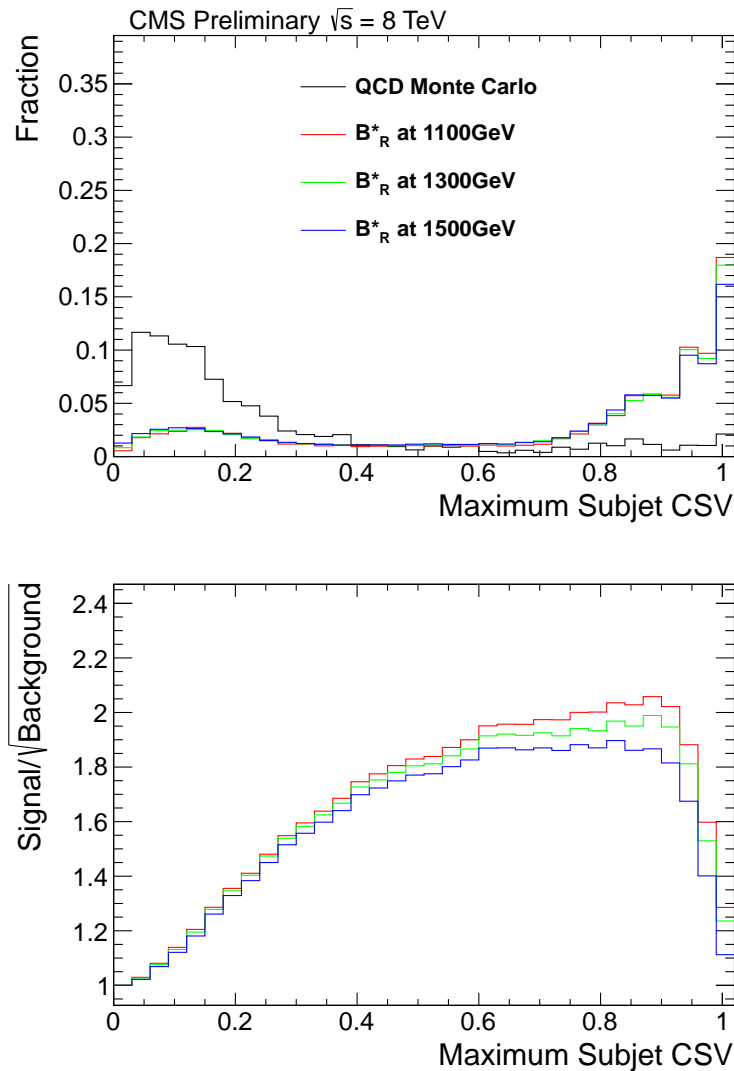


Figure 13.6: Maximum subjet CSV distributions in Signal and QCD Monte Carlo samples (top). Plot of Signal/ $\sqrt{\text{Background}}$ (bottom), derived from the top plot.

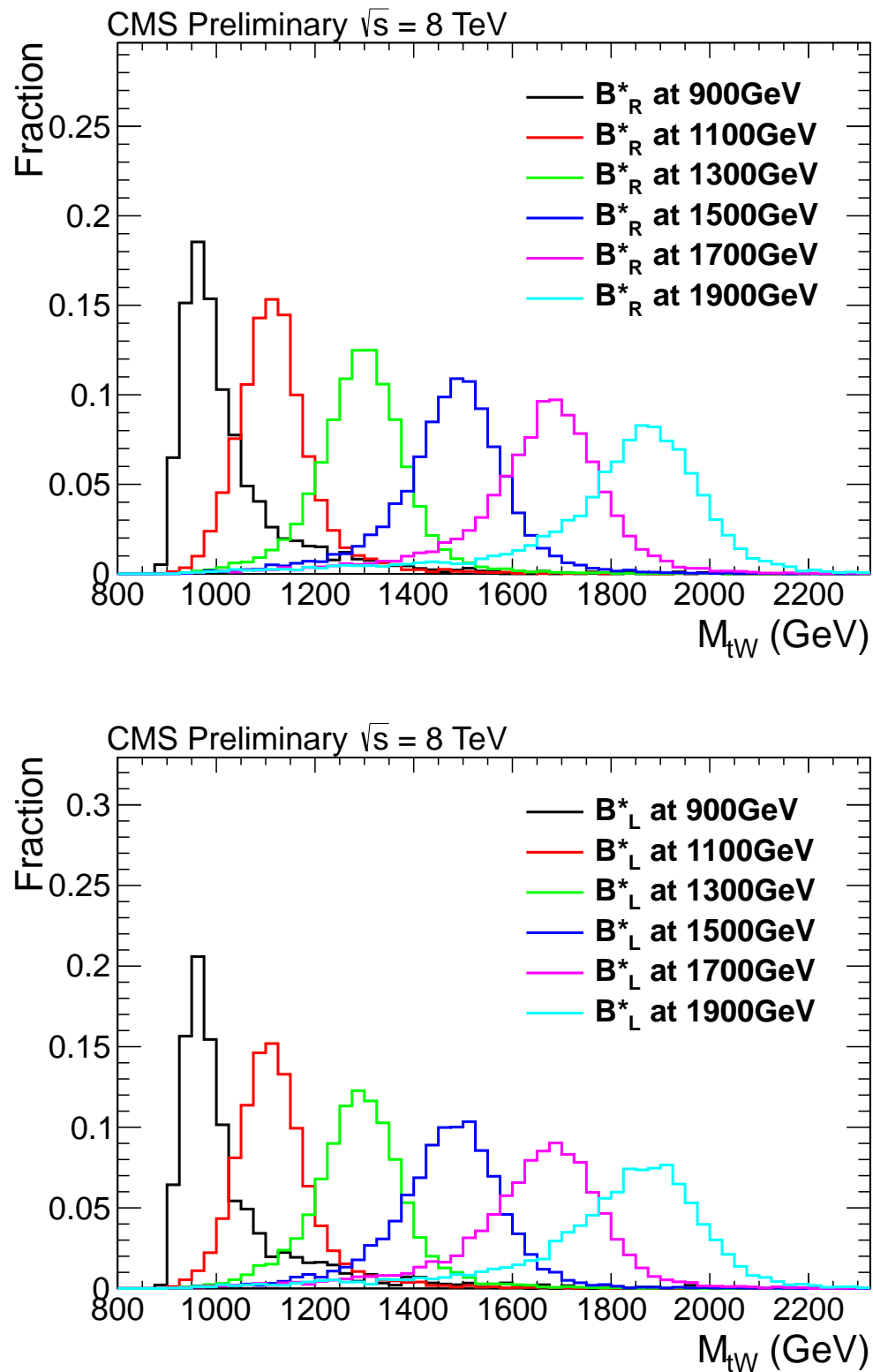


Figure 13.7: Full selection applied to b_R^* (top) and b_L^* (bottom-left).
137

Chapter 14

Background Estimation

The primary sources of Standard Model background for this analysis are QCD multijet and $t\bar{t}$ production. The shape of the $t\bar{t}$ contribution to the background is taken from Monte Carlo, and the normalization is derived from data by using a $t\bar{t}$ rich control region. The QCD multijet background contribution is derived from data by inverting the W candidate mass requirement for W-tagging.

14.1 QCD Background Estimation

In order to extract the QCD multijet background contribution, we determine the mistagging rate for the CMS top tagging algorithm (see Section 5.8). To measure this top mis-tagging rate, we turn to a control region based on inverting the W-tagging mass requirement. We look in a W candidate mass window around of the signal

CHAPTER 14. BACKGROUND ESTIMATION

region requirement ($30 \text{ GeV} < M_{jet} < 70 \text{ GeV}$ or $100 \text{ GeV} < M_{jet}$).

After applying this selection, we take the inverse ratio of top candidate jets to top candidate jets that are top-tagged to define the top-mistagging rate. To keep the kinematics similar in the sideband and similar region when reconstructing M_{tw} , the top candidate mass requirement is kept on the jets in both regions. To extract a QCD background estimate, we weight the events that pass the W-tagging requirements in the full selection by the top-mistagging rate.

The parameterization of the top-mistagging rate is two dimensional and considers both the $|\eta|$ and p_T of the top candidate jets. We break down data into two distinct regions in $|\eta|$.

- Low ($0.0 < |\eta| \leq 1.0$)
- High ($1.0 < |\eta| \leq 2.4$)

The regions in $|\eta|$ are then individually parameterized in p_T to produce the average top-mistagging rate. We perform this parameterization of the top-mistagging rate in an attempt to constrain the kinematic correlations inherent in top-tagging.

To smooth out the binning of the average top-mistagging rate, a study of functional fits was conducted for the top-mistagging rate (see Figure 16.14). We use the same functional form for the top-mistagging rate fit as the average b-tagging rate in the W' search (see Section 6.2) with the bifurcation points set to be 640 GeV and 590 GeV for the low and high η regions respectively.

CHAPTER 14. BACKGROUND ESTIMATION

The errors on the top-mistagging rate are then extracted using the full covariance matrix as obtained from output of the fitting algorithm. Additionally, we assign a systematic uncertainty to cover the choice of the fit function (see Section 16) based on several alternative functional forms. Figure 14.1 shows the tags (numerator) and probes (denominator) of the top-mistagging rate. Figure 14.2 shows the two fitted top-mistagging rates parameterized in p_T .

In the creation of the top-mistagging rate, $t\bar{t}$ is subtracted using the prescription outlined in Section 6.3

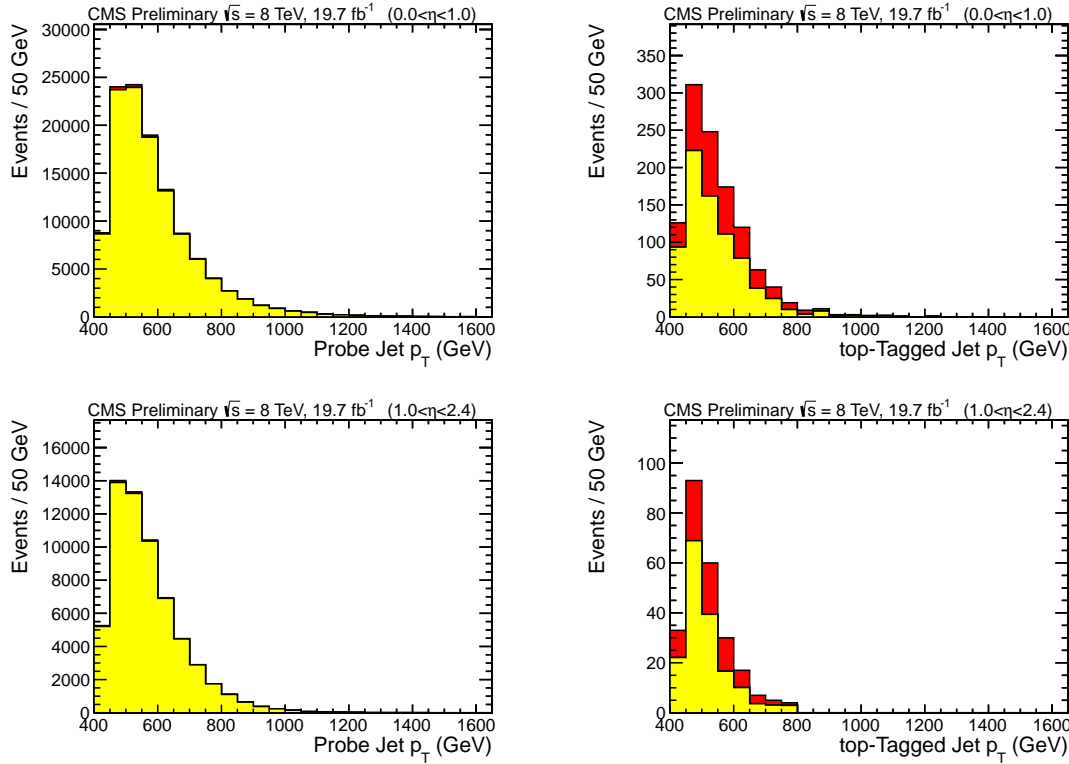


Figure 14.1: The tags and probes used for the average top-mistagging rate for the two regions in $|\eta|$. Here, tags are the numerator and probes are the denominator of the average top-mistagging rate

Background Composition		
region	pre top-tag	post top-tag
signal region QCD	37801	211
signal region $t\bar{t}$	457	129
sideband region QCD	176741	926
sideband region $t\bar{t}$	1758	456

Table 14.1: expected QCD and $t\bar{t}$ yields in the signal region and sideband used for extracting the top-mistagging rate. The QCD expected events are measured after $t\bar{t}$ subtraction.

14.2 Top Candidate Mass Correction

The application of the top-mistagging rate on the pre top-tagged sample provides a close approximation of the shape and normalization of the signal region. However, there is a known shape based discrepancy in the modeling of the top-candidate jet mass (see [14]). Before the number of subjets and minimum pairwise mass requirements, the QCD top candidate mass spectrum is a rapidly falling function, whereas after this selection the QCD top candidate mass spectrum is nearly flat. To investigate this discrepancy, we take the top candidate mass spectrum from QCD Monte Carlo before and after the number of subjets, minimum pairwise mass, and N-subjettiness requirements. The ratio of these normalized templates gives an approximate correction for this effect (see Figure 14.3). The uncertainty for this procedure is taken as half the correction. The correction and uncertainty are both interpolated to roughly correct for binning. This correction can be seen for data in Figure 14.4

The effect of this correction on the M_{tW} and top candidate p_T templates can be seen in figure 14.5.

14.3 Sideband Closure

In order to investigate the applicability and versatility of the QCD background estimation in data, we apply the top-mistagging rate to a control region of our W-tagging selection. We define the following W-tagging sideband:

- **Jet Mass** $30 \text{ GeV} < m_{\text{jet}} < 70 \text{ GeV}$ or $100 \text{ GeV} < m_{\text{jet}} < 130 \text{ GeV}$
- **N-subjettiness** $\tau_2/\tau_1 \geq 0.5$

This sideband does not overlap with the control region used to extract the top-mistagging rate due to the inverted N-subjettiness window. The selection has a lower yield of $t\bar{t}$ than the full selection, making it ideal for investigating the QCD background contribution. The closure test can be seen in Figure 14.6. The termination of the W candidate mass requirement at 130 GeV is due to the fact that above this region there is an increased yield of fully merged tops that pass the W-tagging sideband selection, which makes this region important for pinning down the $t\bar{t}$ normalization.

14.4 Deriving the Normalization of the SM $t\bar{t}$ Production

In order to study the contribution from $t\bar{t}$ to the full background estimate, we investigate the following control region:

CHAPTER 14. BACKGROUND ESTIMATION

- **Jet Mass** $m_{\text{jet}} > 130 \text{ GeV}$
- **N-subjettiness** $\tau_2/\tau_1 \geq 0.5$

This selection has an amplified $t\bar{t}$ fraction and is statistically independent from all other sidebands in the analysis. We extract the $t\bar{t}$ normalization by comparing the QCD background (extracted using the same top-mistagging rate as the signal region) and $t\bar{t}$ Monte Carlo to the selection in data. The fit allows the QCD background template to move only within its errors, whereas the normalization on $t\bar{t}$ is unconstrained. We use the top candidate mass spectrum for fitting, which minimizes the correlation between the QCD and $t\bar{t}$ templates within the fit due to the top mass peak. This fit can be seen in Figure 14.7. For this maximum likelihood fit we use the Theta package.

$t\bar{t}$ is subtracted from the numerator and denominator of the top-mistagging rate when extracting the QCD background estimate in the signal region. Additionally, $t\bar{t}$ contamination (see section 6.3) is subtracted from the QCD background estimate after the application of the top-mistagging rate. This $t\bar{t}$ contamination is estimated by weighting the pre top-tagged $t\bar{t}$ selection by the top-mistagging rate. The fitting procedure needs to implement both of these subtractions in order to isolate the $t\bar{t}$ normalization constant, because through these mechanisms the QCD shape is dependent on the $t\bar{t}$ normalization.

The fit implements the $t\bar{t}$ subtraction in the QCD estimate by fitting un-subtracted QCD to the $t\bar{t}$ full selection. The output of the fitter is then corrected by $(1+S/F)$,

CHAPTER 14. BACKGROUND ESTIMATION

where S/F is the ratio of the number of events in $t\bar{t}$ subtraction to the $t\bar{t}$ full selection.

The fit additionally implements $t\bar{t}$ subtraction in creation of the top-mistagging rate by creating two QCD components. One component is anticorrelated with the $t\bar{t}$ normalization factor, and the other is independent of this normalization factor. The anticorrelated QCD component fraction of the QCD estimate is taken as the difference of the QCD estimate with and without $t\bar{t}$ subtraction. The independent QCD component fraction of the QCD estimate is taken as the difference of the QCD estimate and the anticorrelated component.

This study suggests after all scale factors applied in the analysis, the $t\bar{t}$ contribution needs to be scaled by 0.79 ± 0.17 . This normalization is used for all $t\bar{t}$ distributions in the analysis, and the uncertainty is then the full normalization uncertainty for $t\bar{t}$.

14.5 Control Region Scale Factors

The W-tagging control regions mentioned in sections 14.4 and 14.1 are used for measurements that impact the background estimate in the signal region. These inverted selections do not have known scale factors, so we derive them using the semileptonic sample mentioned in section 13.5. The scale factor for the control region mentioned in section 14.1 is determined to be 0.97 ± 0.06 , and the scale factor for the control region mentioned in section 14.4 is 1.12 ± 0.09 .

The scale factors are a product of the W candidate mass window scale factor and

CHAPTER 14. BACKGROUND ESTIMATION

the τ_2/τ_1 window scale factor. The W candidate mass used for this measurement can be seen in figure 14.8. Given the mass window, we then investigate τ_2/τ_1 for the jet. This can be seen in figure 14.9 for the scale factor of the control region mentioned in section 14.1 and figure 14.9 for the scale factor of the control region mentioned in section 14.4.

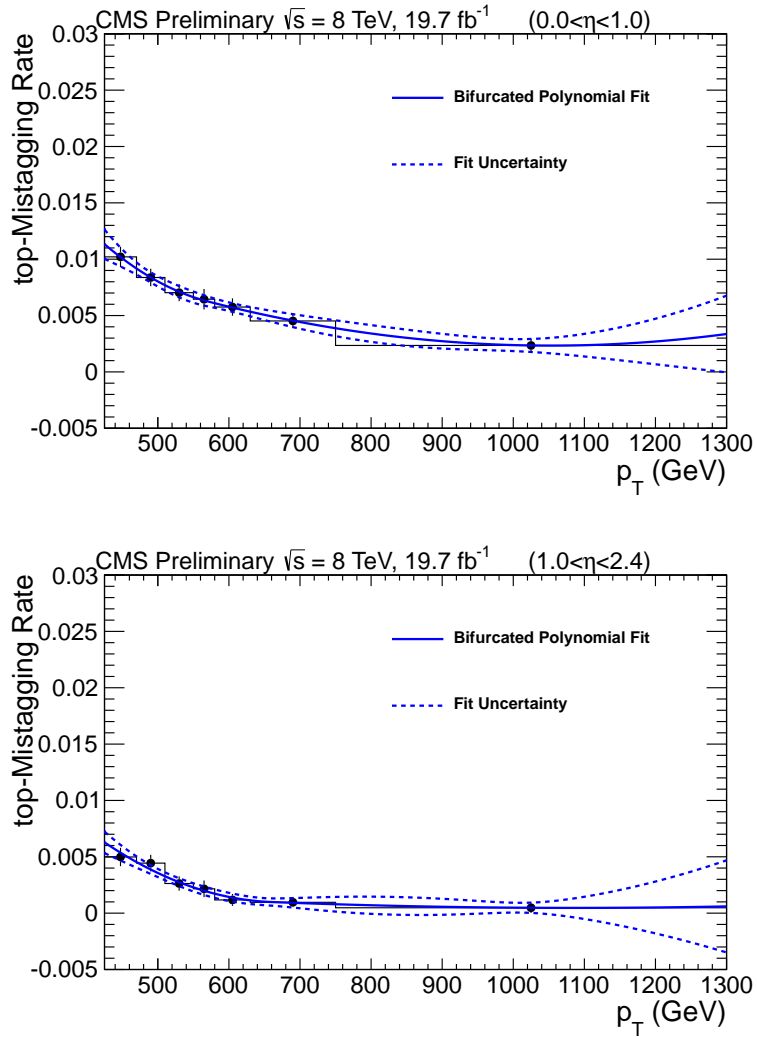


Figure 14.2: p_T parameterized average top-mistagging rate from the low (top) and high (bottom) η regions. The top-mistagging rate is shown in black, the polynomial fit is shown in blue, and the propagated errors from the fit are shown as a blue dashed line.

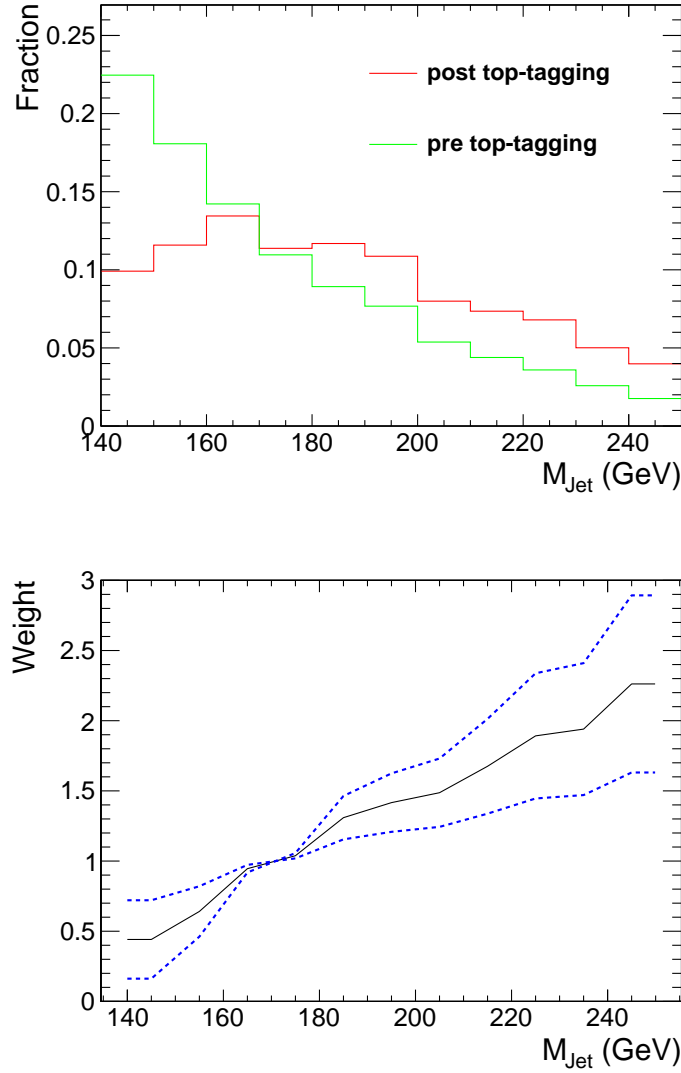


Figure 14.3: A plot of the top candidate mass spectrum in QCD Monte Carlo before and after top-tagging (top). The correction used for this discrepancy (bottom) created by dividing the templates in the top plot. The uncertainty used for this correction is shown as the blue dashed line.

CHAPTER 14. BACKGROUND ESTIMATION

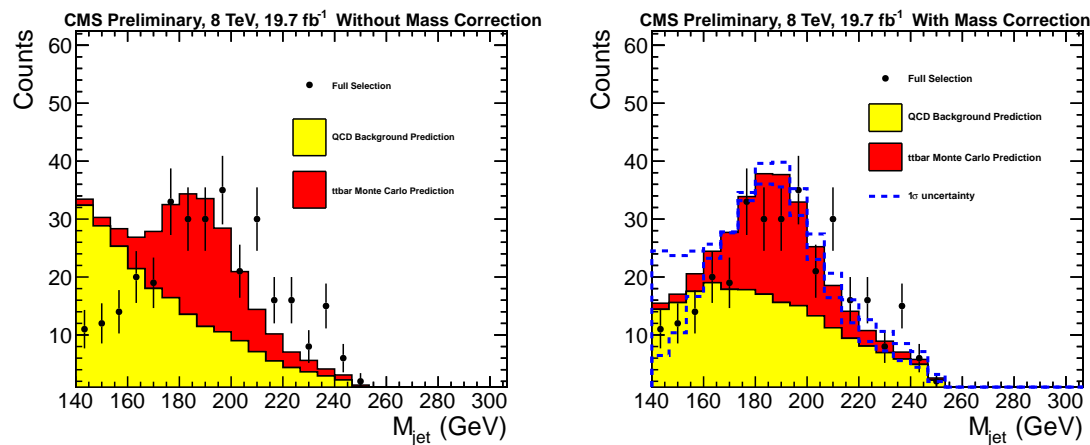


Figure 14.4: Top candidate mass before (left) and after (right) the top candidate mass correction. The selection for this plot is the full selection in the signal region.

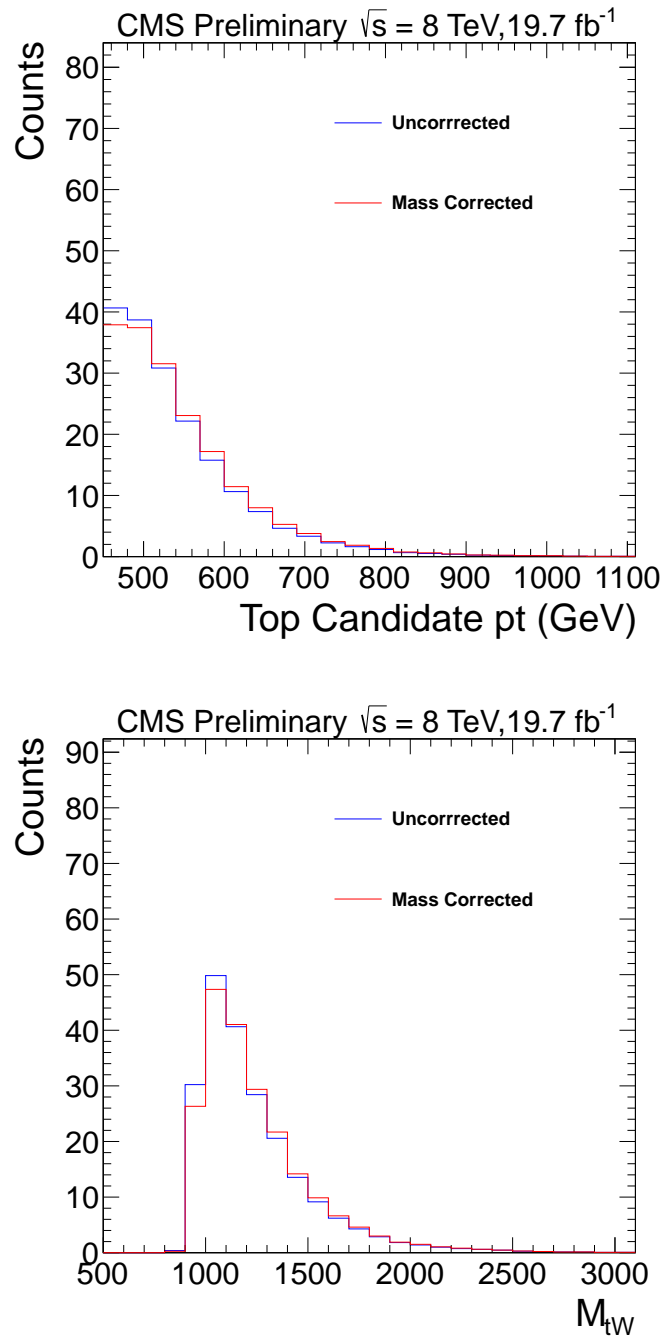


Figure 14.5: A plot of the QCD background estimate before and after the top mass correction. the top plots show the effect on top p_T , and the bottom plot shows the effect on M_{tW} .

CHAPTER 14. BACKGROUND ESTIMATION

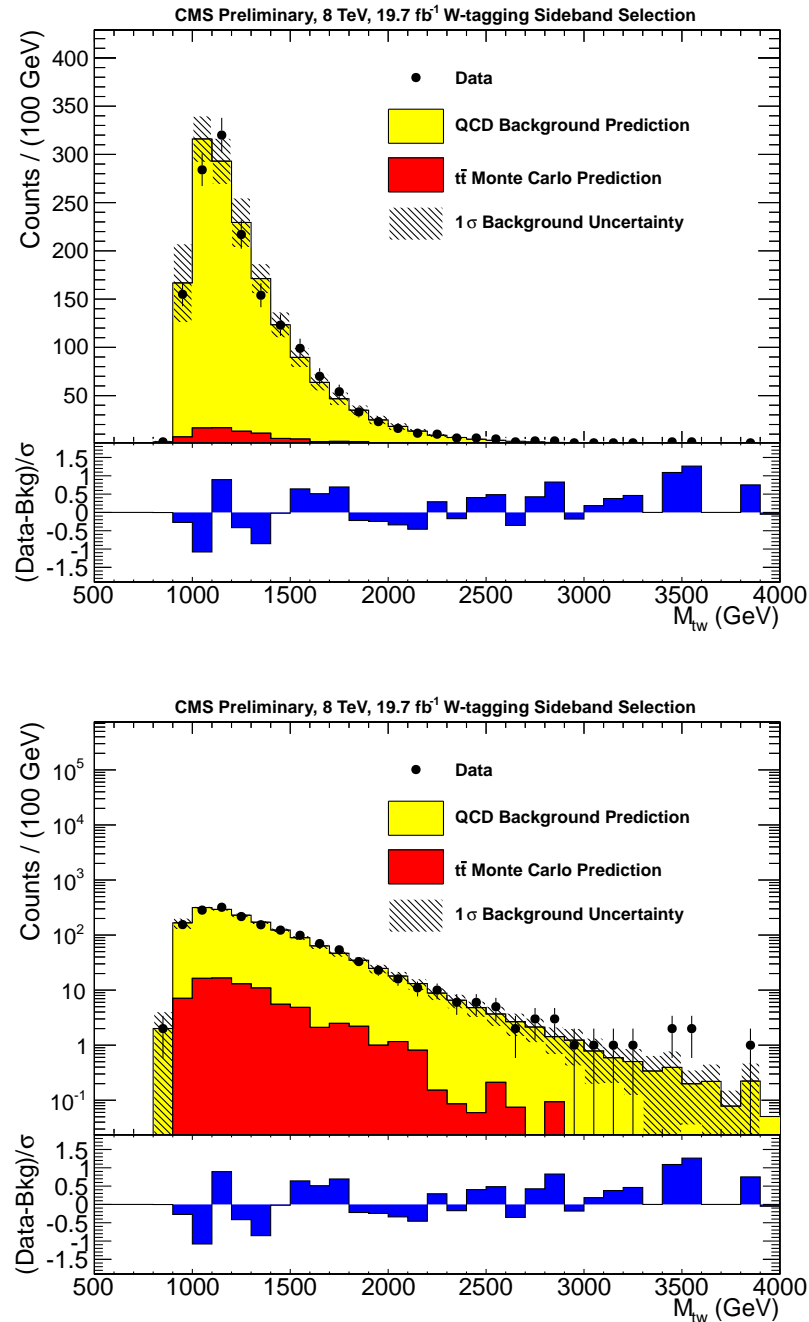


Figure 14.6: A plot of M_{tW} in the W-tagging sideband selection. The top and bottom plots are the same but with linear and log y-axis scale.

CHAPTER 14. BACKGROUND ESTIMATION

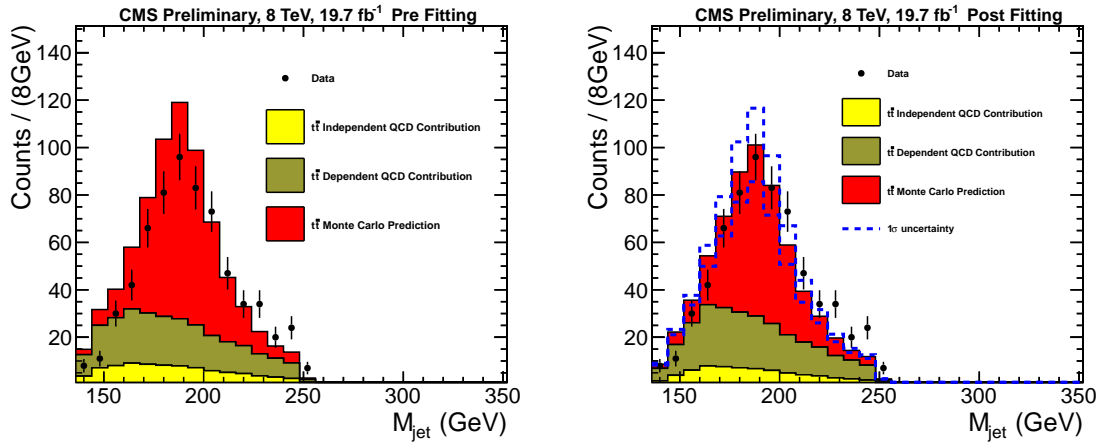


Figure 14.7: top candidate jet mass as extracted from the high mass W-tagging sideband. Pre fraction fit (left) and post fraction fit (right). The two QCD components use identical template shapes, but the normalization is such that one component can be considered independent from $t\bar{t}$, and the other will be anticorrelated $t\bar{t}$ normalization constant.

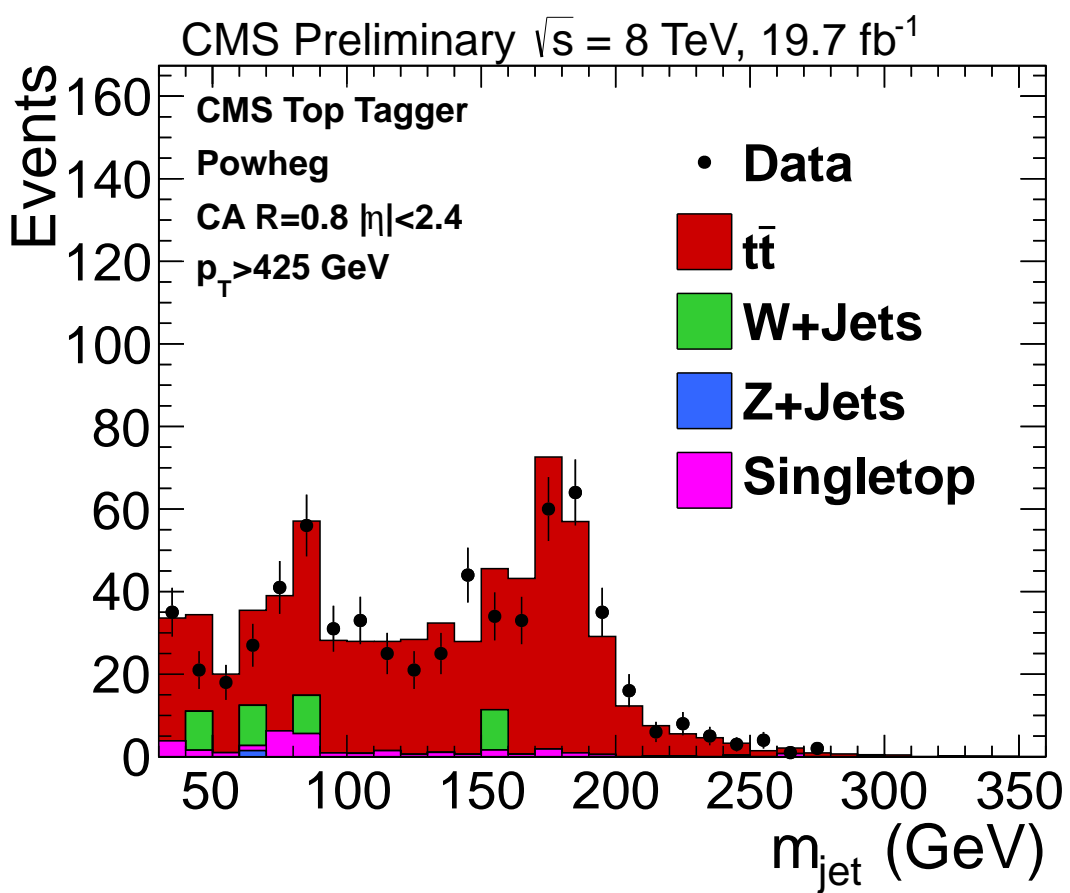


Figure 14.8: A plot of W candidate jet mass used for determination of the control region scale factors.

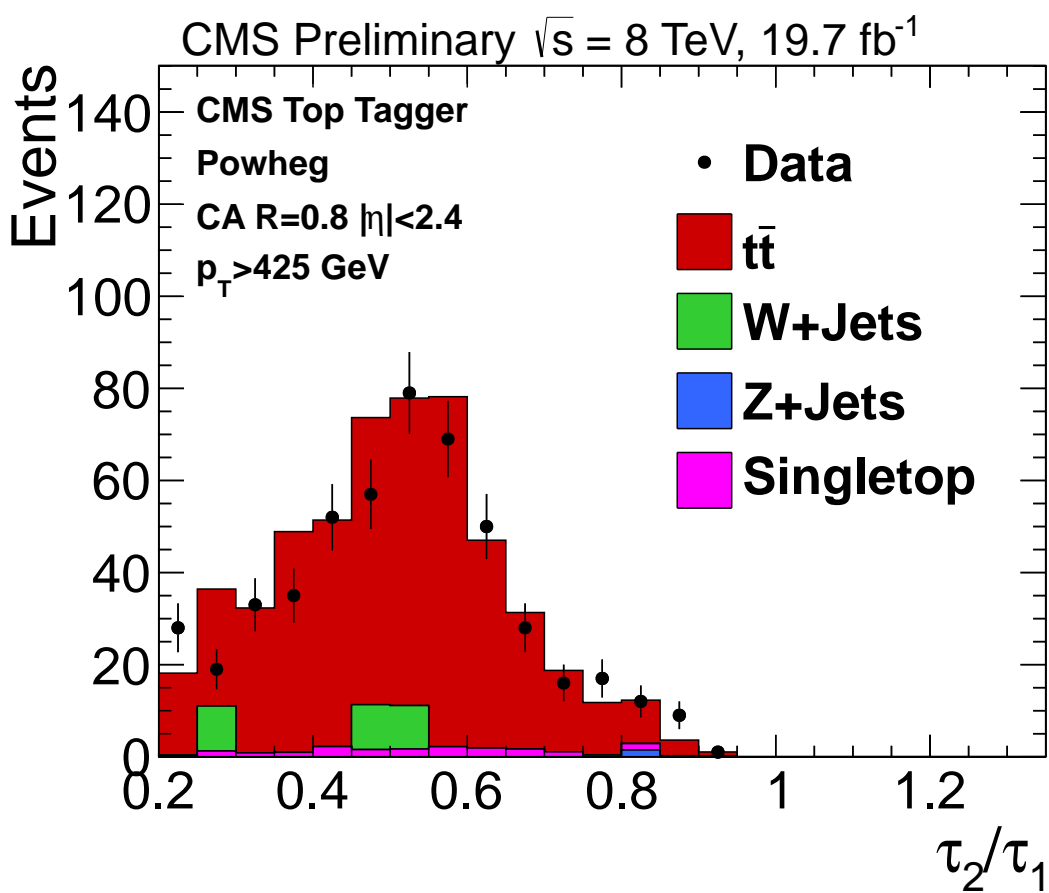


Figure 14.9: A plot of τ_2/τ_1 used for determination of the scale factor for the control region used for extracting the top-mistagging rate.

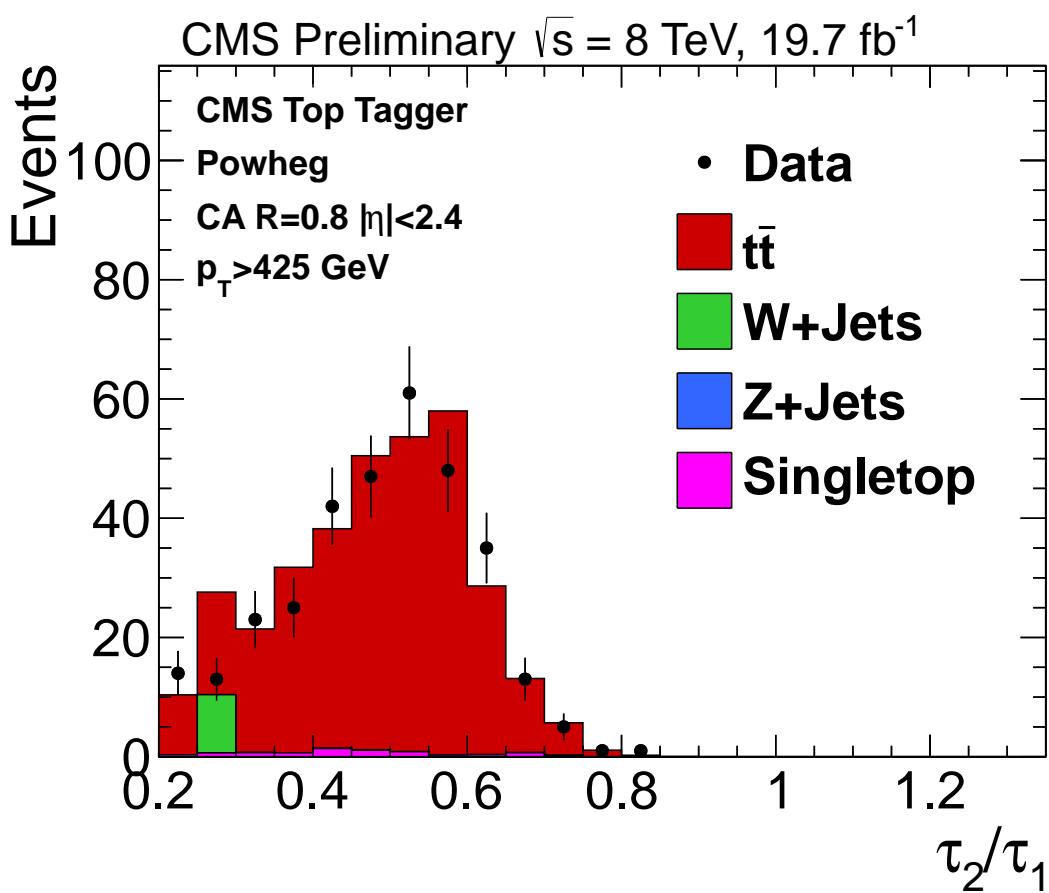


Figure 14.10: A plot of τ_2/τ_1 used for determination of the scale factor for the control region used for extracting the $t\bar{t}$ normalization.

Chapter 15

Data Results

After closure of the background estimation procedure within the control region 14.3, we investigate signal region. The results in the signal region are shown in Figure 15.1. We proceed to compute limits on the b^* cross-section. Background estimation of selected relevant variables can be seen in Figures 15.2 and 15.3.

The expected number of events in the signal region is 359 ± 58 , the observed number of events is 318. Table 15.1 gives the signal efficiency in the signal region for the three signal coupling hypotheses.

CHAPTER 15. DATA RESULTS

b* signal region efficiency			
M_{b^*}	ϵ_R	ϵ_L	ϵ_{LR}
800	0.0014	0.0010	0.0012
900	0.0076	0.0063	0.0070
1000	0.0301	0.0243	0.0272
1100	0.0502	0.0411	0.0456
1200	0.0653	0.0522	0.0588
1300	0.0746	0.0590	0.0668
1400	0.0788	0.0636	0.0712
1500	0.0809	0.0629	0.0719
1600	0.0795	0.0616	0.0706
1700	0.0760	0.0596	0.0678
1800	0.0749	0.0569	0.0659
1900	0.0707	0.0536	0.0622
2000	0.0660	0.0499	0.0583

Table 15.1: b* signal efficiency for left-handed, right-handed and vectorlike b* samples

CHAPTER 15. DATA RESULTS

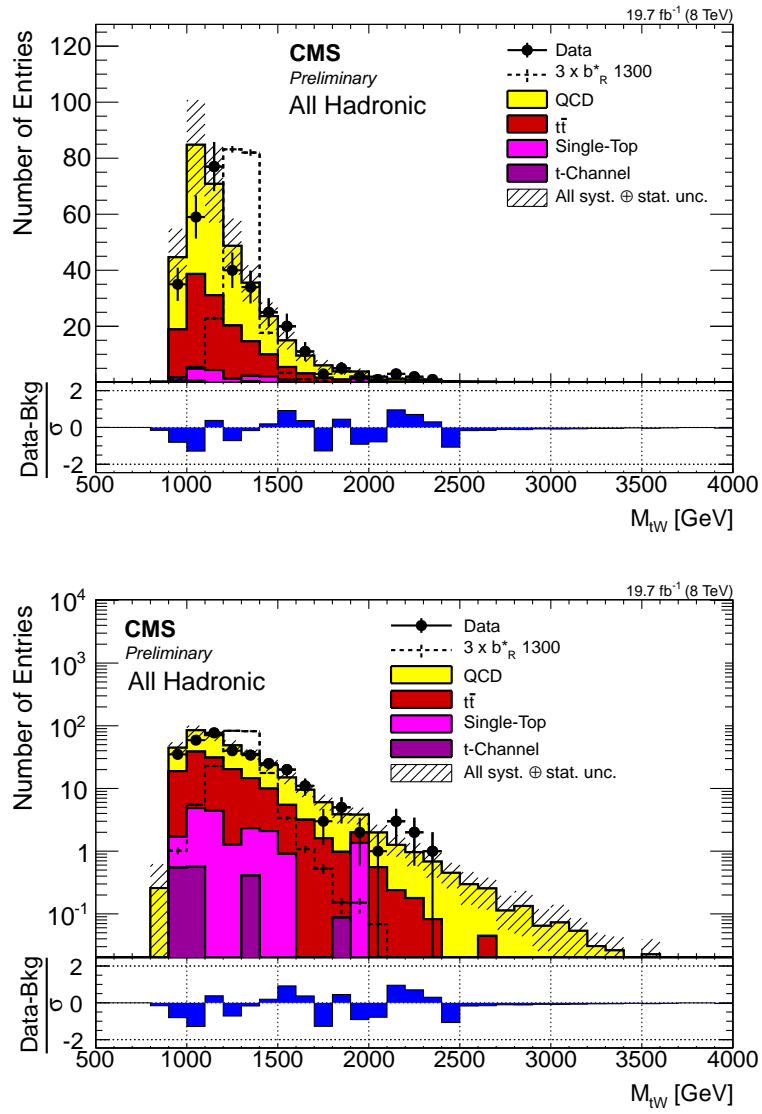


Figure 15.1: A plot of the full selection comparing data, signal and background. Top and bottom plots are the same but on linear and log y-axis scale.

CHAPTER 15. DATA RESULTS

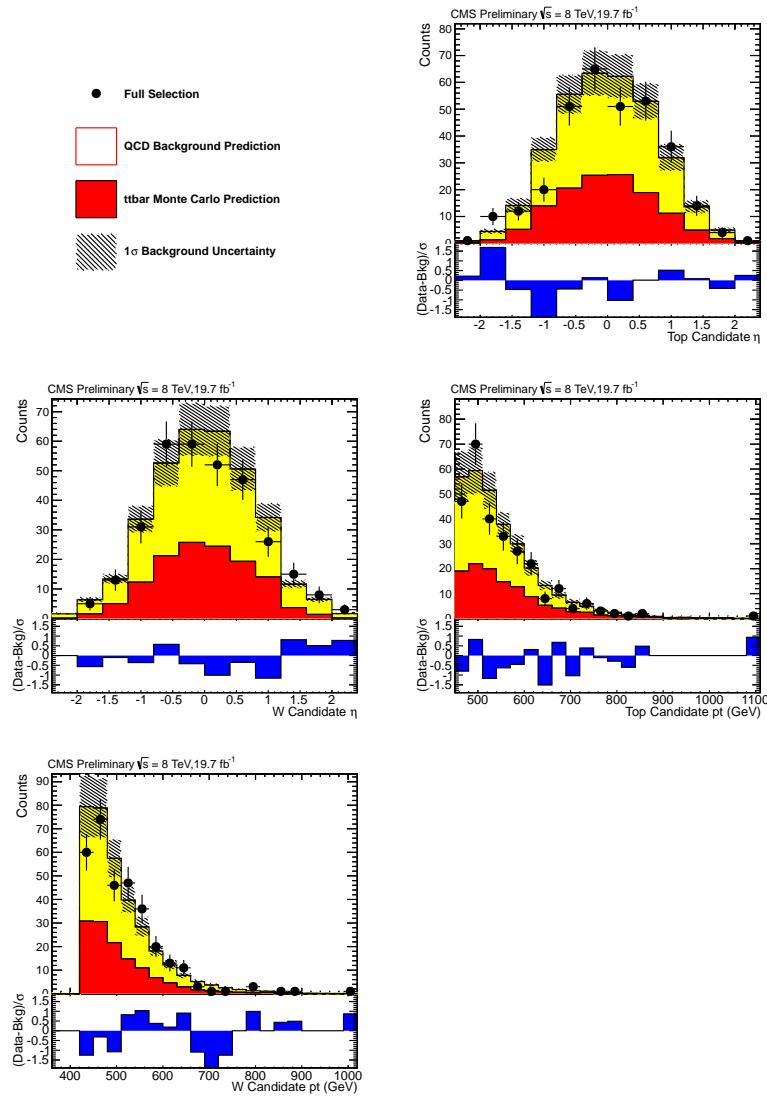


Figure 15.2: Background estimation of kinematic variables. The error bars shown are from the three primary sources; uncertainty on the fit, choice of fit, top mass modification, $t\bar{t}$ normalization, and $t\bar{t} Q^2$ uncertainty

CHAPTER 15. DATA RESULTS

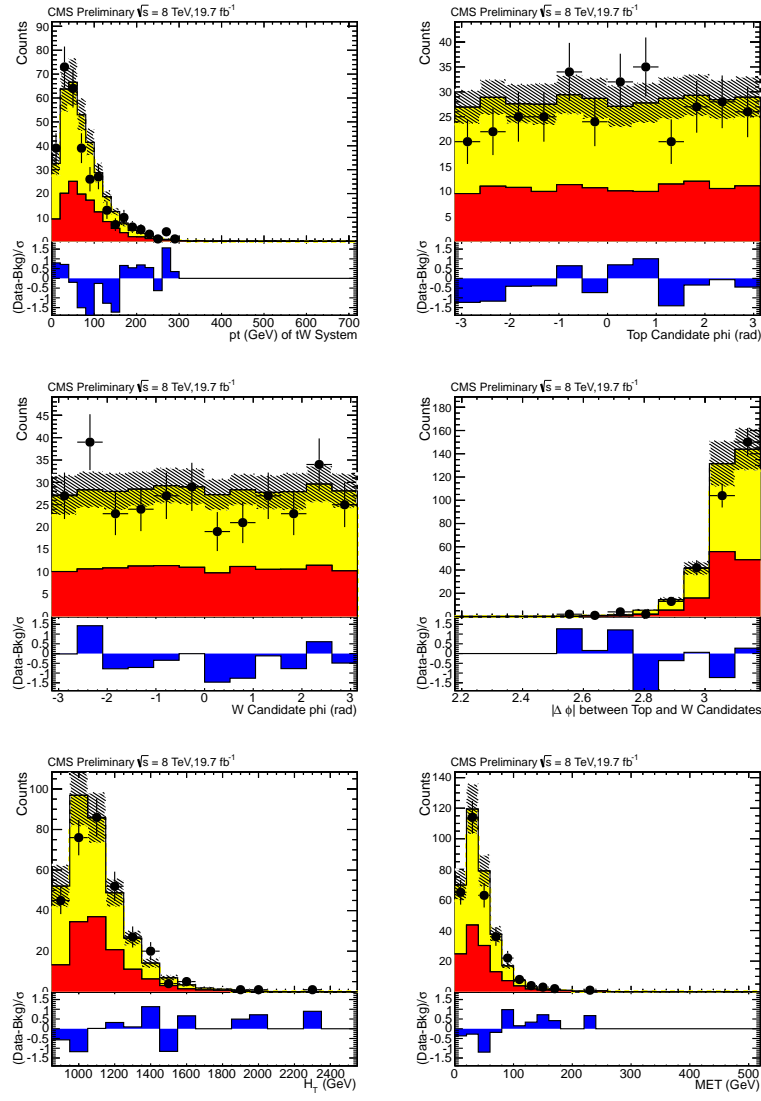


Figure 15.3: Background estimation of kinematic variables. The error bars shown are from the three primary sources; uncertainty on the fit, choice of fit, top mass modification, $t\bar{t}$ normalization, and $t\bar{t} Q^2$ uncertainty

Chapter 16

Systematic Uncertainties

Various systematics are taken into account, both on our expected signal and background estimate. Some systematic uncertainties will affect only the normalization of certain event rates, and are reported as overall normalization uncertainties. Other systematics affect the shapes of the reconstructed signal or backgrounds, as well as their normalization.

16.1 Jet Energy Scale

We evaluate the effect of uncertainty on the jet energy scale on samples derived from Monte Carlo simulation. To do so, we vary the jet four-momentum up and down by the jet energy scale uncertainty, which is p_T and η dependent. We take an additional 3% uncertainty to account for the use of CA8 jets as derived from the

CHAPTER 16. SYSTEMATIC UNCERTAINTIES

difference in measured and simulated W masses [31].

Varying the jet momentum can cause a jet to fall below or rise above the p_T cut in the analysis, thus shifting the invariant mass spectrum of the signal and reconstructed $t\bar{t}$ samples. Figure 16.4 shows the systematic shapes from the jet energy scale on the $t\bar{t}$ distribution. Jet Energy scale variation on signal Monte Carlo is shown in Figure 16.3 for 1200 GeV, 1300 GeV, and 1400 GeV mass points.

16.2 Trigger

We include an uncertainty based on the measured trigger efficiency for all Monte Carlo Samples. The trigger efficiency is discussed in Section 13.2. To obtain shape systematics from this effect, we vary the trigger by half the trigger *inefficiency* (figure 16.1). The effects of this on the $t\bar{t}$ distribution is shown in Figure 16.6. Trigger weighting on signal Monte Carlo is shown in Figure 16.5 for 1200 GeV, 1300 GeV, and 1400 GeV mass points. The uncertainty is low in the mass range of interest for limit setting.

16.3 Jet Energy Resolution

We apply a systematic due to the known differences in jet energy resolution in data and simulation. We use the nominal η dependent smearing (see [31]) as recommended by the JER group. We apply the recommended systematic uncertainty to this nominal

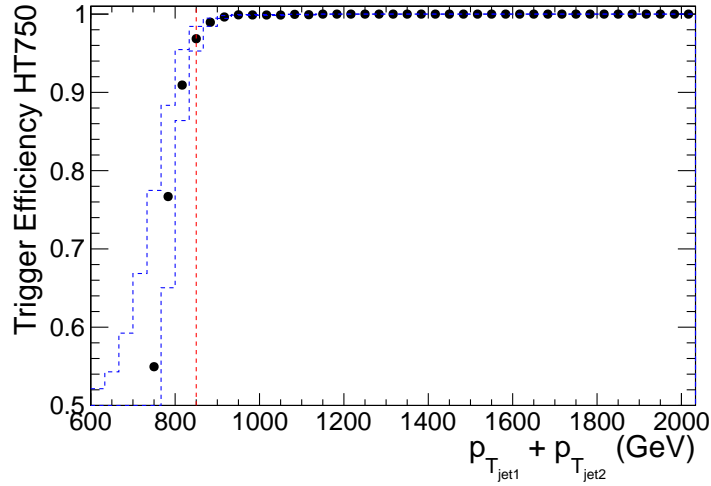


Figure 16.1: Trigger efficiency systematic variation.

smearing to the $t\bar{t}$ and signal M_{tW} distribution. The jet energy resolution variation in $t\bar{t}$ Monte Carlo can be seen in Figure 16.8. Jet energy resolution variation on signal Monte Carlo is shown in Figure 16.7 for 1200 GeV, 1300 GeV, and 1400 GeV mass points.

16.4 Jet Angular Resolution

A smearing of 10% is assumed on η and ϕ and shape uncertainties are generated by considering smearing 10% lower and higher. We apply this systematic uncertainty to the $t\bar{t}$ and signal M_{tW} distribution. The jet angular resolution variation in $t\bar{t}$ Monte Carlo can be seen in Figure 16.10 . Jet Angular Resolution variation on signal Monte Carlo is shown in Figure 16.9 for 1200 GeV, 1300 GeV, and 1400 GeV mass points.

CHAPTER 16. SYSTEMATIC UNCERTAINTIES

The effect is very small and thus not considered in setting limits.

16.5 PDF Uncertainty

The uncertainty in the parton distribution function used for Monte Carlo sample generation is investigated. We take the average of the $\pm 1\sigma$ eigenvalue variation of the pdf master equations [32] for the NNPDF, MSTW2008nnlo, and CT10 pdf sets to weight the signal and $t\bar{t}$ Monte Carlo samples and investigate the impact on the full selection. From this we get three approximations of the PDF uncertainty. Of these uncertainty approximations, the PDF set that provides the maximum uncertainty is then used for the $\pm 1\sigma$ PDF uncertainty. For the $t\bar{t}$ sample this set is NNPDF and for the signal samples this set is either NNPDF or CT10. PDF variation on signal Monte Carlo is shown in Figure 16.11 for 1200 GeV, 1300 GeV, and 1400 GeV mass points. PDF variation on $t\bar{t}$ Monte Carlo is shown in Figure 16.12. The effect is very small and thus not considered in setting limits.

16.6 Pileup

A study of pileup uncertainty is conducted by varying the minimum bias cross-section by 5% as a measure of systematic uncertainty. The results can be seen in figure 16.13. The effect is very small and thus not considered in setting limits.

16.7 Q^2 Scale Uncertainty

We use additional $t\bar{t}$ samples generated with twice and half the nominal Q^2 scale used in the $t\bar{t}$ samples listed in table ???. These samples vary the renormalization and factorization scales to account for missing higher order corrections in our simulation. Figure 16.2 shows the shape based uncertainty due to this effect.

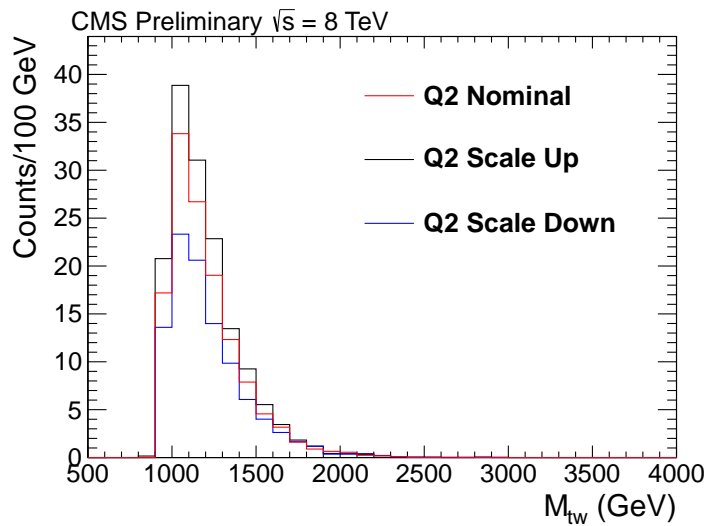


Figure 16.2: Q^2 systematic variation for $t\bar{t}$ Monte Carlo

16.8 Normalization Uncertainties

As mentioned in Section 14.4, the uncertainty on the overall normalization scale factor used for $t\bar{t}$ is extracted from data and is 22%.

We must apply a 13% uncertainty on the top tagging scale factor described in Section 13.5 to signal Monte Carlo events due to uncertainty in the difference in

CHAPTER 16. SYSTEMATIC UNCERTAINTIES

subjet efficiency from data to Monte Carlo.

The cross-section uncertainty of 20%,15%,30% applies single-top quark background tW,t, and s channels respectively are applied.

We also include a 2.6% uncertainty in the luminosity for the signal Monte Carlo [33].

16.9 Uncertainties Related to the QCD Background Estimate

We use the result of the fit to the top-mistagging rate (see Section 14) to weight pre top-tagged events in order to create the QCD background estimate. Uncertainties in the fitting algorithm and statistical uncertainties in the sideband are taken into account (see figure 14.2). Statistical uncertainties in the pre b tagged signal region are also taken into account.

16.9.1 Choice of the Functional Form for the Average Top-Mistagging Rate

The functional form used is a bifurcated polynomial. However there is a systematic uncertainty associated with this choice. The uncertainties due to this effect are taken into account by studying alternative functional forms seen in figure 16.14. The background estimation from these alternative fits are seen in figure 16.15. The uncertainty due to the choice of fit is taken as the Mean Squared Error of these alternative backgrounds bin by bin and can be seen in figure 16.16.

16.9.2 Top Candidate Mass Correction

The correction of the top candidate mass is detailed in section 14.2. The uncertainty on this procedure is taken as one half of the correction and is shown in Figures 14.3 and 14.4.

16.9.3 Two-Dimensional vs. Three-Dimensional Parameterization of the Average Top-Mistagging Rate

Additionally, we place an uncertainty on the inability of the background estimate to capture all kinematic correlations through the parameterization of the top-mistagging rate in p_T and η . This uncertainty is calculated by investigating a parameterization in p_T , η and M_{tW} . We define P_i as the top-mistagging rate described in Section 14 in one η bin and P_{ij} as the top-mistagging rate if parameterized with M_{tW} as well. P_{ij} can be seen in figure 16.17. Each bin in P_i can be thought of as a column average over all M_{tW} bins per p_T bin. If P_{ij} a function of M_{tW} (index j) is not constant, then averaging over P_{ij} over j while projecting onto M_{tW} axis to obtain the QCD background estimate can result in a bias.

We assess the approximate size of the uncertainty due to our choice of parameterization by explicitly comparing the three-dimensional and two-dimensional background

CHAPTER 16. SYSTEMATIC UNCERTAINTIES

estimates in the sideband. Using these two parameterizations, the uncertainty in the M_{tW} distribution due to parameterization is approximately $\sum_{j=0}^n m_{ij}(P_{ij} - P_i)$ where m_{ij} refers to the number of pretag events for a bin in p_T and M_{tW} . Fig. 16.18 shows the uncertainty due to this effect. The addition of a dimension to the top-mistagging rate parameterization leads to lower statistical power. The additional uncertainty from including M_{tW} in the top-mistagging rate parameterization is taken into account by an additional uncertainty on the QCD shape. For this, we use the $\pm 1\sigma$ deviations from the 3d parameterized top-mistagging rate to extract the M_{tW} shape instead of the nominal value. Additionally, the uncertainty due to the 2d parameterization is subtracted from this shape in quadrature due to the fact that this is already included as an uncertainty. The uncertainty due to this can be seen in figure 16.19.

These uncertainties are taken in quadrature to produce an overall uncertainty in the data derived background estimate that is applied in a shape based manner in the limit-setting macro.

CHAPTER 16. SYSTEMATIC UNCERTAINTIES

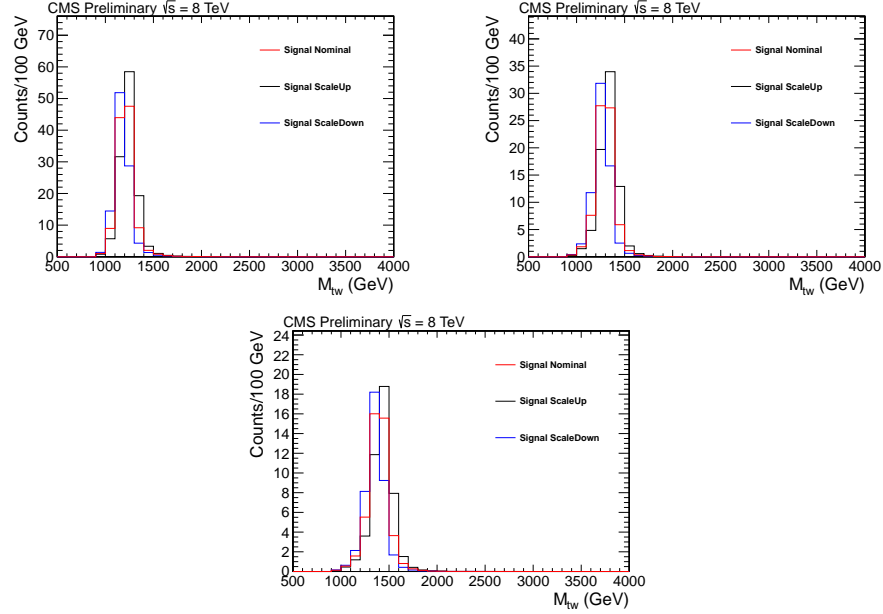


Figure 16.3: Jet Energy Scale systematic variation for right-handed b^* Monte Carlo at the following mass points (a) $M_{b^*} = 1200 \text{ GeV}$ (b) $M_{b^*} = 1300 \text{ GeV}$ (c) $M_{b^*} = 1400 \text{ GeV}$

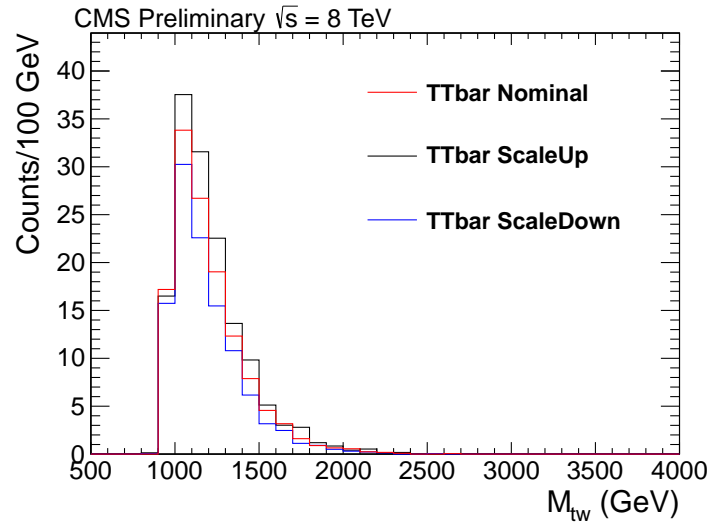


Figure 16.4: Jet Energy Scale systematic variation for $t\bar{t}$ Monte Carlo

CHAPTER 16. SYSTEMATIC UNCERTAINTIES

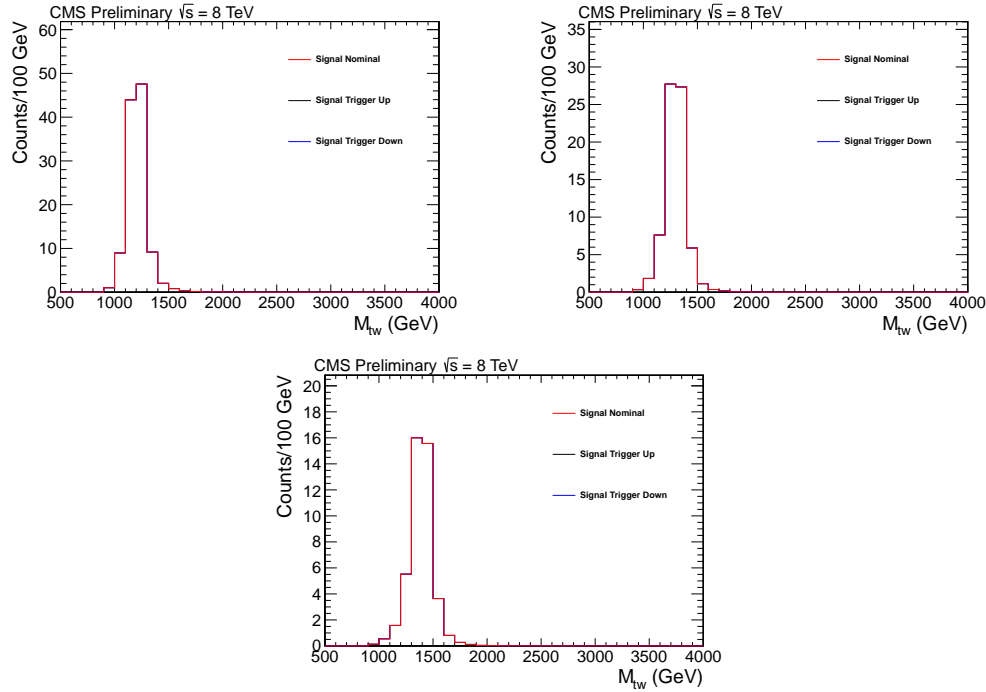


Figure 16.5: Trigger Weighting systematic variation for right-handed b^* Monte Carlo at the following mass points (a) $M_{b^*} = 1200 \text{ GeV}$ (b) $M_{b^*} = 1300 \text{ GeV}$ (c) $M_{b^*} = 1400 \text{ GeV}$

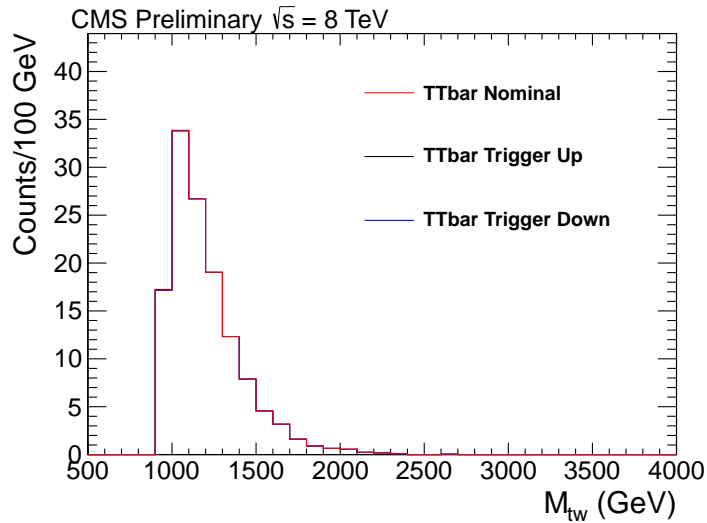


Figure 16.6: Trigger Weighting systematic variation for $t\bar{t}$ Monte Carlo

CHAPTER 16. SYSTEMATIC UNCERTAINTIES

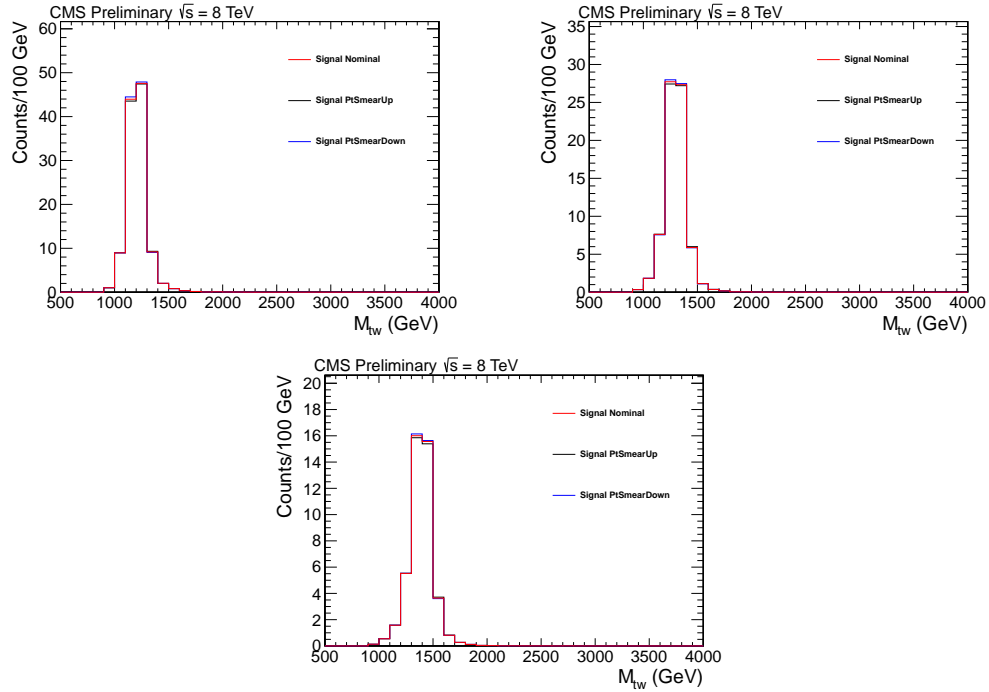


Figure 16.7: Jet Energy Resolution systematic variation for right-handed b^* Monte Carlo at the following mass points (a) $M_{b^*} = 1200 \text{ GeV}$ (b) $M_{b^*} = 1300 \text{ GeV}$ (c) $M_{b^*} = 1400 \text{ GeV}$

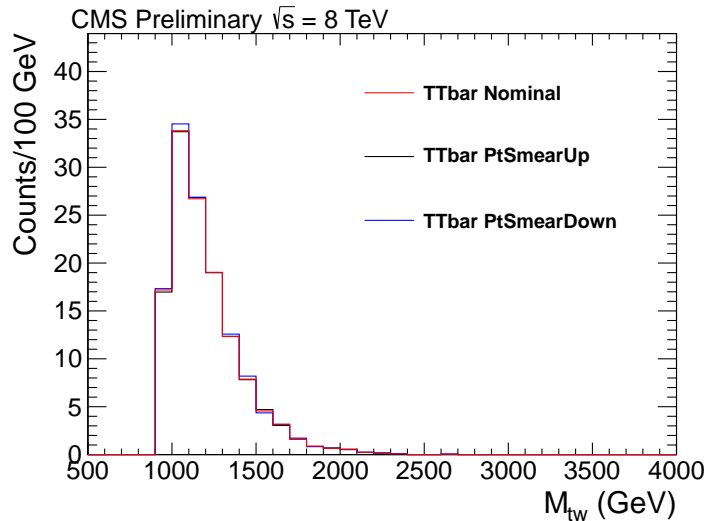


Figure 16.8: Jet Energy Resolution systematic variation for $t\bar{t}$ Monte Carlo

CHAPTER 16. SYSTEMATIC UNCERTAINTIES

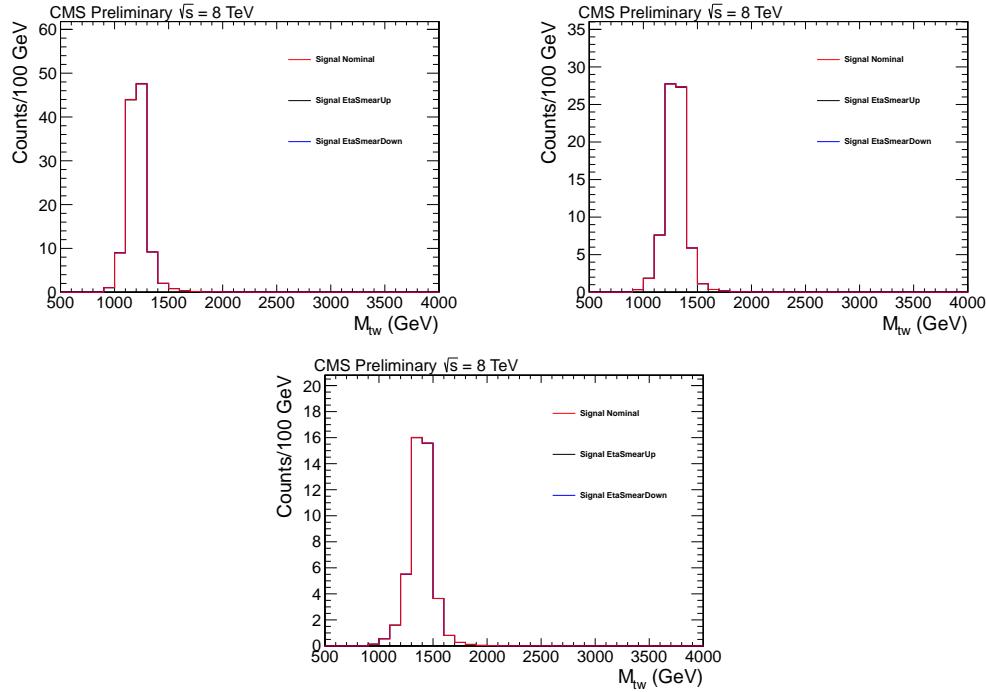


Figure 16.9: Jet Angular Resolution systematic variation for right-handed b^* Monte Carlo at the following mass points (a) $M_{b^*} = 1200 \text{ GeV}$ (b) $M_{b^*} = 1300 \text{ GeV}$ (c) $M_{b^*} = 1400 \text{ GeV}$

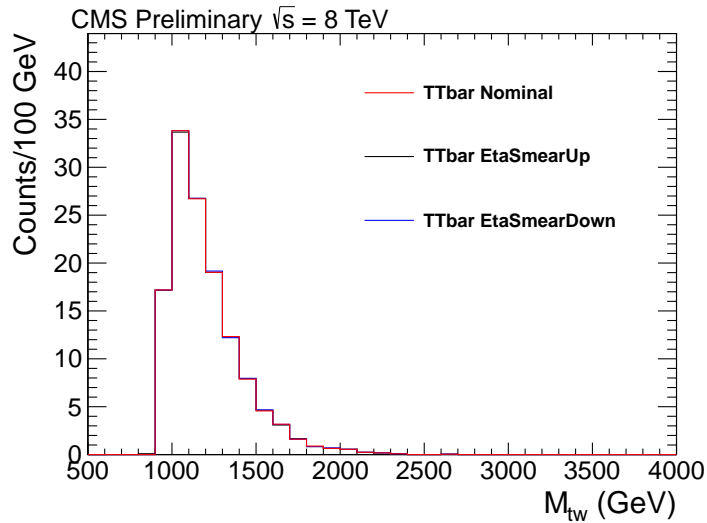


Figure 16.10: Jet Angular Resolution systematic variation for $t\bar{t}$ Monte Carlo

CHAPTER 16. SYSTEMATIC UNCERTAINTIES

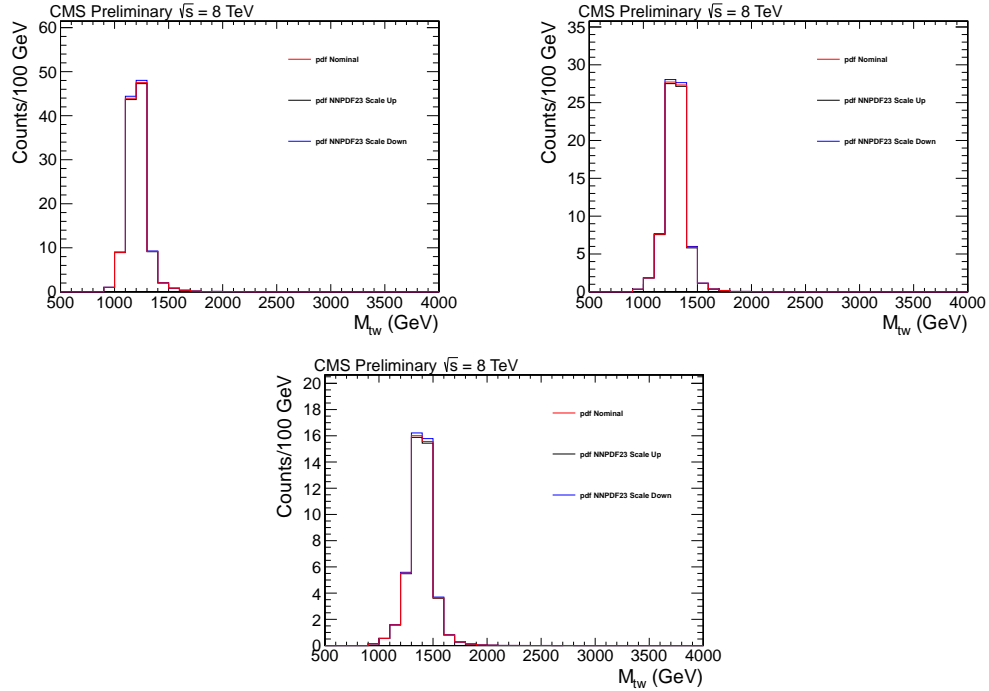


Figure 16.11: PDF systematic variation for right-handed b^* Monte Carlo at the following mass points (a) $M_{b^*} = 1200 \text{ GeV}$ (b) $M_{b^*} = 1300 \text{ GeV}$ (c) $M_{b^*} = 1400 \text{ GeV}$

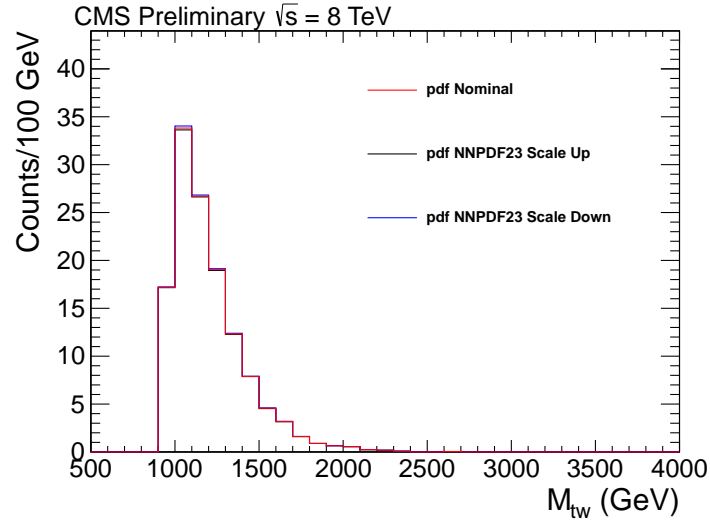


Figure 16.12: PDF systematic variation for $t\bar{t}$ Monte Carlo

CHAPTER 16. SYSTEMATIC UNCERTAINTIES

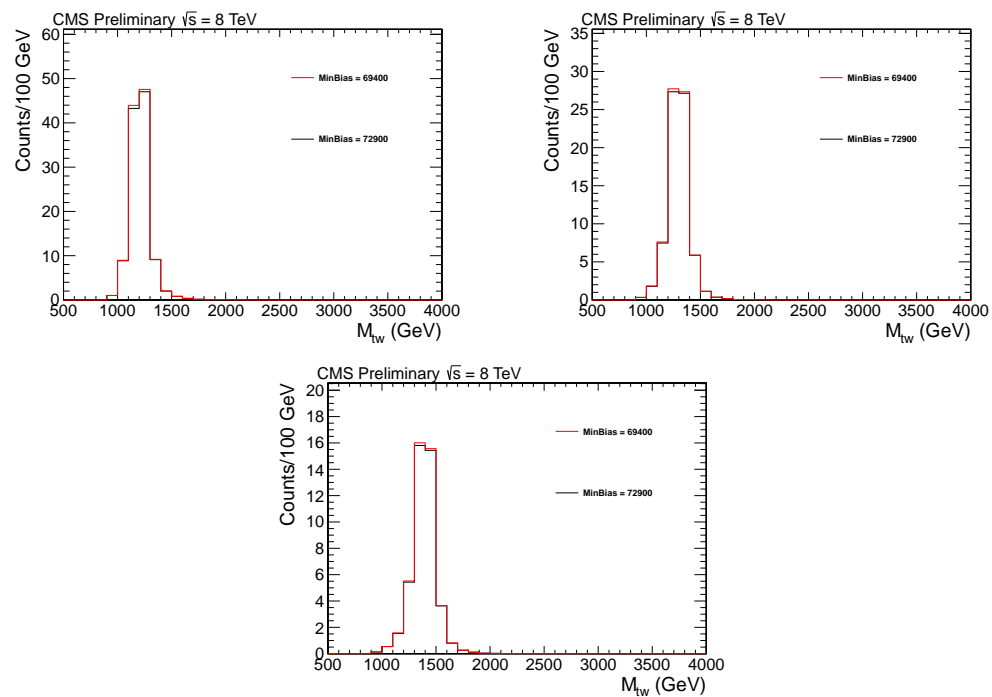


Figure 16.13: Pileup systematic variation for right-handed b^* Monte Carlo at the following mass points (a) $M_{b^*} = 1200 \text{ GeV}$ (b) $M_{b^*} = 1300 \text{ GeV}$ (c) $M_{b^*} = 1400 \text{ GeV}$

CHAPTER 16. SYSTEMATIC UNCERTAINTIES

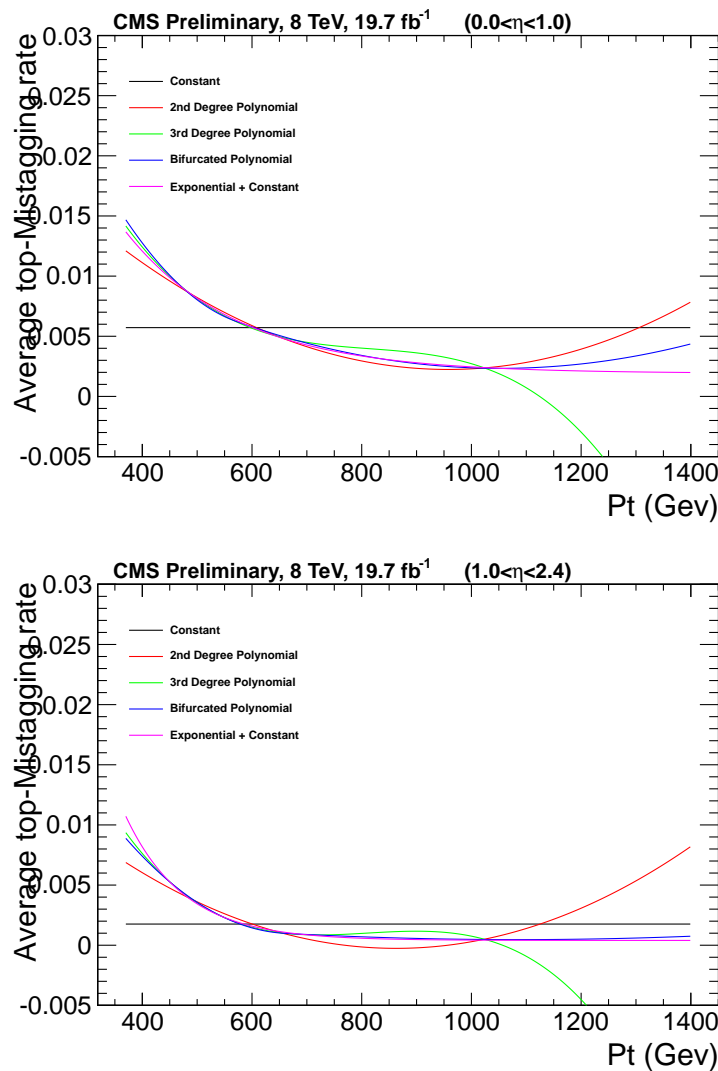


Figure 16.14: Alternative fit functions for the top-mistagging rate in η regions (a) Low (b) High

CHAPTER 16. SYSTEMATIC UNCERTAINTIES

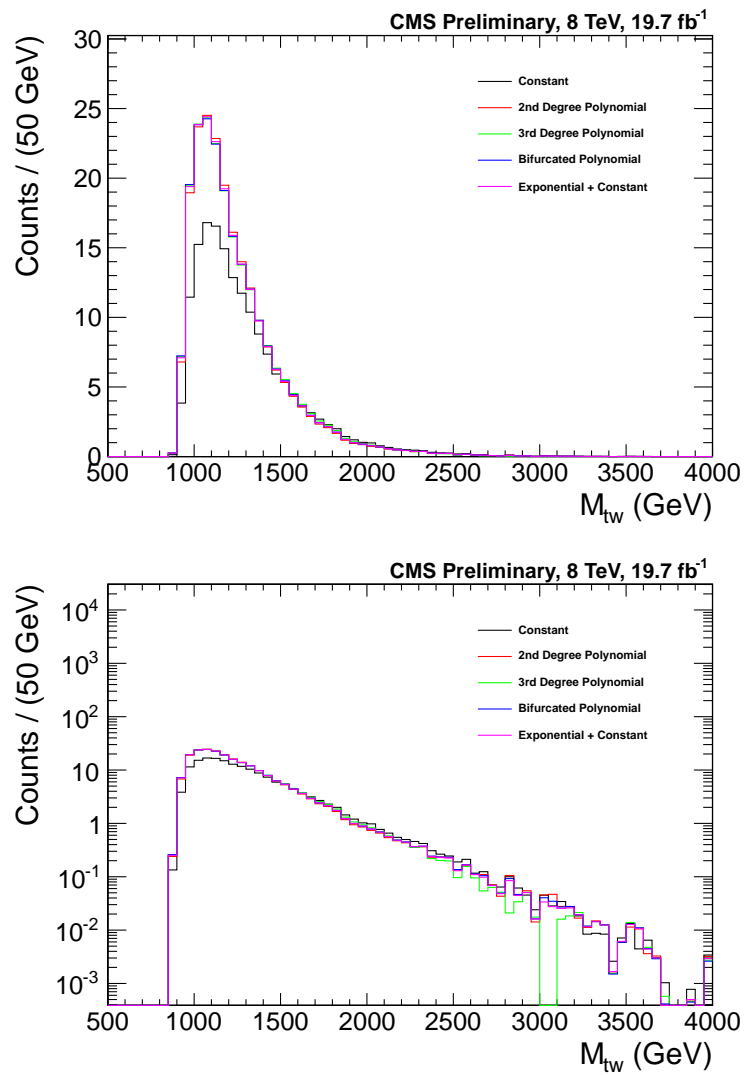


Figure 16.15: QCD background estimation from alternative fit functions seen in 16.14. Top and bottom plots are the same but on linear and log y-axis scale.

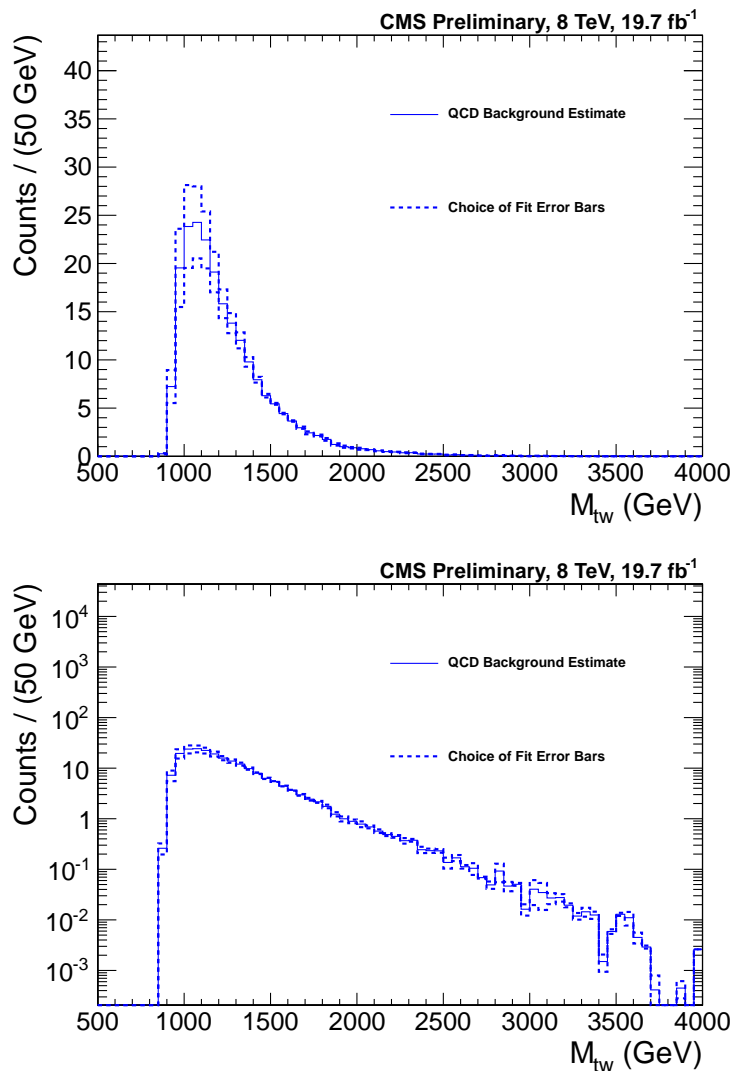


Figure 16.16: Uncertainty on the choice of fit as extracted from the alternative background estimations seen in 16.15. Top and bottom plots are the same but on linear and log y-axis scale.

CHAPTER 16. SYSTEMATIC UNCERTAINTIES

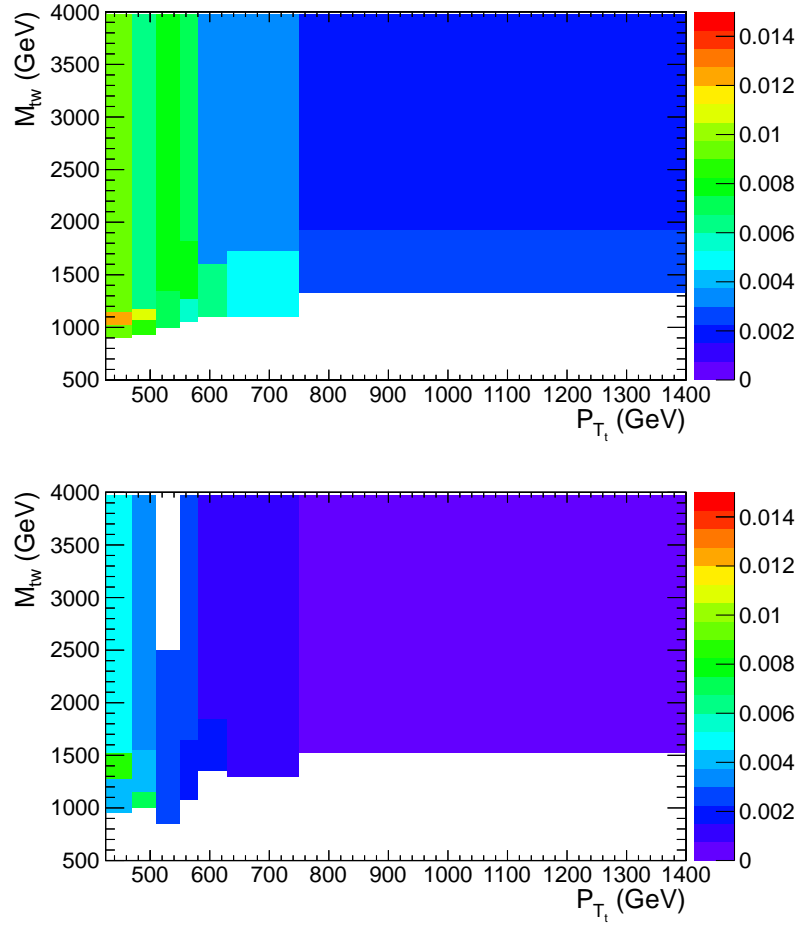


Figure 16.17: Two dimensional parameterization of top-mistagging rate in p_{T_t} and M_{tw} . The x axis binning is identical to the binning in Section 14. The y-axis is binned adaptively to approximate equivalent statistics over each y-axis bin per x axis bin. (a) Low η Region (b) High η Region

CHAPTER 16. SYSTEMATIC UNCERTAINTIES

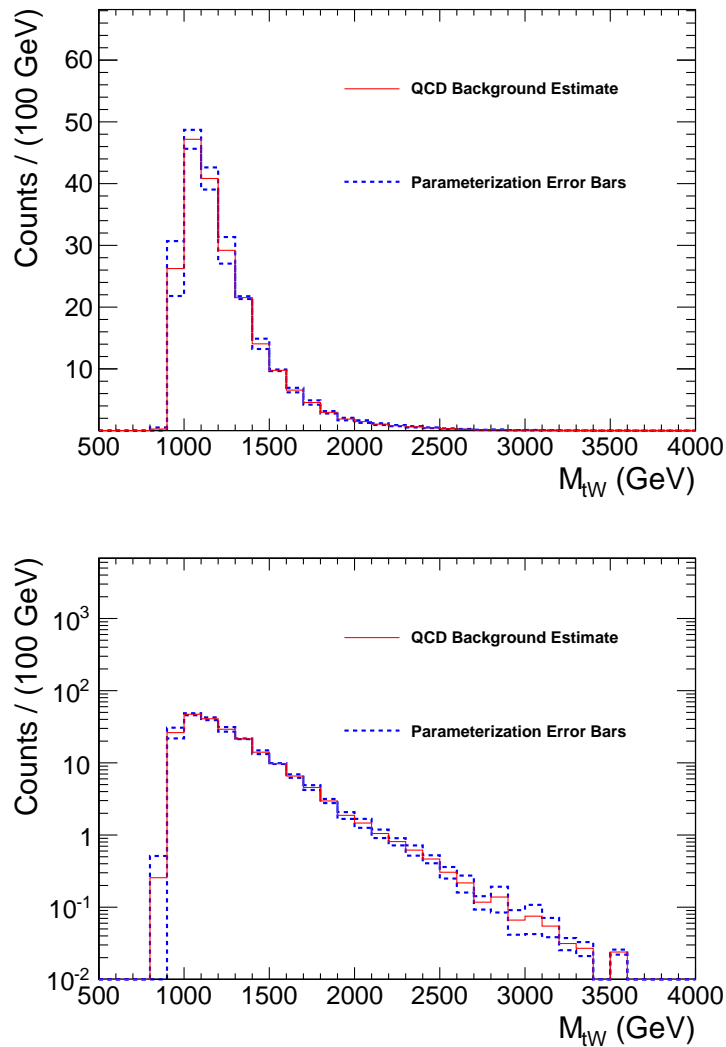


Figure 16.18: Uncertainty on the parameterization choice. Top and bottom plots are the same but on linear and log y-axis scale.

CHAPTER 16. SYSTEMATIC UNCERTAINTIES

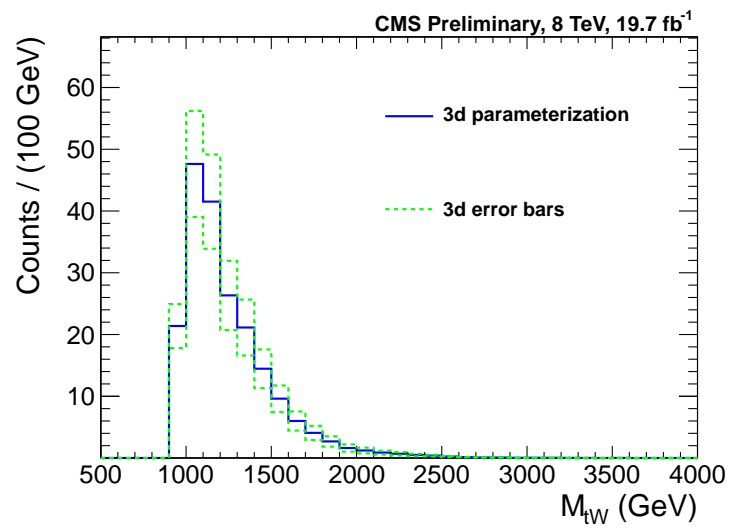


Figure 16.19: Statistical uncertainty on the three dimensional parameterization top-mistagging rate nominal shapes.

Chapter 17

Results

17.1 Limits

We set limits on the production cross-section of the b^* quark. We compare the number of observed events to the number of events expected given the new physics model. We use the following formula:

$$N_{\text{expected}} = \sigma_{b^*} \times B_{b^* \rightarrow tW; W \rightarrow \text{hadrons}} \times \varepsilon \times L \quad (17.1)$$

where σ_{b^*} is the b^* cross-section, $B_{b^* \rightarrow tW; W \rightarrow \text{hadrons}}$ is the branching ratio $b^* \rightarrow tW$ with both W boson decays constrained to the hadronic branching fraction, ε is the efficiency and L is the integrated luminosity of our dataset.

We perform a shape analysis using the M_{tW} distribution. This analysis uses a

CHAPTER 17. RESULTS

binned likelihood fit to compare the distribution from the b^* quark signal hypothesis with the Standard Model distribution produced by our background estimation procedure.

We use a Bayesian method to extract 95% CL upper limits on the production of a left- and right-handed b^* particle.

The statistical procedure for setting limits is described in Section 9.1.

The uncertainty in the jet energy scale, Q^2 scale, trigger, QCD background uncertainties, and jet energy resolution are taken as shape based uncertainties, and the other sources of uncertainty are taken as overall normalizations.

The limits from Theta are shown in Figure 18.7. The expected(observed) exclusion region for the right-handed b^* quark hypothesis is between 0.88 TeV and 1.55 TeV (0.82 TeV and 1.43 TeV). The expected(observed) exclusion region for the left-handed b^* quark hypothesis is between 0.89 TeV and 1.48 TeV (0.88 TeV and 1.40 TeV). The expected(observed) exclusion region for the vectorlike b^* quark hypothesis is between 0.82 TeV and 1.70 TeV (0.8 TeV and 1.53 TeV). Cross-section upper limits for right-handed, left-handed, and vectorlike b^* are summarized in Tables 18.1,18.2, and 18.3 respectively.

Table 17.1 gives the values for nuisance parameters after limit setting for each b^* mass hypothesis.

The cross section upper limits can be generalized due to the fact that the b^* cross-section is dependent on the unknown constants κ and g as can be seen in equations

CHAPTER 17. RESULTS

Rate Effects of Systematic Uncertainties										
Sample	JER	JES	Q^2	QCD total	Lumi	top-tagging SF	W-tagging SF	Trigger	t̄t Norm	
$M_{b^*} = 1000$	-0.81,+0.51	+17.91,-21.34	—	+2.63,-2.57	+12.50,-11.11	+7.60,-7.06	+0.14,-0.14	—	—	
$M_{b^*} = 1100$	-0.51,+0.60	+9.07,-12.13	—	+2.63,-2.57	+12.50,-11.11	+7.60,-7.06	+0.07,-0.07	—	—	
$M_{b^*} = 1200$	-0.41,+0.60	+6.12,-9.76	—	+2.63,-2.57	+12.50,-11.11	+7.60,-7.06	+0.04,-0.04	—	—	
$M_{b^*} = 1300$	-0.42,+0.41	+4.98,-8.06	—	+2.63,-2.57	+12.50,-11.11	+7.60,-7.06	+0.03,-0.03	—	—	
$M_{b^*} = 1400$	-0.53,+0.40	+4.20,-7.65	—	+2.63,-2.57	+12.50,-11.11	+7.60,-7.06	+0.02,-0.02	—	—	
$M_{b^*} = 1500$	-0.46,+0.42	+4.50,-7.76	—	+2.63,-2.57	+12.50,-11.11	+7.60,-7.06	+0.02,-0.02	—	—	
$M_{b^*} = 1600$	-0.48,+0.37	+3.79,-7.33	—	+2.63,-2.57	+12.50,-11.11	+7.60,-7.06	+0.01,-0.01	—	—	
$M_{b^*} = 1700$	-0.34,+0.35	+3.91,-6.43	—	+2.63,-2.57	+12.50,-11.11	+7.60,-7.06	+0.01,-0.01	—	—	
$M_{b^*} = 1800$	-0.48,+0.39	+3.71,-7.64	—	+2.63,-2.57	+12.50,-11.11	+7.60,-7.06	+0.01,-0.01	—	—	
$M_{b^*} = 1900$	-0.46,+0.44	+3.31,-7.12	—	+2.63,-2.57	+12.50,-11.11	+7.60,-7.06	+0.01,-0.01	—	—	
$M_{b^*} = 2000$	-0.46,+0.41	+3.14,-7.29	—	+2.63,-2.57	+12.50,-11.11	+7.60,-7.06	+0.01,-0.01	—	—	
$M_{b^*} = 800$	-0.00,+0.56	+29.42,-25.25	—	+2.63,-2.57	+12.50,-11.11	+7.60,-7.06	+0.19,-0.19	—	—	
$M_{b^*} = 900$	-0.18,+0.42	+46.46,-35.69	—	+2.63,-2.57	+12.50,-11.11	+7.60,-7.06	+0.28,-0.28	—	—	
qcd	—	—	+28.14,-27.56	—	—	—	—	—	—	
sts	+nan,+nan	+nan,+nan	—	+2.63,-2.57	+12.50,-11.11	+7.60,-7.06	+nan,+nan	—	—	
stt	-0.11,+17.70	+47.87,-16.85	—	+2.63,-2.57	+12.50,-11.11	+7.60,-7.06	+0.13,-0.13	—	—	
sttW	+0.01,-0.00	+17.42,-13.16	—	+2.63,-2.57	+12.50,-11.11	+7.60,-7.06	+0.09,-0.09	—	—	
ttbar	-0.22,+1.05	+13.20,-14.75	+16.24,-23.58	—	+7.60,-7.06	+0.10,-0.10	+22.00,-18.03	—	—	

Table 17.1: Rate effects of the systematic uncertainties as extracted from Theta. The numbers listed under sample specify b* signal Monte Carlo mass.

CHAPTER 17. RESULTS

b_R^* Cross-Section Upper Limits				
M_{b^*}	observed	expected	expected 1σ	expected 2σ
800	3.298	6.325	3.584,11.675	1.999,22.481
900	0.283	0.549	0.323,0.953	0.202,1.961
1000	0.087	0.172	0.113,0.243	0.083,0.355
1100	0.122	0.112	0.077,0.162	0.056,0.223
1200	0.081	0.076	0.053,0.110	0.039,0.155
1300	0.051	0.052	0.036,0.077	0.026,0.107
1400	0.059	0.041	0.029,0.059	0.022,0.087
1500	0.062	0.034	0.024,0.049	0.017,0.071
1600	0.056	0.029	0.020,0.043	0.015,0.060
1700	0.035	0.025	0.018,0.038	0.013,0.053
1800	0.023	0.023	0.016,0.033	0.011,0.046
1900	0.021	0.022	0.015,0.031	0.011,0.044
2000	0.023	0.021	0.015,0.031	0.011,0.045

Table 17.2: b_R^* cross-section upper limits for given b_R^* mass values. Cross-section is in units of pb.

11.1 and 11.1. The limits can be extrapolated to the g,κ plane as can be seen in figures 18.8 and 18.8 for observed and expected limits respectively.

CHAPTER 17. RESULTS

b_L^* Cross-Section Upper Limits				
M_{b^*}	observed	expected	expected 1σ	expected 2σ
800	7.681	8.588	5.106,15.127	2.798,27.319
900	0.355	0.674	0.395,1.211	0.237,2.369
1000	0.106	0.204	0.137,0.297	0.099,0.424
1100	0.148	0.140	0.096,0.200	0.069,0.273
1200	0.107	0.100	0.069,0.143	0.050,0.203
1300	0.068	0.067	0.047,0.102	0.035,0.140
1400	0.072	0.051	0.036,0.075	0.027,0.108
1500	0.081	0.045	0.031,0.066	0.023,0.092
1600	0.074	0.038	0.027,0.057	0.020,0.079
1700	0.049	0.034	0.023,0.050	0.017,0.070
1800	0.031	0.030	0.021,0.044	0.015,0.061
1900	0.028	0.029	0.021,0.041	0.015,0.058
2000	0.032	0.029	0.021,0.043	0.015,0.060

Table 17.3: b_L^* cross-section upper limits for given b_L^* mass values. Cross-section is in units of pb.

b_{LR}^* Cross-Section Upper Limits				
M_{b^*}	observed	expected	expected 1σ	expected 2σ
800	3.917	6.568	4.072,11.122	2.342,18.857
900	0.317	0.603	0.361,1.048	0.219,2.099
1000	0.095	0.187	0.124,0.269	0.087,0.386
1100	0.131	0.124	0.085,0.182	0.063,0.244
1200	0.094	0.086	0.060,0.124	0.044,0.177
1300	0.059	0.059	0.041,0.088	0.031,0.121
1400	0.065	0.046	0.033,0.066	0.024,0.097
1500	0.070	0.039	0.027,0.056	0.019,0.082
1600	0.065	0.033	0.023,0.049	0.017,0.069
1700	0.042	0.029	0.020,0.043	0.014,0.059
1800	0.026	0.026	0.018,0.038	0.013,0.053
1900	0.025	0.025	0.017,0.035	0.013,0.051
2000	0.026	0.025	0.017,0.036	0.013,0.050

Table 17.4: b_{LR}^* cross-section upper limits for given b_{LR}^* mass values. Cross-section is in units of pb.

CHAPTER 17. RESULTS

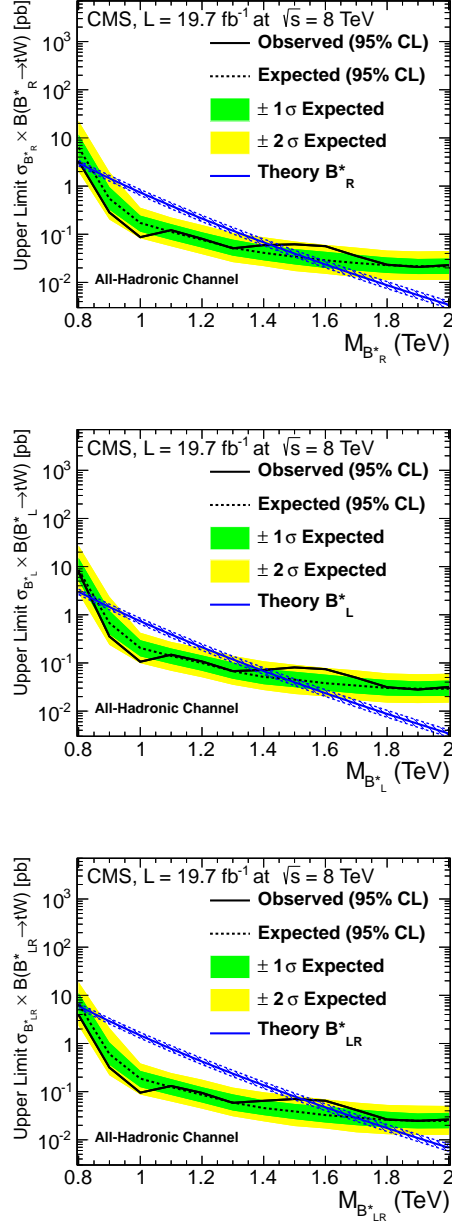


Figure 17.1: The b^* quark 95% C.L. production cross-section limits. The expected (dashed black) and observed (solid black) limits as well as b^* quark theoretical cross-section (blue) are plotted for comparison. The uncertainty in the expected limit band is shown in green ($\pm 1\sigma$) and yellow ($\pm 2\sigma$). These limits were extracted using the Theta limit setting framework. Here, the signal hypotheses of a right-handed, left-handed, and vectorlike b^* quark are shown on the top, middle, and bottom plots respectively.

CHAPTER 17. RESULTS

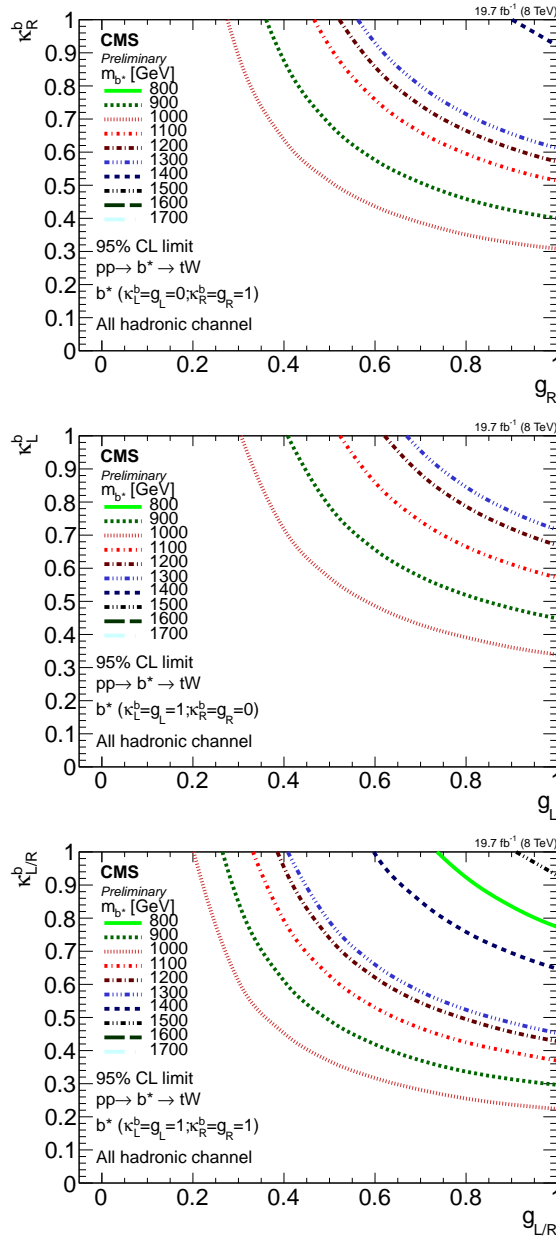


Figure 17.2: observed limit plot in the κ, g plane. The top, middle, and bottom plots show limits for right, left and vectorlike coupling hypotheses respectively.

CHAPTER 17. RESULTS

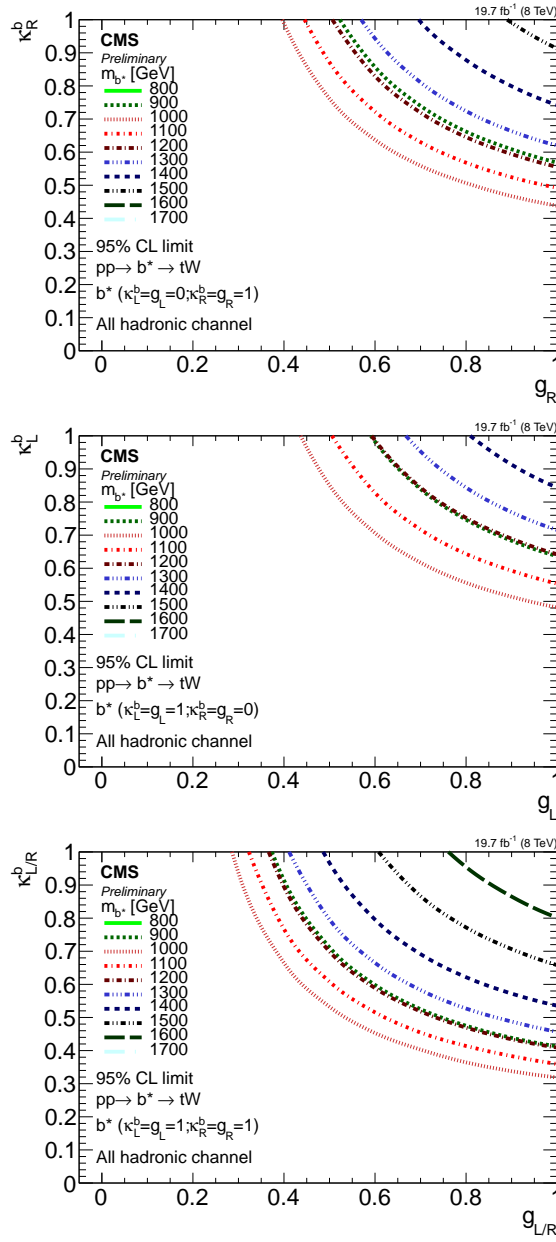


Figure 17.3: expected limit plot in the κ, g plane. The top, middle, and bottom plots show limits for right, left and vectorlike coupling hypotheses respectively.

Chapter 18

Combination

Here we detail the combination of the signal cross section upper limit sensitivity for the semileptonic, all-hadronic, and dileptonic b^* decay channels. The specifics for the three searches are detailed in the analysis notes [37–39]. Identical sources of systematic uncertainty are correlated across the channels. The overlap of the signal region events is negligible. There is no overlap between the all-hadronic channel and the other selections. The dileptonic channel and semileptonic have four overlapping events out of 7900 lepton+jets events and 17559 dilepton events. and we set limits using the Bayesian statistical method as implemented by the theta framework to set 95% C.L. upper limits on the $b^* \rightarrow tW$ cross-section.

The following systematic uncertainties are correlated across multiple channels (see Chapter16):

- **Jet Energy Scale**

CHAPTER 18. COMBINATION

- **Jet Energy Resolution**
- **Luminosity**
- **DiBoson Cross-Section:** The semileptonic and dileptonic channels use the recommended 30% uncertainty on the di-boson cross-section. The all-hadronic channel does not include this background source.
- **Single-top Cross-Section**
- **Z+jets Cross-Section:** The semileptonic and dileptonic channels use the recommended 20% uncertainty on the Z+jets cross-section. The all-hadronic channel does not include this background source.
- **tt** Cross-Section: The semileptonic and dileptonic channels use the recommended 5.3% uncertainty on the tt> cross-section. The all-hadronic channel does not include this uncertainty due to a measurement of the tt> normalization and uncertainty in the analysis.

Statistical uncertainties are taken into account by using the Barlow-Beeston lite method.

The rate effects of the systematic uncertainties that only affect the semileptonic channel are given in tables 19.1 and 19.2 for the electron and muon channels respectively. The rate effects of the systematic uncertainties that only affect the all-hadronic channel are given in table 19.3. The rate effects of the systematic uncertainties that

CHAPTER 18. COMBINATION

only affect the dileptonic channel are given in table 19.4. The rate effects of the systematic uncertainties that are correlated over multiple channels are given in table 19.5, 19.6, 19.8, 19.7 for the semileptonic electron, semileptonic muon, all hadronic, and dilepton channels respectively.

The nuisance parameters after the Theta fit can be seen in figure 18.10.

The distributions given to the limit setting macro are shown in figures 18.1, 18.2, and 18.3 for the semileptonic, dileptonic, and all-hadronic channels respectively. The limits for the three channels before combination are shown in figure 18.4, 18.5, and 18.6 for the semileptonic, dileptonic, and all-hadronic channels respectively. The combined limits are shown in Figure 18.7.

The cross section upper limits can be generalized due to the fact that the b^* cross-section is dependent on the unknown constants κ and g . The limits can be extrapolated to the g, κ plane as can be seen in figures 18.8 and 18.9 for observed and expected limits respectively.

The cross section upper limits for left-handed right-handed and vectorlike b^* coupling hypotheses are shown in Tables 18.2 18.1 and 18.3 respectively.

The b^* mass exclusion point for each channel is given in table 18.4

CHAPTER 18. COMBINATION

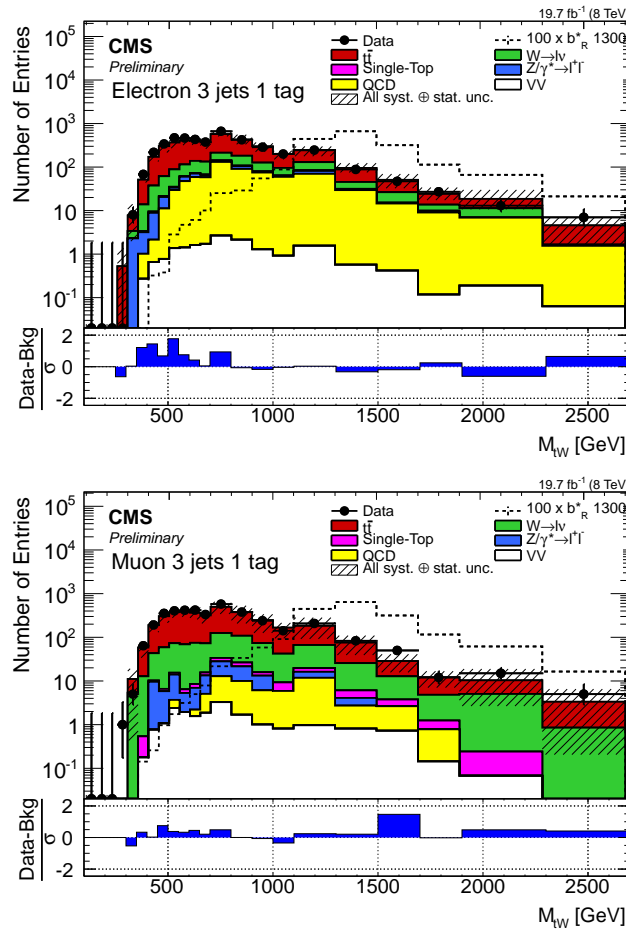


Figure 18.1: The reconstructed b^* invariant mass distribution in data, background, and signal. The channel is semileptonic in the electron+jets (top) and muon+jets (bottom).

CHAPTER 18. COMBINATION

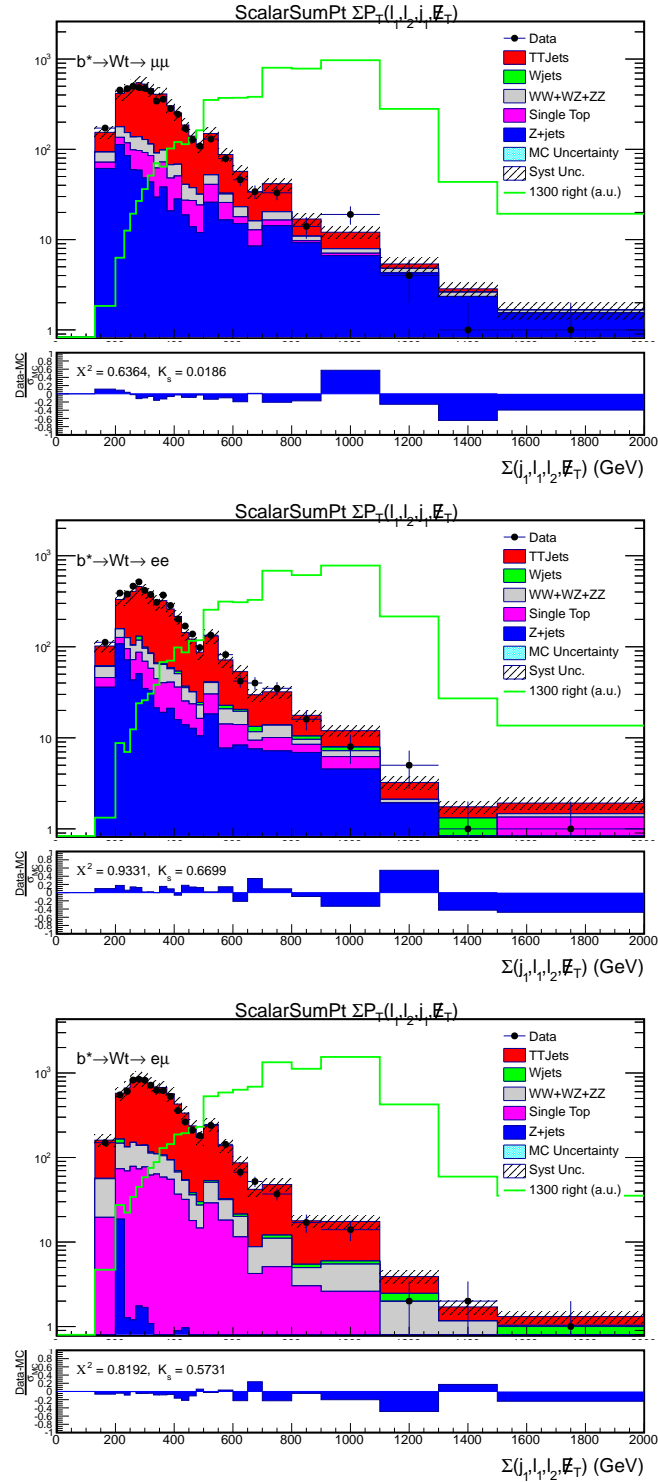


Figure 18.2: The reconstructed scalar p_T sum distribution in data, background, and signal. The channel is dileptonic in the muon+muon (top) electron+electron (middle) and electron+muon (bottom).

CHAPTER 18. COMBINATION

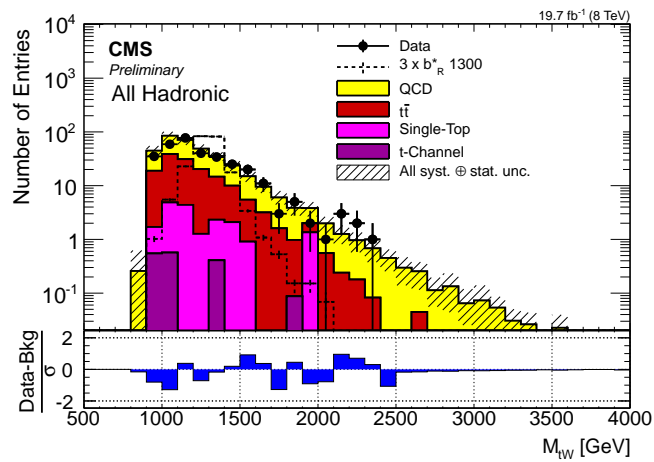


Figure 18.3: The reconstructed b^* invariant mass distribution in data, background, and signal. The channel is all-hadronic.

CHAPTER 18. COMBINATION

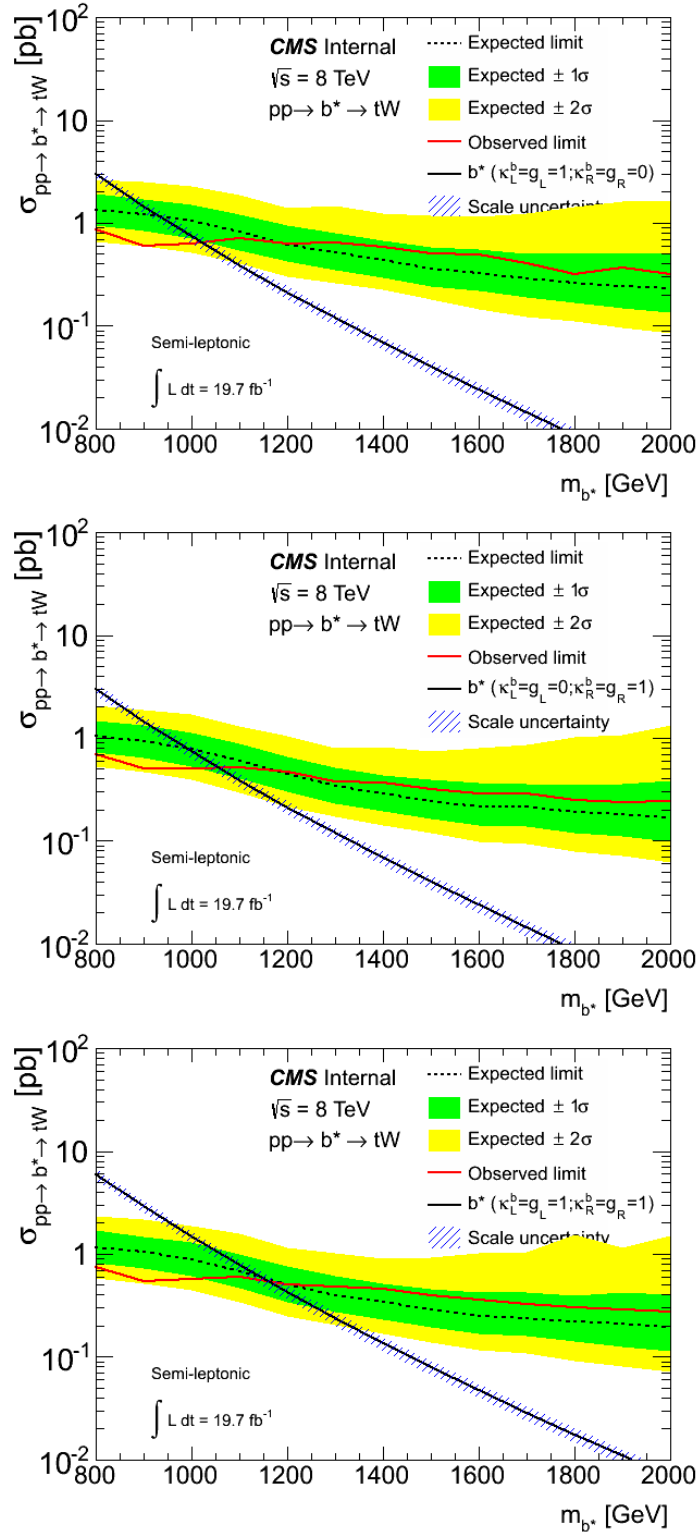


Figure 18.4: limit plot for the left-handed b^* (left plot), right handed (middle plot) and vector like (right plot) b^* for lepton+jets channel only. The theory error band including scale uncertainties.

CHAPTER 18. COMBINATION

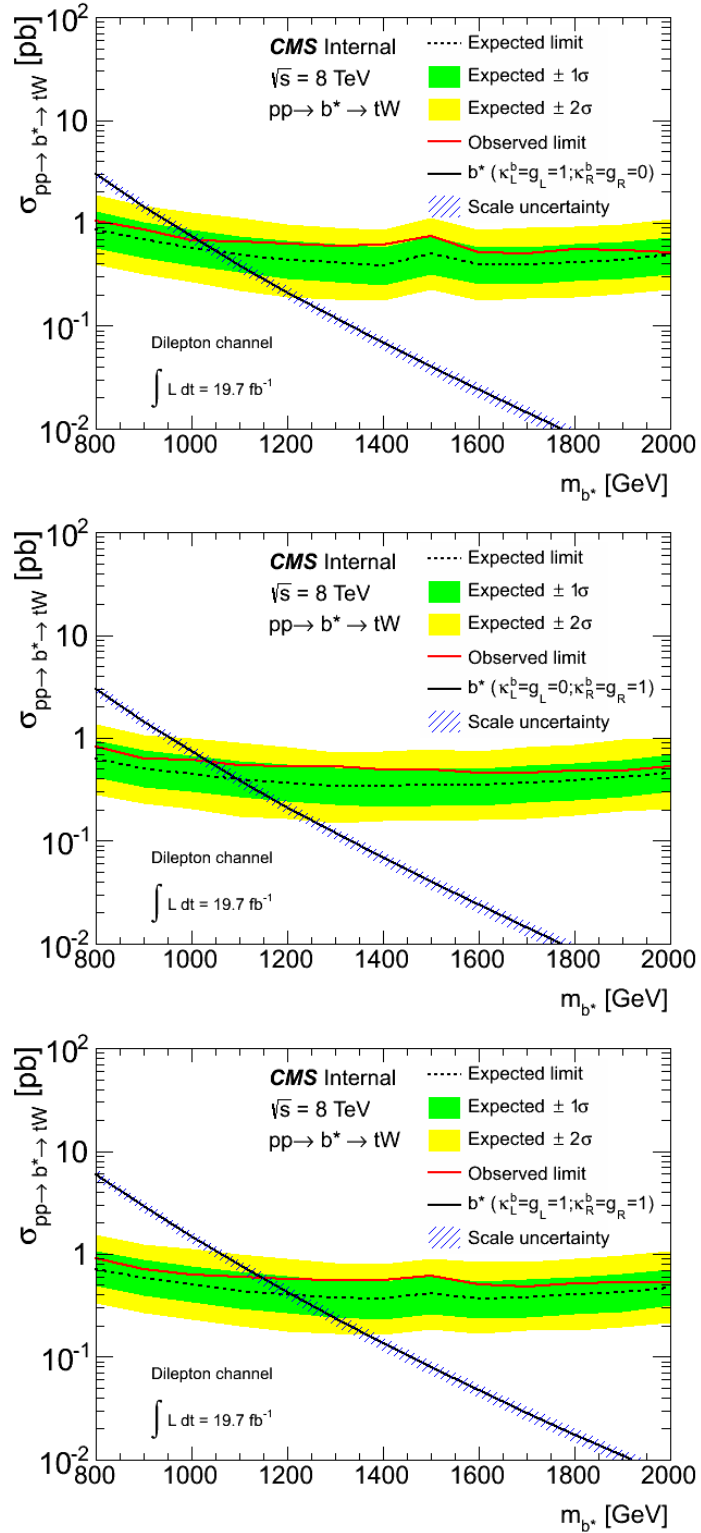


Figure 18.5: limit plot for the left-handed b^* (left plot), right handed (middle plot) and vector like (right plot) b^* for dilepton channel only. The theory error band including scale uncertainties.

CHAPTER 18. COMBINATION

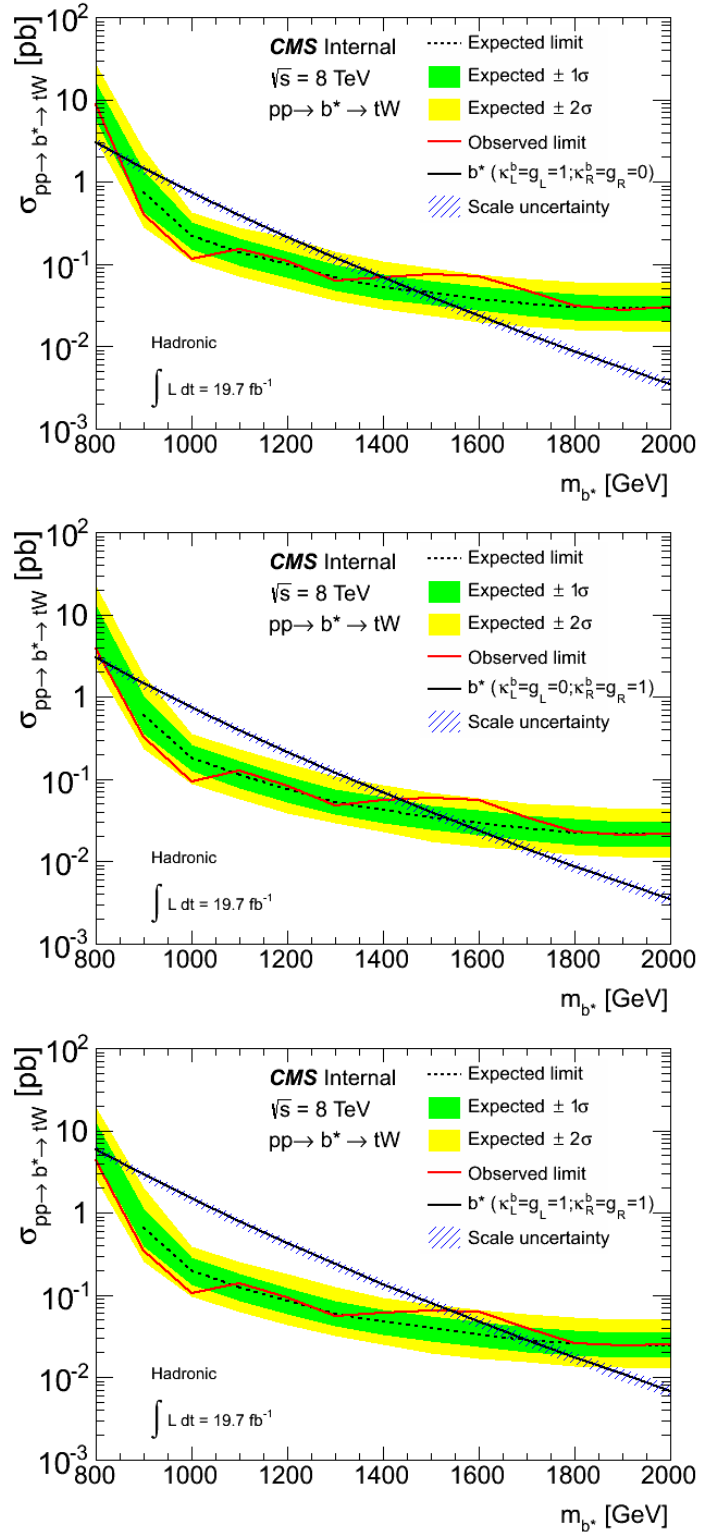


Figure 18.6: limit plot for the left-handed b^* (left plot), right handed (middle plot) and vector like (right plot) b^* for full hadronic channel only. The theory error band including scale uncertainties.

CHAPTER 18. COMBINATION

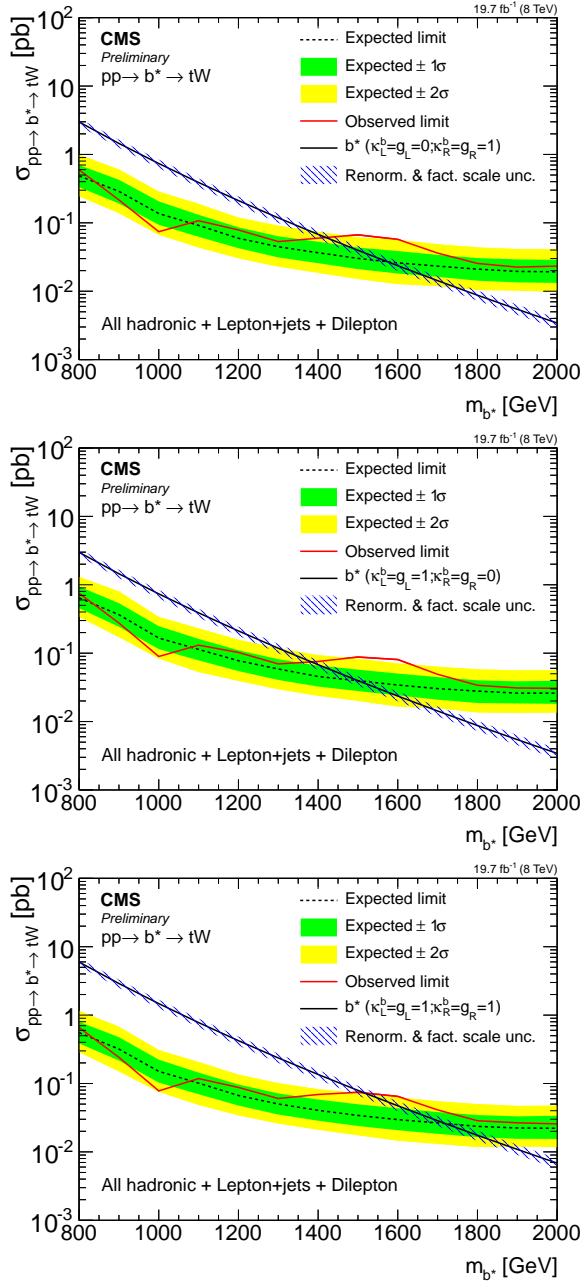


Figure 18.7: The b^* quark 95% C.L. production cross-section limits. The expected (black) and observed (red) limits as well as b^* quark theoretical cross-section (blue) are plotted for comparison. The uncertainty in the expected limit band is shown in light ($\pm 1\sigma$) and dark grey ($\pm 2\sigma$). These limits were extracted using the Theta limit setting framework. Here, the signal hypotheses of a right-handed, left-handed, and vector-like b^* quark are shown on the top, middle, and bottom plots respectively.

CHAPTER 18. COMBINATION

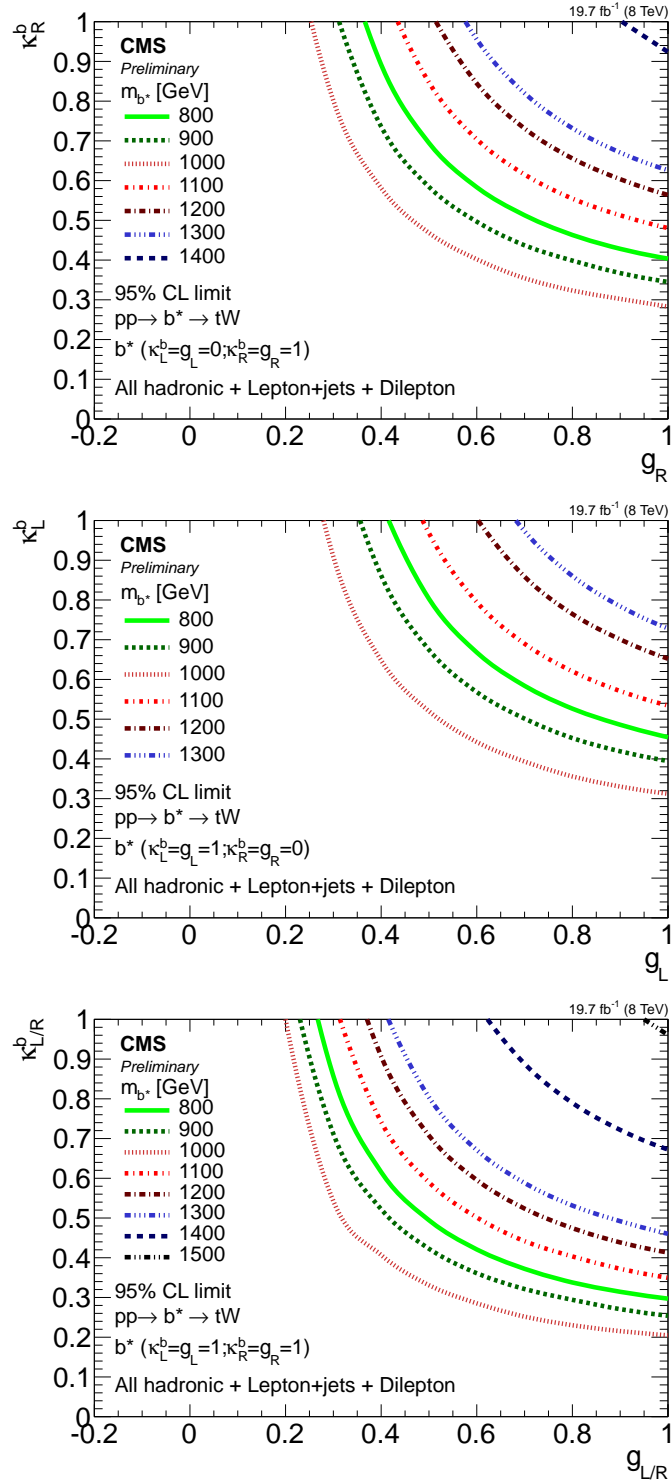


Figure 18.8: observed limit plot in the κ, g plane. The top, middle, and bottom plots show limits for right, left and vector-like coupling hypotheses respectively.

CHAPTER 18. COMBINATION

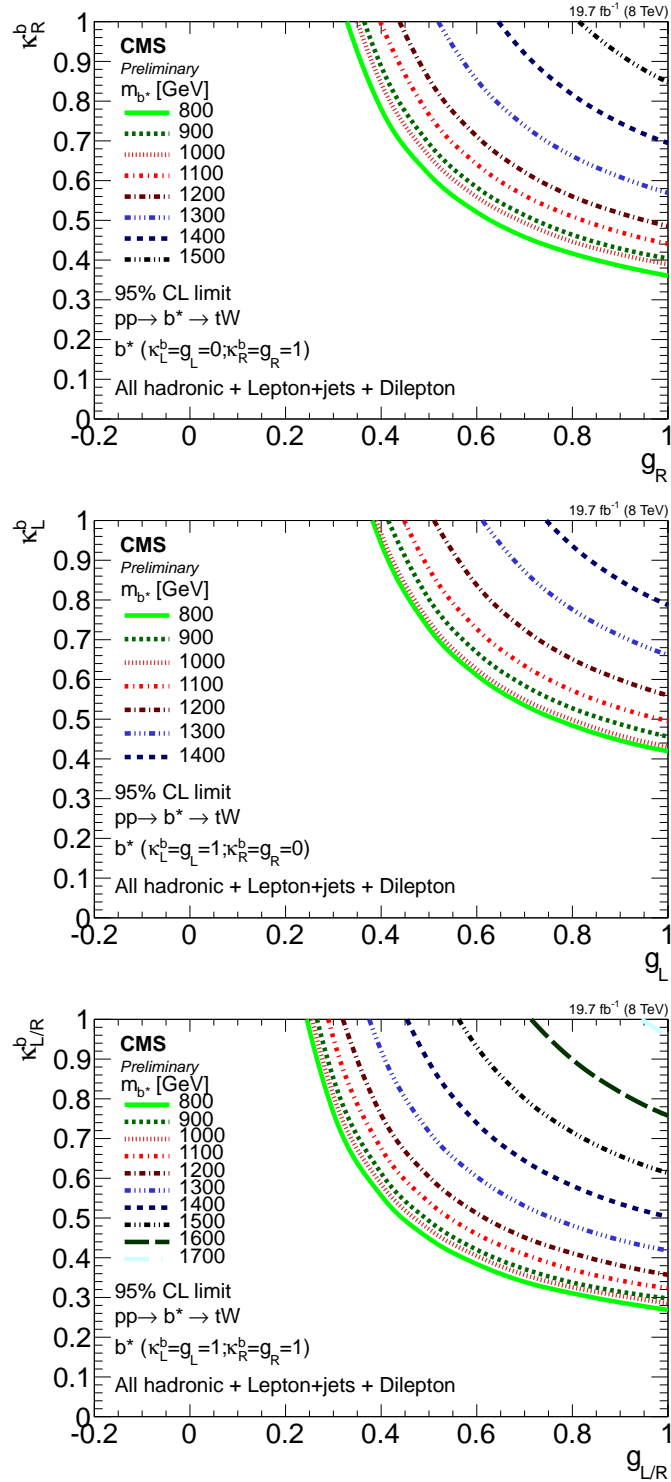


Figure 18.9: expected limit plot in the κ, g plane. The top, middle, and bottom plots show limits for right, left and vector-like coupling hypotheses respectively.

CHAPTER 18. COMBINATION

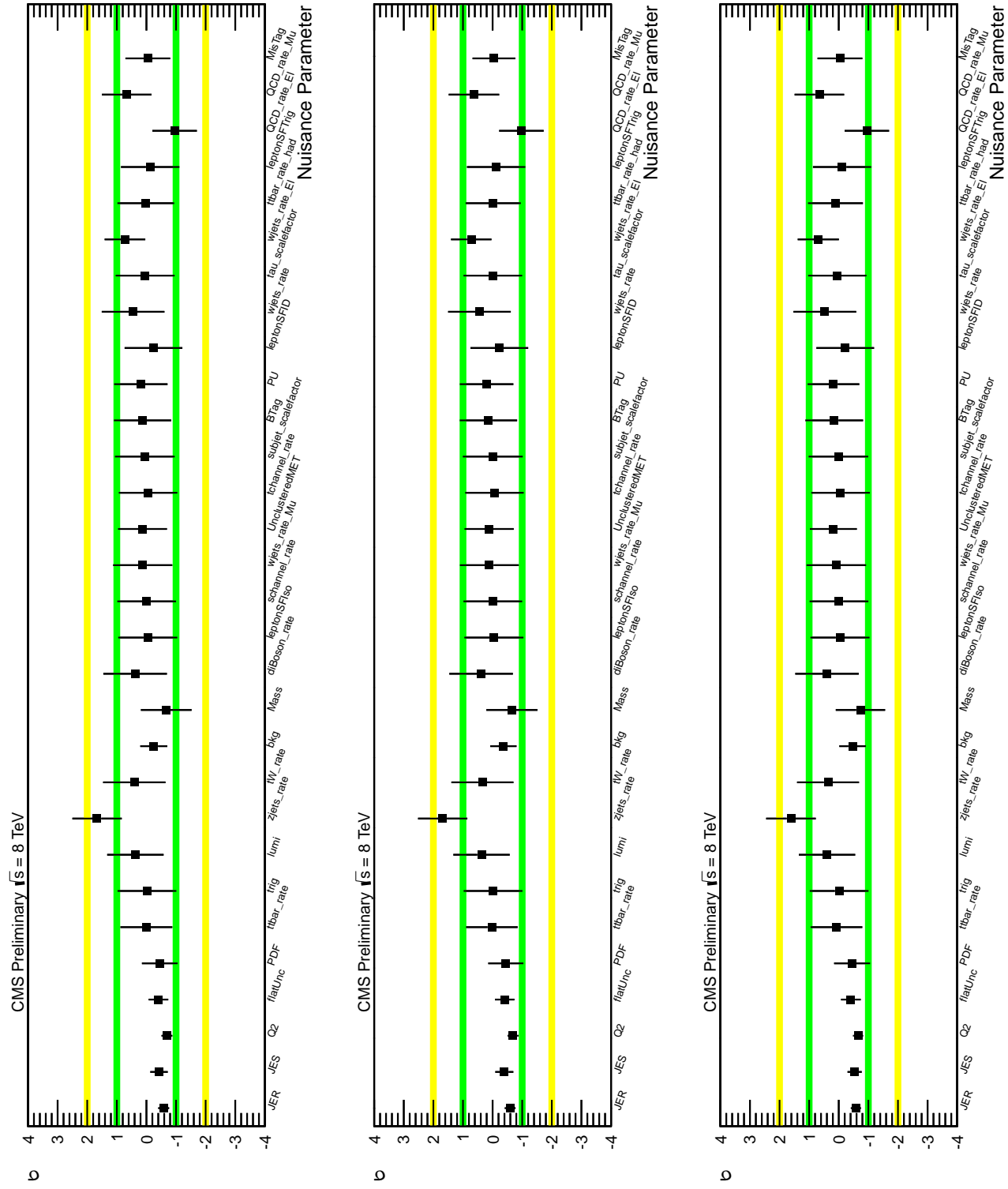


Figure 18.10: Nuisance parameters after the Theta fit. The Signal mass points here are 1200, 1400, and 1600 GeV for the top, middle, and bottom plots respectively.

CHAPTER 18. COMBINATION

b_R^* Cross-Section Upper Limits				
M_{b^*}	observed	expected	expected 1σ	expected 2σ
800	0.490	0.492	0.335,0.723	0.243,1.039
900	0.188	0.303	0.202,0.446	0.140,0.611
1000	0.070	0.141	0.097,0.203	0.070,0.279
1100	0.103	0.096	0.068,0.138	0.050,0.186
1200	0.074	0.063	0.044,0.092	0.032,0.129
1300	0.052	0.045	0.032,0.067	0.023,0.098
1400	0.063	0.038	0.027,0.053	0.020,0.076
1500	0.067	0.030	0.021,0.043	0.015,0.061
1600	0.056	0.025	0.018,0.037	0.012,0.052
1700	0.037	0.023	0.016,0.034	0.011,0.049
1800	0.023	0.021	0.014,0.030	0.010,0.044
1900	0.021	0.020	0.014,0.030	0.010,0.042
2000	0.021	0.020	0.013,0.030	0.010,0.043

Table 18.1: b_R^* cross-section upper limits for given b_R^* mass values. Cross-section is in units of pb.

CHAPTER 18. COMBINATION

b_L^* Cross-Section Upper Limits

M_{b^*}	observed	expected	expected 1σ	expected 2σ
800	0.617	0.666	0.454,0.984	0.344,1.366
900	0.236	0.387	0.258,0.571	0.172,0.782
1000	0.086	0.173	0.119,0.251	0.087,0.337
1100	0.123	0.119	0.085,0.174	0.063,0.236
1200	0.097	0.083	0.057,0.120	0.042,0.173
1300	0.068	0.059	0.042,0.088	0.030,0.127
1400	0.074	0.048	0.033,0.067	0.025,0.096
1500	0.088	0.040	0.028,0.057	0.020,0.082
1600	0.077	0.034	0.023,0.049	0.016,0.068
1700	0.049	0.030	0.021,0.044	0.014,0.062
1800	0.032	0.028	0.019,0.040	0.013,0.059
1900	0.031	0.027	0.018,0.039	0.013,0.057
2000	0.032	0.027	0.018,0.040	0.014,0.060

Table 18.2: b_L^* cross-section upper limits for given b_L^* mass values. Cross-section is in units of pb.

b_{LR}^* Cross-Section Upper Limits

M_{b^*}	observed	expected	expected 1σ	expected 2σ
800	0.510	0.570	0.384,0.840	0.285,1.137
900	0.208	0.337	0.226,0.496	0.157,0.686
1000	0.080	0.156	0.107,0.220	0.079,0.313
1100	0.112	0.107	0.074,0.152	0.057,0.210
1200	0.084	0.072	0.050,0.104	0.035,0.146
1300	0.058	0.051	0.036,0.076	0.026,0.108
1400	0.064	0.042	0.030,0.059	0.022,0.085
1500	0.074	0.034	0.024,0.050	0.018,0.072
1600	0.067	0.029	0.020,0.042	0.014,0.060
1700	0.041	0.026	0.018,0.038	0.013,0.054
1800	0.027	0.024	0.016,0.035	0.011,0.050
1900	0.025	0.023	0.016,0.033	0.011,0.050
2000	0.024	0.023	0.015,0.033	0.012,0.050

Table 18.3: $b_L^* R$ cross-section upper limits for given b_{LR}^* mass values. Cross-section is in units of pb.

CHAPTER 18. COMBINATION

	left-handed	right-handed	vector like
Lepton + jets, dilepton and full hadronic channel combined			
expected 95% CL limit [GeV]	1500	1580	1730
observed 95% CL limit [GeV]	1390	1420	1520
Full hadronic channel only			
expected 95% CL limit [GeV]	890 - 1480	880 - 1550	820 - 1700
observed 95% CL limit [GeV]	880 - 1390	820 - 1430	1530
Lepton + jets channel only			
expected 95% CL limit [GeV]	940	990	1130
observed 95% CL limit [GeV]	1030	1070	1170
Dilepton channel only			
expected 95% CL limit [GeV]	1060	1100	1210
observed 95% CL limit [GeV]	1020	1050	1160

Table 18.4: 95% CLs limit for the left-, right-handed and vector like excited bottom quark in the full hadronic, lepton+jets and dilepton channel combined and seperately at the benchmark point of unit couplings.

Chapter 19

Appendix

19.1 W' Search

19.1.1 CA8 b-tagging

CA8 jet b-tagging comparison to AK5 jets. A 2% uncertainty is applied to signal Monte Carlo samples in the analysis. Jets are matched between AK5 and CA8 within a Delta(R) size of 0.3. Jets are ensured b flavor from Monte Carlo truth and are within the p_T range of the analysis. The constant fit to the efficiency ratio gives an upper limit to the uncertainty for the change in SF_b for use with CA8 jets. No extra correction is applied to SF_b . The following plots are from Signal Monte Carlo at 2700/ GeV .

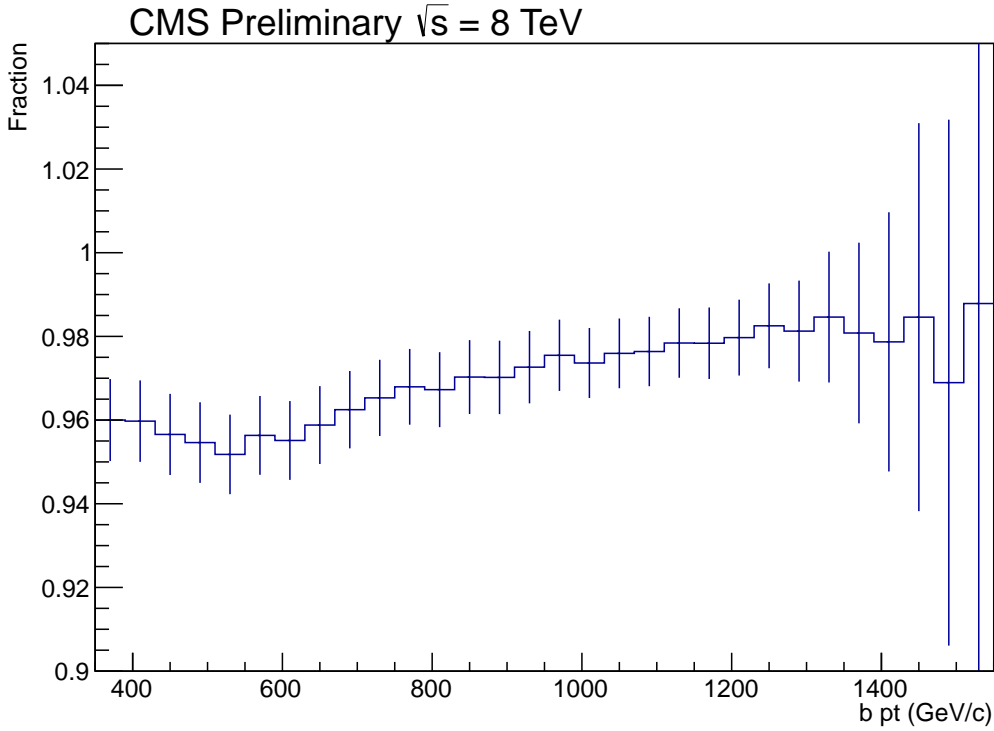


Figure 19.1: Percent of matched jets that register the same value for the CSVM cut.

19.1.2 Signal Region and Sideband Kinematic Comparison

Figure 19.3 shows a comparison in QCD Monte Carlo of kinematic variables of interest in the CMS top tagger selection and number of subjets sideband used for the determination of the average b-tagging rate. There are some discrepancies seen in the two regions, which is the main reason why we use the average b-tagging rate instead of the sideband itself. Variables constrained to the top candidate jet such as top mass have a drastically different shape, so we need to look at the b candidate jet

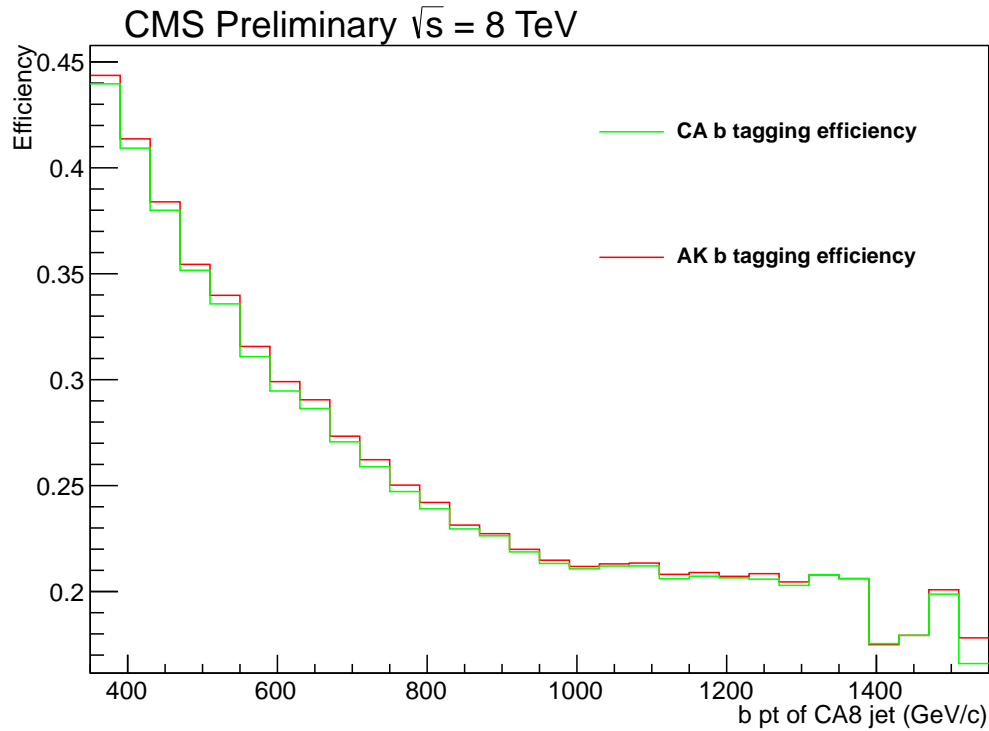


Figure 19.2: Comparison of the efficiency of b-tagging matched CA8 and AK5 jets

in the opposite hemisphere to keep the background estimate unbiased. Additionally, because we parameterize in p_T the influence from the different b candidate p_T shapes does not bias the background estimate. Then the final kinematic variable of interest is b candidate mass which shows good agreement.

19.1.3 Signal Kinematic Comparison

Figure 19.4 shows a comparison of relevant kinematic variables for right, left, and mixed Signal Monte Carlo samples.

CHAPTER 19. APPENDIX

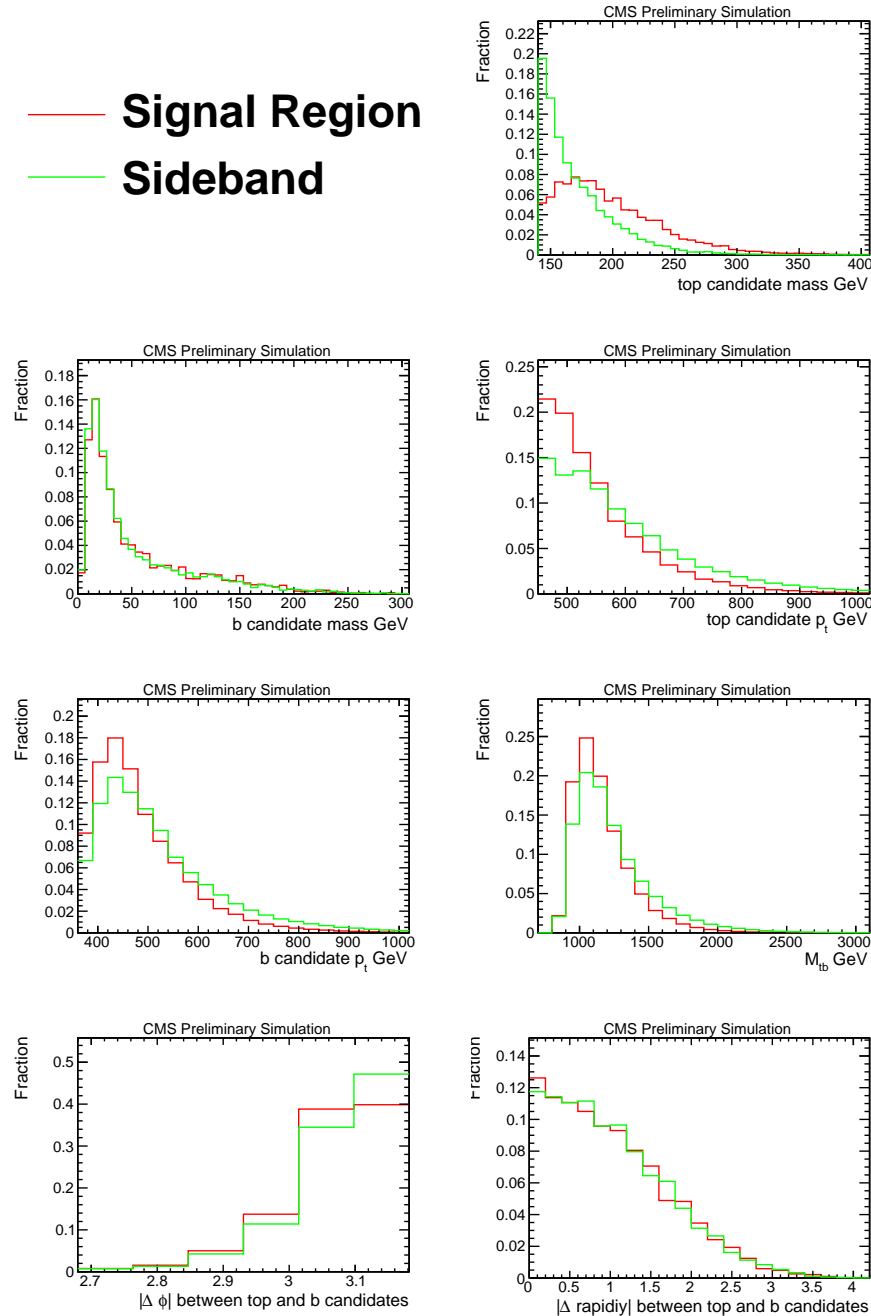


Figure 19.3: Comparison of kinematic variables in QCD Monte Carlo extracted from the CMS top tagger signal region and number of subjets sideband

CHAPTER 19. APPENDIX

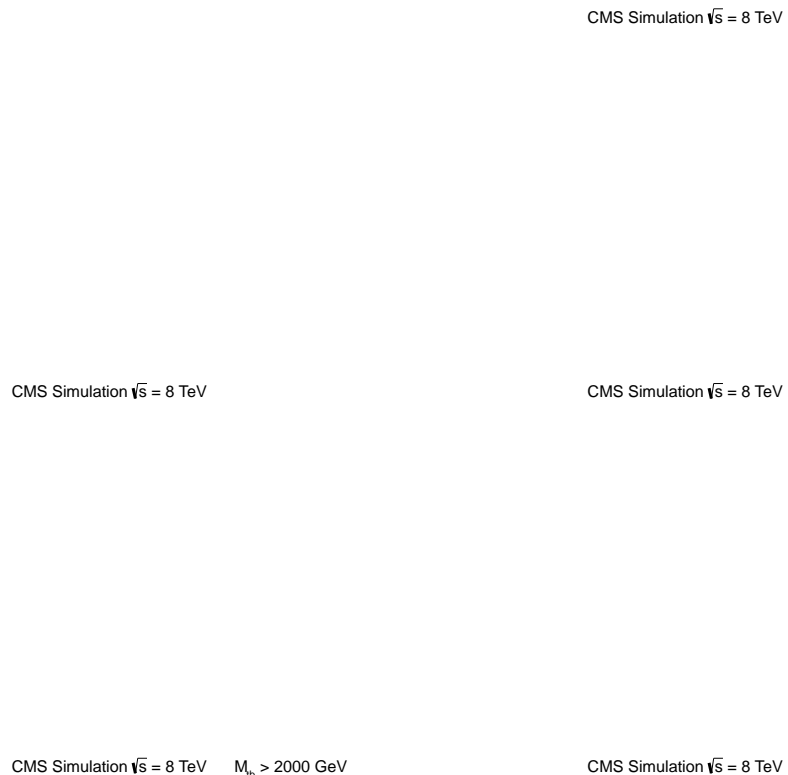


Figure 19.4: Comparison of kinematic variables in Signal Monte Carlo for right, left and mixed coupling all at the 2100 GeV mass point

19.1.4 QCD Parameterization Uncertainty

The QCD background prediction relies on the probability to tag a b jet. We parameterize this probability using physical variables that have a large effect on the b-tagging rate (p_T and η of the b candidate jet). However, the variable of interest in the analysis is M_{tb} , and the background estimate involves integrating, for every bin in M_{tb} , along the p_T axis. To see this more explicitly, let us consider the signal region only, with pre-b-tag data divided into a two-dimensional matrix along p_T and M_{tb} axes, indexed by indices i and j respectively. Thus n_{ij} is the number of pre-b-tag events within a given p_T bin (index i) and a given M_{tb} bin (index j), \bar{P}_i is the average of true b-tagging probability for a slice in p_T , whereas P_{ij} is the true b-tagging probability for data in n_{ij} .

The true number of b tags in two-dimensional bin (i, j) is then $n_{ij}P_{ij}$. The observed number of events in M_{tb} bin j is $N_j = \sum_i n_{ij}P_{ij}$. However, the background estimate uses the average b-tagging probability, \bar{P}_i , averaged over all values of j – that is, over all values of M_{tb} .¹ So a ‘perfect’ background estimate (using probabilities from the signal region) therefore yields $N_j^{\text{bkg.est.}} = \sum_i n_{ij}\bar{P}_i$.

Our procedure for the estimation of the QCD background *assumes* that P_{ij} is independent of M_{tb} – in other words, that $P_{ij} = \bar{P}_i$. If that is the case, the bias of

¹In the real measurement we furthermore obtain this number from the sideband, but to elucidate the point it is sufficient to consider the average of true b-tagging probabilities, P_{ij} , from the signal region.

CHAPTER 19. APPENDIX

the background estimate

$$\delta N_j = N_j - N_j^{\text{bkg.est.}} = \sum_i n_{ij} (P_{ij} - \bar{P}_i) \quad (19.1)$$

is indeed zero.

If for some reason $P_{ij} \neq \bar{P}_i$, Eq.(19.1), depending on the values of n_{ij} , could result in non-zero bias δN_j – even when the used average tagging probability corresponds to the signal region itself.

Luckily, the assumption that the average b-tagging probability depends only on the jet itself (with p_T and η of the b jet) is a very good one. However, it is conceivable that second- or third-order effects could create small deviations in $P_{ij} - \bar{P}_i$ and thus result in a small bias. These effects could be caused by other activity in the event, which could be a reason that the same values of p_T and η could correspond to events with different p_T of the top jet, and thus M_{tb} . To see that such effects exist (and also that they are small), it is sufficient to consider the top p_T in Figure 7.3, where there seems to be a small but systematic bias of the background estimate, as evidenced by the pull distribution in the lower pane. We have not studied the causes of these effects, but additional activity in the event (from other jets or pile-up) could contribute additional pixel and strip hits inside the volume of the b jet, and thus impact the average tagging rate at a low level.

To investigate the ability of the b-tagging rate parameterization in p_T and η to

CHAPTER 19. APPENDIX

predict M_{tb} , we incorporate M_{tb} into the b-tagging rate parameterization. The effect is first checked in the second sideband described above. The three-dimensional b-tagging rate shown in Figure 8.17 is compared to the two dimensional tagging rate shown in 6.3 to see if this effect can be the cause of the deviations observed in the low M_{tb} region. Figure 19.5 shows the differences in the three and two dimensional background estimates as well as the differences in the full selection of this control region and the background estimate. From this we conclude that there is an effect and the shape of the deviations is well approximated with this method.

19.1.5 Signal Contamination Studies

The following studies investigate signal contamination within our analysis. These plots use the same color scheme seen in Figure 19.6. The signal contamination within the sideband used for extraction of the average b-tagging rate can be seen in Figure 19.7 (this is signal injected into the post b tagged plots in Figure 6.2). The signal contamination for the signal region can be seen in Figure 19.8.

There is also some signal contamination within the sideband cross checks described in Section 6.4. The signal contamination within Figure 6.4 can be seen in Figure 19.9, and the contamination in Figure 6.5 can be seen in Figure 19.10.

19.1.6 Generalized Coupling Signal Sample Comparison

19.2 b^* Search

Figure 19.12 shows a comparison of the top-mistagging rate extracted from the W-tagging sideband described in Section 6.2 and the top-mistagging rate extracted from the signal region. This plot is taken from QCD Monte Carlo.

CHAPTER 19. APPENDIX

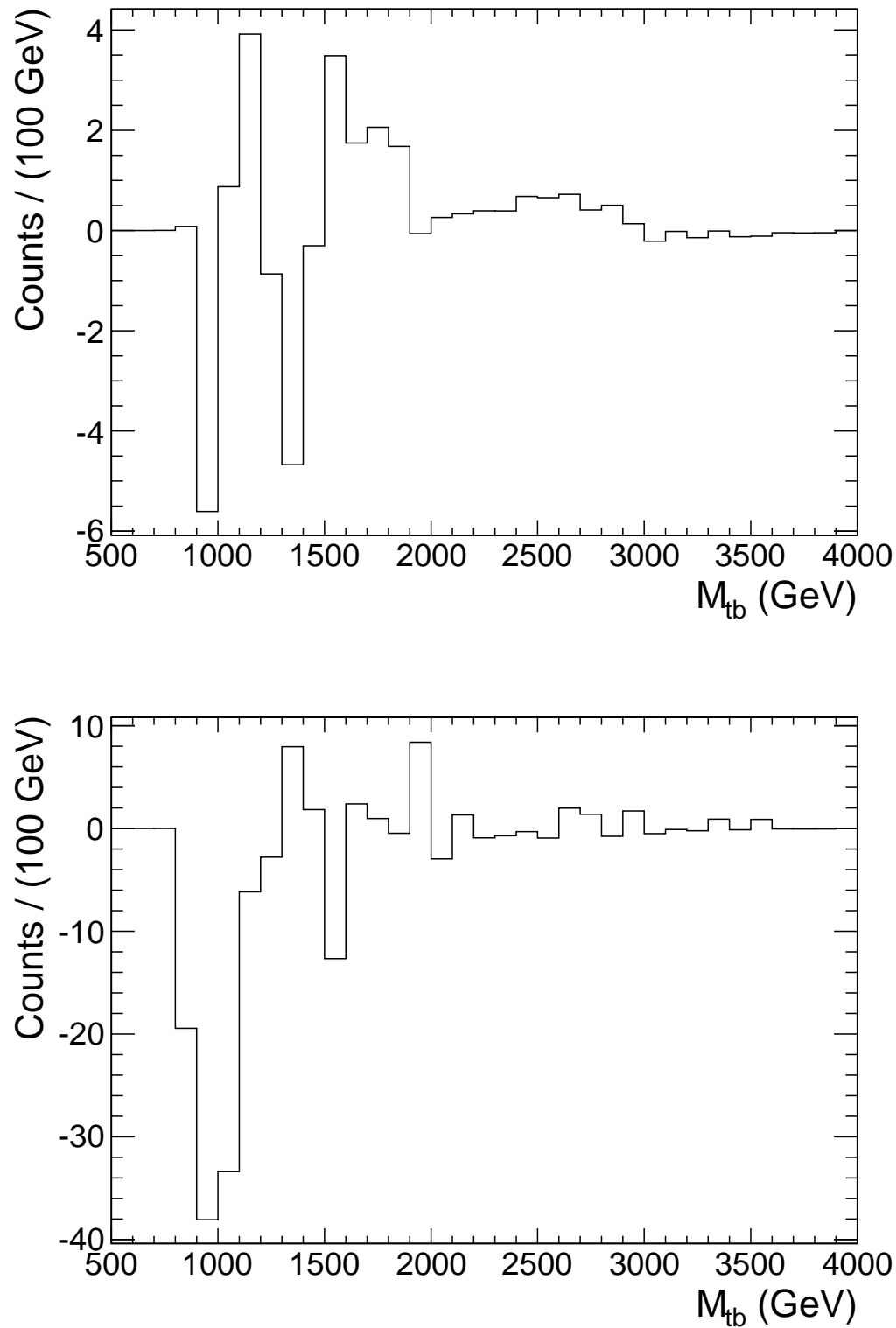


Figure 19.5: (a) Difference of the background estimation from three dimensional and two dimensional tagging rates (b) Difference of the background estimation from second sideband selection and two dimensional tagging rates

CHAPTER 19. APPENDIX

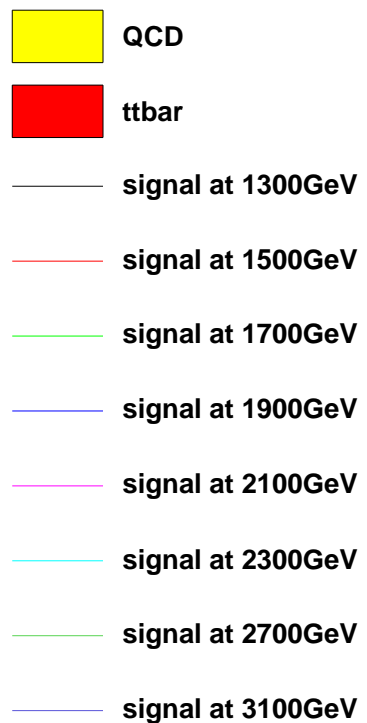


Figure 19.6: Legend for the following studies

CHAPTER 19. APPENDIX

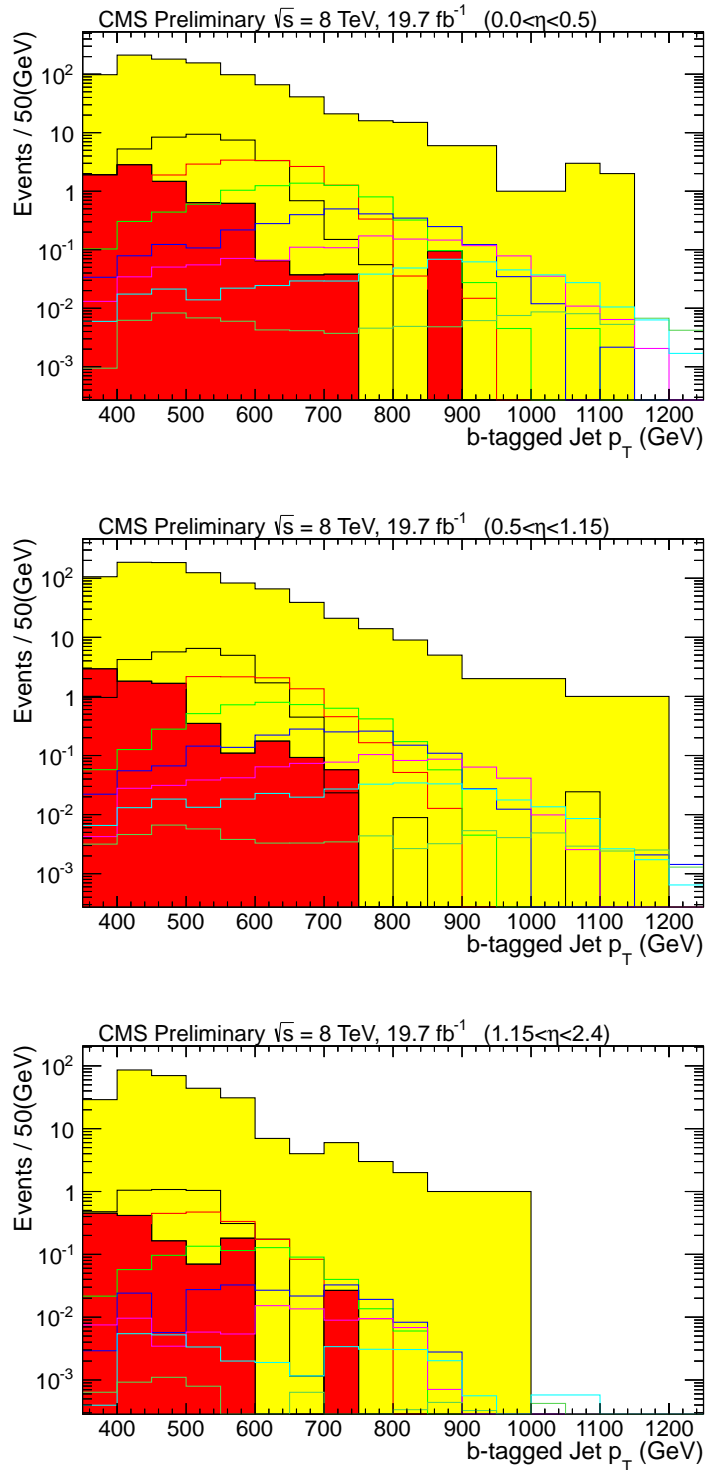


Figure 19.7: Signal contamination in the post b tagged sideband used to extract the average b-tagging rate (a) Low η region (b) Transition η region (c) High η region

CHAPTER 19. APPENDIX

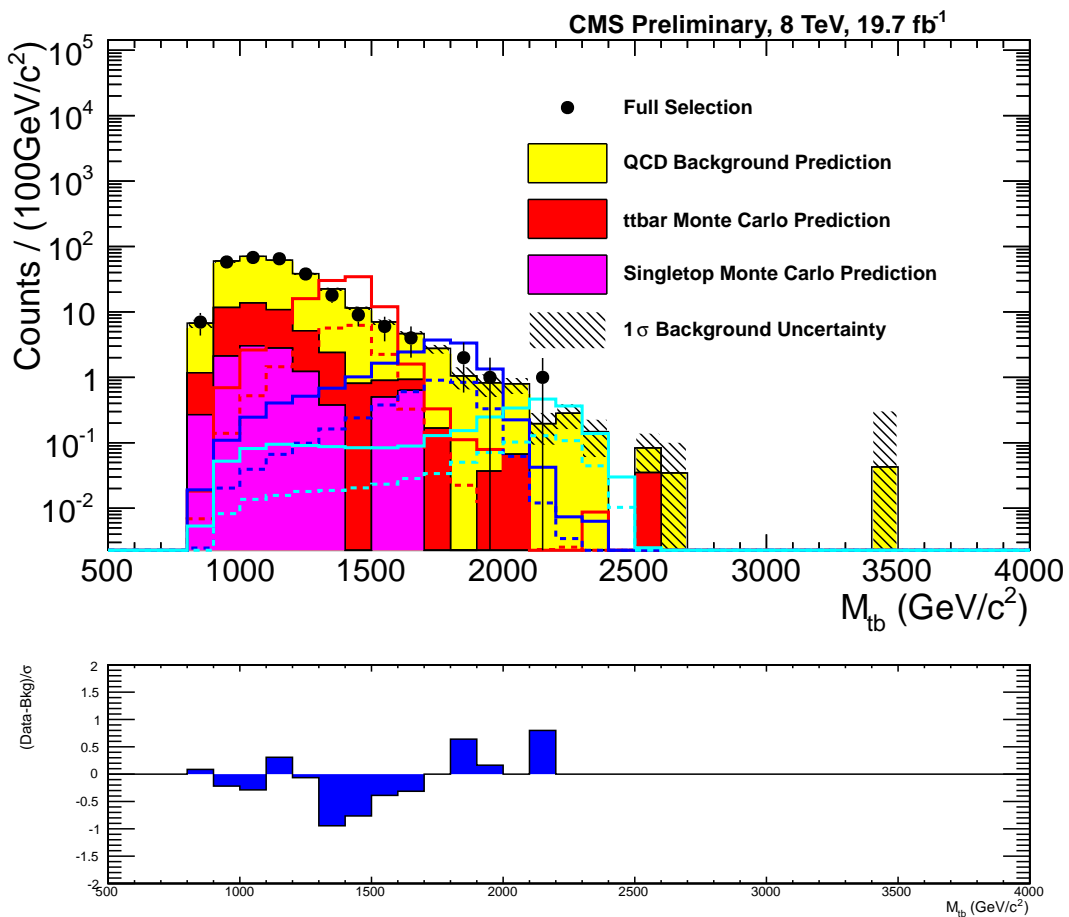


Figure 19.8: Signal contamination for the full selection. The solid lines are the signal that passes the full selection. The dashed lines are the signal that falls through the background estimate.

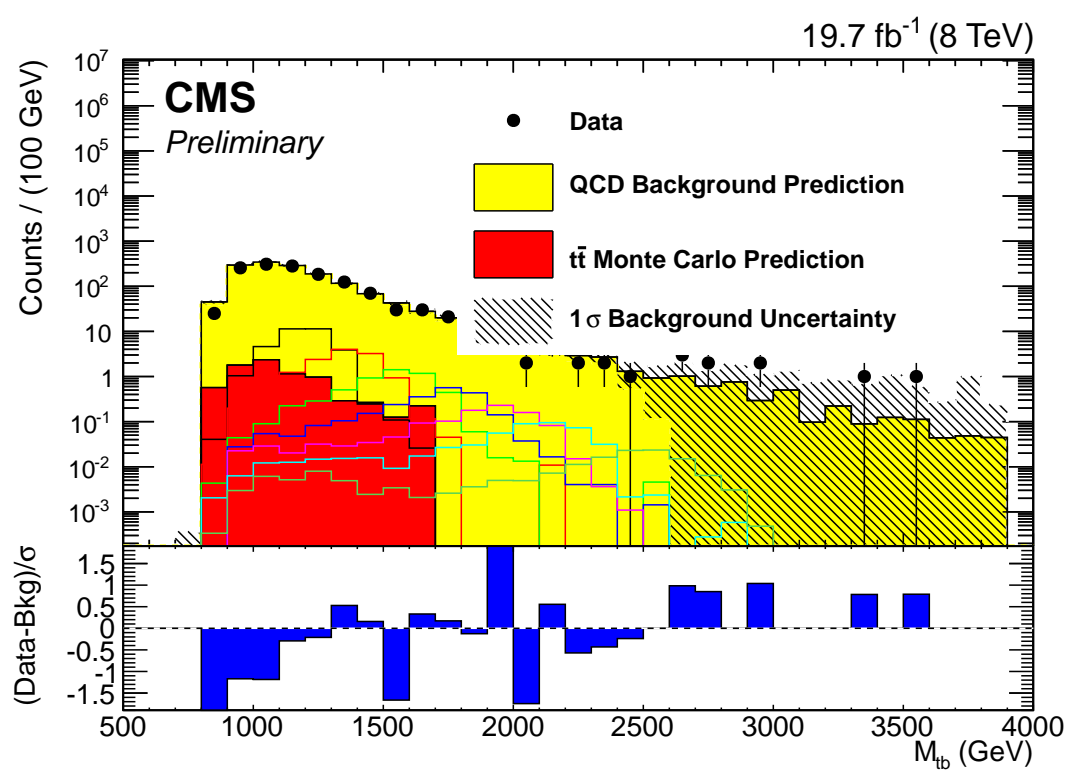


Figure 19.9: Signal contamination in sideband

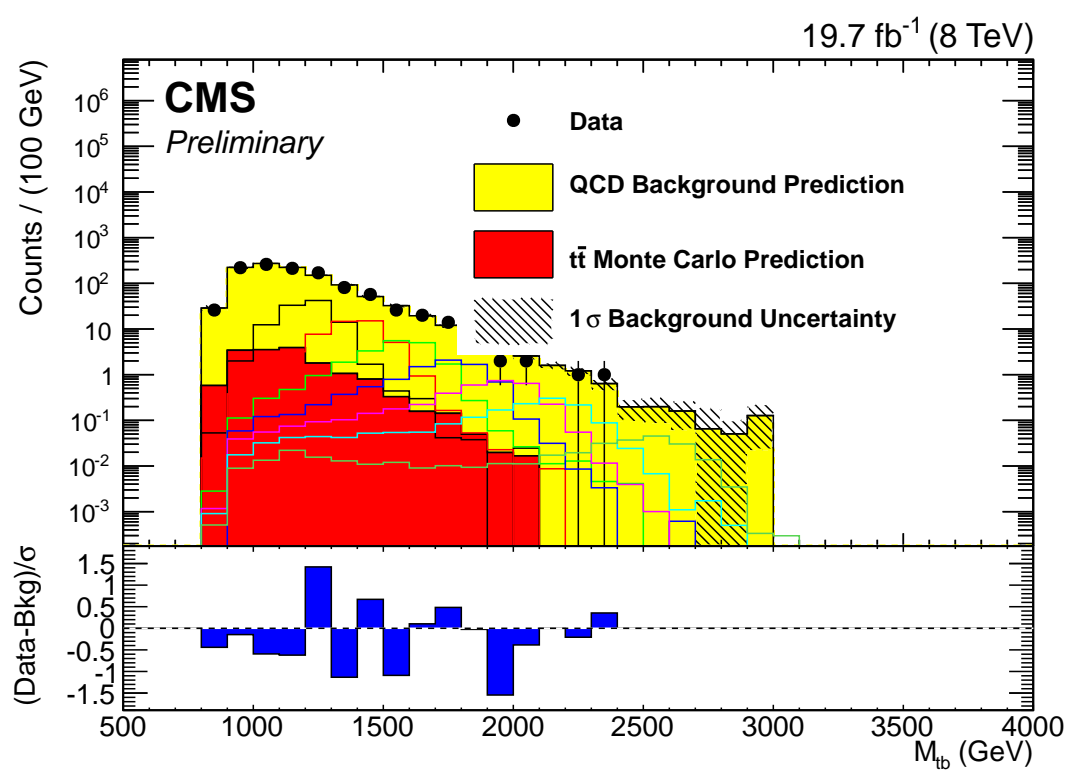


Figure 19.10: Signal contamination in sideband

CHAPTER 19. APPENDIX

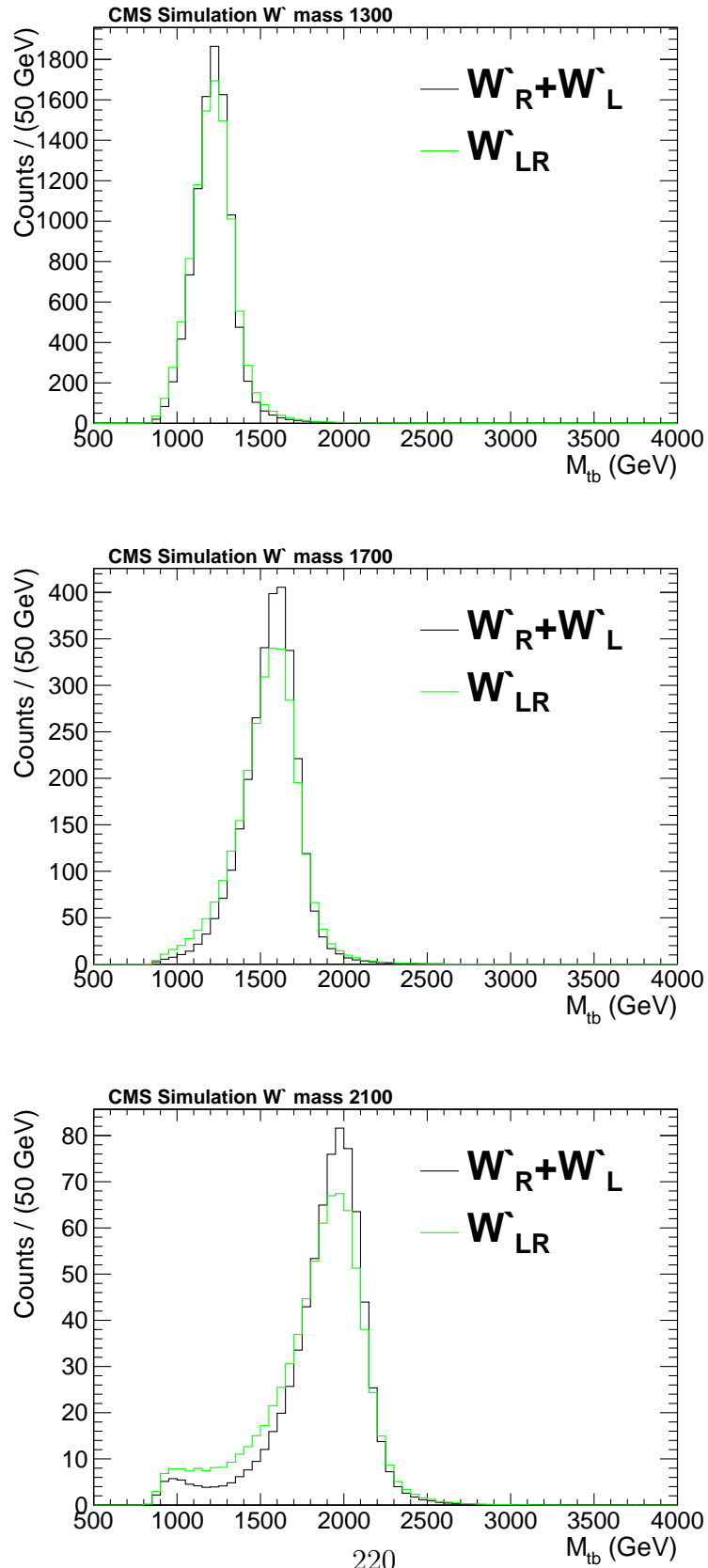


Figure 19.11: M_{tb} spectrum of events comparing the summed W'_R and W'_L templates to the $W'_L R$ template. The selection used for these plots only includes the kinematic

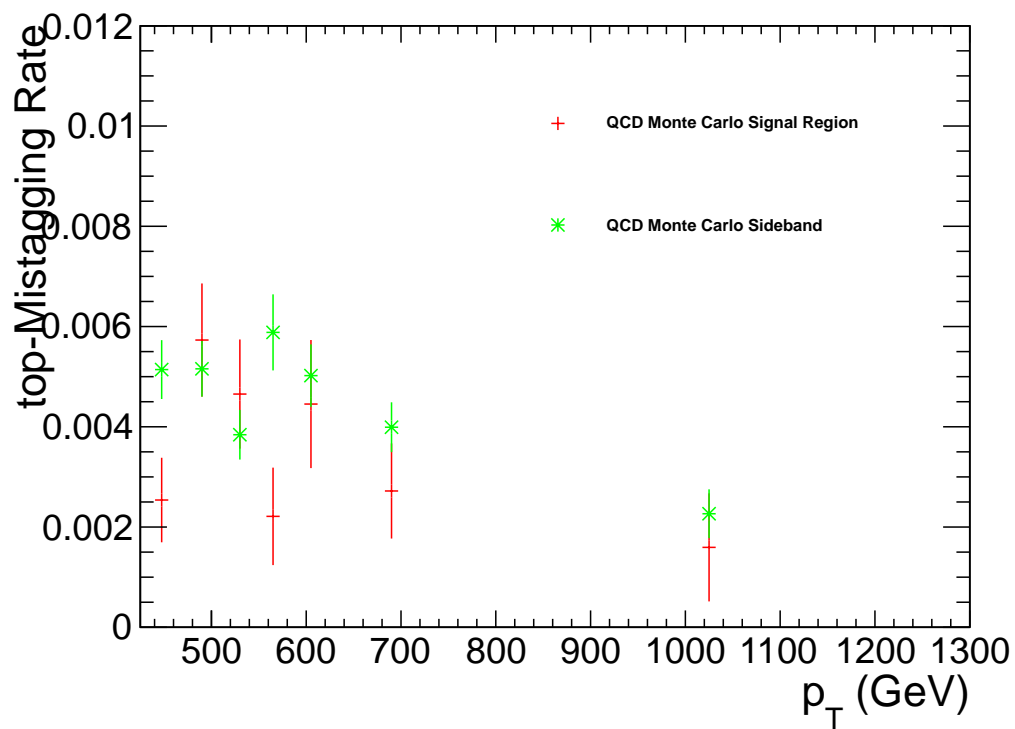


Figure 19.12: A QCD Monte Carlo comparison of the top-mistagging rate extracted from the W-tagging sideband and the top-mistagging rate extracted from the signal region. The QCD Monte Carlo quickly runs out of statistics when full top-tagging is applied.

Rate Effects of Systematic Uncertainties

Sample	B-tagging	Mass	Mistag	Pileup	QCD Rate el.	QCD Rate mu	MET	Lepton ID	Isolation	Trigger	W+jets Rate el.	W+jets Rate mu
Wjets	+4.09/-4.14	—	+14.42/-9.44	+41.28/-27.02	-0.36/-0.30	—	-0.00/-0.00	+0.26/-0.26	+0.00/-0.00	+0.40/-0.36	+45.0/-31.03	—
Zjets	+3.37/-3.41	—	+8.91/-5.88	+8.53/-7.33	-0.09/-0.20	—	-0.00/-0.00	+0.32/-0.29	+0.00/-0.00	+0.34/-0.46	+31.0/-31.03	—
M_b : 0.00	+2.89/-2.99	—	+0.1/-0.11	+2.115/-17.64	-0.15/-0.14	—	-0.00/-0.00	+0.17/-0.17	+0.00/-0.00	+0.26/-0.25	+0.26/-0.25	—
M_b : 1.00	+2.87/-2.99	—	+0.2/-0.14	+24.15/-19.44	+0.10/-0.12	—	-0.00/-0.00	+0.18/-0.18	+0.00/-0.00	+0.27/-0.26	+0.27/-0.26	—
M_b : 1.20	+2.88/-2.96	—	+0.22/-0.15	+26.63/-21.11	+0.17/-0.19	—	-0.00/-0.00	+0.17/-0.17	+0.00/-0.00	+0.26/-0.25	+0.26/-0.25	—
M_b : 1.30	+2.85/-2.97	—	+0.22/-0.14	+29.94/-22.86	-0.28/-0.30	—	-0.00/-0.00	+0.17/-0.17	+0.00/-0.00	+0.26/-0.25	+0.26/-0.25	—
M_b : 1.40	+2.93/-3.08	—	+0.30/-0.20	+33.63/-24.48	+0.07/-0.08	—	+0.00/-0.00	+0.18/-0.18	+0.00/-0.00	+0.27/-0.26	+0.27/-0.26	—
M_b : 1.60	+2.91/-3.07	—	+0.21/-0.14	+37.67/-26.30	-0.44/-0.33	—	-0.00/-0.00	+0.18/-0.18	+0.00/-0.00	+0.27/-0.26	+0.27/-0.26	—
M_b : 1.80	+2.87/-3.03	—	+0.19/-0.13	+41.55/-27.87	+0.19/-0.02	—	-0.00/-0.00	+0.18/-0.18	+0.00/-0.00	+0.27/-0.26	+0.27/-0.26	—
M_b : 2.00	+2.87/-3.02	—	+0.18/-0.18	+43.74/-29.78	+0.36/-0.23	—	+0.00/-0.00	+0.19/-0.18	+0.00/-0.00	+0.28/-0.27	+0.28/-0.27	—
M_b : 2.10	+2.86/-3.04	—	+0.22/-0.13	+49.29/-31.36	+0.11/-0.10	—	-0.00/-0.00	+0.18/-0.18	+0.00/-0.00	+0.28/-0.28	+0.28/-0.28	—
M_b : 2.30	+2.80/-2.93	—	+0.33/-0.21	+51.09/-32.74	-0.20/-0.17	—	-0.00/-0.00	+0.19/-0.18	+0.00/-0.00	+0.28/-0.26	+0.28/-0.26	—
M_b : 2.40	+2.76/-2.88	—	+0.25/-0.16	+53.03/-34.53	-0.30/-0.14	—	-0.00/-0.00	+0.18/-0.18	+0.00/-0.00	+0.27/-0.26	+0.27/-0.26	—
M_b : 2.50	+2.97/-3.03	—	+0.18/-0.11	+61.35/-34.20	-0.47/-0.38	—	-0.00/-0.00	+0.17/-0.17	+0.00/-0.00	+0.27/-0.25	+0.27/-0.25	—
M_b : 2.70	+2.91/-2.99	—	+0.17/-0.11	+18.45/-15.83	+0.13/-0.05	—	-0.00/-0.00	+0.17/-0.17	+0.00/-0.00	+0.27/-0.25	+0.27/-0.25	—
dbBoson	+3.27/-3.36	—	+6.52/-4.28	+4.75/-6.43	-1.06/-1.11	—	-0.00/-0.00	+0.24/-0.23	+0.00/-0.00	+0.37/-0.33	+0.37/-0.33	—
qcd	—	—	—	—	—	+27.00/-21.26	—	—	—	—	—	—
stes	+0.80/-1.07	—	-0.10/-0.07	+5.50/-5.51	-0.18/-0.22	—	+0.00/-0.00	+0.22/-0.21	+0.00/-0.00	+0.32/-0.29	+0.32/-0.29	—
stat	+1.32/-1.50	+1.86/-1.87	-0.01/-0.03	+7.39/-5.39	+0.51/-0.53	—	-0.00/-0.00	+0.17/-0.17	+0.00/-0.00	+0.26/-0.25	+0.26/-0.25	—
sttW	+2.56/-2.64	-0.72/-3.66	+0.2/-0.30	+13.50/-10.30	-0.27/-0.30	—	+0.00/-0.00	+0.18/-0.18	+0.00/-0.00	+0.29/-0.27	+0.29/-0.27	—
tthbar	+2.00/-2.12	+0.48/-0.24	+0.18/-0.12	+10.09/-7.81	+0.18/-0.17	—	+0.00/-0.00	+0.20/-0.19	+0.00/-0.00	+0.30/-0.28	+0.30/-0.28	—

Table 19.1: Rate effects of systematic uncertainties used in limit combination. The uncertainty sources listed here affect the semileptonic analysis and are not correlated with uncertainties in the other channels. This table details the semileptonic electron channel. This table considers the right-handed signal hypothesis.

Rate Effects of Systematic Uncertainties

Sample	B-tagging	Mass	Mistag	PDF	Pileup	QCD Rate el.	QCD Rate mu	MET	Lepton ID	Isolation	Trigger	W+jets Rate el.	W+jets Rate mu
W jets	+4.30,-3.34	—	+15.71,+10.24	-4.45,-14.57	-0.34,-0.13	—	—	-0.000+0.00	+1.88,-1.88	+0.23,-0.28	+1,-45,-1,51	—	—
Z jets	+3.34,-3.38	—	+5.94,+3.88	+7.30,-7.66	-0.02,-0.36	—	—	+0.000+0.00	+1.92,-1.91	+0.23,-0.28	+1,-51,-1,57	—	—
$M_{\pi^+}/1000$	+2.95,-3.05	—	+0.19,+0.12	-21.46,-17.73	-0.15,-0.07	—	—	+0.000+0.00	+1.62,-1.62	+0.21,-0.25	+1,-25,-1,32	—	—
$M_{\pi^-}/1000$	+2.86,-2.97	—	+0.25,+0.16	-24.44,-16.66	-0.03,-0.05	—	—	-0.006+0.02	+1.52,-1.53	+0.20,-0.24	+1,-28,-1,36	—	—
$M_{\pi^0}/1000$	+2.91,-3.04	—	+0.11,+0.07	-27.64,-21.29	-0.26,-0.29	—	—	-0.006+0.02	+1.39,-1.40	+0.18,-0.22	+1,-24,-1,31	—	—
$M_{\pi^+}/1000$	+2.86,-2.95	—	+0.17,+0.11	-30.01,-22.86	-0.03,-0.02	—	—	-0.005+0.04	+1.35,-1.36	+0.17,-0.21	+1,-26,-1,34	—	—
$M_{\pi^-}/1000$	+2.85,-3.01	—	+0.16,+0.10	-33.07,-24.31	-0.01,-0.03	—	—	-0.006+0.00	+1.25,-1.25	+0.16,-0.19	+1,-24,-1,31	—	—
$M_{\pi^0}/1000$	+2.89,-3.04	—	+0.22,+0.14	-36.05,-25.63	-0.59,-0.55	—	—	-0.006+0.00	+1.23,-1.24	+0.16,-0.19	+1,-24,-1,31	—	—
$M_{\pi^+}/1000$	+2.86,-3.02	—	+0.11,+0.07	-42.14,-27.53	-0.10,-0.21	—	—	-0.01+0.01	+1.23,-1.24	+0.16,-0.19	+1,-24,-1,31	—	—
$M_{\pi^-}/1000$	+2.87,-3.02	—	+0.07,+0.04	-45.99,-29.05	-0.77,-0.77	—	—	-0.01+0.01	+1.14,-1.15	+0.14,-0.17	+1,-21,-1,28	—	—
$M_{\pi^0}/1000$	+2.87,-3.06	—	+0.26,+0.16	-48.71,-31.14	-0.94,-0.94	—	—	-0.006+0.04	+1.03,-1.06	+0.13,-0.16	+1,-16,-1,22	—	—
$M_{\pi^+}/1000$	+2.81,-2.94	—	+0.21,+0.13	-52.23,-32.31	-0.30,-0.20	—	—	-0.001+0.04	+1.10,-1.10	+0.13,-0.16	+1,-18,-1,25	—	—
$M_{\pi^-}/1000$	+2.72,-2.84	—	+0.30,+0.19	-57.13,-34.13	+0.05,+0.13	—	—	-0.001+0.00	+1.08,-1.08	+0.12,-0.15	+1,-13,-1,20	—	—
$M_{\pi^0}/1000$	+2.96,-3.02	—	+0.12,+0.27	-63.63,-41.20	-0.37,-0.46	—	—	-0.001+0.00	+1.78,-1.79	+0.24,-0.28	+1,-23,-1,30	—	—
$M_{\pi^+}/900$	+2.96,-3.03	—	+0.25,+0.16	-19.24,-16.06	-0.16,-0.12	—	—	-0.003+0.03	+1.67,-1.68	+0.22,-0.26	+1,-25,-1,33	—	—
dB ason	+3.80,-3.87	—	+10.37,+6.78	+4.75,-5.89	-0.23,+0.20	—	—	-0.000+0.00	+1.80,-1.81	+0.23,-0.28	+1,-41,-1,48	—	—
qed	—	—	—	—	—	—	—	+169.00,-50.00	—	—	—	—	—
sfs	+0.76,-1.03	—	+0.16,+0.10	+5.98,-5.91	-0.45,-0.56	—	—	+0.000+0.00	+1.67,-1.68	+0.23,-0.27	+1,-21,-1,28	—	—
stt	+1.41,-1.59	+0.54,-2.37	-0.08,-0.05	+6.96,-6.50	-0.28,-0.21	—	—	+0.000+0.00	+1.62,-1.63	+0.23,-0.27	+1,-15,-1,21	—	—
stW	+2.53,-2.62	-0.64,-3.62	+0.21,+0.14	+3.40,-10.22	-0.27,-0.26	—	—	+0.000+0.00	+1.71,-1.71	+0.23,-0.27	+1,-20,-1,27	—	—
tthir	+2.01,-2.12	+2.79,-1.07	+0.24,+0.16	+9.37,-7.65	-0.32,+0.31	—	—	-0.001+0.01	+1.67,-1.67	+0.23,-0.27	+1,-18,-1,24	—	—

Table 19.2: Rate effects of systematic uncertainties used in limit combination. The uncertainty sources listed here affect the semileptonic analysis and are not correlated with uncertainties in the other channels. This table details the semileptonic muon channel. This table considers the right-handed signal hypothesis.

CHAPTER 19. APPENDIX

Rate Effects of Systematic Uncertainties

Sample	QCD Uncertainty	top-tagging	W-tagging	Trigger	ttbar Rate
$M_{b^*}=1000$	—	+12.50,-11.11	+7.60,-7.06	+0.14,-0.14	—
$M_{b^*}=1100$	—	+12.50,-11.11	+7.60,-7.06	+0.07,-0.07	—
$M_{b^*}=1200$	—	+12.50,-11.11	+7.60,-7.06	+0.04,-0.04	—
$M_{b^*}=1300$	—	+12.50,-11.11	+7.60,-7.06	+0.03,-0.03	—
$M_{b^*}=1400$	—	+12.50,-11.11	+7.60,-7.06	+0.02,-0.02	—
$M_{b^*}=1500$	—	+12.50,-11.11	+7.60,-7.06	+0.02,-0.02	—
$M_{b^*}=1600$	—	+12.50,-11.11	+7.60,-7.06	+0.01,-0.01	—
$M_{b^*}=1700$	—	+12.50,-11.11	+7.60,-7.06	+0.01,-0.01	—
$M_{b^*}=1800$	—	+12.50,-11.11	+7.60,-7.06	+0.01,-0.01	—
$M_{b^*}=1900$	—	+12.50,-11.11	+7.60,-7.06	+0.01,-0.01	—
$M_{b^*}=2000$	—	+12.50,-11.11	+7.60,-7.06	+0.01,-0.01	—
$M_{b^*}=800$	—	+12.50,-11.11	+7.60,-7.06	+0.19,-0.19	—
$M_{b^*}=900$	—	+12.50,-11.11	+7.60,-7.06	+0.28,-0.28	—
qcd	+28.14,-27.56	—	—	—	—
sts	—	+12.50,-11.11	+7.60,-7.06	+nan,+nan	—
stt	—	+12.50,-11.11	+7.60,-7.06	+0.13,-0.13	—
sttW	—	+12.50,-11.11	+7.60,-7.06	+0.09,-0.09	—
ttbar	—	—	+7.60,-7.06	+0.10,-0.10	+22.00,-18.03

Table 19.3: Rate effects of systematic uncertainties used in limit combination. The uncertainty sources listed here affect the all-hadronic analysis and are not correlated with uncertainties in the other channels. This table considers the right-handed signal hypothesis.

CHAPTER 19. APPENDIX

Rate Effects of Systematic Uncertainties

Sample	Flat Uncertainty	W+jets Rate
WJets	+16.50,-14.16	+30.00,-23.08
ZJets	+16.50,-14.16	—
$M_{b^*}=1000$	+32.80,-24.70	—
$M_{b^*}=1100$	+32.80,-24.70	—
$M_{b^*}=1200$	+32.80,-24.70	—
$M_{b^*}=1300$	+32.80,-24.70	—
$M_{b^*}=1400$	+32.80,-24.70	—
$M_{b^*}=1500$	+32.80,-24.70	—
$M_{b^*}=1600$	+32.80,-24.70	—
$M_{b^*}=1700$	+32.80,-24.70	—
$M_{b^*}=1800$	+32.80,-24.70	—
$M_{b^*}=1900$	+32.80,-24.70	—
$M_{b^*}=2000$	+32.80,-24.70	—
$M_{b^*}=800$	+32.80,-24.70	—
$M_{b^*}=900$	+32.80,-24.70	—
diBoson	+16.50,-14.16	—
sttW	+16.50,-14.16	—
ttbar	+16.50,-14.16	—

Table 19.4: Rate effects of systematic uncertainties used in limit combination. The uncertainty sources listed here affect the Dilepton analysis and are not correlated with uncertainties in the other channels. This table considers the right-handed signal hypothesis.

Rate Effects of Systematic Uncertainties

Sample	JER	JES	Q^2	Dif boson Rate	Luminosity	s Channel Rate	tW Channel Rate	t Channel Rate	tbar Rate	Z+Jets Rate
W Jets	+0.26,-0.17	+3.01,-3.28	—	—	—	—	—	—	—	—
ZJets	-4.73,+4.80	-2.19,-0.30	—	—	+2.63,-2.57	—	—	—	—	+20.00,-16.67
M_b^* =1000	-0.47,+0.27	-0.02,+0.16	—	—	+2.63,-2.57	—	—	—	—	—
M_b^* =1100	-0.72,+0.69	+0.41,-0.36	—	—	+2.63,-2.57	—	—	—	—	—
M_b^* =1200	+0.05,+0.37	+0.09,-0.05	—	—	+2.63,-2.57	—	—	—	—	—
M_b^* =1300	-0.14,+1.11	+0.67,-0.56	—	—	+2.63,-2.57	—	—	—	—	—
M_b^* =1400	-0.73,+0.16	-0.10,-0.05	—	—	+2.63,-2.57	—	—	—	—	—
M_b^* =1500	+0.07,-0.38	+0.07,-0.51	—	—	+2.63,-2.57	—	—	—	—	—
M_b^* =1600	-1.12,+0.14	-0.30,-0.69	—	—	+2.63,-2.57	—	—	—	—	—
M_b^* =1700	-0.99,+0.58	-0.17,+0.12	—	—	+2.63,-2.57	—	—	—	—	—
M_b^* =1800	-0.50,-0.17	-0.32,-0.08	—	—	+2.63,-2.57	—	—	—	—	—
M_b^* =1900	-0.55,+0.61	+0.16,-0.44	—	—	+2.63,-2.57	—	—	—	—	—
M_b^* =2000	-0.76,+0.61	-0.31,+0.82	—	—	+2.63,-2.57	—	—	—	—	—
M_b^* =800	-0.12,+0.73	+1.04,+0.43	—	—	+2.63,-2.57	—	—	—	—	—
M_b^* =900	-0.41,+0.78	+0.45,+0.30	—	—	+2.63,-2.57	—	—	—	—	—
diBoson	+2.20,-1.15	+2.05,-0.97	—	+30.00,-23.08	+2.63,-2.57	—	—	—	—	—
qcd	—	—	—	—	—	—	—	—	—	—
sts	+0.08,+0.34	+1.52,-1.36	—	—	+2.63,-2.57	+30.00,-23.08	—	—	—	—
stt	-0.97,+0.40	+1.73,-2.86	-14.34,-2.92	—	+2.63,-2.57	—	+15.00,-13.04	—	—	—
sttW	-0.21,+0.37	+0.81,-1.04	—	—	+2.63,-2.57	—	+20.00,-16.67	—	—	—
ttbar	-0.48,+0.41	-0.31,-0.23	+9.23,-4.78	—	+2.63,-2.57	—	+5.30,-5.03	—	—	—

Table 19.5: Rate effects of systematic uncertainties used in limit combination. The uncertainty sources listed here are correlated over multiple channels. This table considers the right-handed signal hypothesis And the semileptonic electron analysis.

Rate Effects of Systematic Uncertainties

Sample	JER	JES	Q^2	DiBoson Rate	Luminosity	s Channel Rate	tW Channel Rate	t Channel Rate	ttbar Rate	Z+Jets Rate
W jets	+0.43,-0.74	+2.10,-3.19	—	—	—	—	—	—	—	—
Z jets	+1.41,-2.14	+2.92,+7.70	—	—	+2.63,-2.57	—	—	—	—	+20.00,-16.67
$M_b^* = 1000$	-0.22,+0.41	+0.53,+0.13	—	—	+2.63,-2.57	—	—	—	—	—
$M_b^* = 1100$	-0.47,+0.13	+0.04,+0.15	—	—	+2.63,-2.57	—	—	—	—	—
$M_b^* = 1200$	-0.59,+0.00	-0.05,-0.93	—	—	+2.63,-2.57	—	—	—	—	—
$M_b^* = 1300$	-0.59,+0.19	-0.55,-0.05	—	—	+2.63,-2.57	—	—	—	—	—
$M_b^* = 1400$	-0.40,+0.53	+0.23,-0.36	—	—	+2.63,-2.57	—	—	—	—	—
$M_b^* = 1500$	-0.35,+0.38	+0.42,-0.93	—	—	+2.63,-2.57	—	—	—	—	—
$M_b^* = 1600$	-0.88,+0.17	-0.47,-0.10	—	—	+2.63,-2.57	—	—	—	—	—
$M_b^* = 1700$	-0.33,-0.04	-0.14,+0.03	—	—	+2.63,-2.57	—	—	—	—	—
$M_b^* = 1800$	-0.08,+0.47	-0.39,0.07	—	—	+2.63,-2.57	—	—	—	—	—
$M_b^* = 1900$	-0.10,-0.25	+0.35,-0.15	—	—	+2.63,-2.57	—	—	—	—	—
$M_b^* = 2000$	-0.13,-0.11	+0.43,-0.51	—	—	+2.63,-2.57	—	—	—	—	—
$M_b^* = 800$	+0.12,+0.23	+0.63,-0.25	—	—	+2.63,-2.57	—	—	—	—	—
$M_b^* = 900$	-0.15,+0.51	+0.54,+0.25	—	—	+2.63,-2.57	—	—	—	—	—
diBoson	-1.95,-0.25	+1.88,-5.76	—	+30.00,-23.08	+2.63,-2.57	—	—	—	—	—
qcd	—	—	—	—	—	—	—	—	—	—
sts	-0.38,-0.49	+1.11,-0.99	—	—	+2.63,-2.57	+30.00,23.08	—	—	—	—
stt	-0.30,-0.68	+2.69,-2.35	-17.72,+7.61	—	+2.63,-2.57	—	+15.00,-13.04	—	—	—
sttW	-0.30,+0.38	+1.33,-1.08	—	—	+2.63,-2.57	—	+20.00,-16.67	—	—	—
ttbar	-0.46,+0.10	-0.69,-0.05	+9.31,+0.11	—	+2.63,-2.57	—	+5.30,-5.03	—	—	—

Table 19.6: Rate effects of systematic uncertainties used in limit combination. The uncertainty sources listed here are correlated over multiple channels. This table considers the right-handed signal hypothesis And the semileptonic muon analysis.

Rate Effects of Systematic Uncertainties

Sample	JER	JES	Q^2	Diboson Rate	Luminosity	s Channel Rate	t Channel Rate	tbar	Z+Jets Rate
W Jets	+0.00,+0.00	+0.00,+0.00	—	—	+2.63,-2.57	—	—	—	—
ZJets	-17.13,-45.69	-17.16,-17.13	—	—	+2.63,-2.57	—	—	—	+20.00,-16.67
$M_{b^*}=1000$	+0.00,-0.00	-0.00,+0.00	—	—	+2.63,-2.57	—	—	—	—
$M_{b^*}=1100$	+0.00,+0.00	-0.00,+0.00	—	—	+2.63,-2.57	—	—	—	—
$M_{b^*}=1200$	-0.00,-0.01	-0.01,+0.00	—	—	+2.63,-2.57	—	—	—	—
$M_{b^*}=1300$	-0.00,+0.00	-0.01,-0.00	—	—	+2.63,-2.57	—	—	—	—
$M_{b^*}=1400$	-0.00,-0.02	-0.03,+0.01	—	—	+2.63,-2.57	—	—	—	—
$M_{b^*}=1500$	-0.01,-0.01	-0.03,+0.01	—	—	+2.63,-2.57	—	—	—	—
$M_{b^*}=1600$	-0.01,+0.00	-0.02,+0.01	—	—	+2.63,-2.57	—	—	—	—
$M_{b^*}=1700$	+0.01,-0.01	-0.03,+0.02	—	—	+2.63,-2.57	—	—	—	—
$M_{b^*}=1800$	-0.00,-0.02	-0.04,+0.01	—	—	+2.63,-2.57	—	—	—	—
$M_{b^*}=1900$	+0.00,-0.01	-0.04,+0.03	—	—	+2.63,-2.57	—	—	—	—
$M_{b^*}=2000$	+0.02,+0.00	-0.03,+0.05	—	—	+2.63,-2.57	—	—	—	—
$M_{b^*}=800$	+0.00,-0.00	+0.00,+0.00	—	—	+2.63,-2.57	—	—	—	—
$M_{b^*}=900$	+0.00,-0.00	-0.00,+0.00	—	—	+2.63,-2.57	—	—	—	—
diBoson	-0.00,+0.00	-0.00,-0.00	—	+30.00,-23.08	+2.63,-2.57	—	—	—	—
sttW	-0.00,-0.00	-0.00,+0.00	—	—	+2.63,-2.57	+20.00,-16.67	—	—	—
tbar	-0.00,+0.00	+0.00,+0.00	—	—	+2.63,-2.57	—	—	+5.30,-5.03	—

Table 19.7: Rate effects of systematic uncertainties used in limit combination. The uncertainty sources listed here are correlated over multiple channels. This table considers the right-handed signal hypothesis And the dilepton analysis.

Rate Effects of Systematic Uncertainties

Sample	JER	JES	Q^2	Diboson Rate	Luminosity	s Channel Rate	tW Channel Rate	t Channel Rate	ttbar Rate	Z+Jets Rate
$M_b^* = 1000$	-0.81,+0.51	+17.91,-21.34	—	—	+2.63,-2.57	—	—	—	—	—
$M_b^* = 1100$	-0.51,+0.60	+9.07,-12.13	—	—	+2.63,-2.57	—	—	—	—	—
$M_b^* = 1200$	-0.41,+0.60	+6.12,-9.76	—	—	+2.63,-2.57	—	—	—	—	—
$M_b^* = 1300$	-0.42,+0.41	+4.98,-8.06	—	—	+2.63,-2.57	—	—	—	—	—
$M_b^* = 1400$	-0.53,+0.40	+4.20,-7.65	—	—	+2.63,-2.57	—	—	—	—	—
$M_b^* = 1500$	-0.46,+0.42	+4.50,-7.76	—	—	+2.63,-2.57	—	—	—	—	—
$M_b^* = 1600$	-0.48,+0.37	+3.79,-7.33	—	—	+2.63,-2.57	—	—	—	—	—
$M_b^* = 1700$	-0.34,+0.35	+3.91,-6.43	—	—	+2.63,-2.57	—	—	—	—	—
$M_b^* = 1800$	-0.48,+0.39	+3.71,-7.64	—	—	+2.63,-2.57	—	—	—	—	—
$M_b^* = 1900$	-0.46,+0.44	+3.31,-7.12	—	—	+2.63,-2.57	—	—	—	—	—
$M_b^* = 2000$	-0.46,+0.41	+3.14,-7.29	—	—	+2.63,-2.57	—	—	—	—	—
$M_b^* = 800$	-0.00,+0.56	+29.42,-25.25	—	—	+2.63,-2.57	—	—	—	—	—
$M_b^* = 900$	-0.18,+0.42	+46.46,-35.69	—	—	+2.63,-2.57	—	—	—	—	—
qcd	—	—	—	—	—	—	—	—	—	—
sts	+nan,+nan	+nan,-nan	—	—	+2.63,-2.57	+30.00,-23.08	—	—	—	—
stt	-0.11,+17.70	+47.87,-16.85	—	—	+2.63,-2.57	—	+15.00,-13.04	—	—	—
sttW	+0.01,-0.00	+17.42,-13.16	—	—	+2.63,-2.57	—	+20.00,-16.67	—	—	—
ttbar	-0.22,+1.05	+13.20,-14.75	+16.24,-23.58	—	—	—	—	—	—	—

Table 19.8: Rate effects of systematic uncertainties used in limit combination. The uncertainty sources listed here are correlated over multiple channels. This table considers the right-handed signal hypothesis And the all hadronic analysis.

Bibliography

- [1] C. L. Bennett *et al.*, “The microwave anisotropy probe (map) mission,” *Astrophys. J.*, vol. 583, p. 1, 2003.
- [2] F. An *et al.*, “Observation of electron-antineutrino disappearance at Daya Bay,” *Phys.Rev.Lett.*, vol. 108, p. 171803, 2012.
- [3] T. Appelquist, H.-C. Cheng, and B. A. Dobrescu, “Bounds on universal extra dimensions,” *Phys. Rev. D*, vol. 64, p. 035002, Jun 2001. [Online]. Available: <http://link.aps.org/doi/10.1103/PhysRevD.64.035002>
- [4] M. Schmaltz and D. Tucker-Smith, “Little higgs theories,” *Annual Review of Nuclear and Particle Science*, vol. 55, no. 1, pp. 229–270, 2005.
- [5] L. Vecchi, “The Natural Composite Higgs,” 2013.
- [6] R. Chivukula, E. H. Simmons, and J. Terning, “Limits on noncommuting extended technicolor,” *Phys.Rev.*, vol. D53, pp. 5258–5267, 1996.
- [7] S. Chatrchyan *et al.*, *CMS Physics: Technical Design Report Volume 1: Detector*

BIBLIOGRAPHY

- Performance and Software*, ser. Technical Design Report CMS. Geneva: CERN, 2006, there is an error on cover due to a technical problem for some items.
- [8] D0 Collaboration, “Search for w’ boson resonances decaying to a top quark and a bottom quark,” *Phys. Rev. Lett.*, vol. 100, p. 211803, May 2008. [Online]. Available: <http://link.aps.org/doi/10.1103/PhysRevLett.100.211803>
- [9] V. M. Abazov *et al.*, “Search for $W' \rightarrow tb$ resonances with left- and right-handed couplings to fermions,” *Phys.Lett.*, vol. B699, pp. 145–150, 2011.
- [10] “Search for narrow t + b resonances in the leptonic final state at $\sqrt{s} = 8$ tev,” CERN, Geneva, Tech. Rep. CMS-PAS-B2G-12-010, 2013.
- [11] “Search for leptonic decays of W’ bosons in pp collisions at $\sqrt{s}=8$ TeV,” CERN, Geneva, Tech. Rep. CMS-PAS-EXO-12-060, 2013.
- [12] “Search for W’/technirho in WZ using leptonic final states,” CERN, Geneva, Tech. Rep. CMS-PAS-EXO-12-025, 2013.
- [13] ATLAS, “Search for tb resonances in proton-proton collisions at $\sqrt{s}=7$ TeV with the atlas detector,” *Phys. Rev. Lett.*, vol. 109, p. 081801, Aug 2012. [Online]. Available: <http://link.aps.org/doi/10.1103/PhysRevLett.109.081801>
- [14] “Search for BSM $t\bar{t}$ Production in the Boosted All-Hadronic Final State,” CERN, Geneva, Tech. Rep. CMS-PAS-EXO-11-006, 2011.

BIBLIOGRAPHY

- [15] T. Muller, J. Ott, and J. Wagner-Kuhr, “theta - a framework for template-based modeling and inference,” CMS Internal Note 2010/017, 2010.
- [16] M. Czakon, P. Fiedler, and A. Mitov, “Total Top-Quark Pair-Production Cross Section at Hadron Colliders Through $O(\frac{4}{S})$,” *Phys.Rev.Lett.*, vol. 110, no. 25, p. 252004, 2013.
- [17] N. Kidonakis, “Differential and total cross sections for top pair and single top production,” pp. 831–834, 2012.
- [18] E. Boos *et al.*, “CompHEP 4.4: Automatic computations from Lagrangians to events,” *Nucl.Instrum.Meth.*, vol. A534, pp. 250–259, 2004.
- [19] Z. Sullivan, “Fully differential w’ production and decay to next-to-leading order in qcd,” *Phys. Rev.*, vol. D66, 2002.
- [20] “8 TeV Jet Energy Corrections and Uncertainties based on 19.8 fb^{-1} of data in CMS,” Oct 2013.
- [21] Y. L. Dokshitzer, G. D. Leder, S. Moretti, and B. R. Webber, “Better Jet Clustering Algorithms,” *JHEP*, vol. 08, p. 001, 1997.
- [22] M. Wobisch and T. Wengler, “Hadronization corrections to jet cross sections in deep- inelastic scattering,” 1998.
- [23] M. Cacciari and G. P. Salam, “Dispelling the $N^{**}3$ myth for the k(t) jet-finder,” *Phys. Lett. B*, vol. 641, pp. 57–61, 2006.

BIBLIOGRAPHY

- [24] M. Cacciari, G. P. Salam, and G. Soyez, “FastJet User Manual,” *Eur.Phys.J.*, vol. C72, p. 1896, 2012.
- [25] “A Cambridge-Aachen (C-A) based Jet Algorithm for boosted top-jet tagging,” CERN, Geneva, Tech. Rep. CMS-PAS-JME-09-001, 2009.
- [26] J. Group, “Jet Energy Corrections and Uncertainties. Detector Performance Plots for 2012.”
- [27] “Jet performance in pp collisions at $\sqrt{s} = 7$ tev,” *CMS PAS JME-10-003*, 2010.
- [28] “Boosted Top Jet Tagging at CMS,” CERN, Geneva, Tech. Rep. CMS-PAS-JME-13-007, 2014.
- [29] J. Thaler and K. Van Tilburg, “Maximizing Boosted Top Identification by Minimizing N-subjettiness,” *JHEP*, vol. 1202, p. 093, 2012.
- [30] “Performance of b tagging at $\sqrt{s}=8$ tev in multijet, ttbar and boosted topology events,” CERN, Geneva, Tech. Rep. CMS-PAS-BTV-13-001, 2013.
- [31] “Search for Anomalous Top Quark Pair Production in the Boosted All-Hadronic Final State using pp Collisions at $\sqrt{s} = 8$ TeV,” CERN, Geneva, Tech. Rep. CMS-PAS-B2G-12-005, 2013.
- [32] D. Bourilkov, R. C. Group, and M. R. Whalley, “LHAPDF: PDF use from the Tevatron to the LHC,” 2006.

BIBLIOGRAPHY

- [33] “CMS Luminosity Based on Pixel Cluster Counting - Summer 2013 Update,” CERN, Geneva, Tech. Rep. CMS-PAS-LUM-13-001, 2013.
- [34] S. Chatrchyan *et al.*, “Search for $W \rightarrow tb$ decays in the lepton + jets final state in pp collisions at $\sqrt{s} = 8$ TeV,” *JHEP*, vol. 1405, p. 108, 2014.
- [35] T. M. Tait and C.-P. Yuan, “Single top quark production as a window to physics beyond the standard model,” *Phys.Rev.*, vol. D63, p. 014018, 2000.
- [36] G. Aad *et al.*, “Search for single b^* -quark production with the ATLAS detector at $\sqrt{s} = 7$ TeV,” *Phys.Lett.*, vol. B721, pp. 171–189, 2013.
- [37] P. M. Kevin Nash, “Search for single b^* -quark production in the all hadronic final state.”
- [38] G. C. X. M. S. S. H. Zhang and S. Zhu, “Search for singly produced b^* decaying to Wt in the lepton+jets channel with the CMS detector at $s = 8$ TeV.”
- [39] H. Z. Rachel Bartek, Freya Blekman, “Search for single b^* -quark production in the dilepton final state.”

Education

- Ph.D. Experimental Particle Physics, Johns Hopkins University, February 2015.
- B.S. Physics, James Madison University, 2009